

Sheared convective boundary layers

turbulence kinetic energy
and entrainment
dynamics

Joel S. Schröter

Sheared convective boundary layers TKE and entrainment dynamics J. S. Schröter

Propositions

1. In sheared atmospheric boundary layers the so-called 'Process Partitioning' should not be applied to ensemble averaged turbulence properties such as turbulent kinetic energy. (this thesis)
2. Wave drag at the top of daytime convective boundary layers contributes significantly to the momentum exchange between the boundary layer and the higher troposphere. (this thesis)
3. The dispute over the reasons for the extinction of the American mammoth resembles the 'climate change debate', as it involves an inter-disciplinary debate that is not free from ideological interferences.
4. The recent discovery of epigenetic mechanisms has surprised professional biologists more than scientific amateurs.
5. The potential impacts on the climate of large scale use of wind-energy gets too little attention.
6. To think out of the box is also very useful to get to know the boundaries of the box.
7. Various reasons that are supposed to explain the 'Brexit' can ultimately be traced back to the UK's unique geographical situation.
8. One does not have to believe in 'Free Will' to have ethical values, to experience a moral impetus or to feel a desire for the Good.

Propositions belonging to the thesis, entitled

'Sheared convective boundary layers: turbulence kinetic energy and entrainment dynamics'

Joel Schröter

Wageningen, 5 June 2018

**Sheared convective boundary layers:
turbulence kinetic energy and
entrainment dynamics**

Joel S. Schröter

Thesis committee

Promotor

Prof. Dr A.A.M. Holtslag
Professor of Meteorology
Wageningen University & Research

Co-promotor

Dr A.F. Moene
Associate professor, Meteorology and Air Quality Group
Wageningen University & Research

Other members

Prof. Dr E. Fedorovich, University of Oklahoma, Norman, USA
Dr J.P. Mellado, Max Planck Institute for Meteorology, Hamburg, Germany
Prof. Dr B. van de Wiel, Delft University of Technology
Prof. Dr A.J.F. Hoitink, Wageningen University & Research

This research was conducted under the auspices of the SENSE Research School

Sheared convective boundary layers: turbulence kinetic energy and entrainment dynamics

Joel S. Schröter

Thesis

submitted in fulfilment of the requirements for the degree of doctor
at Wageningen University
by the authority of the Rector Magnificus,
Prof. Dr A.P.J. Mol,
in the presence of the
Thesis Committee appointed by the Academic Board
to be defended in public
on Tuesday 5 June 2018
at 4 p.m. in the Aula.

Joel S. Schröter

Sheared convective boundary layers: turbulence kinetic energy and entrainment dynamics,
256 pages.

PhD thesis, Wageningen University, Wageningen, the Netherlands (2018)

With references, with summary in English

ISBN: 978-94-6343-265-8

DOI: <https://doi.org/10.18174/444909>

Contents

1	Introduction	9
1.1	The turbulent atmospheric boundary layer	9
1.2	Current understanding of shear effects on entrainment in CBLs	13
1.3	General research objectives	15
1.4	An additional research project: the inertial oscillation of mid-latitude CBLs	16
2	Theory and preliminaries	19
2.1	An idealized representation of the atmospheric boundary layer	20
2.2	High Reynolds number turbulence	21
2.3	Statistical description of turbulent flows	25
2.4	Governing equations	27
2.4.1	Budgets of mean variables	28
2.4.2	Velocity variances and the TKE budget	30
2.5	Basic characteristics of the CBL	33
2.5.1	CBL buoyancy dynamics	33
2.5.2	Sheared CBL wind dynamics	37
2.5.3	The 0 th -order model (ZOM) approach	38
2.5.4	The equilibrium entrainment regime and the constant ZOM-entrainment ratio	43
2.6	The impact of the stratified free atmosphere on the entrainment zone dynamics according to Garcia and Mellado (2014)	50
2.7	Research questions and preliminary results	59
2.7.1	Evaluation of Conzemius and Fedorovich's (2007) ZOM for sheared CBLs	60
2.7.2	Particular research objectives with respect to the equilibrium entrainment regime	62
2.7.3	Research questions	64
3	LES of sheared CBLs	67
3.1	Principles of Large Eddy Simulations	68
3.2	Experimental setup	69
3.2.1	General aspects of the LES experimental setup	70
3.2.2	The choice of the LES physical parameter space	73
3.2.3	Spatial flow discretization and computational significance	75
3.3	Data preparations and classification	78

3.4	LESs of sheared CBLs – first results	80
3.4.1	Evolution of the CBL structure	81
3.4.2	EZ structure and entrainment ratio	81
4	The integral TKE-budget of sheared CBLs	89
4.1	Analysis of the integral TKE-budget	89
4.1.1	Preliminary considerations	89
4.1.2	The integrated TKE budget	90
4.1.3	The TKE budget of the purely convective CBL	92
4.1.4	The TKE budget of CBLs with varying shear	96
4.2	Parameterizing the integral TKE-budget of sheared CBLs	114
4.2.1	General considerations	114
4.2.2	A simplified reference flow: sheared CBLs under a neutral free atmosphere	117
4.2.3	Scaling the integral TKE budget of sheared CBLs	119
4.2.4	Pragmatic parametrization of the TKE budget.	126
5	A 0th-order TKE-model for sheared CBLs	127
5.1	Derivation of a new 0 th -order model (NZO)	127
5.1.1	Formulation of TKE-budget in terms of ZOM variables	127
5.1.2	The NZO TKE-budget terms versus LES	132
5.2	The CFM and process partitioning	136
5.3	Comparison of NZO and CFM to LES	137
5.3.1	NZO and CFM – comparison of the buoyancy terms	138
5.3.2	NZO and CFM – entrainment velocity	139
5.4	Equilibrium entrainment and the NZO vertical structure	140
6	Direct interfacial influences on the entrainment zone structure of sheared CBLs	145
6.1	A preliminary evaluation of the problem	146
6.2	Integral scales for the quasi-stationary CBL with varying wind shear	149
6.2.1	The integral entrainment ratio A_S	150
6.2.2	Scaling the local buoyancy increment Δb_{zi} for $S_* > 0$	154
6.3	Influence of shear on interfacial turbulence, entrainment and the EZ buoyancy structure	155
6.3.1	Shear dependence of the eddy penetration depth δ	156
6.3.2	Significance of δ , b_δ and the EZ buoyancy fluctuations	159
6.3.3	Interfacial effects on entrainment	160
6.3.4	Interfacial effects on the buoyancy structure	164
6.3.5	Scaling of direct interfacial influences in the neutral limit	168
7	Discussion	169
7.1	Empirical evidence and simple arguments for Eulerian Partitioning	169
7.2	The neutral limit of sheared CBLs	171
7.2.1	DNSs of neutral BLs as reference base	171
7.2.2	The NZO in the neutral limit	172
7.2.3	The integral TKE-budget in the neutral limit	174
7.2.4	Conclusions	176

7.3	Locality of turbulence in neutral BLs and its implications	177
7.3.1	Interfacial length scale	177
7.3.2	Coupling between upper and lower half of the neutral EZ	177
7.3.3	Entrainment and momentum dynamics in a neutral BL	178
7.3.4	The character of the integral length scale $\sim z_S$	179
7.4	The structure of turbulence shear-production in CBLs	180
7.4.1	Decoupling between entrainment and TKE shear-production in the surface- and mixed-layer	180
7.4.2	Shear-induced variation of the EZ turbulence regime and the generation of gravity waves	183
8	Summary and perspectives	189
8.1	Summary of the most relevant findings	189
8.1.1	The integrated TKE-budget and a 0 th -order model for quasi-stationary sheared CBLs	189
8.1.2	Deviations from the linear characteristics due to local interfacial processes	191
8.2	Perspectives	192
A	The critical Richardson number for CBLs, $Ri_{U,B}$	197
B	The NZO in the neutral limit: Reanalysis of Jonker <i>et al.</i>'s (2013) DNS results	199
C	Mutual rescaling of the CFM and the NZO	205
D	TKE budget of an independent LES-CBL	207
E	Inertial Oscillations and surface stress in the CBL	211
E.1	Introduction	212
E.2	Governing equations	215
E.3	Convective boundary layer model	217
E.4	Limiting cases of the CBL wind oscillations	222
E.5	CBL wind oscillations and the general stability dependence	233
E.6	Conclusions	240
E.7	Appendix	241
	Financial support / colophon	253
	SENSE Certificate	255

Chapter 1

Introduction

In this thesis we investigate fundamental aspects of atmospheric turbulence, which is generated by the direct impact of the Earth's surface on the lowest part of the atmosphere. This surface-induced turbulence creates a very distinct layer, which is called the turbulent 'atmospheric boundary layer' (ABL). The ABL (Figure 1.1) forms a very active zone between the surface and the higher, more quiescent parts of the troposphere¹, which is also called 'free troposphere' or 'free atmosphere' (FA, henceforth). The ABL is closely coupled to the Earth's surface, which means that its dynamics and its properties, such as wind velocity, temperature, humidity and the concentration of pollutants are largely determined by intensive exchange processes with the surface. Due to its intermediate position, the ABL also interacts and exchanges properties with the FA above. For example, moist thermal updrafts that form in the ABL and then overshoot into the FA, are the source for shallow and deep convective clouds (Figure 1.1). Stress divergence in the ABL due to surface friction is a major cause for the filling of cyclones and the related large scale vertical motions (Ekman pumping). Hence the ABL is coupled to various dynamical processes in the higher troposphere and therefore plays a crucial role in the weather system. However, the final importance of the ABL is given by the fact that it is the part of the atmosphere that environs practically all life on Earth. Thus, to predict the state of the ABL is the ultimate aim of any 'weather forecast'.

In the remainder of this chapter we first present some basic features of the turbulent ABL². We then introduce our basic research objective, which will be further elaborated in the following chapters.

1.1 The turbulent atmospheric boundary layer

Commonly the ABL is defined as the part of the atmosphere that *"is directly influenced by the presence of the Earth surface and responds to surface forcings within a time scale of an hour or less"* (Stull, 1988). A time scale of 'an hour or less',

¹The atmosphere above the ABL is more quiescent in terms of mean turbulence intensity, but some weather phenomena (e.g. thunderstorms, etc.) occurring there are associated with vigorous turbulence.

²Unless mentioned otherwise, we refer to the textbooks of Stull (1988); Wyngaard (2010)

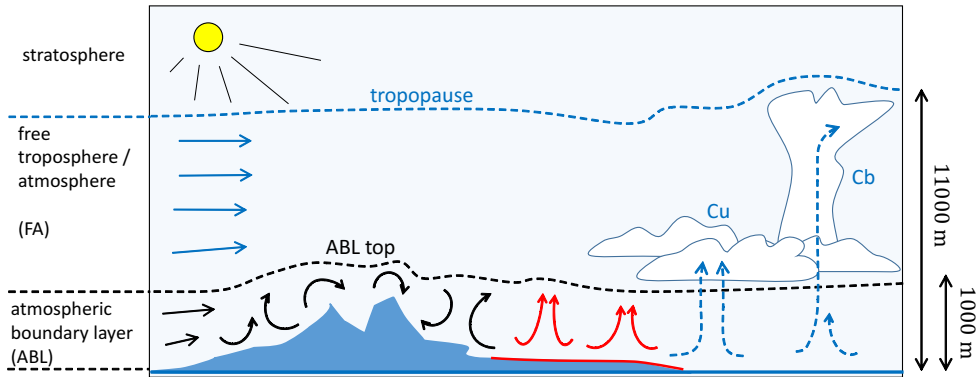


Figure 1.1: Schematic, strongly simplified vertical cross section through the Earth's atmosphere. Black arrows indicate turbulence in a shear-driven ABL. Red arrows represent the rising plumes in a dry convective ABL without clouds formation. Blue dashed arrows indicate plumes that reach a critical level for condensation, which leads to formation of e.g. Cumulus (Cu) or even Cumulonimbus (Cb) clouds. The resulting cloud-topped convection consists of a cloud layer that is connected with the ABL below.

which is small by meteorological standards, is very typical for atmospheric turbulence. The reason that the above definition does not mention turbulence explicitly, is that in very stably stratified ABLs also other flow phenomena, such as gravity waves and terrain-induced gravity flows can contribute significantly to the ABL dynamics. However, in practically all other meteorologically relevant conditions, ABL dynamics are dominated by turbulence. Hence the ABL is typically a turbulent boundary layer, and turbulence is by far the most important transport mechanism. As we only study turbulent ABLs in this thesis, the adjective 'turbulent' becomes self-evident and will therefore be mostly omitted in the following. Turbulent boundary layers occur in various types of wall bounded flows and are not at all restricted to the atmosphere³. Even though we conducted this study with the atmosphere in mind, we do not so much focus on the ABL as specific part of the atmosphere, but rather on its essential properties as a turbulent flow phenomenon. That means that, in principle, this study addresses also any other turbulent boundary layer flow that is physical similar.⁴ We can therefore also omit the adjective 'atmospheric' and talk more generally about 'boundary layers' (BLs, henceforth), as we often will do in the remainder of this thesis.

ABL turbulence. In fluid dynamics, turbulence is considered as a flow regime that is characterized by a chaotic, complex pattern of pressure and velocity changes in space and time. It contrasts with the laminar flow regime, where a fluid moves undisturbed in parallel layers. The velocity field of developed turbulence features the evolution of irregular whirls and vortical structures of various sizes and intensity,

³In many engineering flows, e.g. above airfoils, turbine blades, in boiler tubes, etc. turbulent BLs are very relevant and therefore have widely been studied.

⁴To find characteristic dimensionless quantities, which define such a dynamic similarity, is a major goal of this study and will be dealt with in detail.

which entail strain and strong variations of momentum, and strongly interact with each other. All natural fluids are viscous. Even though the viscosity of the air is

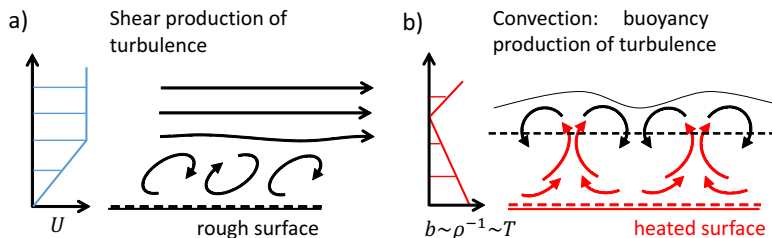


Figure 1.2: Schematic representation of shear production of turbulence (a) and buoyancy production of turbulence (b). The graph in Figure (a) represents the vertical profile of the velocity of the mean flow U . The graph in Figure (b) represents the vertical profiles of the buoyancy force b , which is anti-proportional to the mean density ρ and proportional to the temperature T .

rather low⁵, ABL turbulent motions are damped by viscous molecular forces and their kinetic energy is dissipated into heat. Thus, to maintain a turbulent state, turbulence must be continuously produced and the ABL must be supplied with energy for this production by an external forcing.

In the ABL there are two different mechanisms that can create turbulence⁶. The first mechanism is the production of turbulence by vertical shear of the horizontal mean flow⁷ as very schematically shown in Figure 1.2(a). Shear is induced by surface friction and shear production of turbulence is therefore especially strong close to the surface. In a sheared turbulent BL some portions of the horizontal mean momentum are injected into turbulent motions. Note that shear production of turbulence is a very common cause for BLs. It is also the most common cause for BLs in technical applications.

The second turbulence producing mechanism in the ABL is the so called buoyancy production of turbulence, which is associated with 'convection'. Convection here refers to the vertical motions of fluid parcels due to vertical density variations in the presence of gravity. In the ABL buoyancy (or density) gradients are mainly caused by temperature differences. But also differences in the concentration of water vapor can be significant. Convection is maintained as long as the vertical mean density gradient is negative. This means that heavier fluid is overlaying lighter fluid. This state is called statically 'unstable' as parcels of lighter fluid at the bottom of the BL are positively buoyant and therefore rise, as so called 'thermals' or 'convective plumes'. The heavier fluid at the top of the BL is negatively buoyant and therefore sinks down. This resulting overturning motions (Figure 1.2(b)) create a highly turbulent ABL⁸.

⁵As compared to the inertia forces in the ABL. These conditions are represented by a very high Reynolds number. See section 2.2.

⁶See also section 2.4.2

⁷In the atmosphere commonly called wind.

⁸Convection in a highly viscous fluid can also be laminar. Turbulent convection is caused by comparably strong instability and low viscosity of the fluid. This can be translated into a high Raleigh number Ra , which must exceed a certain threshold. This is quite analogous to a critical

Convection results in strong turbulent mixing that tends to decrease the vertical buoyancy (or density) gradient. Thus, the unstable stratification can only be maintained by a likewise forcing, e.g. by a continuous surface heating or evaporation. In energetic terms, convection represents a constant transfer of potential energy into the kinetic energy of the turbulent motions.

A BL that is driven by convection, is called a 'convective BL' (CBL, henceforth). CBLs are very characteristic for the daytime atmosphere, when solar radiation creates a positive surface heat flux and significant instability. If effects of wind-shear are insignificant we call a CBL 'pure' or 'non-sheared'. If both buoyancy production and shear production of turbulence are significant, we mostly talk about a 'sheared CBL' henceforth. Sheared CBLs are very typical for daytime atmospheric conditions and form the main subject of this thesis.

A BL that is only driven by shear is denoted as 'neutral BL', if the surface heat flux is zero (or more precise: the surface buoyancy flux is zero). Both pure CBLs and neutral BL are rare in the atmosphere as the surface heat flux and wind velocity are typically finite. However they represent the asymptotic limits for sheared CBLs and are therefore of interest in this study.

A shear-driven BL that is additionally affected by a surface cooling (a negative surface buoyancy flux) is called a 'stable BL' (SBL, henceforth). SBLs are typical for nocturnal ABLs under a clear sky, where surface long-wave radiation in to space causes local cooling. The surface cooling enforces a stable stratification within the SBL, which dampens turbulent motions. This is in contrast to a sheared CBL, where buoyancy forces create or at least enhance turbulence. Hence to maintain turbulence in a SBL, the damping effects by buoyancy must be overcome by shear production. Certain aspects of SBL are important for our reasoning later on, however, we do not specifically study SBLs dynamics in this thesis.

ABL turbulent mixing. A very crucial aspect of ABL turbulence is the fast mixing of air, which results in quick dispersion of air properties within the ABL, as indicated by the mentioned times scale of 'an hour or less'. Turbulent mixing strongly tends to reduce differences of air properties within the flow, which implies an efficient transport regime against the mean gradients⁹. Due to the efficient turbulent transport, ABL mean properties respond very quickly to changes at the surface. As a result of this close coupling to surface conditions, ABL mean properties typically differ significantly from the properties of the quiescent non-turbulent FA above.

Typically the FA is stably stratified, which means that lighter fluid is overlaying heavier fluid. The stable stratification limits the rise of convective plumes (schematically indicated in Figure 1.2(b)) and dampens turbulence. Thus the FA acts like a soft lid for the BL turbulence and creates a rather sharp interface between the turbulent BL and the non-turbulent FA.

Reynolds number Re , which characterizes the transition from the laminar to the turbulent state in shear flows.

⁹This similarity with molecular diffusions has led to the analogue concept of 'turbulent diffusion' as a simple model for turbulence transport. Even though the analogy is rather shallow (e.g. see Wyngaard, 2010, chapter 2.8) it illustrates the significance of the turbulent ABL: One finds that for a given gradient of heat, momentum or a trace gas, turbulent transport in the ABL is typically several orders of magnitude more efficient than molecular diffusion, which can roughly be associated with the weak dynamics that characterizes the non-turbulent air above the ABL.

ABL entrainment and growth dynamics. Due to its dispersive character ABL turbulence continuously spreads into the non-turbulent FA. This happens as turbulent eddies intrude into the FA and transfer momentum, vorticity to the non-turbulent air, which as result becomes turbulent. This erosion of non-turbulent fluid by adjacent turbulence is generally called 'entrainment'. In the ABL, entrainment leads to a continuous incorporation of FA air into the ABL. Thus, the interface between ABL and FA moves upwards and the ABL continuously deepens. The stable stratification of the FA reduces but does not prohibit entrainment. Due to intensive turbulence, ABL-entrainment can in fact be very substantial, particularly in the daytime ABL. It is very probable that entrained air has different properties than the ABL, with respect to temperature, momentum and the concentration of trace gases and aerosols. This means that entrainment modifies the ABL mean properties. Hence the correct prediction of entrainment and CBL growth-dynamics are essential for the prediction of BL characteristics.

Due to its significance, ABL entrainment and growth-dynamics have been studied intensively, as soon as the meteorological significance of the planetary boundary layer, particular for the emerging numerical weather forecast, was acknowledged (early studies e.g. Ball (1960); Deardorff *et al.* (1969)). Since then a wide range of different ABL models have been developed. ABL turbulence parametrization are integrated in any weather prediction or global circulation model (earlier examples in e.g. Arya, 1977). These seem to simulate CBL dynamics with respect to their purpose fairly well. But also recent studies show that state-of-the-art parametrization in operational weather prediction models are still affected by uncertainty and systematic errors in well defined conditions (e.g. Rodier *et al.*, 2017).

Moreover, a systematic analysis reveals that, despite its fundamental character, the entrainment dynamics of BLs with varying intensity of shear and convection are only partly understood. That holds even for the most basic case of a horizontally homogeneous cloud-free BLs under a linearly stratified FA (Conzemius and Fedorovich, 2006a,b, 2007).

1.2 Current understanding of shear effects on entrainment in CBLs

To understand the current state of knowledge about sheared CBL entrainment-dynamics, which form the background for our investigations, a brief, condensed look on the recent research history seems helpful.

Earlier efforts to understand and quantify BL entrainment-dynamics have always been hampered by uncertainties and limitation of data, which were obtained by both direct atmospheric observations and lab experiments. Nevertheless, for the case of the pure CBL, which due to its remarkable features is often considered as prototypical daytime ABL, a simple integral mixed-layer model based on a constant entrainment-rate scaling was proposed by Lilly (1968). This model, further investigated by e.g. Deardorff *et al.* (1969); Tennekes (1973); Zilitinkevich (1991), proved rather satisfactory. Since then the basic validity of this model has been frequently confirmed with data (e.g. Fedorovich *et al.*, 2004b). However, a recent study by Garcia and Mellado (2014) points out some limitations and, based on a very similar approach, suggests a

generalization and a significantly refined understanding of CBL entrainment dynamics.

However, purely convective BLs are rare in the atmosphere, as typically some horizontal wind is present. The entrainment dynamics of sheared CBLs that are driven by both convection and wind shear, turned out to be a more challenging issue. Based on an extensive atmospheric observations Driedonks (1982) found that wind shear can significantly enhance the diurnal growth of fair weather CBLs, which rather well corresponded with prediction of a simple bulk model. However, as typical for atmospheric observations, uncertainties remained very high. But also very elaborate laboratory experiments (e.g. Fedorovich *et al.*, 2001a,b), did not provide a clear view on how the presence of wind-shear within the CBL modifies entrainment and influences the CBL growth-rate. Particularly, it remains unclear under which condition and to what extent wind shear actually enhances CBL entrainment or even reduces entrainment. This long lasting uncertainty and lack of empirical evidence triggered speculations and resulted in a multitude of different models, often based on very similar, but partly also conflicting assumptions (e.g. Conzemius and Fedorovich, 2006b).

The development of the techniques of Large-Eddy Simulation (LES, first LES of an entraining CBL by Deardorff, 1974a) and Direct Numerical Simulation (DNS) (see chapter 3.1) and the rise of sufficient computational power in the last decades opened new possibilities for numerical studies of atmospheric flows. Although possibilities to simulate complex and large atmospheric scenarios are still today constrained by very high computational demands, the essential advantage of these numerical methods are the perfect control over experimental conditions and the access to a physically complete data set. Many of these earlier efforts concentrated on pure CBLs, which due to the basic significance of convection for the daytime atmosphere and lower computational demands seemed especially attractive. But with increased computational resources also basic aspects of sheared CBLs could be investigated via LESs, as shown by e.g. Schumann and Moeng (1991) and particularly Moeng and Sullivan (1994), who demonstrated the strong structural variability of sheared CBLs and pointed out important open issues.

Further enhanced access to computational power enabled LESs of more complicated phenomena, such as heterogeneous BLs (e.g. Van Heerwaarden *et al.*, 2014), but most of all cloud covered BLs of various forms (e.g. Siebesma and Cuijpers, 1995; Khairoutdinov *et al.*, 2009; Schalkwijk *et al.*, 2015). From a meteorological perspective clouds are fascinating, complex and at the same time very relevant phenomena, whose physics were rather poorly understood. Thus, cloud dynamics have attracted much attention of the meteorological LES community, whose efforts contributed fundamentally to the recent, vastly improved understanding of clouds. The simple basic entrainment problem of cloud-free BLs, however, faded into the background.

Nevertheless, a case study by Pino *et al.* (2003) stressed the importance of shear enhancement for the CBL evolution once more. Pino *et al.* (2006a) then showed that these effects can be reproduced by LES CBLs and translated into simple models. However strong quantitative uncertainties remained, not least due to a rather limited range of the used data. Finally Conzemius and Fedorovich (2006a,b) used the improved computational opportunities for a more intensive exploration of the parameter space of basic sheared CBLs. Using a large set of LESs they tested and evaluated a

wide variety of existing entrainment models for sheared CBLs. This analysis resulted in two significantly improved entrainment models (Conzemius and Fedorovich, 2007) of different complexity. But the authors also showed that even these improved models frequently and strongly deviate from the LES data. Although these errors clearly point to a substantial misrepresentation of the underlying physics, they are not yet understood (Conzemius and Fedorovich, 2007).

This situation was the starting point for our analysis. Using an improved data representation and a similar set of LESs, we soon found that the deviations between LES and the approach of Conzemius and Fedorovich (2007) and precursors can indeed be significant. We also found that these deviations are of very systematic nature. The

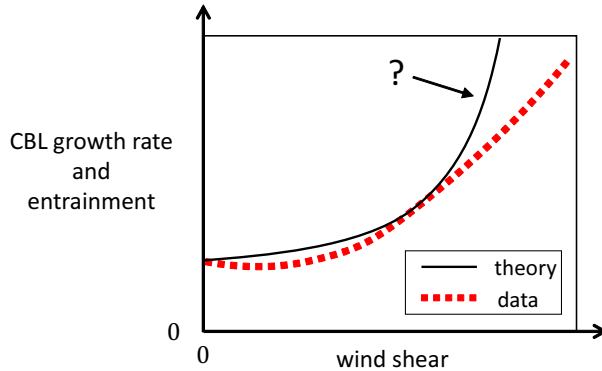


Figure 1.3: Schematic representation of the current uncertainty of shear effects on CBL entrainment. A detailed quantitative presentation of the issue is later given by Figure 2.10.

result of these preliminary investigations are shown in detail in chapter 2.7.1. But for clarity, we already here shortly sketch the basic problem in Figure 1.3. It schematically shows the dependency of the CBL growth rate on wind-shear. As expected, the CBL growth rate tends to increase with additional production of turbulence by shear, a mechanism, which is also denoted as 'shear enhancement'. But the best known model (continuous line) differs systematically from the LES data (dashed line). The reason for these deviations are unknown and the issue demands a physical explanation.

1.3 General research objectives

In this thesis we re-investigate the entrainment problem of CBLs with varying wind shear, with the objective of a more thorough and consistent understanding of the underlying dynamics. In particular, we want to find an explanation for the observed discrepancies between LES data and current theory. It should then be possible to directly translate such findings into an improved entrainment model.

Our main motivation is scientific curiosity and an interest in the most basic mechanisms behind ABL evolution. However, significant progress in the understanding of sheared-CBL entrainment dynamics is also useful to test and potentially improve the

performance of the ABL parameterizations in various applied atmospheric models. Moreover better knowledge of BL entrainment might be helpful to understand other, similar interfacial processes, e.g. in cloud layers or marine BLs at the sea surface. No study is complete. Thus, we finally like to draw a clear picture about remaining issues and come forward with concrete suggestion for further investigations.

Chapter 2 starts by introducing the theoretical framework needed to analyze and described entrainment in the CBL. Next, we discuss and evaluate a CBL entrainment model of Conzemius and Fedorovich (2007), which is exemplary for current knowledge (see the dashed line in Figure 1.3). The combination of the theoretical framework and this evaluation enables us to derive our definite research objectives and research questions, as well as the strategy to address these in our main analysis (chapters 4 till 7).

1.4 An additional research project: the inertial oscillation of mid-latitude CBLs

In another, separate study, we investigated the inertial oscillation (IO) of the mid-latitude CBL wind. Some basic results that address the influence of CBL surface friction on the IO, were published as Schröter *et al.* (2013). As this subject is only indirectly related to the main part of the thesis. We included it in form of the full paper in appendix E.

The IO is a horizontal rotational oscillation of the mean wind vector, which is enabled by the horizontal component of the Coriolis force in the mid latitudes. In a BL, the IO is initiated by an imbalance between the Coriolis force, the pressure-gradient force and turbulent friction. In our paper we investigate the influence of surface friction on the IO of a sheared CBL. This means that we **apply** an existing turbulence model to study and characterize the oscillatory properties of the CBL mean flow. This is systematically different from the main topic of this thesis, where we **develop** a turbulence model.

To give the interested reader a link between Schröter *et al.* (2013) and the main topic of the thesis, we shortly have to comment on the evolution of the thesis research. The research of which this thesis is an account, was initially triggered by a research project aiming at a comprehensive characterization of the impact of turbulent stresses on the IO in a CBL. Considering the vertical structure of a CBL with an upper and a lower boundary, this problem can be separated in two sub-problems. The first is the influence of turbulent surface friction and the second is the influence of momentum entrainment on the IO.

For turbulent surface friction rather well established models exists, and hence the first part of the characterization of the effect of friction on the IO was feasible and led to the paper Schröter *et al.* (2013). To solve the second part of the problem, a model for turbulent entrainment that takes the variation of shear during an inertial oscillation into account, is needed. However, as described above, current models appeared to be hampered by systematic errors. Thus, for a really satisfactory characterization of the IO, one would have had to develop a proper model for entrainment in sheared CBLs first. If done thoroughly, this appeared to be a major task in itself. On the other hand, with a more systematic approach than in previous studies, the prospects

to significantly improve the current understanding of entrainment in sheared CBLS looked rather good. As we found the CBL entrainment problem more relevant and interesting, we finally decided to change the focus of this thesis.

Chapter 2

Theoretical framework and preliminaries

In this chapter we present existing concepts and theories for the physical representation of turbulent BLs, which form the basis for our analysis. To begin with, we present two basic elements that are prerequisites for our investigation of sheared CBLs. The first is the basic experimental setup, which is a reasonable idealization of the real world ABL and commonly used in ABL studies (section 2.1). The second is the most basic statistical theory of turbulence dynamics, which can be seen as a prototype of all ABL turbulence models (section 2.2). Afterwards in the sections 2.3 till 2.5, we introduce some more specific common basic concepts to describe and model turbulent BLs, with an emphasis on CBLs. Finally, we present and discuss two rather recently published models of the CBL evolution, which both represent the status of current knowledge and serve as starting points for our own investigations.

The first model is an integral CBL entrainment model, published by Conzemius and Fedorovich (2007), which accounts for shear effects, and the second is a rather detailed model for the impact of FA stratification on the entrainment zone structure and dynamics in pure, non-sheared CBLs by Garcia and Mellado (2014). Their theory is summarized in section 2.6 and could rather directly be used as basis for our generalization of their concept, which additionally takes CBL shear into account (chapter 6).

However, before we were able to find a conclusive interpretation of Conzemius and Fedorovich's (2007) results (and similar precursory work) and devise a follow up research line, some critical reflection as well as a very practical evaluation of the weaknesses and strengths of their approach had been necessary. As an outcome of this evaluation we could further specify our research questions and define a detailed research strategy. All steps of this review process are presented in section 2.7.

2.1 An idealized representation of the atmospheric boundary layer

In this study we want to analyze the intrinsic properties of an ABL that is driven by the combination of shear and convection, which is typical for daytime conditions. To this end we want to make use of an appropriate experimental setup that represents the essential impact of these turbulence producing mechanisms on the ABL evolution. As a further essential property, the ABL is capped by a stratified FA.

By combining these most basic features one can construct an idealized BL, which is a frequently studied prototype of the ABL. It is vertically bounded at the bottom by a flat surface and on top by a linearly stratified non-turbulent zone (the FA). But it is infinite and uniform in the horizontal directions. Turbulence is created by a horizontally homogeneous surface heating and a horizontally homogeneous surface stress. Thus ensemble statistics of flow properties can only vary in the vertical direction and in time¹. Our numerical experiments very closely replicate such idealized BLs (details in chapter 3), which therefore quite directly reflects our object of research in this study.

It is clear that real ABLs form above the heterogeneous Earth's surface, are frequently cloud-covered and are embedded in the large-scale weather. Therefore real ABLs are always heterogeneous and instationary to a certain degree. However, observations show that mean gradients and fluxes in the typical daytime ABL are much larger in the vertical direction than in horizontal directions. Furthermore, the characteristic ABL turbulent time scale (< 1 h) is typically significantly smaller than the temporal variations of the surface forcings, which are mostly coupled to the diurnal cycle or even slower synoptic variations. Hence, if one leaves cloud condensation aside (an additional and very significant process in its own right), the idealized, horizontally homogeneous and constantly forced BL should approximate real ABLs rather well. Regarding the homogeneity, we should add that the approximation is valid as long as we consider a local domain with a size that is a few times the characteristic length scale of ABL turbulence (say L), which is typically assumed to be similar to the ABL depth h .

It is therefore a common practice to decompose² the ABL flow into a turbulent contribution, which is horizontally homogeneous (in its statistical properties) at a scale that is a few times the characteristic ABL length scale L , and into a mesoscale contribution to motions and processes on a scale that is significantly larger than L (accounting for the typical atmospheric heterogeneity). Hence the scale separation around $\sim L$ is associated with a process separation between ABL turbulence and other motions.

It is worth of note that this concept is widely applied in global (so called 'general circulation models', GCMs), or limited-area (mesoscale) atmospheric numerical models as used for weather forecast, as it allows a relatively coarse computational grid. According to the typical layout, the GCM's horizontal grid size $l_{x,y}$ of 5...50 km acts as a spatial filter, with a size that is in the order of, but larger than, $L \sim 1$ km. Thus it

¹That is different to many engineering BLs that vary 'horizontally' or in the flow direction respectively and are typically stationary in time. For instance, BLs that form on an airfoil or a turbine blade, etc.

²In the sense of a Reynolds decomposition (section 2.3).

is assumed that most of the mesoscale and large scale synoptic motions and processes are directly resolved, whereas all turbulence and other ABL processes, including cloud convection, are entirely parametrized as small-scale subgrid-processes. The ABL is approximated as a piecewise homogeneous turbulent layer and the applied turbulence models represent horizontally homogeneous, continuously forced BLs, which completely correspond to the BLs that we investigate in this thesis. Thus, in principle, the results of our analysis can be directly transferred to ABL parametrization of GCMs.

Although justified in basic aspects and rather successfully applied in operational GCMs, the mentioned process separation remains a somewhat rough approximation and a comprehensive characterization of the relationship between ABL turbulence and other flow mechanisms remains a difficult issue.³

2.2 The inviscid self-similarity of high Reynolds number turbulence

A basic property of ABLs is their distinct turbulent state, which is more specifically denoted as high Reynolds-number turbulence. The classical, phenomenological picture of high Reynolds-number turbulence as a dynamical system (Wyngaard, 2010) was laid down by contributions of L. F. Richardson, G. I. Taylor and finally A. N. Kolmogorov (particularly in Kolmogorov, 1941)⁴. Still today this well-known theory (Kolmogorov theory henceforth) forms the most important approach to high Reynolds-number flows. In fact, one can argue that the Kolmogorov theory is the conceptual basis for all statistical BL turbulence models and thus also for the ones that we test and develop in this thesis. Although implicitly present, we feel that these conceptual roots have been somewhat neglected in recent studies on CBL entrainment. We find a more explicit linkage to the Kolmogorov theory quite helpful and therefore decided to shortly introduce it here and point out relevant aspects and basic implications for our research.

The Reynolds number. An important, basic flow characteristic is represented by the dimensionless Reynolds number (after Osborne Reynolds). It is defined by the ratio between the inertial and viscous forces within a flow and commonly written as

$$\text{Re} = \frac{VL}{\nu}, \quad (2.1)$$

³For instance, the basic assumption that the vertical length scale L_z , which is constrained by the ABL depth, also determines the horizontal scale of turbulence variations ($L_{x,y} \sim L_z$) indeed holds for some quantities, with buoyancy as the most essential one. But observations show that for other relevant quantities, such as momentum and moisture, $L_{x,y}$ is not bounded (De Roode *et al.*, 2004) and grows in time. As frequently observed, $L_{x,y}$ can finally exceed $L_z \sim 1$ km by more than an order of magnitude. This means that the statistically 'random' variations of ABL turbulence can not easily be distinguished from the 'deterministic' signal of other mesoscale (> 1 km) processes. Thus, scale overlap and the implicit direct interaction between ABL turbulence and mesoscale processes make it very difficult to formulate their relationship in a closed theory.

⁴If not mentioned differently we refer to the textbooks of Tsinover (2001); Wyngaard (2010); Kundu and Cohen (2004).

where L and V , are the characteristic length and velocity scale of the flow and ν is the kinematic viscosity of the fluid. Generally Re can be considered as a measure of the flow's affinity to turbulence. For laminar flows Re measures the flow's dynamical stability and a critical minimum value of Re defines the transition to turbulence, when the inertial forces represented by VL overcome the stabilizing effects of viscosity. But Re is also meaningful for developed turbulent flows. Here it represents the complexity and the state of turbulence formation. Particularly, Re can be interpreted as a measure for the span between the largest and the smallest turbulent scales.

In the ABL Re is typically large and can reach values of 10^9 . As a result the 'size' of turbulent scales can span several decades (see also the introduction of chapter 3). In high- Re turbulence, the characteristic length and velocity scales L and V are related to those of the largest eddies, which have scales of the same order but smaller than the dimensions of the mean flow \mathcal{L} and \mathcal{V} .⁵ These large-scale motions contain most of the kinetic energy within the turbulent flow (called 'turbulence kinetic energy', TKE) and as they are only very weakly sheared they do not feel viscosity directly. But through decay and complex interaction, the large-scale motions transfer their energy to smaller and the smallest scales and so maintain the complex turbulent field. The smallest scale motions are best associated with areas of strong shear (Tsinober, 2001, chapter 5.4), where kinetic energy is dissipated into heat by viscosity. This scale is also called the 'Kolmogorov scale' or 'dissipation scale', with a characteristic velocity scale v and the length scale η .⁶ The dynamic linkage between the large-scale and small-scale motions is a vary basic, but only partly understood feature of turbulence.

To summarize: high- Re turbulence appears as a dynamical system where the largest scale motions extract energy from the mean flow (e.g. via unstable stratification or shear) and turns it over to the smallest scales, where it is finally dissipated.

Reynolds number similarity. Aiming at a conceptual statistical understanding of high- Re turbulence, Kolmogorov was the first to stress the quantitative importance of the dissipation rate. One result of his elaborate reasoning is the following scaling (Cadot *et al.*, 1997)

$$\varepsilon_x \sim \frac{V^3}{L}. \quad (2.2)$$

Here ε_x is the ensemble mean viscous dissipation rate⁷ (energy per time) and L and V are again the characteristic dimensions of the largest scale motions. Accordingly, the following considerations refer to integral, statistical properties of turbulent ensembles.

Eq. 2.2 expresses a crucial scale invariance of high- Re flows, as it implies that, as long as viscosity is small enough, dissipation is independent of the actual value of viscosity and only depends on the dimensions of the large energy-containing fluctuations. In stationary high- Re flows, turbulence dissipation represents the complete energy turnover in the flow domain. Thus it also equals the rate at which energy is

⁵In the ABL $L \approx 10^1 \dots 10^3$ m and $V \approx 10^0 \dots 10^1 \text{ms}^{-1}$. $\nu(\text{air}) \cong 1.510^{-5} \text{m}^2 \text{s}^{-1}$ of the dry air. According to Eq. 2.1, the Re of the ABL is then in the in order of $\approx 10^6 \dots 10^9$.

⁶The Kolmogorov velocity scale is defined as $v = (\nu\varepsilon)^{1/4}$. The Kolmogorov length scale is defined as $\eta = (\nu^3/\varepsilon)^{1/4}$. Both are linked with the large production scale via Eq. 2.2. In the ABL η is on the order of ~ 1 mm.

⁷The subscript x indicates that this is a local property, as opposed to an integrated property as will be introduced later.

injected into turbulence, P , which we commonly denote as 'TKE production'. So we can also write

$$\varepsilon_x \approx P_x \sim \frac{V^3}{L}. \quad (2.3)$$

Hence, if Re is large enough, the large-scale motions determine the net turnover of TKE within the flow and the composition of the smallest dissipating scales of the turbulent field adapt to this need. The main flow characteristics become 'inviscid' and thus independent of Re , which is commonly denoted as 'Reynolds-number similarity'. Note that, for convenience, Eq. 2.3 can also be written in terms of the dimensionless dissipation rate

$$\alpha_\varepsilon = \varepsilon_x \frac{L}{V^3} \approx \text{const.} \quad (2.4)$$

Originally, the scaling Eq. 2.2ff was suggested for ideal circumstances, implying isotropic and stationary turbulence, and the absence of influence of the flow boundaries or 'special regions' (Tsinober, 2001).⁸ However, in practice it has been applied to various sorts of inhomogeneous and anisotropic flows (Cadot *et al.*, 1997) and is **assumed** to be valid in these cases, as soon as Re is large enough.⁹ Observations make it clear that for real turbulence the value of $\alpha_\varepsilon \approx \text{const}$ (Eq. 2.4) strongly depends on the specific type of flow, as defined by its geometry, the typology of its forcing and boundary conditions (e.g. Cadot *et al.*, 1997).

The scale-invariance that is given by expression (2.2) is therefore commonly interpreted in a much broader sense. As it directly couples the flow's dynamics with the flow's basic dimensions, it represents a basic 'self-similarity' of the turbulent flow. A similar scaling with the basic dimensions of the largest scale motion can be observed for various other statistical properties and in various types of flows and therefore appears to be inherent to high- Re turbulence.

An important analogy (or extension) of Kolmogorov's model is the finding that at high Reynolds numbers also entrainment turns out to be independent of viscosity (Tsinober, 2001, chapter 8.3) and only depends on the large-scale dimensions.¹⁰ If we, similarly to dissipation, consider entrainment E as a sink of TKE (or as TKE consumption), this would suggest

$$E_x \propto \frac{V^3}{L}, \quad (2.5)$$

which defines the dimensionless constant entrainment

$$\alpha_E = E_x \frac{L}{V^3} \approx \text{const.} \quad (2.6)$$

⁸For his reasoning Kolmogorov does not refer to fully isotropic turbulence, but used the narrower concept of 'local isotropy', "*which is realized with good approximation in sufficiently small domains of the four-dimensional space (x_1, x_2, x_3, t) not lying near the boundary of the flow or its other singularities*" (Kolmogorov, 1941), which can be interpreted as to refer to any scale that is still significantly larger than the dissipating scales (Cadot *et al.*, 1997). This however should not be confused with the fact that "*U [V in our case] and L denote the typical length and velocity for the flow in the whole.*" (Kolmogorov, 1941).

⁹Even though Cadot *et al.* (1997) showed that this is not generally the case.

¹⁰Similarly to dissipation, this does not mean that the small scales are unimportant for the entrainment process. It rather means that "*small scales do the 'work', but the amount of work is fixed by the large scales in such a way that the outcome is independent of viscosity*" (Tsinober, 2001, page 194f).

Note that following common notation ' \propto ' means 'proportional to', whereas ' \sim ' means 'proportional to and of similar order'. If we again assume that the flow is approximately stationary, then E_x plus ε_x must balance the TKE production P_x . Hence with $P_x = E_x + \varepsilon_x$ and the observations that all terms are assumed to be proportional to V^3/L , we can write

$$E_x \propto P_x \sim \frac{V^3}{L}, \quad (2.7)$$

which suggests an entrainment ratio c_E (entrainment divided by production)

$$c_E = \frac{E_x}{P_x} \approx \text{const.} \quad (2.8)$$

Analogously to Eq. 2.6, we can define a dimensionless production rate

$$k_P = P_x \frac{L}{V^3} \approx \text{const}, \quad (2.9)$$

so that

$$E_x \simeq c_E k_P \frac{V^3}{L} \quad \text{and} \quad \alpha_E \simeq c_E k_P. \quad (2.10)$$

Accordingly, the self-similarity of an entraining turbulent flow would actually consist in two parts. The first part is represented by the fixed portion of the TKE production that is used for entrainment, $E \simeq c_E P_x$, and the second part is the proportionality between the TKE production and a corresponding estimate, based on the characteristic scales of the large scale motions¹¹, $P_x \sim V^3/L$.

The fact that an inviscid entrainment behavior (as expressed by Eq. 2.5ff) has frequently been observed (see our results in the sections 4 and 5, and references e.g. in Tsinober, 2001, page 195) in real flows is remarkable, insofar as entrainment is an interfacial process which necessarily creates an anisotropic flow. Apparently, for a certain type of flow, with a certain geometry, forcing, etc. the effects of heterogeneity and anisotropy seem to be systematic in a way, so that the inherent inviscid self-similarity of the flow is retained.

To determine the evolution of a flow, one is not only interested in the entrainment E_x but also in its impact on the flow's dimensions (e.g. on its growth rate), which might be associated with characteristic velocity and length scales of its own (V_E and L_E). Thus, assuming again a 'self-similarity' of the flow one might suggest¹²

$$\frac{V_E^3}{L_E} \propto E_x. \quad (2.11)$$

To apply and test scalings Eq. 2.7 and 2.11 on real flows, one needs to determine E_x , P_x , L , V , L_E and V_E , which requires to identify and localize both entrainment and TKE production within the flow domain.

¹¹The characteristic scales L and V are often at least partly estimated via the dimensions of the mean flow \mathcal{L} and \mathcal{V} . Thus, one often does not sharply distinguish between both set of scales.

¹²BL entrainment in a stably stratified environment is often associated with TKE buoyancy consumption (section 2.4.2). This requires a modified formulation of entrainment based on buoyancy scale, as shown in detail later on.

A particular challenge for modeling the ABL is the presence of two different sources of TKE, i.e. shear and buoyancy (e.g. here formally introduced by the subscripts S and B). The most simplistic approach, which is again inspired by idealized homogeneous and isotropic turbulence, assumes that both turbulent sources are quantitatively independent so that they superimpose. If we schematically combine this idea with the above scalings we get

$$E_x \simeq \alpha_{E,B} \frac{V_B^3}{L_B} + \alpha_{E,S} \frac{V_S^3}{L_S}, \quad (2.12)$$

which entails the intermediate step (analogous to Eq. 2.8)

$$E_x \simeq c_{E,B} P_B + c_{E,S} P_S, \quad (2.13)$$

with the similarities

$$P_B \simeq k_{P,B} \frac{V_B^3}{L_B} \quad \text{and} \quad P_S \simeq k_{P,S} \frac{V_S^3}{L_S} \quad (2.14)$$

and $\alpha_{E,B} = c_{E,B} k_{P,B}$, $\alpha_{E,S} = c_{E,S} k_{P,S}$ and $c_{E,B}$, $k_{P,B}$, $c_{E,S}$ and $k_{P,S}$ are all constants.¹³ This simple prototypical concept (Eq. 2.11 till 2.14) resembles the various integral approaches that have been used to model sheared CBLs (as reviewed in Conzemius and Fedorovich, 2006a, 2007)¹⁴ and it will also be the basis for our analysis and our modeling approach in this thesis.

However, in the case of sheared CBLs the assumption of independence of the turbulence sources is not evident as both convection and shear are quite different processes that each create highly inhomogeneous and anisotropic turbulence with quite different characteristics. So it might well be that both turbulence producing mechanisms significantly interact and do not simply superimpose. Furthermore, the multitude of existing CBL models indicates that the identification of proper integral scales in sheared CBLs is not clear either, which poses another major modeling challenge. Note that both issues are closely connected and it therefore seems difficult to solve them independently.¹⁵

All these uncertainties imply that expressions 2.13 and 2.14 do not represent a proven theory but should rather be considered as a conceptual framework that could guide our research.

2.3 Statistical description of turbulent flows

Turbulence features a characteristic, seemingly chaotic pattern of irregular whirls and vortical structures of varying size and intensity. These structures entail strong variations of velocity and other quantities (e.g. density, pressure and concentrations)

¹³Note that (1) in the case of ideal isotropic turbulence both sources would have identical properties and therefore the respective constants would be the same, (2) dissipation is supposed to scale analogously.

¹⁴However, direct links to Kolmogorov's theory are rare in these applied meteorological studies. Probably such a linking is considered as trivial.

¹⁵Without knowledge of the proper scales, it seems difficult to evaluate the joint impact of the turbulence producing mechanism. Without knowledge of their relationship, it is difficult to evaluate the choice of proper scales.

in space and time. They are commonly called 'eddies' and the differences in their size, momentum and turnover time are commonly associated with different characteristic 'scales' of length, velocity and time.

Reynolds decomposition. In order to access the phenomenon of turbulence quantitatively, a turbulent flow is traditionally considered as a **stochastic** system, which represents an infinitely large ensemble of possible realizations of the turbulent field. Thus, the state of a quantity c within the turbulent flow can be expressed as the sum of a mean (or rather an expected value) for a specific location and time, and a deviation from this mean:

$$c(x, y, z, t) = \bar{c}(x, y, z, t) + c'(x, y, z, t). \quad (2.15)$$

Here the mean of the turbulent ensemble is denoted by an overbar and the deviation from that mean by a prime.

However, there are two problems with the above decomposition. First, in experimental practice, we usually do not have access to a complete ensemble of realizations that we would need to know the true flow properties. Second, we are usually not interested in the ensemble mean at every location in the flow and at every time, but rather want to consider more global properties of the flow. Therefore, ensemble averaging is usually replaced by averaging along a dimension in which statistical properties are assumed to be homogeneous. Those can be one or more spatial dimensions, but also time, if the flow can be considered stationary over the length of the averaging period.

With the transition from an ensemble mean to a spatial or temporal mean one additional step is made implicitly: the averaging over an infinite number of realizations is replaced by averaging over a finite sample. This is due to the fact that real turbulent flows are limited in time and space and their fields always represent a random subsample of a 'true' turbulent ensemble. Hence their stochastic properties can only be estimated from a finite sample of a turbulent field (a subsample of the ensemble). But if the number of independent realizations is large enough, convergence between the statistical mean and the expected value is assumed (details, e.g., in Wyngaard, 2010, chapter 2.2). Pragmatically and without further considerations, we can control convergence in our analysis by controlling the size of the sample. We do this either by selecting an appropriate domain size or by the time period over which averaging takes place. This can be augmented by combining different subsamples of an assumed turbulent ensemble, e.g. by comparing data of different experiments (independent subsamples).¹⁶

Ensemble statistics in horizontally homogeneous BLs. In this study we investigate horizontally homogeneous BL flows (section 2.1). This means that ensemble averaging can be approximated by spatial averaging in both horizontal directions. As a result, only z remains as a spatial direction in which the flow is inhomogeneous. As we study evolving flows, time is an independent variable as well. Hence the Reynolds decomposition of c can be written as

$$c(x, y, z, t) = \bar{c}(z, t) + c'(x, y, z, t), \quad (2.16)$$

¹⁶In the following we do not sharply distinguish between statistical averages over limited samples and the 'true' ensemble means and generally use the latter term.

Note that from hereon the overbar implies an approximate ensemble averaging over the homogeneous directions, in this case the x and y direction. Now we can define a number of mean turbulent statistics. The variance of c becomes

$$\sigma_c^2(z, t) = \overline{c'(x, y, z, t)c'(x, y, z, t)}, \quad (2.17)$$

Another, for us even more important, feature in a turbulent flow is transport. Neglecting molecular diffusion, which is mostly irrelevant within the ABL, transport equals the kinematic flux of a quantity c . It is a vector and given by the ensemble average of the product of c and the velocity vector.¹⁷ In horizontally homogeneous BLs, net transport in the horizontal directions is zero. Thus only the vertical flux component is important.

$$\overline{wc}(x, y, z, t) = \overline{w(z, t) \bar{c}(z, t)} + \overline{w'(x, y, z, t)c'(x, y, z, t)}. \quad (2.18)$$

The first term represents mean advection, the second term is the turbulent flux. For a surface-bounded flow, horizontal homogeneity implies that the vertical mean flow $\overline{w}(z, t) = 0$, so that the advection becomes zero and the total vertical flux becomes the turbulent flux. Hence

$$\overline{wc}(z, t) = \overline{w'(x, y, z, t)c'(x, y, z, t)}. \quad (2.19)$$

Using this basic statistical concept of turbulence, evolution of any ensemble-averaged quantity within a turbulent flow can be expressed by Reynolds-averaged prognostic (or budget) equations.

Notation. Before continueing we will slightly adapt our notation to ensure that at a later stage our notation can be as compact and economical as possible. First, as we study evolving flows, time is an independent variable. But in many cases the actual time to which the turbulent field is related is irrelevant. In those cases we rather consider relationships between variables within that field. Then we will not state this dependence on time explicitly and drop the functional dependence. Second, to make the notation more compact, the dependence of a variable on z will be indicated by a subscript rather than as a functional dependence between parentheses (c_z rather than $c(z)$). Finally, for (approximate) ensemble averages of single variables we will drop the overbar (c_z rather than \bar{c}_z), while for covariances the overbar will be retained.

2.4 Governing equations

The Reynolds-averaged prognostic budget equations that describe the evolution of horizontal momentum, buoyancy and the turbulence kinetic energy (TKE) in the cloud-free (dry) ABL, are presented in the following. They can be derived from the conservation of momentum of a Newtonian fluid (denoted as the Navier-Stokes equations), the conservation of mass and the conservation of heat, using common simplifications, such as incompressibility, hydrostatic equilibrium of the mean state, the ideal gas law and the Boussinesq approximation for density fluctuations. For details

¹⁷If c is a vector, then the kinematic flux becomes a tensor.

see (Stull, 1988, chapter 3). As a further simplification we here restrict ourselves to horizontally homogeneous BLs. This means that the ensemble averages only vary in the vertical direction, horizontal turbulent fluxes are zero and advection is zero in all directions.

2.4.1 Budgets of mean variables

The prognostic budget for any mean quantity c at the height z in a horizontal homogeneous ABL is given by

$$\frac{\partial c_z}{\partial t} = -\frac{\partial \overline{w'c'_z}}{\partial z} + S_{c_z}. \quad (2.20)$$

The term on the left-hand side (lhs henceforth) is the tendency or storage of c_z , the first term on the right-hand side (rhs henceforth) is the turbulent flux-divergence and the second term on the rhs is the source of c_z .

Horizontal mean momentum. The budget for the horizontal mean momentum vector $\mathbf{U}_z = (u_z, v_z)$ is given by the budgets for each component. These read

$$\begin{aligned} \frac{\partial u_z}{\partial t} &= -\frac{\partial \overline{w'u'_z}}{\partial z} + S_{u_z}, \\ \frac{\partial v_z}{\partial t} &= -\frac{\partial \overline{w'v'_z}}{\partial z} + S_{v_z}. \end{aligned} \quad (2.21)$$

Here the respective term on the lhs is the tendency of momentum (per unit mass), which represents the acceleration of the flow. The first terms on the rhs is the turbulent momentum flux divergence (also called turbulent stress divergence), which represents the impact of turbulent friction and the second term on the rhs comprise the source of respective component. In the rotating coordinate system of the Earth, this consists of two contributions

$$\begin{aligned} S_{u_z} &= -\frac{1}{\rho} \frac{\partial p}{\partial x} + f_c v_z, \\ S_{v_z} &= -\frac{1}{\rho} \frac{\partial p}{\partial y} - f_c u_z. \end{aligned} \quad (2.22)$$

The first contribution (first term on the rhs) is the pressure gradient force and the second contribution (second term on the rhs) is the horizontal component of the Coriolis force, which is always perpendicular to the velocity vector. p is the mean pressure, ρ the air density and f_c the Coriolis parameter, which only depends on the geographical latitude. Close to the Equator $f_c \mapsto 0$ and the horizontal component on the Coriolis force vanishes.¹⁸ But in the following we mostly consider extra-tropical, mid latitude CBLs where f_c is of the order of $\pm 10^{-4} \text{ s}^{-1}$. The steady quasi-frictionless free atmospheric flow above the ABL is often well approximated by the geostrophic

¹⁸The vertical component is generally negligible in the ABL.

wind $\mathbf{U}_g = (u_g, v_g)$, which is defined by a balance of Coriolis force and the pressure gradient force:

$$\begin{aligned} f_c u_g &= -\frac{1}{\rho} \frac{\partial p}{\partial y}, \\ -f_c v_g &= -\frac{1}{\rho} \frac{\partial p}{\partial x}. \end{aligned} \tag{2.23}$$

For most ABLs, \mathbf{U}_g is a useful reference flow and Eq. 2.23 is therefore frequently used to express the pressure gradient force in the momentum budget. \mathbf{U}_g is always aligned with the isobars, thus perpendicular to pressure gradient. It is natural to orient the horizontal coordinates accordingly. Thus, in the following the u-component (x-direction) of the wind vector points in the direction of the geostrophic wind $\mathbf{U}_g = (u_g, 0)$ and the v-component (y-direction) is aligned with the pressure gradient force:

$$\begin{aligned} \frac{\partial u_z}{\partial t} &= -\frac{\partial \overline{w'u'_z}}{\partial z} + f_c v_z \\ \frac{\partial v_z}{\partial t} &= -\frac{\partial \overline{w'v'_z}}{\partial z} - f_c u_z + f_c u_g. \end{aligned} \tag{2.24}$$

Mean buoyancy. The ultimate cause for convective turbulence is the mechanical instability of a fluid with vertical positive density gradient in the gravitational field, which provides potential energy. This so-called statically unstable stratification results in the formation of rising low density plumes (in the ABL also called 'thermals'). Their upward motion is caused by buoyancy, which due to the Archimedes' principle, exceeds the buoyancy of the surrounding fluid with higher density (Figure 1.2(b)). The specific buoyancy b (force per unit mass), which has the dimensions of an acceleration, is therefore the effective measure of the impact of density variations in the ABL flow.

In the ABL buoyancy is raised by reducing the air density by warming or by increasing its humidity. For simplicity we just consider the 'dry' ABL and temperature effects on buoyancy in our study. However, to relate temperature and buoyancy in a consistent way, it is necessary to correct for vertical temperature variations due to variations of hydrostatic pressure, which has no impact on buoyancy. It is therefore common to refer to the potential temperature θ_z instead of the absolute temperature T . Different to T , θ is a conserved variable for all dry adiabatic air motions. Using the ideal gas law, θ is given by

$$\theta = T \left(\frac{p_0}{p} \right)^{R_a/c_p}. \tag{2.25}$$

Here p is the pressure, $p_0 = 100$ kPa is the reference pressure at normal conditions, R_a the gas constant of air, c_p is the specific heat capacity at constant pressure. In hydrostatic equilibrium, p and hence the proportionality between θ and T only varies with height.

Buoyancy b_z is proportional to the potential temperature θ_z and the buoyancy flux $B_z = \overline{w'b'_z}$ proportional to the potential heat flux $\overline{w'\theta'_z}$.¹⁹ The absolute value of buoyancy is commonly defined as

$$b_z = \frac{g}{\theta_0} \theta_z \quad \text{and} \quad B_z = \overline{w'b'_z} = \frac{g}{\theta_0} \overline{w'\theta'_z}. \quad (2.26)$$

Here g is the Earth's gravitational acceleration and θ_0 a rather arbitrary background reference level, often set to normal conditions ≈ 300 K. Thus 'warming' correlates with an increase of buoyancy and can be used analogously. With Eq. 2.26 the buoyancy budget directly follows from the similar heat budget. Assuming horizontal homogeneity and no sources and sinks, the buoyancy budget at height z is given by

$$\frac{\partial b_z}{\partial t} = -\frac{\partial B_z}{\partial z}, \quad (2.27)$$

which is simply the balance of the tendency (first term on the lhs) and the turbulent flux divergence (second term on the lhs) of buoyancy.

2.4.2 Velocity variances and the TKE budget

As for the mean part of a fluctuating quantity, one can also determine the budget for its variance, e.g. for the variance of buoyancy or the velocity components, which represent important properties of ABL turbulence. However, in this study we only marginally investigate the evolution of buoyancy or particular velocity fluctuation. Instead, we primarily focus on the kinetic energy that is associated with turbulent velocity fluctuation. It is denoted as turbulence kinetic energy (TKE) and commonly used to quantify the intensity of turbulence. The search for an integral model for the TKE-budget of sheared CBLs is the core topic of this study. The specific TKE (per unit mass) of a flow is defined by the magnitude of the velocity variance

$$e = 1/2 \left(\overline{u'^2} + \overline{v'^2} + \overline{w'^2} \right). \quad (2.28)$$

For a horizontally homogeneous ABL the ensemble-averaged TKE (e_z) budget at a height z (subscript z) is given by (e.g. Stull, 1988, chapter 5):

$$\frac{\partial e_z}{\partial t} = B_z + S_z + \phi_z + \varepsilon_z, \quad (2.29)$$

with

$$B_z = \overline{b'w'_z}, \quad (2.30)$$

$$S_z = -\overline{w'u'_z} \frac{\partial u_z}{\partial z} - \overline{w'v'_z} \frac{\partial v_z}{\partial z}, \quad (2.31)$$

$$\phi_z = -\frac{\partial \overline{e'w'_z}}{\partial z} - \frac{1}{\rho_z} \frac{\partial \overline{p'w'_z}}{\partial z}. \quad (2.32)$$

¹⁹Effects of humidity (water vapor) on buoyancy can be analogously accounted for by using the similar virtual potential temperature θ_v .

Here $\partial e_z / \partial t$ is the tendency of TKE, B_z , which equals the buoyancy flux, is the buoyancy production of TKE and S_z is the shear production of TKE along the velocities components u and v .²⁰ ϕ_z is the divergence of TKE fluxes and in the following also called the TKE-transport term. It consists of two contributions: The first is the divergence of the turbulent TKE-flux (first term on the rhs in Eq. 2.32) and the second is the divergence of the pressure correlation term (second term on the rhs), where p is the pressure and ρ the air density. ε_z is the rate of viscous dissipation of TKE into heat (simply denoted as 'dissipation rate' henceforth), which is the main sink for TKE. As each term of the TKE-budget is relevant for our analysis later on, we here already indicate their physical significance briefly.

TKE shear-production always acts as a source of TKE. In the ABL it is induced by the combination of horizontal wind and surface friction. As a nearly ubiquitous phenomenon, it is often considered as the most elementary source of ABL turbulence.

Due to the typical large ratio of buoyancy forces and inertial forces, ABLs (and other geophysical flows) are also very susceptible to the influence of buoyancy (Wynngaard, 2010, chapter 9.3.1), which are practically present in any atmospheric scenario. The significant role of buoyancy is a prominent characteristic that distinguishes ABLs from most engineering BLs, which are predominately shear-driven. Differently to shear production, and depending on the stratification of the flow, buoyancy production can act as a source or as a sink for TKE. If $B_z = \overline{b'w'_z} > 0$ the flow is usually statically unstable ($\partial b_z / \partial z < 0$) and TKE is produced by a transformation from potential energy. $B_z > 0$ represents the upward transport of lighter (warmer) fluid and, due to continuity a downward transport of heavier (cooler) fluid. Hence the potential energy of the system decreases and is accordingly transformed into the kinetic energy of positively buoyant updrafts and negatively buoyant downdrafts. But if $B_z < 0$, which is typically associated with a statically stable stratification ($\partial b_z / \partial z > 0$), a downward transport of lighter (warmer) fluid takes place and in turn, due to continuity, an upward transport of heavier (cooler) fluid. This means that the potential energy of the system increases. At the same time turbulence is weakened, as vertical turbulent motions act against the buoyancy. Hence TKE is 'consumed' and transformed into potential energy. In the ABL buoyancy-consumption is caused by turbulent mixing over the stably stratified interface to the FA and therefor used as measure for the 'entrainment' process (see the next section).

In an evolving BL the TKE-tendency (lhs of Eq. 2.29), which represents the in-stationarity of the TKE-budget, is typically positive, as the amount of TKE stored in the flow grows. As this can be associated with a 'spin-up' process of the turbulent motions, the TKE-tendency term is commonly called 'TKE spinup' term. Similar to the TKE buoyancy-consumption, TKE spinup 'consumes' TKE (by increasing the storage) and is similarly a result of BL growth. However, in mature ABLs TKE spinup is generally smaller than TKE buoyancy-consumption. Simple modeling approaches of the CBL dynamics assume approximately stationary TKE-dynamics. An explicit treatment of the spinup term is therefore often omitted (discussed in more detail later on).

Both TKE transport terms (Eq. 2.32, rhs) are mostly associated with distribution

²⁰In section 2.2 we already introduced $P = P_S + P_B$, which are also measures of the TKE production and have the same dimensions. The difference is that P_S and P_B are representative for the whole flow, whereas S_z and B_z are just the local values at height z .

of TKE within the turbulent BL and in total assumed to be zero when integrated over the whole turbulent layer. However, the pressure fluctuation term is not limited to turbulence as it also represent transport of fluctuation energy by gravity waves in the stratified FA.²¹ Therefore it should become relevant in case of significant turbulence-wave interactions across the upper ABL interface occur.

In fully developed turbulence the viscous dissipation rate ε_z is by far the largest destruction term and therefore a very essential quantity for the characterization of high Reynolds-number flows. As we focus on entrainment in this study, we only shortly deal with the dissipation rate directly. But we make use of some basic similarities between integral dissipation and entrainment rate, as already suggested in section 2.2.

The Richardson number. To characterize a turbulent flow that is affected by shear and buoyancy, it is natural to compare the TKE-buoyancy and shear production with each other, e.g. by examining the ratio of appropriate measures for both quantities. Such a ratio is commonly called 'a' Richardson number Ri .²² The most basic Ri is the flux Richardson number Ri_f , which is the ratio of the local buoyancy and shear-production (first term and second term on the rhs in Eq. 2.29)

$$Ri_f(z) = -\frac{B_z}{S_z} = -\frac{\overline{b'w'_z}}{-\overline{w'u'_z} \frac{\partial u_z}{\partial z} - \overline{w'v'_z} \frac{\partial v_z}{\partial z}}. \quad (2.33)$$

In our analysis later on, we will use several similar but more specific integral dimensionless quantities, to characterize sheared CBLs.

In stably stratified flows vertical turbulent motions act against buoyancy, which therefore dampens or even suppresses turbulence. When we only would consider the balance between shear production and buoyancy consumption, turbulence would decrease if Ri_g is > 1 throughout the flow, as in this case the TKE consumption exceeds production. If $Ri_f > 1$ is sustained, then turbulence finally vanishes and the flow becomes laminar. However, to maintain turbulence, Ri_f must be clearly < 1 as production not only has to feed buoyancy consumption but also viscous dissipation, which is by far the largest loss term. This indicates that critical values of the Richardson number can be used to characterize the transition between turbulent and laminar state in stably stratified flows.²³

However, Ri_f is only defined in the turbulent state, as $\overline{w'U'_z}$ has to be finite. Thus, to characterize the transition between turbulence and the laminar state in both directions, a more universal measure is required. Referring to the idea of 'turbulent

²¹Note that TKE and gravity-wave fluctuation-energy are defined equally and can not be distinguished in a first instance. Any differentiations depend on the perception of respective flow conditions. Fluctuation energy in a stratified quasi-laminar layer is associated with gravity waves. Fluctuation energy in a turbulent layer is considered as TKE.

²²Named after Lewis Fry Richardson (1881 – 1953).

²³There is basic analogy between a Richardson number Ri and a Reynolds number Re , which also compares 'production scale' properties with those of a TKE sink.

In the ABL Reynolds numbers are generally much larger than the critical values and viscosity is therefore not limiting the vertical proliferation of ABL turbulence. It is the FA stable stratification that confines the turbulent ABL. Critical values of appropriately defined Ris are therefore useful to determine turbulence evolution at the interface between ABL and FA.

diffusion',²⁴ one can replace the turbulent fluxes by gradients in Eq. 2.33 and so define the gradient Richardson number

$$\text{Ri}_g(z) = \frac{\partial b_z / \partial z}{(\partial u_z / \partial z)^2 + (\partial v_z / \partial z)^2}, \quad (2.34)$$

which can be determined for both the turbulent and the laminar state. Lab experiments suggest that in purely shear-driven stratified flows two different critical values of Ri_g define the conditions for which either a laminar flow becomes turbulent ($\text{Ri}_g < 0.25$) or turbulent flow becomes laminar ($\text{Ri}_g > 1.0$) (Stull, 1988, page 176).

$\text{Ri}_g(z)$ describes the local TKE balance of TKE production and consumption. But often it is preferable to study BLs as integral system. In this case it is quite common to use vertical differences of integral properties instead of local vertical gradients to define so-called bulk Richardson number(s). In our analysis later on we will consider the specific bulk Richardson number Ri_U (as defined in Eq. 7.3). Laboratory and numerical experiments show that in purely shear-driven stratified BLs a critical value of Ri_U characterizes entrainment and the growth dynamics, as these are the result of a continuous transition from the laminar to a turbulent state at the top of the BL (Jonker *et al.*, 2013).²⁵ In section 5.4 and 7.2 we show that entrainment in a sheared CBL can be characterized similarly.

2.5 Basic characteristics of the CBL

The turbulent boundary layers that we consider in this study, are mostly driven by both buoyancy and wind shear. Nevertheless, in a first instance, we follow Conzemius and Fedorovich (2007) and classify them all as CBL, in case the surface buoyancy flux B_s is positive. The CBL without mean wind-shear, which is the starting point for our considerations, we mostly denote as 'non-sheared' or pure CBL. In case wind-shear is present, we call a CBL a 'sheared' CBL.

2.5.1 CBL buoyancy dynamics

Sketch Figure 2.1 shows the typical buoyancy structure of an atmospheric CBL, as it has developed after several hours from an initially linearly stratified atmosphere (thin black lines in (a)). Panel (a) shows the vertical profile of the mean buoyancy b_z and panel (b) the vertical profile of the buoyancy flux $B_z = \overline{w'b'_z}$, which represents the production rate of TKE by buoyancy (Eq. 2.30).

The upper boundary of the CBL (subscript u) is marked by the height z_{iu} . It separates the turbulent BL from the quiescent, non-turbulent free atmosphere (FA). Consequently, the turbulent flux in the FA is zero ($\overline{b'w'}(z \geq z_{iu})$) and the buoyancy profile equals the linear background or initial profile $b_{ini,z}$. The linear FA stratification is often expressed in terms of the Brunt-Väisälä frequency $b_{ini,z} / \partial z = N^2$.

A well-developed CBL is characterized by a pronounced vertical structure. Depending on which detail or process is considered or which statistical quantity of turbulence is measured, a multitude of layers, transient region, etc. can be identified. But

²⁴This suggests that approximately $\overline{w'u'_z} \propto (\partial u_z / \partial z)$ and $\overline{w'b'_z} \propto (\partial b_z / \partial z)$.

²⁵Note that in some shear-driven BLs the flow profiles can be largely self-similar (e.g. Jonker *et al.*, 2013), so that any bulk Richardson number should also be proportional to $\text{Ri}_g(z)$.

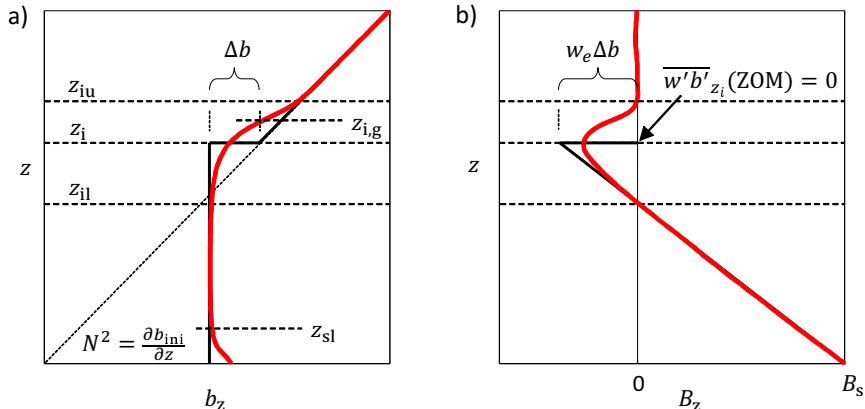


Figure 2.1: Typical profiles of the CBL mean buoyancy (a) and the mean buoyancy flux (b). Red lines shows the flow profiles, black lines the 0th-order model (ZOM) of the CBL. Horizontal black dashed lines in both panels mark the vertical structure of the CBL. The thin dotted line in (a) marks the initial or background buoyancy profile b_{ini} .

considering the essential dynamics of convective turbulence (in terms of the ensemble-averaged TKE) first of all two layers can be distinguished, which are separated at the height of zero-crossing of $\overline{b'w'_z}$ at z_{il} . The lower layer from 0 to z_{il} defines a region with positive buoyancy production ($\overline{b'w'_z} > 0$) and the layer above from z_{il} to z_{iu} , is defined a region with TKE buoyancy consumption ($\overline{b'w'_z} < 0$), which extends until the CBL top $z_{\text{i,u}}$.

The region with positive buoyancy production can be further subdivided in the surface layer (SL) and the mixed layer (ML) above. The SL comprising roughly 10% of the CBL depth, shows a strong negative buoyancy gradient ($\partial b_z / \partial z < 0$) reflecting the static instability of the air caused by the intense heating from the surface. Parcels of warmer positively buoyant air ($b'_z > 0$), which rises, and cooler negatively buoyant air ($b'_z < 0$), which sinks down, create intense turbulent motions and result in a strong upwards flux of buoyancy ($B_z = \overline{w'b'_z} > 0$). The vicinity of a hard boundary in the SL restricts vertical eddies size and therefore enforces deformation (strain) and fragmentation of larger eddies. In a CBL this results in a separation of the 'active' small scale SL turbulence from the very large energy-containing convective motions. Within the SL these large motions appear as horizontal background currents, which result in local shear production of turbulence, even in purely 'free' convective conditions (e.g. Wyngaard (2010), section 10.1 and 10.4 or Akylas *et al.* (2003)). The associated 'locality' and the decoupling of certain turbulence properties from the upper BL regions is relevant for the understating of sheared CBL dynamics (chapter 4 and 7).

Above, in the ML, buoyancy-driven turbulence can organize itself in much larger convective cells, which consist of positively buoyant air concentrated in rising 'plumes' or 'thermal updrafts', which only cover a small area of the horizontal area, and the surrounding slow sinking cooler air, which is negatively buoyant. This organized

convection enables efficient vertical, so-called 'non-local' transport, which does not correlate with the mean gradient, as can be seen by the rather uniform buoyancy profile.²⁶ With respect to the CBL dynamics, the SL plus the ML define a layer (SM, henceforth), where potential energy, which is provided by the surface buoyancy flux, is transferred into TKE ($\overline{w'b'_z} = B_z > 0$).

The TKE consumption-layer above the SM is created by the interaction between convective turbulence and the quiescent free atmosphere (FA). It is stably stratified throughout ($\partial b_z/\partial z > 0$) and is topped by a pronounced inversion, which is significantly more stable than the FA above and forms a well-defined interface between the FA and the CBL. Thus the upper CBL layer is also addressed as 'interfacial layer' (subscript i). Mostly turbulent, the dynamics in this layer are determined by the mixing of quiescent FA air into the turbulent CBL, a process commonly called 'entrainment'. Therefore the interfacial layer is usually called entrainment zone (EZ). A further characteristic measure of the EZ inversion is the maximum buoyancy gradient, which defines the height $z_{i,g}$.

CBL entrainment CBL entrainment is driven by ML plumes that enter into the stably stratified FA. After they have been accelerated within the ML by a buoyancy excess (compared to their surrounding), they overshoot the level where the buoyancy excess vanishes (roughly at about z_{i1}) and finally rise into the warmer and lighter FA, where they are decelerated by gravity due to a lack of buoyancy (compared to the surrounding FA air). Due to continuity, every ML plume that penetrates the FA, forces an equal volume of warmer and lighter FA air to move downwards into the EZ. A penetrating plume is highly turbulent in itself and its boundaries subjected to shear. Therefore it tends to disintegrate and to mix with its surrounding, before some of its remaining air mass – due to its negative buoyancy – sinks down into the ML again. The entraining FA air, on the other hand, is only weakly turbulent in the beginning. Through contact with the plumes and turbulence in the lower EZ it tends to be mixed with turbulent air, thus one could say that it is 'turbulized' and dispersed within the EZ (e.g. see the quadrant analysis in Sullivan *et al.*, 1998). This means that the intrusion of thermal plumes into the FA is to a large extent an irreversible process and the associated vertical exchange of air masses and buoyancy, which results in a continuous entrainment of warm FA air into the CBL, a steady erosion of the capping inversion and a continuous growth of the turbulent layer.

With respect to the TKE dynamics one finds that a significant portion of the TKE that is produced in the SM ($\overline{b'w'} > 0$) is transported upwards into the EZ. In the EZ a significant portion of this TKE is consumed (the area with $\overline{b'w'} < 0$) and transferred into potential energy as it executes mechanical work on the FA by transporting (mixing) cooler and heavier ML air upwards and lighter and warmer FA air downwards against the gravity field. Thus one could say that the two-layer structure of the CBL, given by SM plus EZ, represents essentially the thermodynamic functioning, the 'engine', of an entraining CBL. To characterize CBL dynamics it seems therefore natural to compare the SM-integrated buoyancy production and the EZ-integrated buoyancy consumption, as we will do in our data analysis of the integral TKE budget in chapter 4.1.

²⁶Thus, for the convective ML, turbulent diffusion is obviously not an appropriate concept (e.g. Siebesma *et al.*, 2007).

According to our description above, 'entrainment' can be associated with an exchange of air masses (and related properties) between CBL and FA, as well as the dispersion of TKE into the FA and its consequent consumption. For the investigation of stratified flows in a gravity field, the latter aspects is the most significant and therefore commonly referred to. Hence in the remainder of this study, we consider 'entrainment' as the consumption (or conversion) rate of TKE in the stably stratified interfacial region of the BL.²⁷ TKE-consumption reduces the stratification within the EZ, which results in a steady deepening of the EZ and so contributes to the overall growth of the whole CBL.²⁸

We will study the integral CBL TKE-budget in detail in section 4.1. But to continue here, we here have to prematurely introduce some related, commonly used concepts. As TKE buoyancy production is the driving force for CBL turbulence, it is a natural scale to rate all other terms of the TKE-budget and in this way to characterize the CBL TKE-turnover or the 'CBL dynamics' respectively, as we mostly call it in the remainder of this study. With respect to entrainment, quantities that rate TKE-consumption against TKE-production are typically called 'entrainment ratio'.

The convective scales. A commonly used quantity to measure CBL TKE-production is the integral convective velocity scale w_* , which can be associated with the characteristic vertical velocity of thermal updrafts. Taking the SM depth z_{i1} as the integral length scale of convection, w_* is given by (e.g. Garcia and Mellado, 2014)²⁹

$$w_* = (B_0 z_{i1})^{1/3}. \quad (2.35)$$

Assuming a linear buoyancy flux profile, $1/2 w_*^3$ equals the buoyancy TKE production integrated over the whole SM, which we will use in our data analysis later on. We note that in literature w_* is traditionally defined using z_i as length scale. We consider this choice as much less intuitive and instead prefer z_{i1} as it represent the depth of the layer with (positive) integral buoyancy production. In pure, high Re CBLs, the surface-flux based w_* is a well-known characteristic scale for turbulent velocity fluctuations w' and u' in the SM. A respective buoyancy scale b_* for turbulent buoyancy fluctuation b' is given by

$$b_* = B_0/w_*. \quad (2.36)$$

As soon as the CBL reaches approximately stationary conditions (as defined below) these convective scales are sufficient to scale b' and the velocity fluctuation w' , u' (or e respectively) at any height in the SM (see Figure 2.5).

²⁷In turn, the presence of entrainment (or TKE buoyancy-consumption) defines the EZ. For a mature CBL, this simple concept, which directly reflects the structure of the CBL buoyancy dynamics, turns out to be useful and sufficient. However, for purely shear-driven BLs, further considerations are necessary, as we demonstrate in section 7.2.

²⁸With respect to CBL growth, one should principally also distinguish between (1) the contribution of entrainment, which is caused by mixing in the EZ, driven by overshooting of air parcels above the SM, and (2) the contribution of the underlying SM growth due to warming, which is called 'encroachment'. For more detail see section 2.5.4.

²⁹In non-sheared CBL z_{i1} approximately equals the encroachment height z_{enc} (Eq. 2.62). Hence, our definition practically agrees with (Garcia and Mellado, 2014), who consistently use z_{enc} as elementary integral CBL length scale, which gives $w_* = (b_0 z_{enc})^{1/3}$.

2.5.2 Sheared CBL wind dynamics

The mean wind profile and the momentum dynamics in ABLs are strongly influenced by the spatial and temporal distribution of the momentum sources, which is the pressure gradient force and in extra tropical ABLs the Coriolis force. The latter can induce inertial oscillations of the horizontal mean flow. These interact with turbulence³⁰ and often result in a strong variability of the ABL wind profile. The general

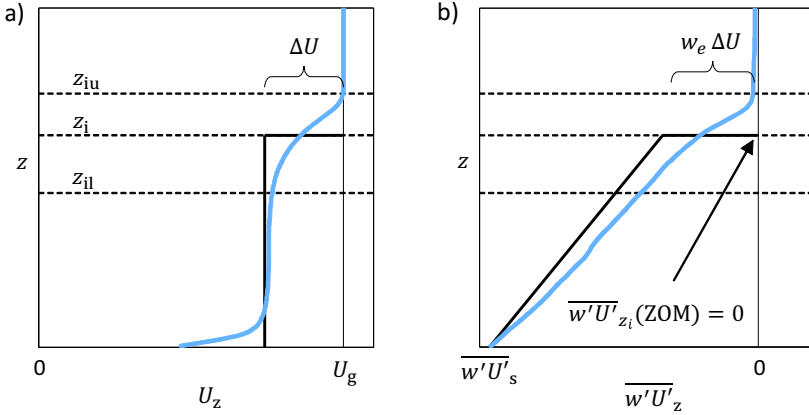


Figure 2.2: Typical profiles of the CBL mean wind speed (a) and the flux of mean momentum (b). Blue lines show the ensemble-averaged mean profiles, black lines the 0th-order model (ZOM).

pattern of the wind-speed and the momentum-flux profile of a sheared CBL are shown in Figure 2.2. As the directional variation of the wind profile will not be relevant for our analysis³¹ only the magnitude of the wind vector (i.e. the wind speed) and the magnitude of the momentum flux is shown. In the following we use the bold capital letter $\mathbf{U} = (u, v)$ for the wind vector and the capital letter U for its magnitude:

$$U_z = |\mathbf{U}_z| = \sqrt{u_z^2 + v_z^2}. \quad (2.37)$$

Accordingly, the magnitude vertical momentum flux (or stress) is given by

$$\overline{w'U'_z} = \overline{w'|\mathbf{U}'|_z} = \sqrt{\overline{w'u_z'^2} + \overline{w'v_z'^2}}. \quad (2.38)$$

Shear in the ABL is basically induced by surface friction, which results in loss ('out-flow') of momentum at the surface. This loss is mediated upwards via turbulent momentum flux, which results in a momentum-flux divergence ($\partial \overline{w'U'_z} / \partial z > 0$), which decelerates the flow and causes shear at the upper boundary between CBL and FA.

Figure 2.2 (a) shows that CBL wind shear $\partial U_z / \partial z$ is concentrated at the lower and upper boundary of the flow in the SL and in the EZ. This structure is typical

³⁰Using a simplified setup, this was investigated by Schröter *et al.* (2013). This study is included in this thesis as appendix E).

³¹As are the other terms of the momentum budget.

for entraining BLs³². The particularly weak shear in the convective ML can be again attributed to the effective 'non-local'-transport by convection.³³

The positive shear and CBL entrainment in the EZ causes an inflow of faster FA air, which is decelerated within the EZ, as can be seen by the enhance stress divergence above z_i (Figure 2.2 (b)). But with respect to the CBL the entrainment of faster FA air equates to an acceleration of the SM mean flow.

The combination of shear and stress divergences within the CBL produces additional turbulence (Eq. 2.31). In this study we investigate to what extent shear-produced turbulence affects and modifies CBL entrainment and the TKE-dynamics. This entails the identification and evaluation of shear-related integral scales that complement the well-known convective scales presented in the previous paragraph.

2.5.3 The 0th-order model (ZOM) approach

One practical goal of this study is a simple representation of the evolution of 1st and 2nd-order turbulent statistics, such as buoyancy, momentum (or a concentration of a trace gas) and their respective fluxes. For this purpose an integral representation of Reynolds averaged prognostic equations, such as provided by the 0th-order model (ZOM) approach, has shown to be useful (e.g. Conzemius and Fedorovich, 2006b, 2007). For the definition of the ZOM bulk approach we mostly follow Conzemius and Fedorovich (2006b) and the precursor studies cited therein.

The basic idea of the ZOM bulk approach is to represent the entire CBL only by layer-averaged quantities and their budgets. For any Reynolds-averaged mean quantity c_z the respective layer-averaged value c_m , from the surface up to the height z_x is given by

$$c_m(t, z_x) = \frac{1}{z_x} \int_0^{z_x(t)} c_z(t) dz. \quad (2.39)$$

As previously shown by the examples of mean buoyancy b_z (Eq. 2.27) and mean momentum $\mathbf{U}_z = (u_z, v_z)$ (Eq. 2.24), a budget equation always consists of a tendency $\partial c_z / \partial t$, which is created by the sum of a vertical flux divergence $\partial w'c'_z / \partial z$ and further contributions, which added up to the net source term Q_z . Using this notation and accounting for time dependency of the upper integration limit $z_x(t)$ for integration (Leibniz-rule), the layer-averaged budget for c_m (subscript m for 'mean') is

$$\frac{\partial c_m}{\partial t} = -\frac{w_{e,z_x} \Delta c_{z_x}}{z_x} - \frac{\overline{w'c'_{z_x}} - \overline{w'c'_0}}{z_x} + Q_{m,c}, \quad (2.40)$$

with $\Delta c_{z_x} = c_{z_x} - c_m$ and $w_{e,z_x} = \frac{\partial z_x(t)}{\partial t}$.

Here w_{e,z_x} is the growth rate of the BL depth, $\overline{w'c'_0}$ is the turbulent surface flux and $Q_{m,c}$ the layer-averaged source term of c . The subscript ' z_x ' designates quantities at

³²See also the normalized wind profile of a neutral BL, Figure B.1 in appendix B

³³For concepts and significance of the non-local convective momentum transport see, e.g., Brown and Grant (1997); Siebesma and Cuijpers (1995).

It is also worth noting that in extra-tropical BLs, the Coriolis force modifies the shape of the wind profile, which can even result in jet like structures and negative-shear. This property e.g. limits the potential depth of shear-driven neutral BLs and is prototypically represented by the well-known idealized Ekman-layer with a scale depth $\sim u_* / f_c$.

the height z_x , where the top of the – yet undefined – characteristic layer is located. Δc_{z_x} is the characteristic jump of c_m at height z_x . The term on the lhs of Eq. 2.40 is the tendency of the layer mean, the first term on the rhs the Leibniz term, which quantifies the flow into the layer due to the movement of its upper boundary at $z_x(t)$. The second term on the rhs is the divergence of the turbulent fluxes, where $\overline{w'c'}_{z_x}$ is the turbulent flux through the upper boundary. As long as $z_x < z_{iu}$, $\overline{w'c'}_{z_x}$ is finite and Δc_{z_x} depends on c_{z_x} . Both $\overline{w'c'}_{z_x}$ and c_{z_x} represent the local state at z_x within the CBL and have to be considered as unknowns of the prognostic problem (Eq. 2.40). Therefore, it would be natural to choose $z_x := z_{iu}$ and to average the CBL over its full depth up to z_{iu} , where turbulence has ceased (Figure 2.1 and 2.2). This would simplify Eq. 2.40 significantly, as $c_{z_{i,u}}$ becomes $c_{ini}(z_{iu})$, which represents the known background value of c_z just above the turbulent layer and the turbulent flux at CBL top $\overline{w'c'}_{z_{iu}}$ becomes zero. Thus, the respective entrainment velocity $w_{e,z_{iu}} = \partial z_{iu} / \partial t$ would remain the only unknown³⁴, which would have to be modeled in order to close the prognostic CBL budget.

However, traditionally, the characteristic CBL depth for ZOMs is associated with z_i , the height of buoyancy flux minimum³⁵. In this study we follow this practice, as the minimum buoyancy flux in itself is a useful scale for the entrainment dynamics. This choice also simplifies comparison with previous work.³⁶

The ZOM approach intends to combine the choice of z_i as characteristic CBL depth with an appropriate integral budget. This is achieved by an enforced adaptation of the real CBL profiles (red lines in Figure 2.1 and blue lines in Figure 2.2) to the ZOM profile (black lines). One virtually removes turbulence above z_i and undoes the respective turbulent transport that has happened and extrapolates the linear FA background profiles (which in our setup equals the initial conditions) down to z_i . The suggested 'undoing' of turbulence effects implies a redistribution of properties between the upper EZ and the ZOM-BL. Using the example of b_z , this is schematically shown in Figure 2.3. With this redistribution the ZOM value for a quantity c is defined

$$c(t) = \frac{1}{z_i} \int_0^{z_i(t)} c_z(t) dz + \frac{1}{z_i} \int_{z_i(t)}^{z_{iu}(t)} (c_z(t) - c_{ini}(z)) dz. \quad (2.41)$$

Here $c_z(t)$ is the vertical mean profile of the quantity c and $c_{ini}(z)$ its initial state (subscript ini). For convenience we use plain letters, e.g. b , $\mathbf{U} = (u, v)$, etc. with no subscripts for the ZOM quantities. In the ZOM framework (Figure 2.1 and 2.2, black lines) the limit $z_x \mapsto z_i$ is the upper boundary of the turbulent layer. Thus the turbulent fluxes at and above z_i are zero and the value of any quantity c at and above z_i is the FA background value that equals the initial conditions. Thus

$$\overline{w'c'}_z(z \geq z_i) = 0 \quad (2.42)$$

and

$$c_z(z \geq z_i) = c_{ini}(z). \quad (2.43)$$

³⁴We here consider the surface flux and the source term as known external forcings for the turbulent BL, although in the atmosphere both may well interact with CBL turbulence.

³⁵Often called 'Deardorff length', after James W. Deardorff. (1928-2014), see, e.g., Deardorff (1974b).

³⁶But due to the self-similarity of the CBL structure one can expect that e.g. also the height of the maximum buoyancy gradient $z_{i,g}$ is similarly suitable to mark the characteristic depth of the ZOM-CBL. See also section 5.4.

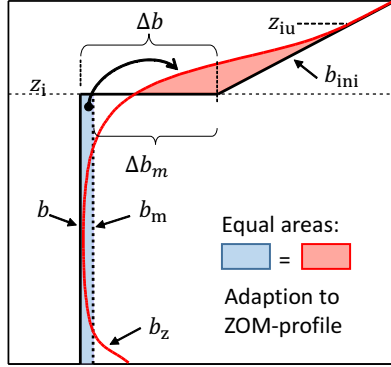


Figure 2.3: Determination of ZOM-profile and related quantities from the CBL-profile according to Eq. 2.41, using the example of buoyancy (adapted from Figure 2 in Conzemius and Fedorovich (2006b)). Note that some ZOM studies use $\Delta b_m = c_{ini}(z_i) - c_m$ instead of Δb , which results in an unclosed buoyancy budget.

These boundary conditions (Eq. 2.42 and 2.43) and the budget of the layer mean (Eq. 2.41) for the limit $z_x \mapsto z_i$ define the ZOM-budget for the quantity c :

$$\frac{\partial c}{\partial t} = -\frac{w_e \Delta c - \overline{w'c'}_0}{z_i} + Q_c, \quad (2.44)$$

with

$$\Delta c = c_{ini}(z_i) - c \quad (2.45)$$

and

$$w_e = w_{e,z_i} = \frac{\partial z_i}{\partial t}, \quad (2.46)$$

which is the CBL growth rate, commonly denoted as 'entrainment velocity'. The lhs in Eq. 2.44 is the tendency of the ZOM value of c , the first term on the rhs is the flux divergence, where $w_e \Delta c$ is the entrainment flux at the upper boundary, and Q_c is the layer-averaged source term. Accordingly, one can derive the ZOM budget equations for buoyancy and momentum from Eq. 2.27 and 2.24.

The ZOM buoyancy-budget. In a cloud-free CBL the source term for buoyancy is zero, thus the ZOM budget equation for buoyancy reads

$$\frac{\partial b}{\partial t} = -\frac{w_e \Delta b - \overline{w'b'}_0}{z_i}. \quad (2.47)$$

Here $\Delta b = b_{z_i} - b$ represent the buoyancy jump at the top of the ZOM BL at z_i .

The ZOM momentum-budget. The pressure gradient force is always a source for momentum, whereas the Coriolis force, which redirects momentum, can acts as a source and a sink. If we again align the x-axis with the geostrophic wind, the pressure

gradient force $\partial p/(\rho \partial y) = f_c u_g$ only affects the v-component of the flow. The ZOM budget-equation for $\mathbf{U} = (u, v)$ then reads

$$\begin{aligned} \frac{\partial u}{\partial t} &= - \frac{w_e \Delta u - \overline{w' u'}_0}{z_i} + f_c v \\ \frac{\partial v}{\partial t} &= - \frac{w_e \Delta v - \overline{w' v'}_0}{z_i} - f_c u + f_c u_g. \end{aligned} \quad (2.48)$$

Here the first term on the lhs is the tendency, the first term on the rhs the flux divergence and further terms are sources and sinks. $\Delta u = u_g - u$ and $\Delta v = -v$, are the components of the velocity jump ΔU at the top of the ZOM BL at z_i . For many application it is useful to parametrize the surface stress with a drag law, which is typically given by

$$\overline{w' u'}_0 = -C_{D,u} U u, \quad \overline{w' v'}_0 = -C_{D,v} U v, \quad (2.49)$$

$$\text{with } U = \sqrt{u^2 + v^2}, \quad (2.50)$$

where the drag coefficient $C_D = (C_{D,u}, C_{D,v})$ is supposed to further depend on the surface roughness, flow stability and on directional shear³⁷.

The ZOM entrainment model. To close the prognostic ZOM budgets, one needs a model for entrainment velocity as a function of ZOM quantities, e.g.

$$w_e = f(B_0, \Delta b, \overline{w' U'}_0, \Delta U, z_i, \dots). \quad (2.51)$$

In this study we regularly refer to any form of a '0th-order jump entrainment model', which is described by Eq. 2.51, as 'ZOM', as it represents the essential turbulence-closure within the ZOM-framework.³⁸ Such a ZOM entrainment-model defines an entrainment ratio, $w_e \Delta b/B_0$, and therefore reflects at least parts of the CBL TKE-dynamics and can therefore considered as a simple 'TKE-model'.

The presented method to force the CBL profiles into the ZOM may seem somewhat artificial at first sight, but it ensures closed budgets (Conzemius and Fedorovich, 2006b). Finally, note that the ZOM is also the most simplistic representation of the natural CBL structure, as given by the buoyancy-flux profile (Figure 2.1(b)). We therefore find the ZOM representation to be a very useful reference framework for a more detailed investigation of the CBL structure (chapter 6).

In some ZOM studies (e.g. Van Zanten *et al.*, 1999), the redistribution term (second term on the rhs in Eq. 2.41) is neglected and ZOM quantities c are approximated by c_m . However, for deep EZs, which are typical for strongly sheared CBLs, the difference

³⁷In barotropic conditions directional shear is represented by the ageostrophic angle $\alpha_c = v/u$. For a typical parametrization, see, e.g., Arya (1977). We found that his integral BL drag-law could be rather well fitted to our sheared LES-CBLs.

³⁸However, in a wider sense the term 'ZOM' is also commonly used for a complete ZOM-based ABL simulation model and then refers to a complete set of prognostic equations, often completed by parametrization of surface processes, clouds, etc..

is significant as illustrated by Figure 2.3 and should result in systematic errors of the ZOM-budgets.³⁹

Finally, with regard to our later analysis we note that the enforcement of the ZOM buoyancy profile implies a modification of the BL's potential energy. This means that a ZOM TKE-budget must differ from that of the real CBL. Hence for any comparison between ZOM and real BL TKE-dynamics this basic difference has to be considered. To keep things simple and clear, we actually will not try to define a 'ZOM TKE-budget' directly. Instead we will consider the integral TKE budget of the real CBL first and then make use of the similarity between the integral TKE-production terms (as defined later on) and their ZOM counterparts.

The ZOM TKE-production terms. The principle of the ZOM suggest to define ZOM TKE-production terms as means or integrals over the whole CBL. For the ZOM TKE shear-production $S(\text{ZOM})$ we follow Conzemius and Fedorovich (2006b), who define it as the layer-integral of the mean shear production (Eq. 2.31)

$$S(\text{ZOM}) \approx S = \int_0^{z_{\text{in}}} \left(-\overline{w'u'_z} \frac{\partial u_z}{\partial z} - \overline{w'v'_z} \frac{\partial v_z}{\partial z} \right) dz. \quad (2.52)$$

The integral shear production S is then approximated using the idealized linear ZOM velocity and momentum flux profiles (Figure 2.2). As a result the ZOM shear production term $S(\text{ZOM})$ consists of surface contribution, which can be associated with the SM (subscript SM) and contribution at the upper boundary, which can be linked to the EZ dynamics (subscript EZ). Hence

$$S(\text{ZOM}) = S_{\text{SM}}(\text{ZOM}) + S_{\text{EZ}}(\text{ZOM}), \quad (2.53)$$

with

$$S_{\text{SM}}(\text{ZOM}) = u \overline{w'u'_0} + v \overline{w'v'_0} \quad (2.54)$$

and

$$S_{\text{EZ}}(\text{ZOM}) = \frac{1}{2} (w_e \Delta u^2 + w_e \Delta v^2) = \frac{1}{2} w_e \Delta U^2. \quad (2.55)$$

Here $\overline{w'\mathbf{U}'_0} = (\overline{w'u'_0}, \overline{w'v'_0})$ is the surface stress, $\mathbf{U} = (u, v)$ the ZOM velocity and $\Delta \mathbf{U} = (\Delta u, \Delta v)$ the ZOM EZ velocity jump, as previously defined.

With respect to a proper definition of the ZOM buoyancy production and consumption (i.e. entrainment) terms, scientific literature is surprisingly inconsistent. Two different, competing concepts coexist and have been both applied. But we could not find a final argument in literature that would clearly favor one over the other. Obviously, this issue deserves more attention. Thus, we will analyze and discuss it in detail later on (chapter 4.1.1, 5 and 7.1). A clear decision on this issue will be one of our basic results.

³⁹But as the differences between Δc and Δc_m obviously depend on depth and structure of the EZ, they should be well scalable. But for consistency we always use the 'correct' ZOM quantities c in this study.

2.5.4 The equilibrium entrainment regime and the constant ZOM-entrainment ratio

The evolution of a CBL can be considered as a succession of three different physical regimes (Garcia and Mellado, 2014). In the very initial stage the quickly growing turbulent layer is so shallow that turbulence does not feel the influence of stratification and therefore resembles convective engulfment into a neutral layer.⁴⁰ In the next phase the impact of FA stratification N^2 becomes significant, TKE is increasingly distributed into horizontal velocity fluctuations and the growth rate diminishes. Still the CBL grows so fast that the TKE dynamics are significantly instationary (i.e. the TKE tendency is large compared to the buoyancy consumption). However, after a certain moment the CBL has deepened so much that the growth rate of the CBL given by e.g. $w_e = \partial z_i / \partial t$ has become small compared to the characteristic velocity of the rising, penetrating and overturning thermals, which is in the order of w_* . Thus, with $w_e / w_* \leq 0.05$ the rate of change of the turbulent fields is so small that the CBL dynamics has become 'quasi-stationary' and, as we show later, integral buoyancy consumption (entrainment) finally exceeds the integral TKE tendency (or 'TKE spinup'). In these conditions the CBL develops a largely self-similar structure, which is essentially determined by SM properties and appears to be rather insensitive to FA stratification.⁴¹ This is illustrated by Figure 2.5 (or 3.8), which shows that the SM profiles of mean buoyancy, the buoyancy flux and the velocity fluctuations become approximately self-similar, when normalized by convective scales. Furthermore, this self-similarity is reflected by a fixed ratio between EZ and SM depths, which we here call the CBL's '**constant layering**'. Using the characteristic heights z_{i1} , z_i and $z_{i,g}$ (Figure 2.1), a measure of the relative EZ depth in these conditions is given by

$$\beta_g = \frac{z_{i,g} - z_{i1}}{z_{i1}} \approx const \quad (2.56)$$

or

$$\beta = \frac{z_i - z_{i1}}{z_{i1}} \approx const. \quad (2.57)$$

The very high resolution DNS of Garcia and Mellado (2014) suggests $\beta_g \simeq 0.265$ and $\beta \simeq 0.174$ (using data from their Table 2). The latter value refines the estimation derived from previous observations somewhat, which commonly support a value of $\beta \approx 0.2$ (Fedorovich *et al.*, 2004b).

Considering the geometry of the ZOM buoyancy flux profile (Figure 2.1(b)), $\beta \approx const$ equally represents a constant ratio between ZOM entrainment buoyancy flux and surface buoyancy flux:

$$\beta = \frac{w_e \Delta b}{B_0} \approx const. \quad (2.58)$$

Hence, the self-similar structure (Eq. 2.57) can be translated into a self-similar entrainment regime, where a fixed fraction of the buoyancy TKE production, which is

⁴⁰that is, as long as the background buoyancy variation $\Delta b_0 = N^2 z_i$ over the layer depth z_i is much smaller than the typical buoyant excess b' of the plumes. For more detail see Garcia and Mellado (2014), particularly appendix A.

⁴¹Which does not imply that the FA stratification is unimportant. Rather the opposite, as FA stratification is now the dominant factor that limits the growth rate.

driven by the surface heating, maintains a turbulent entrainment flux. This feature is commonly addressed as **constant entrainment-ratio** and represents the so-called **equilibrium entrainment regime** (Fedorovich *et al.*, 2004b). Furthermore, a ZOM representation of the CBL with $\beta = \text{const}$ is independent of the rate of change of TKE within the CBL (TKE tendency). Thus it automatically implies 'quasi-stationary' flow conditions. In section 4.1.3.2 and chapter 6 we evaluate the conditions in the 'equilibrium entrainment regime' in more detail and try to better reconcile it with the fact that entrainment itself is a cause for instationarity, as shown by a TKE-tendency that is significant throughout our data set.

As an essential prototype of the daytime BLs, the shear-free CBLs have been frequently studied via tank and wind channel experiments (e.g. Deardorff *et al.*, 1969; Fedorovich *et al.*, 2001a,b; Jonker and Jiménez, 2014), LES (e.g. Deardorff, 1974a; Van Zanten *et al.*, 1999; Fedorovich *et al.*, 2004b) and DNS (Garcia and Mellado, 2014)). In typical experimental setups⁴² the quasi-stationary equilibrium entrainment regime is reached after a rather short initial period and as a characteristic feature of mature, developed CBLs, it has attracted much attention. The CBL in the equilibrium entrainment regime frequently approximates atmospheric conditions well. As a consequence ZOMs that are based on a constant entrainment ratio β are widely and successfully applied in atmospheric research and the 'equilibrium entrainment regime' is widely considered as a realistic representation of atmospheric BL dynamics. However, Garcia and Mellado (2014) suggest that the conditions for a quasi-stationary equilibrium-entrainment regime are often not met and early-phase instationarity is supposed to affect the CBL structure and dynamics rather frequently. But the significance of these transitional situations for the modeling of ABLs seems still unclear. In any case, due to its simplicity, the well-developed, mature, quasi-stationary CBL⁴³ with a constant entrainment ratio remains an important and characteristic reference flow.⁴⁴

As in most previous studies, we restrict our analysis to quasi-stationary, equilibrium entrainment conditions, and focus on the very relevant effect of wind shear. However, as a basic step towards a more complete view on sheared-CBL dynamics, which would include the instationary early-phase, we also investigate and characterize the **local** instationary behavior, which is also present in equilibrium entrainment conditions (chapter 6).

The evolution of the ZOM CBL. In the equilibrium entrainment regime with $\beta = \text{const}$ analytical solutions for the prognostic equations (Eq. 2.47) exist for several conditions (Ouwensloot and Vilà-Guerau de Arellano, 2013, and citations therein). In a first instance these solutions reflect the evolution of the shear-free CBL. But they are also useful to interpret the evolution of sheared CBLs, as we show later on.⁴⁵ For this purpose, a setup that only represents the essential physical aspects is most suitable. We therefor consider an idealized CBL that is driven by constant B_0

⁴²Most setups produce CBLs that grow into a linearly stratified, quiescent layer.

⁴³Or BL in general, as the same basic reasoning applies to shear-driven BLs. See section 7.2.

⁴⁴For instance, it could serve as a reference base to characterize deviations in the highly instationary dynamics of fast growing CBLs in the early phase of their evolution.

⁴⁵The idea is to express the entrainment ratio as a function of an appropriate measure of 'CBL shear', X_S . Hence $\beta = f(X_S)$. For the special case $X_S = \text{const}$ follows that $\beta = \text{const}$, and so the sheared CBL shows the same type of evolution as the non-sheared case.

only and initialized by a linearly stratified atmosphere with $b_{\text{ini},z} = N^2 z$. We further choose the initial conditions $z_i(t=0) = 0$ and $\Delta b(t=0) = 0$, which means that in this case the inversion Δb develops 'naturally' by CBL growth. For this case, which covers the essential dynamics, the dependence of Δb and b on z_i are given by

$$b = \frac{1 + \beta}{1 + 2\beta} N^2 z_i, \quad \Delta b = \frac{\beta}{1 + 2\beta} N^2 z_i. \quad (2.59)$$

With these relationships the explicit solution for the temporal evolution of the CBL depth $z_i(t)$ (Ouwensloot and Vilà-Guerau de Arellano, 2013) is given by the square-root function

$$z_i(t) = \sqrt{2(1 + 2\beta) \frac{B_0}{N^2} t}. \quad (2.60)$$

Entrainment versus encroachment. To discriminate between the effects of entrainment and surface warming, the latter is also considered separately and denoted as 'encroachment' (Stull, 1988, page 454). Encroachment represents the 'virtual' evolution of a CBL-SM by surface warming only, without turbulent interaction between ML and the adjacent inversion, which defines entrainment. For clarity, the concept is shown in Figure 2.4. Here the CBL evolution is interpreted as the combined ef-

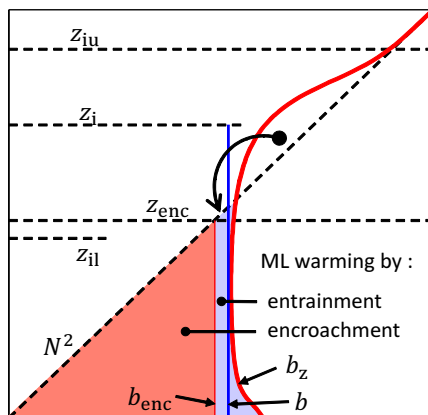


Figure 2.4: Illustration of encroachment and entrainment. The shown profile represents the instantaneous conditions for a 'realistic' strongly sheared CBL, as given by one of our LES.

fect of encroachment and entrainment. The light red area represents warming by encroachment and the light blue area warming by entrainment, which is the result of downward flux of buoyancy from the EZ, as indicated by the black arrow. Starting from an initial profile $b_{\text{ini},z} = N^2 z$ and assuming a perfect mixing, surface heating creates an encroachment mixed-layer with the characteristic height z_{enc} , the characteristic buoyancy $b_{\text{enc}} = N^2 z_{\text{enc}}$ (thin red line), and the accumulated buoyancy $B_{\text{enc}} = 1/2 b_{\text{enc}} z_{\text{enc}}$ (red area), which equals the time integral over the surface flux

$$B_{\text{enc}}(t) = \frac{1}{2} N^2 z_{\text{enc}}^2(t) = \int_0^t B_0(t) dt, \quad (2.61)$$

if one assumes a constant surface heating $\int_0^t B_0(t) dt = B_0 t$.⁴⁶ Thus the height of the encroachment layer at time t can be computed as

$$z_{\text{enc}}(t) = \sqrt{2 \frac{B_0}{N^2} t}. \quad (2.62)$$

The SM warming due to encroachment, $b_{\text{enc}}(t)$, is then given by

$$b_{\text{enc}}(t) = N^2 z_{\text{enc}}(t) = N^2 \sqrt{2 \frac{B_0}{N^2} t}. \quad (2.63)$$

With Eq. 2.60 and 2.62, the CBL depths $z_i(t)$ can be shown to be proportional to $z_{\text{enc}}(t)$

$$z_i(t) = \sqrt{1 + 2\beta} \sqrt{2 \frac{B_0}{N^2} t} = \sqrt{1 + 2\beta} z_{\text{enc}}(t). \quad (2.64)$$

The time derivative of this equation describes the temporal evolution of the entrainment velocity⁴⁷ $w_e = \partial z_i / \partial t$ (Eq. 2.46). A further substitution of t via Eq. 2.62 leads to following relationship

$$w_e = \sqrt{1 + 2\beta} \frac{B_0}{N^2} \frac{1}{z_{\text{enc}}}, \quad (2.65)$$

which links the CBL growth rate to state variables only.⁴⁸

For later use we here present some further analytical expressions. With the definition of β (Eq. 2.57) and Eq. 2.64 the relationship between z_{enc} and the SM depth z_{il} is given as

$$z_{\text{il}}(t) = \frac{\sqrt{1 + 2\beta}}{\beta + 1} z_{\text{enc}}(t). \quad (2.67)$$

Using the expression for b_{enc} (Eq. 2.63) also the ZOM buoyancy measures $b(t)$ and $\Delta b(t)$ (Eq. 2.59) are found to be proportional to the encroachment scale b_{enc} :

$$b(t) = \frac{1 + \beta}{\sqrt{1 + 2\beta}} b_{\text{enc}}(t), \quad \Delta b(t) = \frac{\beta}{\sqrt{1 + 2\beta}} b_{\text{enc}}(t). \quad (2.68)$$

The above expressions show that for $\beta = \text{const}$ the ZOM scales b and z_i or z_{il} are proportional to the respective encroachment scales b_{enc} and z_{enc} . Hence, both set of

⁴⁶The state of the CBL in the moment t only depends on $\int_{t_0}^t B_0(t) dt$ (Ouwersloot and Vilà-Guerau de Arellano, 2013). Thus it is independent of the precise temporal evolution of $B_0(t)$. Just for formal simplicity we use $B_0 = \text{const}$.

⁴⁷Note that w_e is commonly called the 'entrainment velocity'. This may seem inconsistent, as with $w_e = \partial z_{\text{il}} / \partial t + \partial(z_i - z_{\text{il}}) / \partial t$, it in fact accounts for both growth processes, encroachment and entrainment. But w_e is also the characteristic velocity scale for exchange process across the upper BL interface and therefore generally associated with turbulent entrainment. In this respect the term makes sense.

⁴⁸Analogously to Eq. 2.64 the growth of $z_{i,g}$ can be expressed as

$$z_{i,g}(t) = \sqrt{1 + 2\beta_g} z_{\text{enc}}(t) = \sqrt{1 + 2\beta_g} \sqrt{2 \frac{B_0}{N^2} t}. \quad (2.66)$$

scales can be exchanged freely. Eq. 2.64 also illustrates that for the shear-free CBL, with $\beta \approx 0.2$ the entrainment increases the CBL depth significantly relative to pure encroachment, as indicated by $z_i/z_{\text{enc}} \approx 1.18$. But the contribution of entrainment to warming is rather weak, as $b/b_{\text{enc}} \approx 1.014$. For sheared CBLs the entrainment ratio can be substantially larger and the warming due to entrainment can be significant (for $\beta \approx 0.8$, b/b_{enc} becomes ≈ 1.12), as shown by the example in Figure 2.4. For neutral BLs ($B_0 = 0$) or stably stratified BLs ($B_0 < 0$), entrainment finally becomes the only cause for warming (increase of buoyancy).

FA stratification, constant layering of the CBL and local instationarity.

Physically, the FA stratification limits the penetration depth of convective plumes at the upper interface of the CBL and is therefore the elementary steering factor for CBL growth dynamics. The FA stratification is also the ultimate cause for TKE-consumption (i.e. entrainment), which dominates the EZ dynamics in the equilibrium entrainment regime (where entrainment has become approximately(!) proportional to the surface buoyancy forcing). However, the most crucial outcome is the fact that the 'constant layering' of the CBL buoyancy structure (in the equilibrium regime, as expressed by a constant β , or β_g) appears to be quantitatively independent of the FA stratification N^2 . This significant property is also reflected in the analytical solution for the ZOM CBL evolution (Eq. 2.59 and 2.60), if we take into account that the dependence of z_i on N^2 (Eq. 2.60) is only a result of its proportionality to encroachment (Eq. 2.62). Thus for a given encroachment regime, the relative contribution of entrainment as expressed by z_i/z_{enc} , b/b_{enc} or $\Delta b/\Delta b_{\text{enc}}$ only depends on $\beta = \text{const}$ (Eq. 2.64 and Eq. 2.68).

For mature, pure CBLs with $w_e/w_* < 0.1$, these relationships are very well supported by observations. But observation also show that, despite the constant layering, the shapes of the profiles of buoyancy, buoyancy flux and buoyancy variance in the EZ still systematically vary. This is illustrated by Figure 2.5 (inspired by Figure B1 in Garcia and Mellado, 2014), which shows normalized profiles of various quantities of the non-sheared CBL at the beginning of the equilibrium entrainment regime (red lines) and at a later stage (black lines). These variations can be explained by the continuous growth and the subsequent inflow of FA air masses through the upper CBL boundary, which modifies the EZ dynamics (i.e. entrainment). During CBL evolution the relative importance of this inflow, as e.g. measured by w_e/w_* , decreases continuously. Hence the **local** influence of the FA on the EZ decreases as well, resulting in an increase of the local entrainment ratio B_{z_i}/B_0 (see also Fedorovich *et al.*, 2004b, and older references therein; see also our Figure 2.7(b)) and the buoyancy variance in the EZ ($\overline{b'v'_z}/b_*^2$).

In literature one can find two different approaches to specify the interfacial dynamics. Approach (1) focuses on the fact that growth of the BL into the FA causes a positive TKE tendency, which was earlier introduced as 'TKE-spinup'. Approach (2) directly considers the local impact of the stratified FA on penetrating turbulent eddies. Note that both concepts represent correct but complementary views on the TKE budget.⁴⁹ Depending on the context we will refer to both ideas to discuss our results. But following the example of Garcia and Mellado (2014) we will use approach (2) for

⁴⁹Approach (1) rather takes an indirect outcome of CBL entrainment into account, whereas approach (2) directly focuses on the entrainment process.

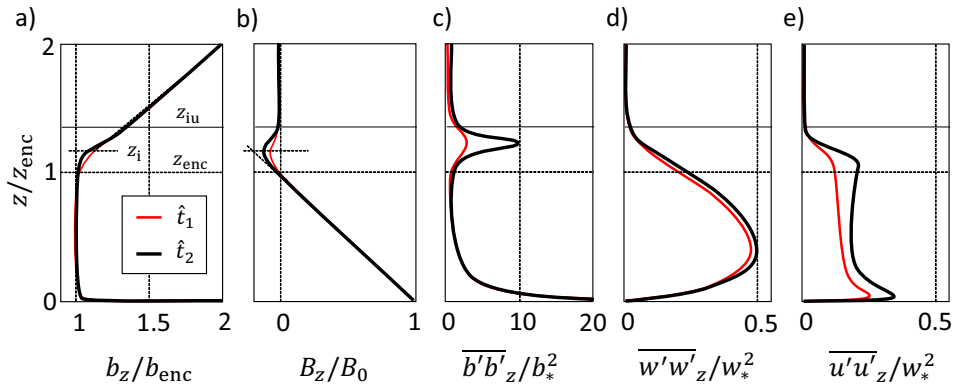


Figure 2.5: Vertical profiles of the mean buoyancy (a), the buoyancy flux (b), the buoyancy variance (c), the variance of the vertical velocity (d) and the variance of the horizontal velocity (e) of a non-sheared CBL in two different stages of its evolution, with $\hat{t}_1 < \hat{t}_2$. The profiles are normalized by encroachment or convective scales. \hat{t}_1 (red lines) marks the begin of the equilibrium entrainment regime and is defined by $z_{\text{enc}}/L_0 \simeq 10$ or $\delta/z_{\text{enc}} \simeq 0.12$. \hat{t}_2 (black lines) mark a later stage with $z_{\text{enc}}/L_0 \simeq 18$ or $\delta/z_{\text{enc}} \simeq 0.08$. The profiles result from the high resolution DNS of Garcia and Mellado (2014) and were traced from their Figure B1.

a quantitative model.

The awareness of these interfacial dynamics led to the development of more complex 1st-order jump models (FOMs) for the pure CBL (e.g. Van Zanten *et al.*, 1999) and for sheared CBLs (Pino *et al.*, 2006b; Kim *et al.*, 2006; Conzemius and Fedorovich, 2007). These FOMs feature an explicit representation of the upper EZ-layer. However, reliable data and a consistent view on interfacial dynamics still seem lacking in these studies.⁵⁰

Only recently, the detailed study by Garcia and Mellado (2014) provides a comprehensive, satisfactory understanding and characterization of EZ dynamics, the direct influence of FA stratification and the particular role of the interfacial upper EZ. We present the basic elements of their theory in detail in the following section 2.6. It forms the conceptual basis for our own reasoning that resulted in a generalization of their concepts to sheared CBLs (chapter 6).

Summary, conclusions and guiding remarks. The set of encroachment scales z_{enc} , b_{enc} or the similar set of ZOM scales z_{il} , z_i , b , together with the related convective scales w_* and b_* (Eq. 2.35 and 2.36) are sufficient to describe the overall quasi-stationary properties of CBLs in the equilibrium entrainment regime, as shown in Figure 2.5. One finds that either the encroachment length scale ($z_{\text{enc}} \approx z_{\text{il}}$) or the ZOM length scales (z_{il} , z_i and similarly $z_{i,g}$) very well represent the constantly layered

⁵⁰The EZ representations in the quite complex FOMs, particularly the scaling of the upper EZ depth, seem rather speculative. Important aspects of these models contradict basic findings of our data analysis. The assumed systematic superiority of these FOMs is questionable, as illustrated by the very good performances of the relatively simple ZOM that we developed in this thesis (chapter 5).

CBL structure (subfigures a-e), which can be translated into a constant ZOM entrainment ratio. One also finds that in the SM, profiles of buoyancy and buoyancy-flux are well represented by their ZOM counterparts (a, b, thin dashed lines). Furthermore, b_* and w_* scale the intensity of buoyancy and velocity variances well (c, d, e), indicating the largely quasi-stationary conditions in the equilibrium entrainment regime. However, the clearly visible temporal variation of the profiles of b_z , $\overline{b'v'_z}$ and B_z in the EZ (red versus black lines in a, b and c), are a clear sign of instationarity and the decreasing influence of FA stratification during the CBL evolution.

Hence, the ZOM with a constant entrainment ratio β (Eq. 2.58), which directly follows from CBL's constant layering, forms an idealized but correct, integral representation of CBL dynamics, which are in reality more complex and instationary. Different to the actual entrainment ratio, the idealization $\beta = const$ represents a quasi-stationary entrainment regime, which is independent of the direct influence of the FA stratification.

From these two properties – quasi-stationarity and independence of direct FA influences – we can further conclude that the ZOM scales z_{i1} , $z_i - z_{i1}$, B_0 , Δb , w_e (and ultimately also ΔU or u_*) should represent a useful integral reference framework⁵¹ to determine and rate the instationarity that is still present in the EZ, despite the fact that we consider the *equilibrium* entrainment regime.

This basic conclusion may seem obvious as it can be rather directly drawn from existing knowledge, as summarized by Figure 2.5. Nevertheless, in its full depth we consider this reasoning as innovative, as it has not been used consistently in previous studies on sheared CBLs. Apparently, this is related to the fact that our understanding of a ZOM differs in a significant aspect from interpretations in previous studies. Those generally interpret $\beta = const$ as an 'entrainment ratio' (Eq. 2.58) only, whereas its actual empirical justification, which is the 'constant layering' of the CBL's TKE-dynamics (Eq. 2.57), is not acknowledged. As a result the published ZOMs (and similar FOMs) rely on z_i as a joint scale for both buoyancy production and entrainment, which is counterintuitive to our interpretation⁵² and prevents a consistent representation of the sheared EZ, as we show in detail later on. As a further consequence, previous studies tend to replace ZOMs by FOMs or even more complex concepts (e.g. the 'general structure model' of Fedorovich *et al.* (2004b)), when attempting to address EZ in-stationarity and varying influences of FA stratification. These FOMs are then based on other specific CBL scales, but do not exploit the potential of the constant entrainment-ratio ZOM as an invariant reference to which a quantification of interfacial processes can be added.

A clear exception to this rule is the study of Garcia and Mellado (2014) on non-sheared, pure CBLs. As Garcia and Mellado's (2014) findings are the basis for our analysis of the EZ instationarity in chapter 6, we present the essential aspects of their

⁵¹This reference framework includes (from their definition) the well-known convective scales w_* and b_* (Eq. 2.35 and 2.36).

⁵²To our knowledge, this holds for all newer and more detailed CBL studies since Van Zanten *et al.* (1999), including all LES studies about sheared CBLs (since Moeng and Sullivan (1994); Kim *et al.* (2003)). In fact the choice of z_i as the singular convective length scale is related to a specific interpretation of entrainment, the so-called 'process partitioning' (PP). We will evaluate this concept later on. Interestingly, however, an elder ZOM for sheared CBLs by Stull (1976a) already concurs with our understanding. But this model features other serious shortcomings, as demonstrated by Conzemius and Fedorovich (2006b).

theory in the following section.

2.6 The impact of the stratified FA on the EZ dynamics according to Garcia and Mellado (2014)

The central topic of the Garcia and Mellado's (2014) study is the influence of the FA stratification on entrainment in shear-free CBLs. Considering the CBL's basic boundary conditions, it is clear that the EZ is created by the interaction of both SM convective turbulence and the stratified FA. Garcia and Mellado (2014) (GM14 henceforth) found that as a result of this dual influence, the EZ dynamics can be best described as a composition of two overlapping layers that are characterized by different types of turbulent dynamics.

The lower EZ sublayer extends from z_{enc} (which is very similar to z_{il})⁵³ to about $z_{\text{i,g}}$ and therefore extends over nearly the entire EZ (Figure 2.6). Its formation is caused by the confinement of convective turbulence by the stratified FA inversion and therefore its general evolution also depends on N^2 (Eq. 2.66). However, beyond the framing conditions its turbulence dynamics are entirely determined by the closely coupled SM. Both the lower EZ and the SM form a quasi-stationary system, which is well characterized by the SM scales, as e.g. given by the encroachment height z_{enc} and the convective velocity scale w_* . Accordingly the depth of the lower EZ $z_{\text{i,g}} - z_{\text{enc}}$ is proportional to the SM depth z_{enc} , what we denoted as the CBL's 'constant layering' (Eq. 2.56, with $z_{\text{enc}} \approx z_{\text{il}}$) before.

The upper EZ sublayer has a quite different character. It forms directly at the interface to the FA around the height of the maximum gradient $z_{\text{i,g}}$ and therefore partly overlaps with the lower sublayer (Figure 2.6). It is determined by the intermittent regime of overshooting updrafts that intrude into the quiescent FA (see also GM14's very illustrative Figures 6 and 7). As part of the convective system the upper sublayer is likewise driven by non-local convective turbulence. But differently to the lower EZ, the upper EZ is also directly governed by the stratified FA, which forms the environment of the penetrating thermals. As a result its dynamics and evolution are additionally controlled by local scales.

The upper EZ length-scales. To define a characteristic local length scale δ for the upper EZ, GM14 use a gradient thickness definition, which is sketched in Figure 2.6 and leads to the expression (GM14's Eq. 21)

$$\delta = \frac{b(z_{\text{i,g}}) - b_{\text{ini}}(z_{\text{i,g}})}{\frac{\partial b}{\partial z}(z_{\text{i,g}}) - N^2}. \quad (2.69)$$

The corresponding characteristic buoyancy scale for the upper EZ layer (Figure 2.6) is then given by:

$$b_\delta = \frac{\partial b}{\partial z}(z_{\text{i,g}}) \delta. \quad (2.70)$$

⁵³GM14 use consistently z_{enc} and b_{enc} as characteristic integral scales. This choice is very elegant as via $b_{\text{enc}} = b_{\text{enc}} N^2$ both scales are linked to the FA stratification. But note that $z_{\text{enc}} \sim z_{\text{il}}$ and $z_{\text{enc}} \sim b$.

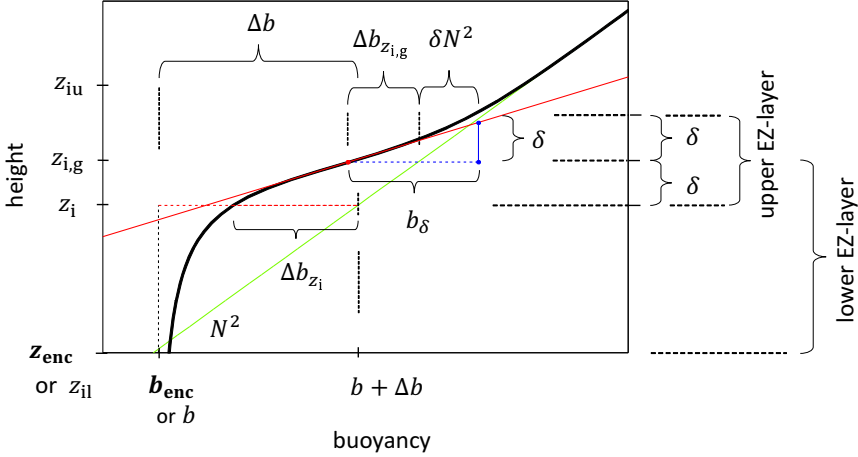


Figure 2.6: Sketch showing the mean buoyancy structure in the entrainment zone of a shear-free CBL.

Physically, δ can be interpreted as the typical penetration depth of convective plumes into the stratified FA above $z_{i,g}$. Thus, it depends on the FA stratification N^2 and the initial velocity of the plumes at the level of neutral buoyancy w'' , which can be well associated with the typical vertical velocity fluctuation (standard deviation or 'root means square' of the vertical velocity) at $z_{i,g}$. Hence GM14 propose $w'' \sim w'$. Observations further show that in the equilibrium entrainment regime the local $w'(z_{i,g})$ scales well with the integral convective velocity scale w_* (Figure 2.5(c)), which GM14 defined as

$$w_* = (B_0 z_{\text{enc}})^{1/3}. \quad (2.71)$$

With $z_{\text{enc}} \approx z_{i1}$ this agrees with our previous definition (Eq 2.35). Hence GM14 found

$$w'(z_{i,g}) \simeq c_{w2} w_*, \quad (2.72)$$

with $c_{w2} \simeq 0.2$. Therefore δ can be well modeled by

$$\delta = w''/N \simeq c_\delta (w_*/N), \quad (2.73)$$

with $c_\delta \approx 0.55$. The relative importance of the upper EZ sublayer can be expressed by the ratio of its length scales δ and the characteristic integral lengths scale of the SM, z_{enc} . With Eq. 2.71, Eq. 2.73 and 2.62 on directly gets the dependency on the growing SM depth $z_{\text{enc}}(t)$

$$\delta/z_{\text{enc}} \simeq c_\delta B_0^{1/3} z_{\text{enc}}(t)^{-2/3}. \quad (2.74)$$

Hence, with a growth of z_{enc} during the CBL evolution the intensity of interfacial dynamics represented by δ/z_{enc} decreases. δ/z_{enc} can therefore also be interpret as a measure of the CBL 'maturity' and the inverse of z_{enc}/δ could be seen as a dimensionless time scale. GM14 found that in the equilibrium entrainment regime, $\delta/z_{\text{enc}} \approx \delta/z_{i1}$ is ≈ 0.12 or smaller, which we finally use as criterion in this study.

GM14's Parametrization for the entrainment ratio and the upper EZ. The evolution of the EZ buoyancy structure due to the diminishing influence of the upper EZ layer is illustrated by Figure 2.7. The shown profiles cover the whole range of the equilibrium entrainment regime ($0.12 \geq \delta/z_{\text{enc}} \geq 0$) and are constructed according to GM14's theory that we here present. To quantify the impact of the interfacial upper EZ layer on integral entrainment dynamics, GM14 consider the entrainment-ratio A at the height of the minimum buoyancy flux z_i (Figure 2.1(a)), which is defined as

$$A = -\frac{1}{B_0} \Delta b_{z_i} w_e, \quad \text{with} \quad \Delta b_{z_i} = b_{\text{ini}}(z_i) - b_{z_i} \quad \text{and} \quad w_e = \frac{dz_i}{dt}. \quad (2.75)$$

It consists of two contributions, which both vary during CBL evolution:

$$A(t) = A_t(t) + A_d(t). \quad (2.76)$$

Here

$$A_t(t) = -\frac{B_{z_i}}{B_0} \quad (2.77)$$

and

$$A_d(t) = -\frac{1}{B_0} \frac{d}{dt} \int_{z_i}^{z_{\text{iu}}} (b_z - b_{\text{ini}}(z)) dz. \quad (2.78)$$

A_t is the local turbulent contribution at z_i , and A_d is the shape contribution term that measures the direct contributions caused by the temporal change in the shape of the upper EZ buoyancy flux profile. GM14 found a very slight decrease in the intensity of A_d during CBL evolution, which, however, is so weak that practically $A_d \approx -0.02 = \text{const}$, indicating that the normalized shape of the buoyancy profile in EZ changes only slowly in time.⁵⁴ But, as GM14 show, even a small variation of the profile shape in the upper EZ, as e.g. represented by the change of the ratio b_δ/b_{enc} (Figure 2.6) has a significant steering effect on the integral entrainment ratio, as illustrated by sketch Figure 2.7(b)). Even though the shape of the buoyancy flux profile in the EZ changes somewhat in time, the overall vertical distribution of the flux remains rather constant (GM14's Figure 4(a), or Figure 2.7(b)). Therefore A_t is a rather representative measure for integral EZ entrainment.

For completeness and clarity we here also mention the linking between A and the ZOM entrainment rate β , which is given by:

$$\begin{aligned} \beta &= A(t) + A_{\text{sm}}(t) \\ &= A_t(t) + A_d(t) + A_{\text{sm}}(t). \end{aligned} \quad (2.79)$$

Here

$$A_{\text{sm}}(t) = -\frac{1}{B_0} \frac{d}{dt} \int_0^{z_i} (b_z - b_m) dz \quad \text{with} \quad b_m = \frac{1}{z_i} \int_0^{z_i} b_z dz. \quad (2.80)$$

⁵⁴In contrast, A_t is in the order of 0.1 and varies significantly during CBL evolution, as shown in detail below.

A_{sm} is the SM shape redistribution term, analogously to A_{d} .⁵⁵ It represents the virtual energy that is needed for the redistribution of buoyancy within SM to create a uniform profile for the ZOM.

With a detailed analysis of the EZ buoyancy structure GM14 finally derived a model for the dependency of A_t on δ/z_{enc} (their Eq. 50), which was then independently confirmed by data. It is given by the linear relationship

$$A_t = \gamma_0 - \gamma_1(\delta/z_{\text{enc}}), \quad (2.81)$$

where $\gamma_0 \approx 0.12$ and $\gamma_1 \approx 0.31$ are constants.⁵⁶ The first term on the rhs, γ_0 is a constant entrainment ratio and the second term represents the reduction that is caused by the finite thickness of the upper EZ layer, with the length scale δ as steering parameter. With the growth of the SM (z_{enc}) the relative importance of δ/z_{enc} continuously decreases (Eq. 2.74) as ‘the upper EZ sublayer recedes towards $z_{i,g}$ ’ (GM14, see Figure 2.6) and its effect on B_{z_i} , given by the second term on the rhs, decreases as well. Simultaneously, the lower EZ sublayer becomes more important and finally its length scale $\sim z_{\text{enc}}$ dominates entrainment. That is commensurate with a constant entrainment ratio γ_0 that is asymptotically reached for $z_{\text{enc}}/L_0 \mapsto \infty$ and $\delta/z_{\text{enc}} \mapsto 0$. Quantitatively the presence of the upper sublayer reduces the integral entrainment ratio. This implies that the mixing in the upper interfacial layer is less effective than in the lower EZ, which reflects the intermittent character of turbulence in the upper EZ. Hence, the less effective turbulence in the upper EZ ‘dilutes’ the more effectively mixing lower EZ, which results in less entrainment and steeper gradients. This is illustrated by Figure 2.7, which shows the variation of the CBL buoyancy structure (a) and the related entrainment flux (b) as given by GM14’s theory, which we present in more detail in the following.

Derivation of $A_t = f(\delta/z_{\text{enc}})$ via the parametrization of the the EZ buoyancy profile. The following derivation is not essential to understand our later analysis in section 6, but useful to place them in the context of GM14. We here also do not reconsider all aspects of GM14’s elaborated line of argumentation but focus on the central steps.

In their derivation of Eq. 2.81, GM14 basically work out the difference of an underlying integral self-similarity of the CBL dynamical structure, as given by the ‘constant layering’ of the CBL, the related encroachment scales z_{enc} and b_{enc} , which represent the SM, on one hand, and the systematic local deviation due to a finite upper EZ-layer, represented by δ and b_δ on the other hand. w_* , which represents thermally driven velocity fluctuations within the whole CBL, serves as an overarching velocity scale for both layers (e.g. Figure 2.5(d)). Due to the constant layering the SM length scale z_{enc} has a similarly overarching function, as it also scales the position of the upper EZ-layer with respect to the lower layer (Figure 2.6). As $b_{\text{enc}} = N^2 z_{\text{enc}}$ (Eq. 2.63) the SM scales directly depend on the FA stratification.

Based on their high quality data set, GM14 suggest two parametrizations to characterize the EZ buoyancy structure, as schematically shown in Figure 2.8 by the green

⁵⁵Note that A_{d} equals the EZ buoyancy redistribution term that defined the difference between ZOM value b and the CBL means b_m (second term on the rhs in Eq. 2.41, Figure 2.3).

⁵⁶Greek letters denote parameters that are composites of basic constant parameters, which GM14 tested on their data set independently.

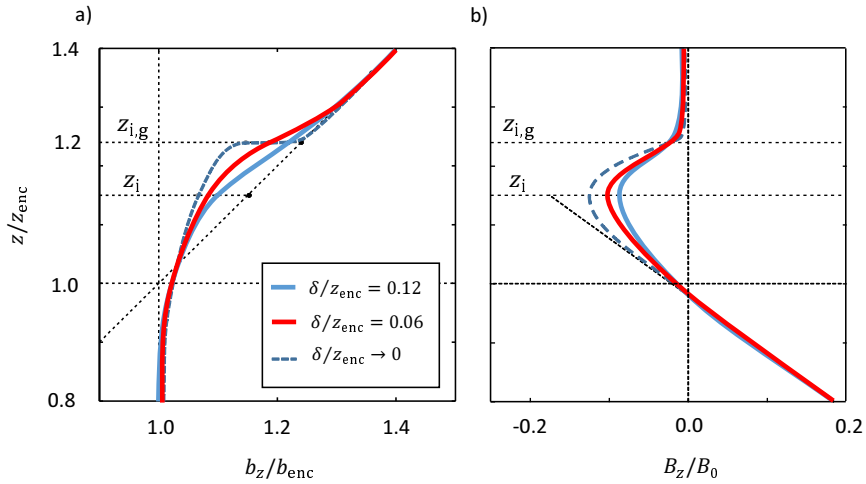


Figure 2.7: Sketch illustrating the evolution of the EZ buoyancy structure for a shear-free CBL. (a) shows the normalized buoyancy profile and (b) the normalized buoyancy flux. Depicted are three consecutive states, which comprise the whole equilibrium entrainment regime. These are defined by $\delta/z_{enc} = [0.12, 0.6, \mapsto 0]$ or equally by $z_{enc}/L_0 = [10, 30, \mapsto \infty]$. The profiles are free-hand sketches, but follow the theory of Garcia and Mellado (2014) at $z_i, z_{i,g}, z_{enc}$.

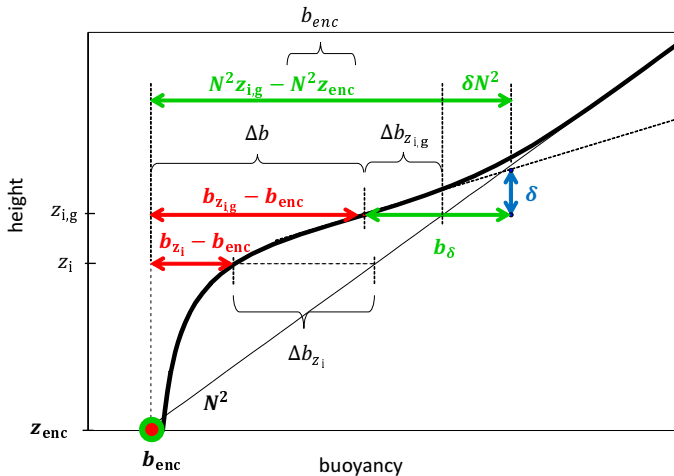


Figure 2.8: Sketch illustrating the EZ buoyancy structure for a shear-free CBL and the quantities used for GM14's parametrizations. Green arrows represent the parametrization Eq. 2.82 and red arrows the parametrization Eq. 2.88.

and red arrows. These parametrizations, which we present below, define the relationship between δ or b_δ respectively and the local buoyancy scales $\Delta b_{z_{i,g}}$ and Δb_{z_i} . The final linkage with entrainment A_t is then established via Eq. 2.75 and 2.76.

The first parametrization relates the characteristic buoyancy scale of the upper EZ, b_δ with the other relevant scales of the EZ buoyancy structure. GM14 found that b_δ is a fixed fraction of the mean buoyancy variation over the lower and upper EZ, which can be formulated as

$$b_\delta = c_{b1} [N^2\delta + (N^2z_{i,g} - N^2z_{\text{enc}})], \quad (2.82)$$

where $c_{b1} \simeq 0.39$ is a constant. The respective quantities are displayed by the green arrows in Figure 2.8.⁵⁷ Note that b_δ is a very good scale for the buoyancy standard deviation b'_z at $z_{i,g}$, which practically equals the characteristic maximum value in the EZ (Figure 2.5(c)). According to GM14

$$b'_z(z_{i,g}) = c_{b2}b_\delta, \quad (2.83)$$

and $c_{b1} \simeq 0.55$.

With $z_{i,g}/z_{\text{enc}} = \text{const}$ and Eq. 2.63, Eq. 2.82 can be written as

$$\frac{b_\delta}{b_{\text{enc}}} = \xi_0 + \xi_1(\delta/z_{\text{enc}}), \quad (2.84)$$

where $\xi_0 = c_{b1}(z_{i,g}/z_{\text{enc}} - 1) \simeq 0.094$ and $\xi_1 = c_{b1} \simeq 0.39$ being constants. ξ_0 represents the asymptotic value for infinitely developed CBLs with $\delta/z_{\text{enc}} \mapsto 0$ and $\xi_1(\delta/z_{\text{enc}})$ determines the actual deviation from this asymptotic state. Thus, GM14 found that the variation of the relative upper EZ depth δ/z_{enc} determines the relative buoyancy scale b_δ/b_{enc} .

Note that for $\delta \mapsto 0$, b_δ stays finite, which implies that the buoyancy gradient $\partial b/\partial z(z_{i,g}) \mapsto \infty$, which also represents the local maximum, grows infinitely. From Eq. 2.84 and 2.70 we can directly derive the respective expression for the evolution of the dimensionless maximum buoyancy gradient as

$$\frac{\partial b/\partial z(z_{i,g})}{N^2} = \xi_2 + \xi_0(\delta/z_{\text{enc}})^{-1}, \quad (2.85)$$

with $\xi_0 \approx 0.094$, as defined above, and $\xi_2 = c_{b1} - 1 \approx 0.61$ being constants (GM14's Eq. 35).

With the above findings, one can finally compute the actual buoyancy profile at $z_{i,g}$ with respect to b_{enc} . From Eq. 2.84 (or GM14's Eq. 32), the definition of δ and b_δ (GM14's Eq. 30, similar to Eq. 2.69 and 2.70) and the definition of b_{enc} (Eq. 2.63), one gets:

$$b_z(z_{i,g}) - b_{\text{enc}} = \xi_3 b_\delta, \quad (2.86)$$

⁵⁷We here shortly note an idea that directs toward the parametrization Eq. 2.82: According to GM14 $b_\delta = \delta N^2 + (N^2z_{i,g} - b_z(z_{i,g}))$ (small green arrow in Figure 2.8) consists of two parts. δN^2 represents the contribution of the penetrating thermal plumes to b_δ , whereas $b_{\text{ini}}(z_{i,g}) - b_z(z_{i,g}) = N^2z_{i,g} - b_z(z_{i,g})$ rather represents the contribution of non-thermal regions.

where $\xi_3 = 1/c_{b1} - 1 \simeq 1.56$ is a constant. Similarly one can find an expression for the local buoyancy jump $\Delta b_{z_{i,g}} = b_{ini}(z_{i,g}) - b_z(z_{i,g})$, which we here include for completeness:

$$\frac{\Delta b_{z_{i,g}}}{b_{enc}} = \xi_0 - \xi_2(\delta/z_{enc}). \quad (2.87)$$

Here ξ_0 and ξ_2 are constants as previously defined. ξ_0 is again an asymptotic value and $\xi_2(\delta/z_{enc})$ the respective reduction due to the finite thickness of the upper EZ layer.

Having scaled the buoyancy structure in the upper EZ, GM14 next consider the buoyancy profile in the lower EZ layer (at z_i). GM14 reason that in the lower EZ the buoyancy profile b_z tends to be rather steady, when normalized by the SM value b_{enc} . In a certain distance to the upper interface, it is well mixed and closely coupled to the quasi steady-state SM. In the upper EZ sublayer however, the buoyancy profile is determined by the local interfacial dynamics, characterized by the typical local buoyancy increment b_δ which grows within a limited upper sublayer layer (Eq. 2.84), whose relative depth of about two times δ/z_{enc} decreases in time. As a result the buoyancy gradient in the upper EZ $\partial b/(\partial z(z_{i,g})N^2)$ grows infinitely as shown by Eq. 2.85 and Figure 2.7(a).

At the same time the turbulent mixing over the whole EZ is sufficiently strong to create a rather smooth mean buoyancy profile. When the upper sublayer recedes towards $z_{i,g}$ the buoyancy gradient at EZ top increases and the rather straight well-mixed profile from the lower EZ extends further upwards. The curvature within the EZ, which marks a transitional region between the upper and the lower sublayer⁵⁸ becomes sharper and concentrates in a narrower region higher up in the EZ, as illustrated by Figure 2.7(a). As a result the evolution of b_{z_i} is effectively governed by the change of the buoyancy profile at $z_{i,g}$.

GM14 finally demonstrate that, with respect to b_{enc} , the variation of buoyancy at z_i is simply a fixed portion of the variation at $z_{i,g}$. Hence as second parametrization GM14 propose

$$b_z(z_i) - b_{enc} = c_{b3} [b_z(z_{i,g}) - b_{enc}], \quad (2.88)$$

where $c_{b3} \simeq 0.45$ is a constant. With this parametrization, which is illustrated by the red arrows in Figure 2.8, we can also directly determine the characteristic buoyancy increment

$$\Delta b_{z_i} = b_{z_i} - b_{ini}(z_i) = b_{z_i} - N^2 z_i \quad (2.89)$$

as a representative measure for the EZ buoyancy profile (Figure 2.7(a)). Hence, by combining Eq. 2.88 with Eq. 2.84 (GM14's Eq. 33) Eq. 2.86 (GM14's Eq. 34) and $z_i/z_{enc} = const \simeq 1.15$ one gets the parametrization for the characteristic buoyancy increment at z_i :

$$\frac{\Delta b_{z_i}}{b_{enc}} = \mu_0 - \mu_1(\delta/z_{enc}), \quad (2.90)$$

⁵⁸This region includes the overlap of the two sublayers.

where $\mu_0 = z_i/z_{\text{enc}} - 1 - c_{b3}(1 - c_{b1})(z_{i,g}/z_{\text{enc}} - 1) \simeq 0.086$ and $\mu_1 = (1 - c_{b1}) \simeq 0.27$ are constants. μ_0 is the asymptotic value for the buoyancy scale at z_i and μ_1 a factor that determines its reduction due to the finite size of the interfacial sublayer.

In a final step GM14 recalculate the variation of the EZ mean buoyancy profile in terms of the entrainment ratio A_t . By inserting this expression into the definition of A (Eq. 2.75), substituting w_e by an expression of state variables (Eq. 2.65), replacing $N^2 z_{\text{enc}}$ by b_{enc} (Eq. 2.63), taking notice of the composition of A (Eq. 2.76) and the finding that $A_d \approx \text{const} = -0.02$, one finally gets the desired relationship between A_t and δ/z_{enc} (Eq. 2.81). The respective constants are $\gamma_0 = z_i/z_{\text{enc}} \mu_0 - A_d \simeq 0.12$ and $\gamma_1 = z_i/z_{\text{enc}} \mu_1 \simeq 0.31$ (GM14's Eq. 50 and 51).

Further measures of the CBL maturity. It is worth noting that the measure δ/z_{enc} is defined by two internal scales of the CBL system. However, for a more comprehensive view on the evolution of a system, good research practice would suggest to better characterize the system's state by comparing internal scales with external scales. For the idealized shear-free CBL, buoyancy forcing and boundary conditions can be merged in a single external reference length scale L_0 . Therefore GM14 prefer the ratio of z_{enc}/L_0 to δ/z_{enc} in their study. L_0 , which can be interpreted as a convective Ozmidov scale, is given by

$$L_0 = (B_0/N^3)^{1/2}. \quad (2.91)$$

For the equilibrium entrainment regime, one can directly derive the relationship between δ/z_{enc} and z_{enc}/L_0 from Eq. 2.73 and 2.91:

$$\delta/z_{\text{enc}} = c_\delta (z_{\text{enc}}/L_0)^{-2/3}. \quad (2.92)$$

GM14 find that the transition to the equilibrium entrainment regime occurs when the $z_{\text{enc}}/L_0 \approx 10$ or $\delta/z_{\text{enc}} \approx 0.12$ respectively. In this stage δ is quantitatively similar to L_0 and both are an order of magnitude smaller than SM depth z_{enc} .

The ratio $\hat{t} = z_{\text{enc}}/L_0$ increases during CBL evolution and therefore can be considered as dimensionless universal time for the evolution of shear-free CBLs and another measure of their 'maturity'.

However, it turned out to be rather difficult to find a direct analog of L_0 that would work for the more complicated conditions in sheared atmospheric CBLs. Thus, to define the state of sheared planetary CBLs (section 6), we will only consider quantities that are based on internal scales, similarly to δ/z_{enc} , as these directly reflect the observed dynamics.

Finally, z_{enc}/L_0 appears to be appropriate measure to characterize the entire CBL evolution, which according to GM14 consists of three basic regimes: In the very short initial phase of CBL development, when the turbulent layer is so shallow that $z_{\text{enc}} < L_0$, then convection does not feel stratification and grows in quasi neutral conditions,⁵⁹ characterized by large scale engulfment. This is followed by a short period of the so-called 'weak stratification regime' ($z_{\text{enc}} \simeq L_0$) with a very thick EZ, before stratification effects become more significant with $z_{\text{enc}}/L_0 \simeq 10$. Here the

⁵⁹This is easy to see, if one associates B_0 in Eq. 2.91 with a typical buoyancy excess of the thermals with respect to its environment, b'' . If $b''/N^2 \gg z_{\text{enc}}$, then the buoyancy excess of a thermal rising up to z_{enc} is not significantly altered by the stratified environment.

characteristic CBL structure, with a constant EZ-to-SM-depth ratio forms in the so-called 'strong stratification' or 'equilibrium entrainment regime', which characterizes the CBLs that we investigate in this study. In the subsequent CBL evolution GM14 interpret L_0 as an integral length-scale for turbulence within the EZ, which is influenced by both convection and FA stratification. Accordingly z_{enc}/L_0 becomes a measure that reflects the characteristic scale separation of the CBL structure, as it compares turbulence within the SM and the EZ. With Eq. 2.92 one can express each of the above relationships (Eq. 2.81, 2.84 and 2.90) in terms of the characteristic time scale $\hat{t} = z_{\text{enc}}/L_0$. For A_t this reads

$$A_t = \gamma_0 - \gamma_1 c_\delta (z_{\text{enc}}/L_0)^{-2/3}, \quad (2.93)$$

which is shown in GM14's Figure 9 and reproduced here in Figure 2.9 (all solid lines). As it well recapitulates GM14's findings, we use it here to illustrate some further aspects. According to GM14, typical atmospheric CBLs are characterized

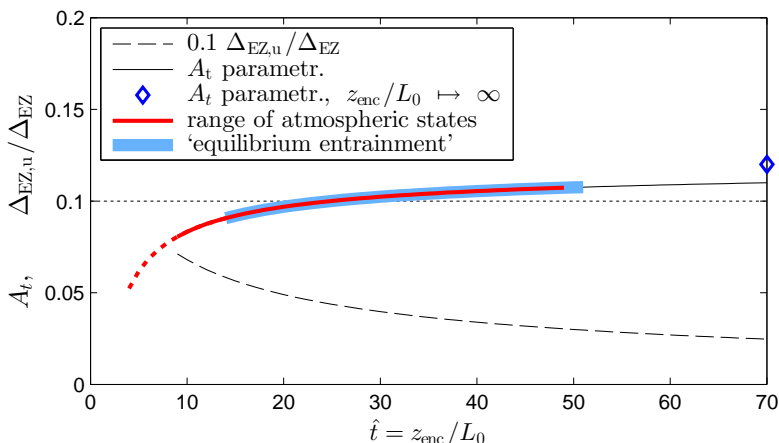


Figure 2.9: The entrainment ratio $A_t = -B_{zi}/B_0$ as function of the dimensionless time z_{enc}/L_0 , parametrized according to Garcia and Mellado (2014). The red line marks the range of states that are supposed to be typical for the atmosphere. The thick light blue line marks the range, where $A_t \approx 0.1$, which represent our understanding of a 'pragmatic equilibrium entrainment regime'. The black dashed line indicates the depth of the upper EZ layer $\Delta_{\text{EZ},u}$ divided by the depth of the whole EZ, Δ_{EZ} . To fit in the plot, the resulting ratio is additionally divided by 10.

by $z_{\text{enc}}/L_0 \approx [5...50]$. For $z_{\text{enc}}/L_0 > 10$ all CBLs are in the equilibrium entrainment regime. This would mean that both ZOM-theory and GM14's two layer-theory cover most of the range of states in the atmosphere (continuous and dashed red line). Immature shallow CBLs in an early evolution phase are restricted to the range $z_{\text{enc}}/L_0 \approx [5...10]$, as indicated by the dashed red line.

We also use this Figure to illustrate a 'pragmatic' notion of equilibrium entrainment e.g. in the range $z_{\text{enc}}/L_0 \approx [15...50]$ (thick blue line). Here not only the CBL structure remains approximately constant but also $A_t \approx 0.1$ (and related measures) changes little, but still differs significantly from its asymptotic value for $z_{\text{enc}}/L_0 \mapsto \infty$

(blue diamond). That means that CBLs in this rather wide range of states show a comparable entrainment dynamics, due to a similar degree of interfacial influence. The general idea is useful for our data analysis later on, as it should help to distinguish variation of entrainment caused by shear from the variations due to interfacial influence.

2.7 Particular research questions and preliminary results

The basic aim of this study is to understand and characterize the evolution and growth dynamics of BLs that are driven by a combination of shear and a positive buoyancy surface flux. Having introduced some essential concepts for the shear-free CBL in the previous sections, we can now further specify our research questions and objectives.

In principle, we consider the whole range, from purely convective BLs to purely shear driven 'neutral' BLs. But inspired by previous studies (particularly Conzemius and Fedorovich, 2007) and with typical fair-weather daytime BLs in mind, we chose the rather well understood, shear-free CBL, as a starting point. By analyzing various LES, we want to find out how turbulent dynamics change, when the CBL is additionally forced by vertical wind shear of varying intensity. Hence to begin with our analysis, we ask, if, how and to what extent the established CBL concepts, can be adopted or modified for shear-driven BLs.

A central element of the CBL theory that we presented above is the 'equilibrium entrainment regime'. We preliminarily defined it as quasi-stationary state of the BL in which the rate of change of the integral TKE turn-over induced by BL growths is small compared to turn-over itself. This implies that the 'equilibrium entrainment regime' is independent of the turbulence creating mechanisms, be it shear or buoyancy. Thus, one can expect that after a short initial phase any continuously forced atmospheric type of BL would reach the state of equilibrium entrainment. Indeed, also quasi-stationary sheared CBLs or fully neutral BLs⁶⁰ have been frequently observed and analyzed (more recently by, e.g. Conzemius and Fedorovich, 2006a; Jonker *et al.*, 2013). Therefore we can, in analogy to the pure CBL, break down our analysis in at least two different parts.

The first and most basic part (A) aims at an understanding of the quasi-stationary nature of developed sheared CBLs and a characterization of the equilibrium entrainment regime. In analogy to the non-sheared CBL, we can expect that also inside quasi-stationary shear-driven BLs interfacial exchange processes cause local stationarity and modify the buoyancy distribution. Thus, in a next step (B), we want to know, how interfacial exchange processes affects the local buoyancy dynamics within the EZ of sheared CBLs.

As a rather fundamental problem of boundary layer meteorology, the entrainment dynamics of quasi-stationary sheared CBLs have frequently been investigated and a

⁶⁰By 'neutral' BLs we here refer to 'naturally neutral BLs' of the atmospheric type. These are only driven by surface induced shear but capped by an inversion. Due to a negative entrainment flux, these BLs are actually stably stratified, so that one could also classify them as 'stable' BLs, in the limit of $B_0 \mapsto 0$. At the same time they can also be considered as sheared CBLs in the limit $B_0 \mapsto 0$. 'Neutral BLs' in a stricter sense are free from any buoyancy effect as it is common for many engineering flows, e.g. BLs that develop above airfoils, etc..

zoo of different bulk models has been published over the years. So one would expect that these multiple efforts have led to clear solid concepts and proven models for this rather well-defined flow problem. However a more recent paper by Conzemius and Fedorovich (2006b) showed that this is not yet or at least not yet fully the case. In this paper the authors reviewed a couple of models on basis of a rather complete set of LESs (Conzemius and Fedorovich, 2006a). Many of the models performed surprisingly poor⁶¹ and none was fully convincing. But the quite simple ZOM approach showed a rather high potential. From this evaluation the authors could draw some very important conclusions and with the lessons learned they constructed their own improved bulk models which were published in a follow up paper (Conzemius and Fedorovich, 2007).

Next to a more complex 1st-order bulk model (FOM) Conzemius and Fedorovich (2007) suggest a strikingly simple ZOM (section 2.5.3). The overall performance of both models to predict CBL depth, mean buoyancy and wind velocity was rather good over a wide range of different states and supposedly systematically better than that of any previously published model (Conzemius and Fedorovich, 2007, 2006b). However, both models still showed systematic limitations, which could not be explained. The much more complex FOM performed somewhat better, but the differences to the ZOM were rather small and the physical reasons behind unclear and ambiguous.⁶² The clear and simple ZOM seemed therefore to be an ideal tool for a study of the CBL's inertial oscillation (IO), according to our original plan, which requires a clean as possible interpretation of the entrainment-shear dependence. Hence we decided to test Conzemius and Fedorovich's (2007) ZOM (Conzemius-Fedorovich model, CFM henceforth) on our own set of LESs, which are – with respect to physical parameter-space and numerical setup – mostly comparable with the LESs used by (Conzemius and Fedorovich, 2007).

2.7.1 Evaluation of Conzemius and Fedorovich's (2007) ZOM for sheared CBLs

For our re-evaluation of the CFM (the Conzemius-Fedorovich model), we modified and advanced the approach of Conzemius and Fedorovich (2007) in two important aspects. Different to the authors, who focused on cases with very strong shear, we also consider cases with moderate shear. More precisely, we were interested in a continuous relationship between shear and entrainment over a wide range of states, representing a smooth transition from pure CBLs to BL, which are dominantly shear-driven. Therefore we also went a small but important step further than Conzemius and Fedorovich (2007) and reformulated the CFM as the relationship between two dimensionless variables, which can be interpreted as a dimensionless wind shear $\Delta\tilde{U}$, which is the inverse of a Bulk Richardson-number, and the dimensionless ZOM entrainment velocity (or growth rate) \tilde{w}_e , which equals the previously defined entrainment ratio β (Eq. 2.58).⁶³

⁶¹One can speculate about the reason, but the lack of a complete and trustworthy experimental data base in the past is for sure a major cause.

⁶²If we understand Conzemius and Fedorovich (2007) correctly, the slight advantage of the FOM over the ZOM seems mostly to be restricted to baroclinic flows, which we here do not consider.

⁶³Note that there is no necessity for an additional variable. The only reason for two different designations is given by the context. If we associate the ZOM entrainment ratio with the CBL growth, we tend to denote it as dimensionless entrainment velocity \tilde{w}_e . In case we consider the ZOM

Hence, in dimensionless form of the CFM reads

$$\tilde{w}_e = C_1 \frac{1}{1 - C_p \Delta\tilde{U}^2}, \quad (2.94)$$

with $\tilde{w}_e = \frac{w_e \Delta b}{B_0} = \beta$ and $\Delta\tilde{U}^2 = \frac{1}{\Delta b z_i} \Delta U^2$.

Here Δb and ΔU are the ZOM buoyancy and wind velocity jump at the CBL top (both determined by Eq. 2.41). As previously defined z_i is the CBL depth at the height of the minimum buoyancy flux and $w_e = \partial z_i / \partial t$ is the corresponding CBL growth-rate (section 2.5.3). $C_1 = \beta \approx 0.2$ and $C_p \approx 0.4$ are constants. In agreement with existing ZOM theory, for shear-free condition ($\Delta\tilde{U} \mapsto 0$) \tilde{w}_e converges to $\beta_0 \approx 0.2$.

Generally, a nondimensionalization of a physical model reveals its intrinsic properties and when comparing with data the potential or limitations should become apparent, with respect to the physical states that are actually possible and that are defined by the dimensionless quantities. Hence, with respect to shear sensitivity of CBL entrainment, the dimensionless form of the CFM (Eq.2.94) should allow a much more meaningful comparison with data than a comparison between times series of data and model outputs of the fully prognostic ZOM⁶⁴, as performed by Conzemius and Fedorovich (2007). This should be particularly relevant, as time itself is not a variable of the entrainment model.⁶⁵ Depending on its physical validity, the dimensionless CFM should enable an effective comparison of various states (Δb , ΔU) of CBLs, which can represent the temporal evolution of a single case, as well as a set of very different cases. Both is shown in the following Figure 2.10. It depicts the dependence \tilde{w}_e on $\Delta\tilde{U}$ as computed for several of our LES. Markers show half-hourly values of various LES-CBLs in the equilibrium entrainment regime. To visually differentiate LESs that are defined by different forcing, the respective begin and end states are marked separately. Furthermore colors signify three different subsets of LES, which differ in domain size and grid resolution.⁶⁶ For comparison the CFM (Eq. 2.94) is shown as black line. The outcome of this preliminary model test, which can be considered as the first result of our data analysis, is twofold:

Firstly, we find that \tilde{w}_e and $\Delta\tilde{U}$, as computed from our set of LES, form a distinct and overall well-defined relationship. This finding basically supports the considerations behind the CFM and the ZOM approach in general.

However, secondly, we also find that for both moderate and high values of $\Delta\tilde{U}$ the CFM predictions for the growth-rate \tilde{w}_e systemically exceed the LES data. The limitation of the CFM for strong shear is inherent. It has also been discussed by Conzemius and Fedorovich (2007) and is similarly present in their FOM. According to Eq. 2.94, \tilde{w}_e becomes infinite for $\Delta\tilde{U} = \sqrt{1/C_p} \approx 1.58$. This contradicts data

entrainment ratio as a measure for the CBL TKE-dynamics or the CBL structure, we rather prefer to call it β .

⁶⁴Eq. 2.94, plus the budget equations 2.47 and 2.48, plus an additional surface drag law.

⁶⁵Driedonks (1982) demonstrated that for a typically very patchy (in space and time) set of atmospheric observations, which also comes with a high statistical uncertainty, the analysis of the temporal evolution of the CBL mean state is the best analytical strategy. This procedure seems to have influenced many CBL studies afterwards, although Driedonks (1982) also explicitly mentioned that these arguments do not hold for more complete data sets with sufficient statistical representativity, as e.g. provided by any reasonable LES or DNS experiment.

⁶⁶For details about LES data-generation and -processing, see section 3.3.

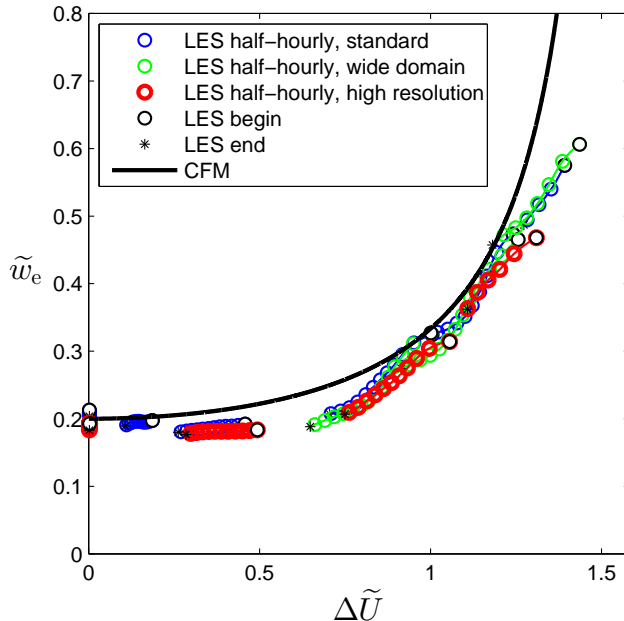


Figure 2.10: Dimensionless entrainment velocity \tilde{w}_e versus dimensionless wind shear $\Delta \tilde{U}$, as given by the CFM (black line) and computed for several LES-CBLs in the equilibrium entrainment regime. For details about the data set see section 3.3.

and could also not interpreted physically by Conzemius and Fedorovich (2007). The shown data represent a series of LESs with widely varying physical forcings but also with different resolutions and domain sizes. Thus it seems rather unlikely that the systematic deviations between CFM and data are caused by problems with the LES experiments.⁶⁷ They also cannot be eliminated by adapting the model constants and therefore ask for a more thorough explanation based on physical arguments. However, the fact that these shortcomings systematically depend on $\Delta \tilde{U}$ indicates that the CFM could be significantly improved by minor, well justified modification or some distinct additions to the concept, while still adhering to the same basic design principles. As a practical approach to the entrainment problem, we therefore decided to recapitulate the derivation of a ZOM and the physical reasoning behind it, using our own set of LES, with the basic underlying goal of an improved ZOM.

2.7.2 Particular research objectives with respect to the equilibrium entrainment regime

Like in most CBL bulk entrainment-models (Lilly, 1968; Stull, 1976a; Pino *et al.*, 2003; Kim *et al.*, 2006; Pino *et al.*, 2006b; Conzemius and Fedorovich, 2006b, and further examples therein) the effect of shear in the CFM is considered by using arguments based

⁶⁷Furthermore, a LES inter-comparisons study (Fedorovich *et al.*, 2004a) demonstrated a very good agreement between the output of the respective computer codes. Therefore we suppose that our LES are largely consistent with the ones analyzed by Conzemius and Fedorovich (2007).

on the integral TKE-dynamics. More precisely, the CFM (or a comparable ZOM) is even supposed to directly represent the integrated CBL TKE-budget (Conzemius and Fedorovich, 2007), and in this way can be likewise considered as a CBL TKE-model. If we consistently stick to this idea, the design of ZOM a entrainment-model can be conceptually divided into two different submodels:

1. Submodel 1 consists in a parametrization of the integral CBL TKE-budget, which represents the essential dynamics of the CBL and can be seen as the actual physical core of the whole concept. Ultimately such a parametrization must relate the integral TKE-production by buoyancy and shear with the integral TKE-consumption by entrainment. But the model might also account for the other terms of the TKE budget, particularly, the TKE-transport term and the tendency.⁶⁸
2. Submodel 2 connects the integral TKE-budget terms with the dimension of the flow, as given by characteristic length, velocity and buoyancy scales.⁶⁹ In the case of 1st-order jump approach, these integral scales are to be associated with ZOM quantities.

In short, submodel 1 represents the composition of the appropriately integrated and scaled TKE-budget and submodel 2 its ZOM representation. Note that we already introduced the conceptual distinction between both submodels in our discussion of a basic inviscid scaling approach (chapter 2.2). Conceptually it obviously makes sense, simply, as each submodel represents physically different types of relationships, based on different assumptions. However, this does not at all imply that they are independent. Rather they merely represent different aspects of the same turbulent flow. Submodel 1 reflects the turnover of TKE across the CBL. Submodel 2 is associated with a simplified representation of the related mean buoyancy and mean momentum distribution, which can be seen as drivers for the TKE dynamics as well as a result of it. Hence both submodels should represent different aspects of the inviscid self-similarity of the high Reynolds-number BL flow.

Considering the most recent studies on bulk models of sheared CBLs (Pino *et al.*, 2003; Kim *et al.*, 2006; Conzemius and Fedorovich, 2006b, 2007), we feel that the distinction between submodel 1 and 2 is common sense as each of these models is explicitly designed to represent the TKE dynamics. Conzemius and Fedorovich (2007) explicitly present and discuss both aspects separately (in a section "ZOM" and another section "scalings"). But even if not stated directly, ZOMs or FOMs seem intrinsically to be designed according to the mentioned pattern. Hence, one should be able to interpret them as scaling of the TKE budget (submodel 1) that is nested in a bulk representation of the CBL (submodel 2).

However surprisingly, when testing ZOMs or FOMs on data this logic is hardly acknowledged and neither submodel is defined and tested independently. In all mentioned studies only composites of both submodels are evaluated or only the final prognostic performance of complete CBL-bulk model is tested.

In a historical perspective the focus on such an 'integrated' approach was often well justified, as suitable direct observations of the TKE-budget terms, which are

⁶⁸Except for or appropriately chosen integration lengths scales based on the flow structure, submodel 1 deals with 2nd-order turbulent statistics.

⁶⁹Hence, it basically links some 2st-order turbulent statistics with 1st-order statistics.

necessary to test and develop both submodels independently, are extremely difficult to get from real flow experiments or atmospheric observations (seemingly impossible). Note that even the evaluation of a simple final ZOM entrainment model, based on much more accessible quantities, remains a downright challenge with lab data (e.g. Deardorff *et al.*, 1969; Deardorff and Wilis, 1985; Fedorovich *et al.*, 2001b) or atmospheric observations (e.g. Stull, 1976a; Driedonks, 1982).

However, if appropriate data are available, which is potentially always the case when using LES or DNS, we find this practice methodologically inconsistent. For such cases we see the danger that the performance of a model cannot appropriately be related to a root cause with the possible consequence that a model is fitted to data, despite large uncertainties in the validity of very basic assumptions. In short, the mentioned practice does not help to improve physical understanding, as it remains unclear why a model works or why not. This e.g. is also the case with respect to the mentioned issues of the CFM, which is structurally very similar to earlier propositions (see the list of models in Conzemius and Fedorovich (2006b)). One does not know, if they are related to the parametrization of the integrated TKE budget (submodel 1) or to the ZOM representation of the flow (submodel 2) or to both. Similarly it is still quite unclear, in which respect and to what extent the often complex apparatus of FOMs (Kim *et al.*, 2006; Pino *et al.*, 2006b; Conzemius and Fedorovich, 2007) really improves the representation CBL TKE-dynamics and to what extent each additional detail is actually beneficial compared to a simple ZOM.

Pino and Vilà-Guerau de Arellano (2008) seemed to have noticed this basic dilemma and conducted a separate evaluation of some aspect of the CBL TKE-dynamics using LES data. However their analysis of the TKE budget remains incomplete, as the assumptions behind the definition of the relevant terms for buoyancy production and entrainment⁷⁰, the so called 'process partitioning' are not questioned. As a consequence, their approach still does not sharply separate between TKE-scaling and ZOM related assumptions, which further reduces the interpretability of their rather limited data-set.

In the following analysis we will correct this particular conceptual weakness of previous studies and demonstrate that an independent investigation of the TKE-budget on one hand and the ZOM scaling assumptions on the other is fruitful⁷¹, not only for the identification and correction of specific CFM shortcomings, but also – within the restriction of our LES data-set – for the understanding of the CBL TKE-dynamics and flow structure.

2.7.3 Research questions

With our reasoning above we can finally formulate our main research questions, hierarchically ordered in two groups:

- (A) deals with the integral nature of quasi-stationary sheared CBLs: How does shear affect the integral properties of CBLs in the equilibrium entrainment regime? How can we characterize these effects? Particularly we want to know:

⁷⁰A concept to differentiate between both contributions is often denoted as 'buoyancy partitioning' (e.g. Randall, 1984).

⁷¹This procedure will very naturally suggest another, physically significantly clearer definition of the integrated buoyancy-production and -consumptions terms, called 'Eulerian partitioning' (EP).

- (I) How does shear in the CBL influence the composition of the CBL TKE-budget, particularly the entrainment term? How can we parametrize these effects (submodel 1)? Specifically, to what extent do observations agree with a simple linear inviscid scaling approach (Eq. 2.13) ?
 - (II) How and how well can we represent the observed integral TKE dynamic with integral scales (submodel 2), e.g. given by ZOM variables?
What causes the deviation between the CFM and our LES? Can we finally combine our results into an improved ZOM (submodel 1 + 2), which corrects the deficiencies of the CFM?
- (B) deals with the local influence of inter-facial exchange processes and local in-stationarity on buoyancy distribution and entrainment: How does shear affect the local interfacial dynamics of a CBL? How can we characterize these effects? What is their influence on integral entrainment ratio? Can we modify or complement GM's theory, so that it works for sheared CBLs?

In the remainder of this study, we want to answer these questions. It comprises the description of LES experiments and their subsequent analysis and is structured likewise.

In the next chapter we present our LES data-set and relevant details of data selection and processing. Based on these data we then (chapter 4) analyze the integrated TKE budget of sheared CBLs considering each single term and suggest a modified scaling for entrainment. Afterwards, in chapter 5, we investigate how the CBL TKE-budget can be appropriately approximated by a 0th-order jump approach and finally come up with suggestion for an improved ZOM. In the subsequent chapter 6 we then use our improved ZOM to scale shear-effects on the local buoyancy distribution in the EZ. With the newly gained overview, we then deal with some remaining issues in chapter 7. Particularly we characterize the sheared CBL's transition to the neutral limit using the results of Jonker *et al.* (2013). We close the thesis with a summary and an outlook on potential further research.

Chapter 3

Material and methods: LES of sheared CBLs

Turbulent flows can be directly simulated by numerically solving the discretized governing fluid equations¹. To this end, it is necessary to resolve all scales that are involved, from the outer flow dimensions and the large production scales down to the dissipation scales. Such a direct solution for a flow problem is called 'direct numerical simulation' (DNS). A DNS is exact within the numerical approximation and therefore an extremely powerful method for turbulence research. However, the number of required grid points in three dimensions is of the order of $Re^{9/4}$ (with a Reynolds number based on the outer length scales, Nieuwstadt *et al.*, 2016). Hence, for high Reynolds number flows very large (dense) computational grids and correspondingly short time-steps are required, which result in very high computational demands. These often limit or prohibit DNSs of real-world flows.

For the simulation of high Reynolds number flows, therefore often an approximate method, called 'large-eddy simulation' (LES), is used. The idea of LES is to fully resolve the larger-scale energy- and variance-containing motions but only indirectly account for the effect of the smaller and smallest scale motions via turbulence modeling. This approach allows much coarser grids and wider time-stepping² and so reduces computational costs tremendously.

In this study we do not focus on the methodology of LES, but rather consider LES as an established method and thus only shortly present the concept here. A more detailed summary of LES and further references can e.g. be found in Wyngaard (2010); Moeng and Sullivan (2015). The DALES 3 computer code that we used for our LESs is documented in Heus *et al.* (2010).

¹These are the governing equations for momentum, commonly called the Navier-Stokes equations, the continuity equation and the buoyancy budget equations. We here only consider the incompressible form of the Navier-Stokes equations, which represent the conditions in ABLs rather well.

²For a given flow, the appropriate temporal resolution scales with the grid spacing, as, for instance, expressed by the 'Courant-Friedrichs-Lewy criterion' (Heus *et al.*, 2010, Eq. 49). Thus we here only discuss the spatial resolution of LESs. The corresponding temporal resolution is implicitly given by the local velocity maximum and a single scaling parameter.

3.1 Principles of Large Eddy Simulations

The basis for an LES are the spatially filtered versions of the fluid equations, where the filtering procedure is based on some low-pass filter. The prognostic equations for the filtered quantities (Heus *et al.*, 2010, Eq. 6 and 7) contain the resolved contributions (fluxes and sources) that depend on resolved quantities, i.e. motions that are larger than the filter length scale Δ_f . But they also contain the so-called 'subfilter-scale' (SFS) flux divergences. The latter represent the impact of motions that are smaller than Δ_f . As the name suggests, the 'resolvable' contributions, can be readily discretized and 'resolved' on a grid with a spacing $\Delta x, \Delta y, \Delta z$, which are typically taken to be proportional, but smaller than Δ_f . The unresolved SFS fluxes, however, which represent the transfer of momentum and scalar properties between resolved and SFS scale motions, are unknown and have to be modeled. Methodically, this necessary 'closure' of the fluid equations represents the basic uncertainty behind LES. In practice, however, numerical errors can be relevant as well (Moeng and Sullivan, 2015).

The essential idea behind LES is to choose Δ_f such that $L \gg \Delta_f \gg \eta$ (where L is representative of the large production scales and the smallest dissipation scales are indicated with η). Hence Δ_f should be in the range of the middle-sized eddies, the 'inertial subrange' of the turbulence spectrum, in clear distance from the production scales and the dissipation scales. An important characteristic of these middle-sized eddies is that they are small enough to contain only little TKE and scalar variance but at the same time they are still large enough to be not directly effected by molecular viscosity and diffusion. For the LES this choice of Δ_f has the desirable consequence that practically all TKE and variance of the flow are represented by the resolved scales.³ It also implies that the interscale transfer is not controlled by viscosity.

Even though only a small part of the momentum fluxes (stresses) in a LES are unresolved SFS fluxes, these are obviously relevant as, in the average, they maintain the transfer of TKE from the large production scales down to the dissipation scales, which is a fundamental integral property of high-Re turbulence dynamics (section 2.2). Hence the modeling of the unresolved SFS fluxes is a crucial aspect of the LES methodology and a field of active research (Wyngaard, 2010, section 6.6.4f).

Empirical studies and theoretical consideration show that simple eddy-diffusivity SFS models can – in an integral, ensemble averaged sense – rather well provide the transfer of kinetic energy and scalar variances out of the resolved scales. But on the local grid-level, the real nature of the interscale transfer appears to be very complex, and eddy-diffusivity models often fail to reproduce the complex behavior of 'real' SFS fluxes. Measurements in the ABL show that the small scale (SFS) motions are frequently anisotropic, intermittent and that kinetic energy can also be transferred both ways, down from the large to the smaller scales (forward scatter), but also upward from smaller to larger scales (back scatter) (e.g. Nguyen and Tong, 2015). This dynamic behavior cannot be reproduced by simple eddy-viscosity SFS models, which always drain energy down from the large to the smaller scales. The deficiencies

³As long as Δ_f is significantly larger as η , the reduction of computational costs compared to an analogous DNS is large as well. However, DNSs in ABL research are typically not supposed to generate the very large atmospheric Re's, but rather aim at the lowest possible value to just achieve Re-similarity (e.g. Jonker *et al.*, 2013; Garcia and Mellado, 2014).

of eddy-viscosity SFS models are especially strong close to a wall (thus in the SL), where backscatter is frequent and strongly affects the integral properties of turbulence dynamics.

However, in the bulk of developed turbulence and free flow boundaries, backscatter seems less relevant and the local interscale transfer can much better be approximated by eddy-diffusivity SFS models. A multitude of studies indicate or even demonstrate that for most atmospheric turbulence, e.g. particularly for dry convective ABLs (Sullivan and Patton, 2011) and cloud layers, a rather high realism, with respect to basic flow statistic (means, variance and covariances) can be achieved⁴, using rather simple eddy-diffusivity SFS-models. Unless there is a particular focus on SL turbulence, most of the recent LES-ABL studies rely therefore on rather simple eddy-diffusivity SFS models (e.g. Van Heerwaarden *et al.*, 2014; Schalkwijk *et al.*, 2015). This indicates a tendency to invest computational resources in larger grids or the description of relevant processes, like cloud physics and radiation, than in more expensive SFS models. Nevertheless SFS model errors remain a basic uncertainty of LES (Moeng and Sullivan, 2015).

Even though LESs are computationally much less expensive than similar DNSs, the basic principle requires a sufficient resolution of the energy containing scales, which seems more difficult to achieve in 'special' flow regions, such as the EZ and even more so in the SL. Typically, one expects that above certain minimum grid-density LESs become insensitive to the resolution and converge. Insensitivity of turbulent statistics to resolution is typically considered as indicator for a successful 'realistic' LES (Moeng and Sullivan, 2015). For the entrainment dynamics of non-sheared CBLs, the resolution sensitivity was analyzed in detail by Sullivan and Patton (2011).⁵

3.2 Experimental setup

Our main data set consists of 17 LES produced with the DALES-3 code (Heus *et al.*, 2010). The design of the experimental setup is generally inspired by Conzemius and Fedorovich (2006a, 2007); Pino *et al.* (2006b) and similar DNS studies (Jonker *et al.*, 2013; Garcia and Mellado, 2014). The general design of the experiments is given in table 3.1 (page 73) and the computational details of the simulations are summarized in table 3.2 (page 75). Two additional LES with a different experimental layout will be presented later on.

All our LES were conducted by Huug Ouwersloot (MAQ Wageningen and later MPI, Mainz), to whom we are very grateful. Huug Ouwersloot was also involved in the planning of the experiments and made most decisions with respect to computational setting of the simulations.

Note that most of our LESs were conducted in the initial period of this research project, when we did not yet have full overview of the scientific challenges and were not completely aware of the limitation of our experimental setup. But with the benefit

⁴Excluding effects that are (1) related to the fact that in LES experiments complex scenarios are usually simplified, and (2) related to uncertainties due to further parametrized process, such as surface interaction and cloud physics. See e.g. the turbulent spectra of 'real world' LES in (e.g. Schalkwijk *et al.*, 2015, Figure 8).

⁵Their findings indicate that the LES-CBLs in most of our reference studies are significantly underresolved.

of hindsight we can now evaluate and discuss our LESs more critically. Nevertheless, supplemented with some improved simulations and carefully analyzed, we consider our LESs dataset as a rather solid and useful basis for our research problems.

3.2.1 General aspects of the LES experimental setup

Spatial discretization. Our LESs are performed in a box-shaped domain, which is discretized using a staggered Cartesian grid that is equidistant in all directions, but has different spatial resolutions horizontally and vertically (Heus *et al.*, 2010, section 2.6, Figure 2). The domain should be large enough to allow a free development of the largest scales motion and also ensure good estimates of ensemble statistics through horizontal plane averages. So the horizontal domain width l_x , l_y is chosen several times the typical BL depth h .

However with respect to the computational expenses, a large domain size competes with the spatial resolution, which still matters as the energy-containing portion of the turbulent spectra must be resolved appropriately. Hence, to conduct a successful LES with a minimum of computational costs, a sufficiently fine computational grid is necessary and a balance between resolution and domain size must be found. These aspects appeared to be crucial and critical factors for our LES experiments.

Numerics and time integration. The DALES-3 code uses finite difference methods in all three directions to compute derivatives. Since in the simulation of turbulence correct momentum advection is essential, we chose a sixth order central differencing scheme for the momentum terms. The time-stepping is determined adaptively according to Heus *et al.* (2010, Eq. 49 and 50). For time integration a third order Runge-Kutta scheme is applied. Further details of the numerical setup, can be found in Heus *et al.* (2010, section 2.6).

Boundary conditions. The simulation of a horizontally homogeneous turbulent BL in a finite domain requires 'turbulent' free-flow conditions at the lateral open boundaries. These are elegantly realized by periodic boundary conditions, which means that the horizontal outflow through one of the lateral boundaries equals the inflow on the opposite side.

The surface is represented by a rigid surface, with no-slip conditions for momentum and an imposed surface buoyancy flux. Related to this, basic limitations of LES have to be addressed. In the surface layer (SL, Figure 2.1) the turbulence length scale is limited by the height above the ground z . That means that in the lowest grid levels of an LES, the whole turbulent spectrum is supposed to be below SFS, which systematically violates the assumption of spectral cut-off in the inertial sub-range. Imposed surface fluxes (buoyancy) and surface fluxes that are determined by interaction between the flow and surface (the surface shear-stress) must therefore entirely be modeled. To that end a surface model, using Monin-Obukhov similarity (MOS) theory is applied (Heus *et al.*, 2010, section 2.4) to determine the relationship between the flux (of buoyancy or momentum) and the vertical gradient (of buoyancy or wind speed). However, MOS represents ensemble averaged properties of SL turbulence and may not be fully appropriate for the local conditions at individual grid points. With the given methodology, LESs can only partly mimic the atmospheric

SL dynamics.⁶ However, with respect to the actual turbulence dynamics, these LES deficiencies should be restricted to the special conditions within the SL and not further influence the free development of the convective turbulence in the ML and the EZ. Hence the poor representation of SL turbulence in LESs is not supposed to have ‘direct’ consequence for the entrainment dynamics.

The upper boundary of the LES flow domain is also realized as a rigid lid, but with a free slip condition, which allow a stress free horizontal flow (wind). In BL experiments, the upper part of the LES domains is supposed to represent the quasi laminar ‘quiescent’ FA and during the experiment the ABL top should stay in safe distance from the upper domain boundary. However the stably stratified FA is an oscillation system and a medium for the propagation of gravity waves, which might be induced by turbulent fluctuations in the adjacent BL. To prevent reflections of gravity waves at the upper lid, the upper part of the domain forms a so called ‘sponge layer’, which dampens horizontal and vertical velocity fluctuation (Heus *et al.*, 2010, section 2.5). The properties of the sponge layer are set so that it dampens all motions with a frequency larger than the Brunt-Väisälä frequency N , which is the limit for internal gravity waves. Hence, physically this setup mimics an open upper boundary for vertically propagating waves, as gravity waves can ‘escape’ the domain, do not return or affect the flow in another way. As gravity wave dynamics appeared to be significant in preliminary test LESs, we chose rather deep, well functioning sponge layers for our setup.

Buoyancy forcing. Each LES is initialized with a linearly stratified domain. During the simulation a constant surface buoyancy flux B_0 (surface heating) is applied. In combination with small initial buoyancy fluctuations, this causes buoyant instabilities. These quickly grow into overturning plumes and subsequently create a fully turbulent, well-mixed CBL (as described in section 2.5), which can freely develop and grow into the stratified FA (Figure 3.2a). Note that all simulations are ‘dry’ in the sense that no water vapour is included. Hence temperature and virtual temperature are equal and buoyancy variations are solely based on temperature variations.

Forcing of the horizontal wind. Except for the purely convective reference simulations, the atmosphere in all our LESs is driven by a horizontal pressure gradient that is constant in time and space⁷, and a Coriolis force that mimics the constant planetary rotation (as in e.g. Moeng and Sullivan, 1994; Conzemius and Fedorovich, 2006a). As common in BL-meteorology we consider the pressure forcing in terms of the geostrophic wind \mathbf{U}_g , which is the equilibrium velocity of the frictionless horizontal wind in the case of straight isobars (Eq. 2.23). In all our simulations the whole domain is initialized in geostrophic equilibrium. At the surface the flow is subject to surface friction, which is determined by a MOS surface-stress model for the first model layer. The MOS model relies on a the roughness length scale z_0 , the local wind

⁶It turns out that most LES models are incapable of representing the MOS-similarity profiles of mean momentum and scalars as obtained from observations. This may be due to the fact that within the SL the simulated turbulence has to transition from fully parameterized (sub-filter) turbulence at the lowest level, to a flow in which a major part of the turbulence is resolved, at the top of the SL.

⁷In contrast to Conzemius and Fedorovich (2006a, 2007), we do not consider a variation of the horizontal pressure gradient with height (baroclinicity).

speed, and local static stability (for details of the implementation see (Heus *et al.*, 2010)).

These settings result in a typical structure and evolution of the mean flow. Due to a lack of friction the FA wind-velocity remains geostrophic. However, within the turbulent BL, which immediately starts to form above the surface, the flow is decelerated by turbulent friction and brought out of geostrophic equilibrium. This leads to a typical inertial oscillations (IO) of the wind velocity (see appendix E), which results in a significant variation of the BL flow velocity in time and space (as shown later in Figure 3.2b and 3.3). Vertical wind shear, close to the fixed surface and at the interface with the FA flow, varies accordingly. At mid-latitudes (45 degrees) the period of the IO is in the order of $2\pi/f_c \approx 17$ h. As this is much larger than the turbulent turnover time scale (e.g. z_{il}/w_*), direct influences of the Coriolis force on atmospheric turbulence processes can be neglected. Furthermore, in our data set we did not find any indication that the IO-related turning of the wind profile, and associated directional shear, would specifically influence the TKE budget. Therefore we do not consider these aspect in our analysis. However for BLs beyond the parameter range that we explore here, the Coriolis force is expected to impact on the entrainment dynamics. This should e.g. be the case for BLs that are relatively deeper (more 'mature' as we call them later) or more shear-driven (neutral) than our LES-CBLs.⁸

As CBL entrainment appears to be largely insensitive to the Coriolis force in typical atmospheric conditions, one can argue that an even more simplified experimental set-up, e.g. similar to the one of Jonker *et al.* (2013), which features a constant surface-stress forcing, would have been preferable. However, the added complexity and realism of our oscillating flow has the distinct advantage that it creates a highly non-linear relationship between surface-stress and shear-stress in the entrainment zone. This regime, which practically mimics a slow but arbitrary variation of surface friction, turns out to be useful to demonstrate the decoupling of the EZ-dynamics from mixed layer shear and the independence of the EZ as a turbulent shear layer (section 4.1.4.1). This feature, which is often overlooked, has to be considered as a very significant characteristic of atmospheric CBLs, as these actually develop very similar oscillatory dynamics and thus are supposed to show the same decoupling between EZ- and surface-stress as our LESs.⁹

Summarizing. The constant external parameters that define our LES experiments are the background stratification $N^2 = db/dz$, the constant surface buoyancy-flux B_0 , the surface roughness length z_0 , the geostrophic wind $\mathbf{U}_g = (\mathbf{u}_g, \mathbf{0})$ (aligned with

⁸For near neutral or stably stratified BLs it is known that CBL growth is restricted due to Coriolis force. The maximum BL depth scales with the so called 'Ekman-layer scale height' $h_{EK} \approx u_*/f_c$ (e.g. Zilitinkevich and Esau, 2002). But the Coriolis force (or the IO respectively) does not affect turbulence directly but enforces an equilibrium wind profile with a shear-less zones around $h \sim h_{EK}$ (often associated with 'low-level jets') that locally restricted TKE shear-production and effectively prevents any turbulent entrainment above $h \sim h_{EK}$. The 'Ekman-layer' is a well-known, simplified linear model of such a growth-restricted neutral BL.

⁹Jonker *et al.* (2013) analyzed a rotation-free neutral flow with constant surface stress. This setup leads to a simple relationship between CBL evolution and surface stress and an analytical solution for the temporal BL evolution that similar is to the one for pure CBLs (section 2.5.3). However, their analysis of the TKE-budget suggests that even in the neutral BL, growth is essentially driven by shear close to the upper interface. The impact of surface shear production is therefore indirect, as we will discuss in detail in section 7.2.

the x-axis of the simulation domain) and the Coriolis parameter f_c .

As typical for meteorological LES studies (like our main references), the physical parameters of the LES are given as absolute values and the buoyancy profile and forcing in terms of a temperature profile and a thermal flux. With Eq. 2.26 the respective buoyancy values can be computed.

3.2.2 The choice of the LES physical parameter space

Parameter space. Inspired by Pino *et al.* (2006b); Conzemius and Fedorovich (2006a, 2007) our data shall be roughly representative for fair weather conditions in the mid-latitudes. Therefore all our LES are forced by a significant surface heating of $\overline{w'\theta'}_0 = 0.06 \text{ Kms}^{-1}$ ($\simeq B_0 = 1.94 \cdot 10^{-3} \text{ m}^2\text{s}^{-3}$) and a rotational forcing that is representative for the northern mid-latitudes, as given by a Coriolis-parameter $f_c = 1.0312 \cdot 10^{-4} \text{ s}^{-1}$ (for 45° N). As initial temperature gradient we chose $\gamma = \partial\theta/\partial z = 0.003 \text{ Km}^{-1}$ ($\simeq N^2 = 0.99 \cdot 10^3 \text{ s}^{-1}$), which is within the typical range of atmospheric conditions. Surface roughness length z_0 is 0.1 m for all simulations.

Starting point for our series of LES experiments is the purely convective CBL with $U_g = 0$. By increasing the constant geostrophic forcing stepwise from 0 to 20 ms^{-1} , we created a set of LES-CBLs with a wide range of wind shear (see table 3.1). As the geostrophic wind U_g represents the velocity equilibrium of the frictionless flow above the CBL it was also used for the initialization of the wind field in the whole domain.¹⁰

Table 3.1: Variation of background stratification and geostrophic forcing in our series of LESs. Variations in resolution and domain size indicated with S (standard LES), H (high resolution), W (wide-domain), as specified in table 3.2. Other parameters are the same for all LESs: surface heating $\overline{w'\theta'}_0 = 0.06 \text{ Kms}^{-1}$, the Coriolis parameter $f_c = 1.0312 \cdot 10^{-4} \text{ s}^{-1}$ and the roughness length $z_0 = 0.1 \text{ m}$.

$\partial\theta/\partial z$ [Km^{-1}]:	U_g [ms^{-1}]:	0.0	2.5	5.0	10.0	15.0	20.0
0.003		S,H	S	S	S,H,W	S,H,W	S,W
0.006		S,H		S	S	S	S

Following the example of Conzemius and Fedorovich (2006a) we conducted an additional similar series of LES which feature a stronger FA background stratification of $\gamma = \partial\theta/\partial z = 0.006 \text{ Km}^{-1}$ (table 3.1). These simulations were mostly used to check the sensitivity of the results to the vertical resolution in the entrainment zone (which decreases in thickness with an increase of the buoyancy gradient at the upper interface).

Physical representativity of the LES-CBLs. All our LES are set up within the range of parameter values that was explored by Conzemius and Fedorovich (2006a,

¹⁰The quiescent flow in FA above the CBL is quasi frictionless and should therefor remain in geostrophic equilibrium during a whole LES. However, in some LESs we actual observe slight variations of the FA mean flow, which are very probably caused the gravity-wave induced stress divergences in the upper domain (see section 4.1.4.3). But the deviations of the FA flow are smaller than $0.06 U_g$ and therefore insignificant for our quantitative considerations.

2007). The presence of moderate but considerable surface heating (about 74 Wm^{-2}) ensures that our LES all represent cases where turbulence production is strong and entrainment and growth are also significant in absolute sense. But we take note that in the 'real' atmosphere of the mid-latitudes convective clear-sky CBLs rarely combine with wind velocities higher than 15 ms^{-1} (surface wind of about 6 Beaufort). Some of our LES therefore could be seen as somewhat excessive (which equally holds for several LESs of Conzemius and Fedorovich (2006a)). However, for a physical meaningful interpretation of the LES experiments, we focus on the dimensionless representation of the flow dynamics. Thus, as long as our LES represent the physical processes of interest (e.g. shear-driven and buoyancy-driven BL growth), they are useful for our analysis.

The relative influence of shear or buoyancy on the BL evolution is commonly characterized by the ratio of shear- and buoyancy-driven contributions to the production of turbulence kinetic energy. Such a quantity, which is also often referred to as 'dynamic stability' of the BL, defines a dimensionless Richardson number (e.g. Eq. 2.33 or 2.34). The question is if there is a single Richardson number that would measure the CBL turbulent composition in a way that is relevant for the CBL evolution.

With the bulk Richardson number $1/\Delta\tilde{U}$ (Eq. 2.94), which directly determines the dimensionless CBL growth rate, we have already found such a characteristic integral measure (Eq. 2.94). However, we do not yet know how to interpret it. Furthermore, as $\Delta\tilde{U}$ is based on the CFM, we expect it to be systematically flawed.

Hence, for a first evaluation of our data set at this points, we rather prefer a simple intuitive measure, like the integral flux Richardson number $-\text{Ri}_{f,\text{CBL}}$. We define this as the ratio of the total TKE buoyancy-production and total shear-production within the CBL.¹¹ We find that our data range from $-\text{Ri}_{f,\text{CBL}} = \infty$, which marks a pure shear-free CBL, to $-\text{Ri}_{f,\text{CBL}} \approx 0.05$, which represents a strongly sheared BL with a shear production that is about 20 times larger than the buoyancy production.¹² This means that our LESs series seem to cover the major part of the atmospheric stability range of sheared CBLs, which comprises the full continuum from 0 to $\text{Ri}_{f,\text{CBL}} = \infty$.¹³ To finally extend our analysis to the limiting behavior $-\text{Ri}_{f,\text{CBL}} \mapsto 0$ we also take Jonker *et al.*'s (2013) recent DNS study of neutral BLs into consideration (chapter 7.2).

Parameter space related to BL development. We tried to set up our LES cases such that neighboring simulations roughly touch or overlap if aligned along the most important dimension, i.e. 'shear'. Using $\Delta\tilde{U}$, this property of our data set has already been demonstrated in Figure 2.10 and is a regular feature in many of the following plots. To understand the typical data arrangement, it helps to keep in mind that overall shear, which is in the order of U_g/z_i , always decreases during the CBL evolution (due to CBL growth). Thus, a CBL with weak pressure forcing experiences in its early stage of evolution a similar shear level as a CBL with a strong pressure forcing in a later stage. This means that a similar shear level can be achieved by LESs experiments that otherwise strongly differ. The temporal evolution of CBL properties

¹¹We only take positive values of the buoyancy production into account.

¹²In chapter 4.1.4, we determine the integral TKE-budget of our LESs. Using the respective integral terms $\text{Ri}_{f,\text{CBL}}$ is given by $-\text{Ri}_{f,\text{CBL}} = -\text{BSM}/(\text{SEZ} + \text{SSM})$.

¹³Excluding stable boundary layers (SBLs), which are defined by a negative buoyancy surface flux.

within a single LES contributes significantly to the parameter range that we cover with the whole series of LESs.

Another important characteristic that determines the dynamics of a CBL is its evolutionary stage or its maturity. This maturity can be measured by the thickness of the interfacial layer at the CBL top relative to the ML depth, thus δ/z_{enc} (section 2.6). As our focus is on the equilibrium entrainment regime, we ensured that our LESs are long enough (physical time ≈ 10 h), so that each CBL reaches the state of equilibrium entrainment and pursues it for a significant amount of time (several convective turnovers). As a consequence, our series of LESs captures the shear-dependence of the quasi-stationary equilibrium entrainment for a wide range of shear levels. Furthermore we find that the interfacial upper EZ dynamics in our LES-CBLs, vary in a similar range as in GM14's DNSs ($\delta/z_{\text{enc}} \approx \delta/z_{\text{il}} \simeq [0.05\dots 0.15]$). But, different to GM14's DNSs, the upper EZ dynamics in our sheared LESs appears to be also driven by local shear, whose intensity and apparent influence also varies significantly (as shown in section 6).

In principle, our LESs also cover the very early phases of CBL evolution. However domain size and grid size are chosen with regard to mature CBLs in the equilibrium entrainment regime. In earlier stages, our LES-CBLs are rather shallow and only fill a small portion of the LES domain. This implies that they are rather poorly resolved, which largely reduces their physical significance.

3.2.3 Spatial flow discretization and computational significance

In this section we document our choices with respect to the spatial representation of our LES and shortly discuss implications for the simulation quality of our data set.

Horizontal and vertical resolution and domain size. Basic dimension of the computational grids of our LES are summarized in table 3.2. A first series of LES,

Table 3.2: Domain sizes and spatial discretization of our LES types.

type of LES	standard	higher resolution	wide domain
abbrev.	S	H	W
vertical grid Δz [m]	12.0	6.0	12.0
horizontal grid $\Delta x = \Delta y$ [m]	50.0	25.0	50.0
number vertical levels, (for $U_g < 10\text{ms}^{-1}$)	200	400	300
number vertical levels, (for $U_g \geq 10\text{ms}^{-1}$)	300 *	400	300
number horizontal grid cells	288	576	576
domain width $l_x = l_y$ [km] (for $U_g < 10\text{ms}^{-1}$)	14.4	14.4	–
domain width $l_x = l_y$ [km] (for $U_g \geq 10\text{ms}^{-1}$)	14.4	14.4	28.8
domain depth l_z [km]	2.4 *(or 3.6)	2.4	3.6
portion sponge layer [km]	0.8	0.8	0.6

which we denote as standard runs ('S' in table 3.1 and 3.2), were all conducted on the

same computational grid, with the same domain size and grid resolution (table 3.2). With confidence in the Conzemius and Fedorovich's (2006a) experiments, we initially only moderately improved the spatial resolution of our experiments (Table 3.2).

For our set of standard LES we chose a somewhat deeper vertical domain of 1600 m (plus 800 m sponge layer) versus 1280 m (plus 320 m sponge layer) in Conzemius and Fedorovich (2006a). Besides, we used a finer vertical spacing ($\Delta z = 12$ m versus 20 m) using significantly more vertical layers (200 compared to 80 layers). This allowed deeper, better resolved CBLs and a longer consecutive CBL development than in comparable LESs by Conzemius and Fedorovich (2006a).

As the strong shear on the LESs with a geostrophic forcing $> 5 \text{ ms}^{-1}$ enhances CBL growth significantly, we extended the domain vertically to 3000 m (plus 600 m sponge layer), which increased the number of computational layers to 300. To accommodate the horizontally extended turbulent structures in deep sheared CBLs and deal with the weaker statistical properties of the momentum flux,¹⁴ the standard runs have a significantly large horizontal domain size (14.4 km versus 5.12 km) based on a slightly larger grid (288² compared to 256²) but also a coarser horizontal spacing ($\Delta x = \Delta y = 50$ m versus 20 m) than Conzemius and Fedorovich's (2006a) LESs.

In order to have further control on the quality of our LES, we repeated the most significant runs two times with the same forcings but different grid configurations. For more certainty with respect to the role of domain size on the LES-CBL dynamics, we conducted three additional wide-domain LES for $U_g > 10 \text{ ms}^{-1}$ ('W' in the tables). These feature the same grid spacing as the respective standard runs, but have a much wider domain, which is doubled in both horizontal dimensions (28.8 km x 28.8 km, with 575x576 grid points). To gain more control over the basic quality of our LES, we further conducted four higher resolution LES ('H' in the tables), which equal the standard type in forcing and domain size, but with doubled mesh density (576² x 400) and half the grid spacing ($\Delta x = \Delta y = 25$ m and $\Delta x = 6$ m).

Evaluation of vertical resolution. Sullivan and Patton (2011) investigated the resolution dependency of LES turbulence (low order statistics) for purely convective CBLs in detail. As they analyzed shear-free LES-CBL of the basically same type and with the same typical atmospheric background stratification of 0.003 Km^{-1} , their results can give us a clearer idea about the significance of our database. Sullivan and Patton (2011) found that CBL entrainment and growth dynamics are rather sensitive to a proper discretization of the sharp vertical buoyancy or potential temperature gradients that form at the interface between EZ and FA. A too low resolution of the EZ implies that the inversion is vertically smeared out and maximum $\partial b_z / \partial z$ at $z_{1,g}$ is underestimated, which results in a too high resolved entrainment flux and too deep EZs.¹⁵ As a further remarkable result, Sullivan and Patton (2011) could also

¹⁴According to a personal comments by Antti Helsteen, FMI, Helsinki.

¹⁵To explain these observations, Sullivan and Patton (2011) point at the influence of $\partial \theta_z / \partial z$ on the flux-budget of the resolved entrainment flux. This influence is given directly via the gradient-production term in the budget of the resolved buoyancy flux, $GP = -w'^2(\partial \theta_z / \partial z)$, and indirectly via the buoyancy production term $BP = g/\theta_0 \theta_z'^2$, which is controlled by $\theta_z'^2$. The respective $\theta_z'^2$ -budget features a similar gradient production term as the buoyancy flux budget. In a too coarse grid, $\partial \theta_z / \partial z$ is too weak and thus the $\theta_z'^2$ -gradient-production is reduced. Thus BP becomes too small, which changes the balance between GP and BP and results in enhanced entrainment, if we interpret Sullivan and Patton (2011) correctly.

demonstrate that the impact of the mentioned discretization errors on the resolved flux are much more relevant than potentially erroneous contribution by the ‘imperfect’ eddy-diffusion SFS model.

In essence, the authors found that for the typical atmospheric background stratification of 0.003Km^{-1} a vertical resolution of less than 65 equidistant layers for the CBL depth (from 0 till z_i) results in a significant overestimation of the EZ depth and the entrainment flux. But for LES-CBLs with > 130 vertical layers within the BL, vertical profiles and growth dynamics well converged to a final, stable values. However, the authors do not determine a clear critical minimum value for the vertical resolution, which therefore should lie in between 65 and 130 layers. If we take the upper value, our CBLs would require an minimum depth of about 1500 m for our standard LES or 750 for the higher resolution LES. For our high-resolution LES, this condition is typically fulfilled for extended periods, comprising several convective turnovers. The shear-free LES with lower resolution however are throughout shallower than 1500 m (< 1400 m) and we indeed observe some slight overestimation of integral entrainment.

There are clear indications that shear decreases this type of resolution sensitivity, particularly as for a given CBL depth the EZ becomes relatively deeper and therefore the mean buoyancy-gradient is better resolved. Accordingly we find that CBL structure and growth dynamics of the low- and high-resolution LESs converge very well (see Figure 3.5 red versus blue lines). We therefore also consider our lower resolution LESs (the standard and the wide-domain type) as appropriate for a further analysis of the integral TKE- and entrainment dynamics.

With regard to other flow properties, e.g. the characteristic evolution of the EZ structure and the interfacial dynamics, the limitations of our LES seem to be more severe.¹⁶ But even here, we find that the more critical non-sheared case agrees at least qualitatively with the recently published very high resolution DNS of GM14 (section 3.4.2).

In summary, we assume that our LESs, which are generally better resolved than in previous studies (Pino *et al.*, 2006b; Kim *et al.*, 2006; Conzemius and Fedorovich, 2007), represents sheared CBL TKE-dynamics generally well and consider them as suitable to study the relationship between shear, buoyancy forcing and entrainment. Due to the computational limitations the LES-CBLs can be slightly under-resolved, particular within the EZ in earlier part of the evolution. However, the convergence of the results suggests that these constraints may mostly affect the proportion of the considered relationships, but not there basic shape or typology. This idea can easily be tested with a better data set in the future.

A further high resolution LES for an independent comparison. Access to a further higher resolution LES-CBL that was produced with a different computer code enabled us to independently evaluate our most important results. This LES was conducted code by Chiel van Heerwaarden¹⁷, who is also the author of the computer code (MicroHH 1.0, Van Heerwaarden *et al.* (2017)). Some details and basic results are given in appendix D. Differences to our LESs and consequences for physical interpretations are mentioned in the respective context later on.

¹⁶Generally, the sensitivity to grid resolution increases with the order of the statistical moment.

¹⁷Then MPI, Hamburg, now Wageningen University.

3.3 Data preparations and classification

The stored LES output data that are the basis for our analysis, consist in 1-minute instantaneous vertical profiles of the slab-averaged quantities b_z , b'_z , $\overline{w'b'_z}$, U_z , U'_z , $\overline{w'U'_z}$, w' and the TKE-budget terms (Eq. 2.29ff).

Selection of usable data. First evaluation of the data time series revealed the necessity to define a range of useful data for our analysis. With the start of the LES,

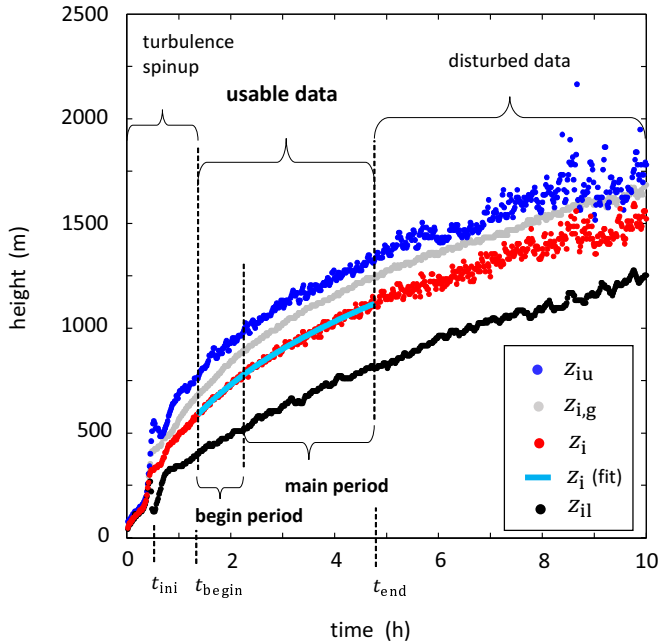


Figure 3.1: Evolution of the vertical structure of a sheared LES-CBL and the related data classification. For clarity the strongly sheared CBL, with $U_g = 20 \text{ ms}^{-1}$ and $d\theta/dz = 0.003 \text{ Kms}^{-1}$ is shown, as it features a long end-phase with pronounced data disturbance.

a BL at the surface begins to form. In its early stage it is shallow and subjected to a fierce forcing, which results in a vigorous spinup of LES turbulence. However due to the shallowness of the BL it is highly underresolved and useless for our purpose. With our focus on well developed entraining turbulent BLs, we define the end of the turbulence spinup phase pragmatically as follows: First we considered the moment t_{ini} , when a well defined CBL structure with a layered entrainment zone (EZ) first occurred (Figure 3.1). To pragmatically fix a reasonable starting point for a range of useful data, we added a further period, which is necessary to let the hefty fluctuations fade away, which are associated with the sudden formation of weakly resolved shallow turbulent BLs. We estimate that this has happened at $t_{begin} \approx 2.5 t_{ini}$. Afterwards all LES-CBLs are characterized by a rather smooth growth regime.

In the end-phase of most LES, when the CBL fills large part of the domain, a relatively sudden change in the EZ turbulence pattern occurs which is characterized by enhanced scatter and a slow oscillatory variation of the EZ structure, as shown in Figure 3.1 after the moment t_{end} . At the same time we observe a strongly enhanced leakage of TKE into the FA, which exceeds the level that we usually observe and which we characterize in detail in section 4.1.4.3 and 4.2. This excessive gravity-wave driven TKE-leakage only occurs, when the CBL top z_{iu} has come within a certain distance to the sponge layer. Hence, as a cause we suspect the interaction between the LES sponge-layer and a near-range wave-layer, which is closely coupled with the CBL below. But also the artificial confinement of the gravity-waves structures by the fixed horizontal domains size¹⁸ might play a role. In any case, we find that this phenomena is strongly domain-size dependent. Therefore we consider it as a defective irregularity. As it seriously distorts the EZ dynamics, we exclude the affected data ($t > t_{\text{end}}$) from our analysis.

Basic temporal classification of the data. An essential physical concept for the following analysis is the subdivision of the usable time series into an 'early period', which is characterized by stronger instationarity, faster growth and relatively deeper EZs than the following quasi-stationary equilibrium entrainment regime. The latter defines the 'main period' (Figure 3.1), which provides the basis for most of our analysis. To diagnose the main period, we use the constancy of the CBL layering or the ZOM entrainment ratio as a criteria, which are both represented by β (e.g. Eq. 2.57). However, as entrainment and the EZ depths can be strongly enhanced by shear (e.g. Figure 2.10), these shear contributions can compensate the relatively reduced entrainment ratio in the instationary early period. Thus for a final identification of the equilibrium entrainment regime, we actually need an appropriate ZOM, $\beta = f(\text{'shear'})$, for sheared CBLs, which at the same time is a main result of the following analysis.

Analogously to GM14 we found that also for sheared CBLs a maximum relative depth of the upper interfacial EZ-layer can be used to define the equilibrium entrainment regime of sheared CBLs (in detail in chapter 6).

Temporal averaging of spatial means. For an improved presentation of second-order statistic (fluxes, variance and TKE-budget terms) we often reduce data scatter by applying some additional temporal filtering of the data time series, using a simple moving-average. This practice is based on the assumption that in a small time frame $\Delta_m t$ the changes of the underlying turbulent ensemble are small and approximately linear. Consequently, we can improve our statistical estimate by additionally averaging over $\Delta_m t$. Practically, we mostly used $\Delta_m t = 15..30$ min averages for our analysis, which roughly equals the convective turnover time $\approx z_i/w_*$ in the equilibrium entrainment regime, during which most quantities show a quasi linear evolution. Systematic errors due to temporal filtering are expect to be small compared the gain by reduced scatter. Mostly, however, we do not consider time series but compare state variables, as already demonstrated in Figure 2.10. In this case it would seem reasonable to cluster data of various LES rather according to their physical state than

¹⁸In the presence of EZ shear, the mean wave-fronts of turbulence induced gravity-waves are expected to be tilted.

by temporal proximity, before filtering. We tested both methods, and did not find significant differences with respect to our result, as long as the filter lengths were kept reasonably small. For simplicity we therefore decided to use a moderate temporal filtering, even when comparing state variables. In this way also the evolution of individual LESs is recognizable in plots. The significance of a relationship between variables is then expressed by both the behavior of a single LES and the degree of agreement between different LESs.

Diagnosis of the CBL structure. The height of the minimum buoyancy flux z_i and the maximum EZ buoyancy gradient $z_{i,g}$ are directly diagnosed from the slab-averaged instantaneous mean profiles. To estimate the height $z_{i,l}$, where the buoyancy flux changes its sign, we linearly interpolate the profile between the adjacent levels with the smallest positive and the smallest negative value below z_i . Our estimate for the upper CBL boundary $z_{i,u}$ is determined by the lowest level above z_i , where the buoyancy flux B_z is smaller than 4% of its surface value B_0 .

The resulting time series of z_i , $z_{i,g}$ and $z_{i,l}$ and $z_{i,u}$, are well defined but show significant scatter (Figure 3.1), due to the limited sample size. This becomes a problem, when we compute the time derivative $w_e = \partial z_i / \partial t$, which is a crucial velocity scale for the entrainment dynamics. To get a smooth estimate of $z_i(t)$, we first followed the approach of (Conzemius and Fedorovich, 2007) and applied a least-square fit using a function that was “*chosen by visual inspection of the simulation data*”. We found the exponential function $y(t) := Bt^A + Ct + D$ to represent the evolution of $z_i(t)$, but also of $z_{i,g}(t)$, $z_{i,u}(t)$ and $z_{i,l}(t)$, rather well, entailing consistent results in our analysis. However, to have some more control about the impact of the fitting procedure we finally used a cubic-spline (blue line in Figure 3.1). By varying the number of knots, one can control the roughness of the fitting function. In this way we can prevent overly smoothing and retain some degree of the original scatter, without disturbing the clarity of our results (as shown e.g. Figure 2.10).

The fitted values are used for direct presentation and the determination of time derivatives. If we integrate flow variable between various characteristic heights, we mostly use the unfitted data as integration limits. However the differences are negligible. For integrals over the whole EZ, we typically do not use $z_{i,u}$ as upper limit but a level that is more safely within the FA (e.g. $1.5 z_{i,u}$).

3.4 LESs of sheared CBLs – first results

In this section we present some direct results of LESs, which should give an general impression about the character of the sheared LES-CBL flows. This includes some general well known characteristics, but also already some less known, unpublished features. Thematically this section covers a conglomeration of different aspects, which might seem somewhat disconnected. However each of them prepares our further reasoning.

At first (section 3.4.1), we show the evolution of the buoyancy and momentum profiles of typical sheared LES-CBL and the CBL growth and its dependency on the geostrophic forcing. At the same time we compare different types of our LESs, which vary by resolution and domain size. Afterwards (section 3.4.2), we shortly compare

the entrainment characteristics of our shear-free LES-CBL with the data and theory of GM. This gives us a clearer idea about the quality and limitations of our LESs, before we actually start to investigate our data set more comprehensively and in detail.

3.4.1 Evolution of the CBL structure

Figure 3.2 displays the evolution of the vertical mean potential-temperature profile, the mean wind profile and the respective fluxes. Shown are hourly data of the high-resolution and the wide-domain simulation (Table 3.2) for a case with a rather strong geostrophic forcing with $u_g = 15 \text{ ms}^{-1}$. The data cover begin- and main-period within the time frame, for which useful data of both simulations are available (about 5 h, due to the shorter high resolution simulation). We generally observe a rather good agreement between both types of LES, which indicates a basic reliability our data set. Figure 3.3 shows the trajectory of the layer averaged ZOM mean wind vector $\mathbf{U} = (u, v)$. The rotational inertial oscillation, which is equally present in the time series of the wind profiles (Figure 3.2b(b)), can be well recognized. Despite the simple looking 'circular pattern' of the trajectory, the momentum dynamics of the growing CBL is actually rather complex.¹⁹ As a result our LES CBLs are governed by an equally complex evolution of SL- and EZ-shear and the related production of TKE, as e.g. given by $S_{SM}(ZOM)$ and $S_{EZ}(ZOM)$ (Eq. 2.52 and 2.53).

Figure 3.4 shows the temporal evolution of the CBL structure defined by the height of the z_{il} , which characterized SM depth and z_i , which measures the ZOM CBL-depth (Schematic 2.1) for several wide-domain LES with varying geostrophic forcing. Compared to the purely convective shear-free case, represented by the black lines, we find that the additional shear forcing enhances CBL growth significantly (evolution of z_i), which results in deeper CBLs. This effect is clear and pronounced for the strongly sheared cases ($u_g = 15 \dots 20 \text{ ms}^{-1}$), but less so and somewhat ambiguous for the weaker sheared case with $u_g = 10 \text{ ms}^{-1}$, which grows slightly faster until the fourth hour of the CBL evolution, but afterwards slower than the shear-free case, so that after 8 h the gain of depth is rather small. Given the fact that the geostrophic forcing is considerable and (as shown later) TKE shear-production in the CBL exceeds buoyancy production, the behavior is remarkable and asks for an explanation.

Figure 3.4 suggests another simple but striking feature that has not been mentioned in previous studies. It seems as if shear mostly affects the evolution of the EZ depth $z_i - z_{il}$, whereas the evolution of the SM depth z_{il} remains largely unaffected. We later come back to both features and explain them based on our more detailed data analysis. Figure 3.5 and 3.6 finally show that also with respect to the CBL structure, defined by z_i , z_{il} and $z_{i,g}$, the wide-domain and the high-resolution LESs for various shear levels agree well.

3.4.2 EZ structure and entrainment ratio

Setup, grid sizes and computational costs of our LESs are similar to the ones in previous studies, such as (Conzemius and Fedorovich, 2007). With GM14 we can now

¹⁹The evolution of the mean wind vector of a growing CBL is significantly more complex than that of a non-growing CBL, which was analyzed by Schröter *et al.* (2013, appendix E).

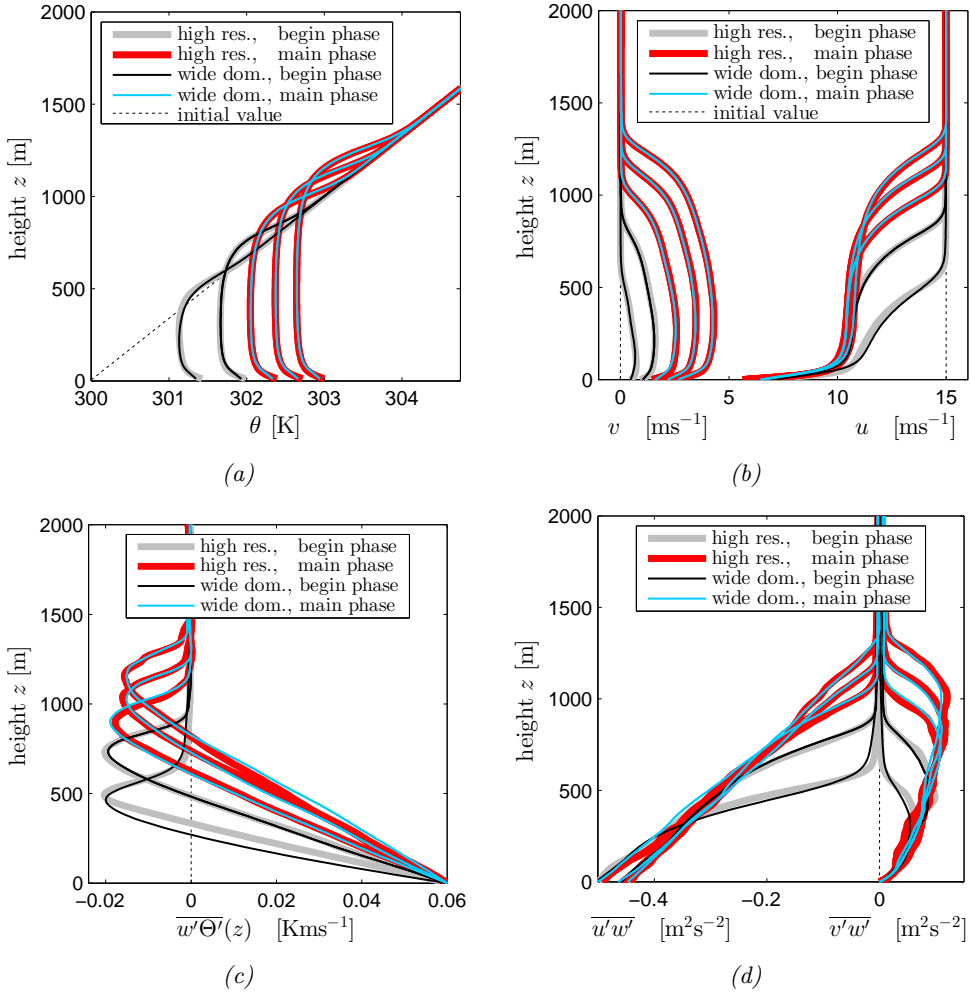


Figure 3.2: Hourly profiles of mean potential-temperature (a), velocity (b), potential-temperature flux (c) and the momentum flux (d) for a high-resolution and wide-domain LES with $u_g = 15 \text{ ms}^{-1}$ and $d\theta/dz = 0.003 \text{ Km s}^{-1}$.

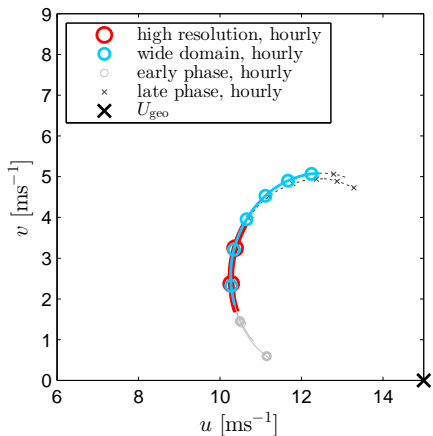


Figure 3.3: Trajectory of the mean CBL wind vector $\mathbf{U} = (u, v)$. The geostrophic forcing is $U_g = 15 \text{ ms}^{-1}$.

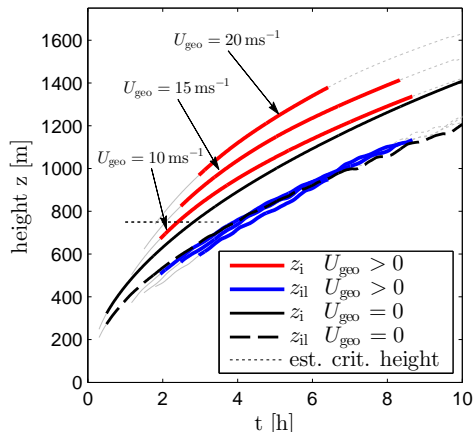


Figure 3.4: Shear-dependent evolution of CBL structure, given by z_i and z_{i1} .

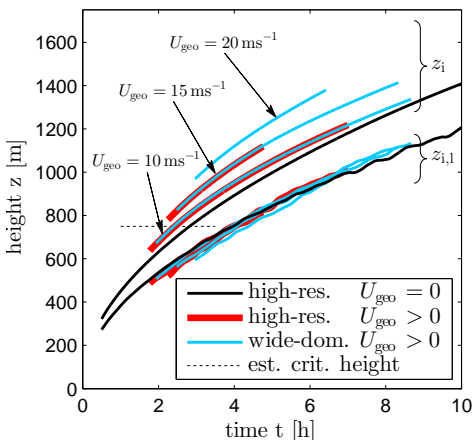


Figure 3.5: Shear-dependent evolution of CBL structure, given by z_i and z_{i1} . Comparison between wide domain and high-resolution LES.

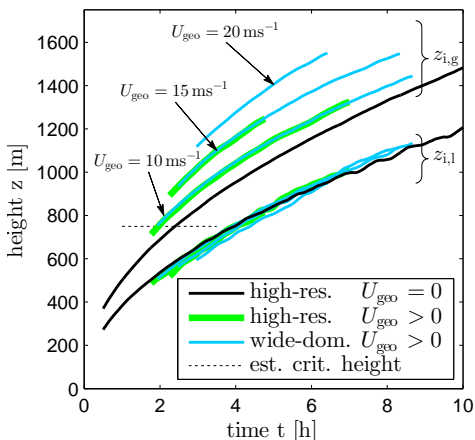


Figure 3.6: Shear-dependent evolution of CBL structure, given by $z_{i,g}$ and z_{i1} . Comparison between wide domain and high-resolution LES.

compare some basic characteristics of our shear-free LES-CBL with the results derived from a state of the art, very high resolution DNS-CBL. To get an impression of the general quality of our LES we evaluate the evolution of the entrainment parameters β , A_t and A_d in the equilibrium entrainment regime. In Figure 3.7 β , A_t

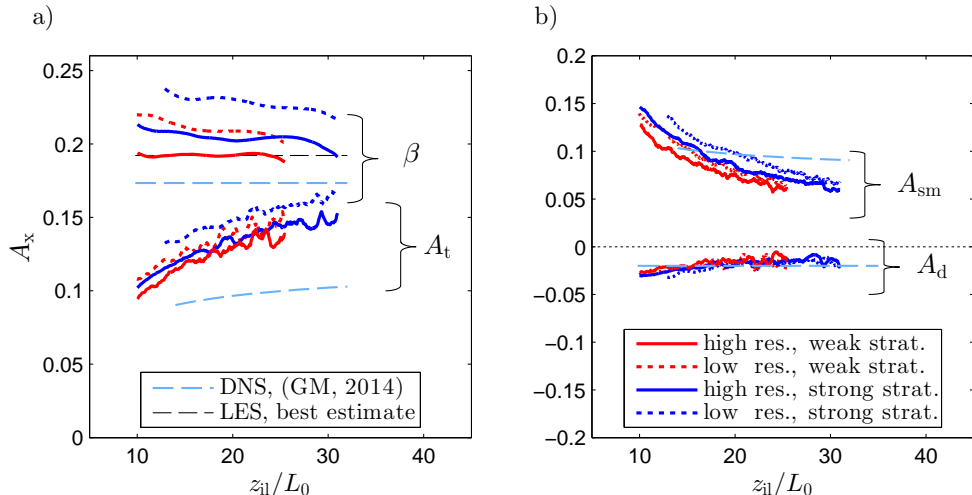


Figure 3.7: Temporal evolution of the entrainment parameters of shear-free (free convective) LES-CBLs. Each legend represents both panels. 'DNS' reference values (light blue, dashed lines) represent the DNS based parametrization of Garcia and Mellado (2014).

and A_d are plotted versus the dimensionless time scale $z_{il}/L_0 \approx z_{enc}/L_0$.²⁰ At first we consider the ZOM parameter β in panel (a), which is supposed to be a consonant value for $z_i/L_0 > 10$. But we find that β still varies significantly between different LESs, showing larger values for lower resolution, stronger FA stratification and earlier simulation stages. All these factors contribute to a relatively weaker resolution of the sharp buoyancy gradient in the upper EZ, which supposedly is the main source for the disagreements (as discussed previously).²¹ For the higher resolution runs (closed lines) β is at least mostly constant and about 0.2, which is the typical value given in literature (Fedorovich *et al.*, 2004b). Our best LES (red closed line) corrects this value to $\beta \approx 1.9$, which however is still significantly larger than $\beta \approx 1.74$, given by GM14's DNS.²² According to GM14, their results are mostly Reynolds-number invariant, which implies that the observed value must be very close to the correct physical value.

To examine the differences between our LES and GM14's DNS more in detail, we next consider the components of β , which are A_t , A_d and A_{sm} (Eq. 2.79). These are shown in panel (a) and (b). As reference for A_t and A_d we use GM14's parametrization Eq. 2.93 and $z_{il} \simeq 0.98z_{enc}$ (their table 2), which represents GM14's DNS data best for

²⁰According to GM14, $z_{il}/z_{enc} \approx 0.98$ for non-sheared CBLs.

²¹Several plots in Conzemius and Fedorovich (2006b) show a similar sensitivity to FA stratification and CBL evolution.

²²The respective value is computed via $\beta = z_i/z_{il} - 1$ (Eq. 2.57) using the data in GM14's table 2.

$z_i/L_0 > 15$ (GM14's Figure 9).²³ We find that a significantly too large $A_t = B_{z_i}/B_0$ is the main reason for the overestimation of entrainment by our LES, which is only partly compensated by a somewhat too small A_{sm} . The EZ shape redistribution term A_d compares rather well with the DNS.

We assume that the bias of our LESs is caused by a too coarse grid. The weak resolution produces a too deep EZ and SL, and apparently also results in a too 'stiff' buoyancy profile, which prevents a sufficient temporal adaption below z_i , which reduces the shape redistribution term A_{ms} in the later simulation stage.²⁴ These

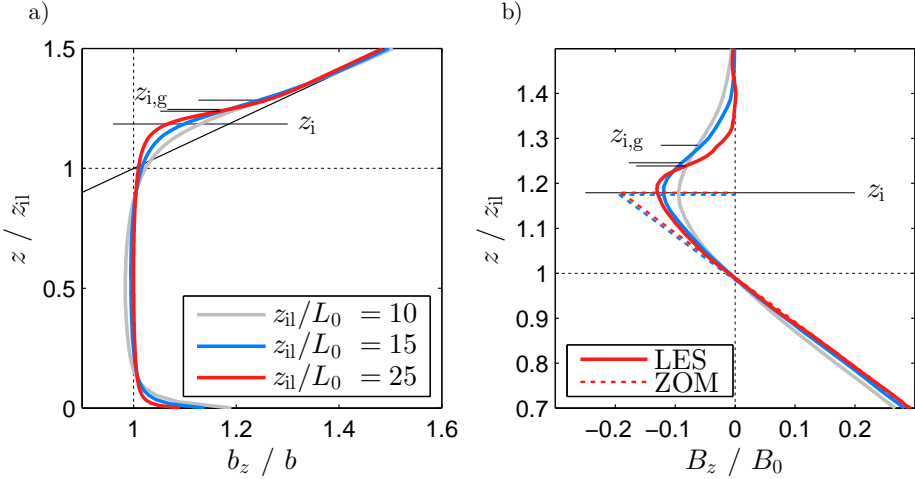


Figure 3.8: Dimensionless profiles of mean buoyancy (a) and the buoyancy flux (b) of a high-resolution shear-free LES-CBL for three different stages of its evolution. Shown are data of the higher resolution LES-CBL, with the moderate FA stratification. Each legend represents both panels.

effects can also directly be seen in the mean buoyancy profiles in Figure 3.8. Shown are normalized vertical profiles of mean buoyancy (a) and the buoyancy flux (b) for your best LES-CBL in three different stages of its evolution. Compared to the buoyancy profiles of GM14's DNS (as reproduced in Figure 2.5(a)), the LES profiles are significantly smoother, the curvature in the SL and EZ characterized by a larger radius, which indicates issues with the reproduction of a strong gradient-variation.

Figure 3.8 (b) further shows that in the beginning of the equilibrium entrainment regime (grey line) the region around the strongest buoyancy gradient (the upper EZ) appears to be bloated and thus the ratio $z_{i,g}/z_{i1}$ has not yet settled at a constant value, as we find for later stages (blue and red lines), as well as for z_i/z_{i1} . For GM14's DNS this delayed stabilization of $z_{i,g}/z_{i1}$ is only very weak.²⁵

The time evolution of the CBL structure for various shear-free LESs is further depicted in Figure 3.9. The well established constancy of z_i/z_{i1} , which corresponds with a constant β , shows that despite its limitations our high resolution LES reproduces

²³The reference value A_{sm} for GM14's DNS is given by $A_{sm} = \beta - A_t - A_d$.

²⁴SL contributions to A_{ms} are positive, contributions from the lower EZ are negative.

²⁵Their data also indicate that $z_{i,g}/z_{i1}$ approaches a constant level more quickly if Re is higher.

the equilibrium entrainment regime rather well.

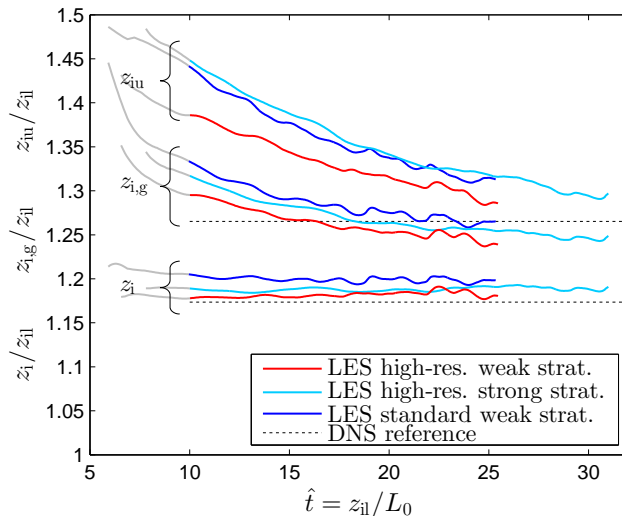


Figure 3.9: Temporal evolution of the CBL structure, defined by the height of the minimum buoyancy flux z_i , the height of the maximum buoyancy gradient $z_{i,g}$ and height of the CBL-top z_{iu} . These are all normalized by the depth of the mixed layer z_{il} , which is defined by the height, where the buoyancy flux changes sign. Time is given by the dimensionless quantity z_{il}/L_0 .

Conclusions. The data comparison above shows that our shear free LES-CBLs suffer from a too coarse computational grid and therefore are not able to fully reproduce the precise EZ structure and dynamics, which is a rather sobering finding. However, we also find that our best LES is well able to reproduce essential patterns and characteristics of CBL entrainment dynamics:

- β and z_i/z_{il} are rather constant for $z_i/L_0 > 10$, which corresponds well with GM14’s definition of the equilibrium entrainment regime. In later stages of CBL evolution this approximately also holds for $z_{i,g}/z_{il}$ and β_g .
- The variation of A_t or A_{sm} during CBL evolution correspond at least qualitatively with GM14’s DNS data.
- A_d is in the same range as GM14’s DNS and is likewise nearly constant for $z_{il}/L_0 > 10$.

For our sheared LES-CBLs we analogous assume that the basic characteristics of their TKE and entrainment dynamics are at least qualitatively similar to real high Reynolds-number CBL. This means that one should be able to identify essential, physically meaningful scales that determine the shear dependence of CBL TKE-dynamics and to depict the basic types of their relationships, even though our data set might not represent the scales in correct proportions.

Although our sheared CBLs are simulated on grids of a similar size and density as the non-sheared CBLs, the significantly deeper EZs for cases with stronger shear (Figure 3.6) result in better resolved and therefore more realistic EZ dynamics. The notion of a better simulation quality for sheared cases is supported by a stronger convergence of various types of LES. Furthermore, we also found that essential properties of our sheared LES-CBLs are well framed by DNSs both in the convective limit, as shown above, and in the neutral limit, as shown in chapter 7.2. These encouraging aspects give us quite some confidence in the following data analysis. However, for final certainty our results have once to be tested on a better data set.

Chapter 4

The integral TKE-budget of sheared CBLs

In this chapter we enter the central territory of this thesis. Our aim is to investigate the integrated TKE-budget of our set of LES-CBLs and to characterize its dependence on shear. The main idea is to reanalyze shear effects on turbulent kinetic energy, using only very basic assumptions and without too much preoccupation with advanced previous concepts (section 4.1). Based on the outcome, we then derive a parametrization for the shear-dependence of the TKE-budget (section 4.2), which is what we previously called submodel 1 (chapter 2.7.2). In the following chapter 5, we then directly implement this parametrization in the framework of a ZOM, which defines what we called submodel 2.

4.1 Analysis of the integral TKE-budget

4.1.1 Preliminary considerations

To characterize the integral CBL-dynamics one wants to condense the rich information contained by the rather complex and variable profiles¹ of the TKE budget terms and reduce it to a minimum of essential scales. Assuming a very basic self-similarity of the CBL, which only depends on the forcings and boundary conditions, it seems natural to consider the layer-integrated TKE-budget and only differentiate between obvious structural features, as given by the characteristic layering of TKE-buoyancy production in a positive production zone (the SM) a negative consumption zone (the EZ). For convenience and clarity this approach is shown once more in Figure 4.1(a). It comes as no surprise that this very intuitive and natural perception of the CBL, has been already used in a very early study on CBL dynamics by Ball (1960). It was then further explored by Deardorff *et al.* (1969); Lilly (1968); Stull (1976a) and has later been denoted as ‘Eulerian Partitioning’ (EP, Randall, 1984) of the buoyancy production. With respect to sheared CBLs, an EP-based model was already suggested

¹Detailed vertical profiles of the ensemble averaged TKE-budget of LES-CBLs have been presented and investigated before (e.g. Deardorff, 1974b; Moeng and Sullivan, 1994; Pino and Vilà-Guerau de Arellano, 2008).

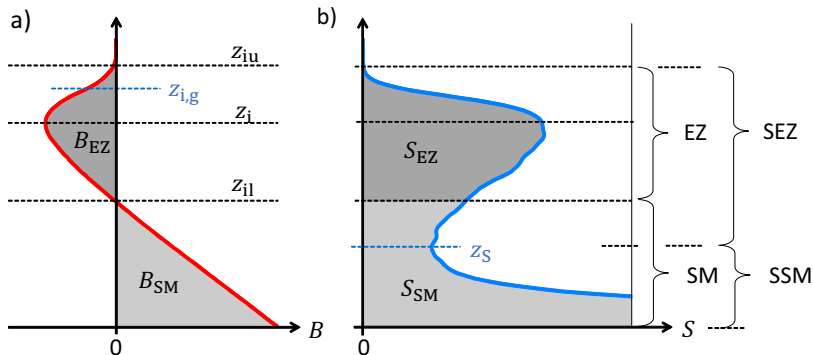


Figure 4.1: Schematic of the vertical CBL structure, as given by the profile of the buoyancy flux (proportional to buoyancy production of TKE) (a). It subdivides the CBL into an entrainment zone (EZ) and the combined surface and mixed-layer (SM). The same division is then applied to the shear production (b).

by Stull (1976a). But afterwards EP has largely been ignored – for reasons that are mostly unclear to us. This particularly holds for the most recent LES-studies on sheared CBLs (e.g. Pino *et al.* (2003); Kim *et al.* (2006); Pino *et al.* (2006a,b); Conzemius and Fedorovich (2006b) and Conzemius and Fedorovich (2007), which in contrast rely on the so called ‘Process Partitioning’ (PP, Randall, 1984, see also section 5), which was first proposed by Manins and Turner (1978). This, however, is surprising, as our analysis demonstrates that the – in our opinion – more intuitive and older EP is the superior concept.

4.1.2 The integrated TKE budget

As our first step we integrate the local TKE-budget (Eq. 2.29) over the whole turbulent layer from 0 to z_{iu} . For convenience we denote the integrated TKE buoyancy production as B , the integrated shear production as S , the integrated TKE transport as ϕ , the integrated TKE simply as e and the integrated dissipation rate simply as ε . With a reordering of the terms, the integrated TKE-budget reads

$$B + S + \phi - \frac{\partial e}{\partial t} + \varepsilon = 0. \quad (4.1)$$

As we integrate over the entire turbulent CBL, the integral turbulent TKE-transport term must be zero, as the turbulent transport over the boundaries is zero (turbulence is absent at the surface, and in the non-turbulent layer above z_{iu}). Thus

$$-\int_0^{z_{iu}} \frac{\partial \overline{e'w'}}{\partial z} dz = 0. \quad (4.2)$$

However, this is not necessarily the case for the TKE transport via pressure fluctuation. Therefore

$$\phi = -\frac{1}{\rho} \int_0^{z_{iu}} \frac{\partial \overline{p'w'}}{\partial z} dz. \quad (4.3)$$

As the FA is stably stratified and non-turbulent, $\phi \neq 0$ would represent the exchange of fluctuation energy between CBL turbulence and FA gravity waves (Fedorovich *et al.*, 2004b).

In the next step, we take the typical two-layer structure of CBL buoyancy dynamics into account and consider positive and negative contributions to the buoyancy production separately (Figure 4.1 (a)). Hence, we subdivide the integrated CBL buoyancy production B into the positive lower contribution B_{SM} in the surface- and mixed layer (subscripts SM) and the negative contribution (B_{EZ}) in the entrainment zone (subscript EZ). B_{SM} represents the actual ‘production’, whereas B_{EZ} represents TKE consumption, which is our basic measure for CBL entrainment:

$$B = B_{SM} + B_{EZ}, \quad \text{with } B_{SM} = \int_0^{z_{il}} B_z dz \quad \text{and} \quad B_{EZ} = \int_{z_{il}}^{z_{iu}} B_z dz. \quad (4.4)$$

Considering buoyancy production as the essential characteristic measure of CBL convection (as discussed before), we normalize the integrated TKE budget with B_{SM} and obtain a dimensionless TKE budget:

$$1 + \frac{B_{EZ}}{B_{SM}} + \frac{S}{B_{SM}} + \frac{\Phi}{B_{SM}} + \frac{-\frac{\partial e}{\partial t}}{B_{SM}} + \frac{\varepsilon}{B_{SM}} = 0. \quad (4.5)$$

Obviously, the dimensionless integral buoyancy consumption, B_{EZ}/B_{SM} , forms an entrainment ratio and can be considered as an alternative definition to A (Eq. 2.75) or β (Eq. 2.58). In the remainder of this analysis we will mostly use the positive quantity $-B_{EZ}/B_{SM} \geq 0$ and refer to it as the ‘dimensionless entrainment ratio’. Analogously $-\varepsilon/B_{SM} \geq 0$ is the dimensionless integrated dissipation rate. The dimensionless CBL shear-production S/B_{SM} can be recognized as the negative inverse of the integrated flux Richardson number $-Ri_{f,CBL}$. For the sake of clarity and consistency of presentation we mostly refer to this and similar quantities in the given form and omit the use of Richardson numbers, despite the fact that their use is more common in literature on shear flows.

In the remainder of this section 4.1 we want to find out if we can identify (in our data set) simple relationships between the integral TKE-production terms and the other terms. These relationships would represent the inviscid self-similarity of the CBL (e.g. similarly as already discussed in chapter 2.2). If such relationships can be identified, the next question will be, how we can appropriately parametrize these relationships. Given the basic goal of our analysis, we are particularly interested in the dependence of entrainment on shear production. But finally we will consider the relationship between shear production and the whole TKE composition, which results in a more comprehensive picture of EZ dynamics. In any case, if one identifies the relationships between single terms in Eq. 4.5, one typically assumes that the other

terms also well-behave in one or the other way, as they are inevitably coupled via the budget.

The basic difference and physical advantage of EP (used in Eq. 4.5) as compared to other bulk approaches is that the EP-based two-layer concept of the CBL structurally separates between the essentially different processes of buoyancy production and buoyancy consumption (in the EZ, i.e. entrainment). This also suggests two different integral length scales, z_{il} and $z_{iu} - z_{il}$, which are readily given by the CBL structure.

4.1.3 The TKE budget of the purely convective CBL

Before investigating the influence of shear on the TKE budget of CBLs, it is very natural to first characterize the TKE budget of the purely convective CBLs as a basic type, to which the modified dynamics of sheared CBLs can be compared.

Following our two-layer concept for the purely convective case ($S = 0$) the dimensionless integrated TKE-budget can be written as the balance between buoyancy production of TKE (lhs) and the sum of all loss terms (rhs)

$$1 = -\frac{B_{EZ}}{B_{SM}} - \frac{\Phi}{B_{SM}} - \frac{-\frac{\partial e}{\partial t}}{B_{SM}} - \frac{\varepsilon}{B_{SM}}. \quad (4.6)$$

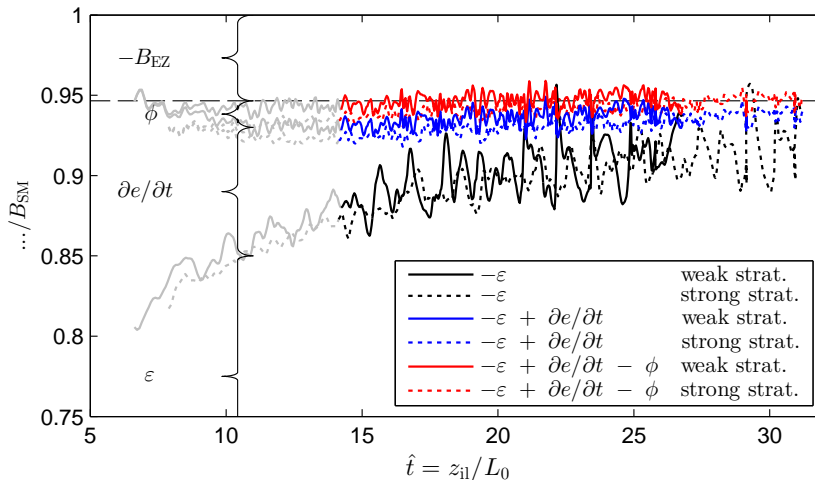


Figure 4.2: Temporal evolution of the integrated TKE budget terms of two high-resolution LES of shear-free CBLs with different FA stratification (weak: solid, strong: dashed). Time given by the dimensionless quantity $\hat{t} = z_{11}/L_0$. Time series unfiltered. The thin grey lines indicate the ‘early phase’.

Figure 4.2 shows the temporal evolution of the terms on the rhs for two high-resolution simulations with different FA stratification. To compare shear-free CBLs with different FA stratification, we follow GM14 and measure time with the dimensionless quantity $\hat{t} = z_{11}/L_0 \approx z_{enc}/L_0$ (see Eq. 2.92), which results in a fully self-similar

representation of both cases. The normalized terms of the TKE budget are plotted cumulatively on the ordinate. The black lines denote the dissipation rate $-\varepsilon/B_{\text{SM}}$, the blue lines denote the dissipation rate and the TKE tendency $(-\varepsilon + \partial e/\partial t)/B_{\text{SM}}$ and the red lines denote the sum of dissipation rate, TKE tendency and wave losses $(-\varepsilon + \partial e/\partial t - \Phi)/B_{\text{SM}}$. The magnitude of each single term is additionally marked by a curly bracket.

4.1.3.1 Entrainment rate as a TKE loss term

The most important aspect in Figure 4.2 and the basis for our further reasoning is represented by the red lines. They represent the sum of all ‘loss terms’ (dissipation, tendency and wave-losses). The difference to unity equals the integrated entrainment rate $-B_{\text{EZ}}/B_{\text{SM}}$, as all ‘losses’ plus entrainment must sum up to unity to balance TKE production. The integrated entrainment ratio appears to be rather constant over most of the simulation time, especially for the main phase and for the LES with the moderate FA stratification (solid line), which we expect to be our best approximation of a real CBL. Thus, for $S = 0$, we find

$$\frac{(-\varepsilon + \partial e/\partial t - \Phi)}{B_{\text{SM}}} \approx 0.95 \quad \text{and} \quad -\frac{B_{\text{EZ}}}{B_{\text{SM}}} = c_{\text{B},0} \approx 0.05. \quad (4.7)$$

The same estimate was already made by Stage and Businger (1981) based on atmospheric observations. However, the constancy over the whole time span is somewhat surprising when we consider the evolution of the entrainment parameter $A_t(t)$. According to GM14’s high resolution DNS (e.g. their Figure 4(a), or our Figure 2.7), the shape of the EZ flux-profile does not change much and we therefore would expect $B_{\text{EZ}}/B_{\text{SM}} \propto A_t(t)$. Hence $B_{\text{EZ}}/B_{\text{SM}}$ should show a similar steady growth as documented for $A_t(t)$ (Figure 2.9). The deviating behavior of $B_{\text{EZ}}/B_{\text{SM}}$ is probably caused by the insufficient vertical resolution in the EZ in the early stage of the CBL evolution, which results in a too deep upper EZ and enhanced integral entrainment (Figure 3.8). However, in the ‘pragmatically’ quasi-stationary entrainment regime ($z_{\text{il}}/L_0 \approx 15\dots35$), an approximately constant value seems appropriate and agrees with our picture for $A_t(t)$.

Next we consider the other terms of the TKE budget and re-examine Figure 4.2. As to be expected, the dissipation rate ε is by far the largest loss term and the main sink for TKE. Before we comment on the TKE-tendency in the next section, a few words need to be spent on the integrated transport term ϕ , which represents transfer from TKE into gravity-wave energy and its subsequent propagation through the stably stratified FA. As predicted by Stull (1976b) and experimentally confirmed by Fedorovich *et al.* (2004b) and lately by GM14, these losses turned out to be very small for shear-free CBLs in the typical range of atmospheric conditions and therefore have been generally neglected in CBL entrainment models. For our LES we approximately find $-\phi/B_{\text{SM}} \approx 0.02$ to be rather small (difference between blue line and red line). GM14 refer to a negligibly small integral transport term and we also find that $-\phi/B_{\text{SM}}$ slightly decreases in time. This could be a sign that the somewhat larger $-\phi/B_{\text{SM}} > 0$ in our case is caused by a low spatial resolution, which gradually improves with the deepening of the LES-CBL.

4.1.3.2 CBL instationarity and TKE-spinup

The integral TKE tendency $\partial e/\partial t$ turns out to be important throughout our whole data set and shows distinct temporal dynamics. Picking up the similar discussion in section 2.5.4, the significance of the TKE tendency can be assessed in two ways. For $z_{i1}/L_0 > 10$ we find that the TKE tendency is less than 10% of the integral buoyancy production. This results in the approximately ‘quasi-stationary’ CBL dynamics that allows the CBL-layering to settle at constant levels (β and $\beta_g \approx const$), which is the main characteristic of the ‘equilibrium entrainment regime’. However compared to the integral entrainment term, the TKE-tendency is quite significant and for our shear-free cases both terms are always of a similar size.² For $z_{i1}/L_0 \approx 15$ the TKE tendency changes only slowly and the approximate constancy for $z_{i1}/L_0 \approx 15\dots35$ well illustrates the ‘pragmatically quasi-stationary’ equilibrium entrainment regime³. Our experimental setup with constant boundaries, a steady forcing and a fully developed turbulence field basically represents a stationary balance between TKE production and dissipation plus consumption. A basic instationarity of the CBL TKE-dynamics is induced by entrainment and the resulting steady growth. As long as the CBL is growing the amount of integrated total TKE stored within the CBL has to grow as well, resulting in an overall positive TKE-tendency term (therefore also called ‘TKE storage term’).

More specifically, one can link the TKE-tendency (or at least a major part of it) directly to the interfacial process that is commonly called entrainment. The continuous dispersion of turbulence into the FA results in the displacement of the boundary between the turbulent flow and the FA. Directly below this boundary, turbulence is not yet fully developed and a continuous transfer of TKE from turbulent eddies to recently entrained parcels of relatively quiescent FA air has to take place. This process is supposed to happen predominantly within the upper EZ (see later Figure 4.22). Hence, a significant amount of the TKE-production is used to ‘spin up’ the turbulent motions of the entrained air. The TKE tendency term is therefor also conveniently denoted as ‘TKE-spinup term’.

One could therefore argue that from all contributions to the TKE-budget, the TKE-spinup term represents the dynamics of the interfacial entrainment process most directly. For flows that are not affected by a stable stratification at the free-flow boundaries, it is even the only contender.⁴ But for ABLs that grow into a stratified fluid, the conditions are different and entrainment-driven TKE-consumption is relevant and in most circumstances dominant.⁵ Hence, although both terms are linked to

²In our sheared LESs $\partial e/\partial t$ becomes significantly smaller compared to $-B_{EZ}$. But both terms are still of the same order of magnitude for our whole data set.

³This could also be denoted as ‘quasi-stationary in-stationarity’.

⁴This holds for many engineering flows, such as a steady turbulent jet, or a turbulent BL that develops on a wing. Both types of flow are dynamically highly instationary in the sense that they feature a strong interfacial exchange (here this is ‘entrainment’) and TKE-spinup at their free flow boundaries. An essential property of both flow types is that they are spatial heterogeneous as they evolve in the direction of the mean flow. But with a temporally constant forcing both flows develop a stationary flow field, with stationary entrainment and TKE-spinup dynamics.

⁵Only for CBLs in an initial evolution stage with $z_{i1}/L_0 \approx 1$, TKE consumption is small and TKE spinup accounts for the complete entrainment dynamics, as reasoned in detail by GM14. But TKE-consumption becomes relevant for more mature CBLs. According to our LESs, TKE consumption dominates as soon as $z_{i1}/L_0 < 15$. Towards the stationary limit with $z_{i1}/L_0 \mapsto \infty$, entrainment is fully represented by integral TKE consumption and TKE spinup becomes insignificant.

the interfacial dynamics, in BL-meteorology TKE-consumption is commonly considered as ‘entrainment’ in a dynamical sense and TKE-spinup rather as an associated process.

The influence of TKE-spinup on the evolution of the CBL TKE-budget is evident. During CBL evolution, the growth rate w_e steadily decreases. Thus, the inflow of quiescent air and the coupled use of TKE by the spinup process decrease likewise. As a result, the amount of TKE-production that is available for other processes increases and, at least partly, enhances entrainment. Hence the decline of growth-induced TKE-spinup appears to be the cause for the asymptotic increase of the entrainment ratio, as e.g. represented by $A_t(t)$ (Figure 3.7). In the past, this idea resulted in several attempts to incorporate TKE spinup as a steering factor into entrainment parameterizations (e.g. Zilitinkevich, 1975)⁶.

This approach, which basically seeks to represent the instationarity of the whole TKE budget, can be considered as complementary to GM14’s concept, which explains the evolution of $A_t(t)$ more directly by local changes in the interfacial dynamics (chapter 2.6). When investigating the instationarity of entrainment (chapter 6), we closely followed GM14’s approach and only occasionally discuss TKE spinup. However as entrainment (or dissipation) and TKE-spinup are deterministically constrained by the TKE budget, it should be straightforward to combine both approaches.

To quantitatively link integral TKE-spinup with integral entrainment and dissipation, one needs to determine how the impact of TKE-spinup is distributed between the two terms. Let $B_{EZ,\infty} = const$ and $\varepsilon_\infty = const$ represent integral entrainment and dissipation in the asymptotic stationary state with $\delta/z_{enc} \mapsto 0$ (or alternatively $\hat{t} = z_{enc}/L_0 \mapsto \infty$, Eq. 2.92). For any other finite δ/z_{enc} the actual entrainment and dissipation rates are expressed as follows

$$B_{EZ} = B_{EZ,\infty} + \alpha_e \frac{-\partial e}{\partial t}, \quad (4.8)$$

$$\varepsilon = \varepsilon_\infty + (1 - \alpha_e) \frac{-\partial e}{\partial t}. \quad (4.9)$$

Here α_e is the fraction of TKE the goes at the expense of entrainment, and is basically unknown.⁷ As $\varepsilon(t)$ is much larger and varies more than $B_{EZ}(t)$, we can at least suppose that TKE spin-up affects dissipation absolutely more than entrainment, hence $\alpha_e < 0.5$.

In this study we do not further investigate α_e . But for a complete and consistent picture, we here shortly sketch, how α_e could be estimated based on existing CBL theory. First we note that GM14’s data suggest that $B_{EZ} \sim A_t$. That means that, an expression for $B_{EZ} = f(\delta/z_{enc})$ and $B_{EZ,\infty} = f(\infty)$, is analogous to Eq. 2.81 and could be easily derived from GM14’s data. Thus, with Eq. 4.8, the relationship

⁶At a first sight, we found the general reasoning behind the model convincing, as it seems to aim at the entrainment ratio $A_t(t)$. But the model is actually constructed like a ZOM and therefore should rather represent $\beta(t)$. However, β becomes constant in the equilibrium entrainment regime, which makes an additional accountancy of the TKE spinup unnecessary (Fedorovich *et al.*, 2004a).

⁷An interesting aspect of α_e could be a linkage with the turbulence spectrum, as it weighs the impact of TKE-spinup between entrainment, which is driven by the large production scales, and dissipation, which represent the smallest turbulent scales.

$\alpha_e = f(\delta/z_{\text{enc}})$ would directly result from their entrainment scaling, with

$$\alpha_e(\delta/z_{\text{enc}}) = \frac{B_{\text{EZ},\infty} - B_{\text{EZ}}(\delta/z_{\text{enc}})}{-\partial e/\partial t}. \quad (4.10)$$

Furthermore, the spinup term can be estimated based on traditional scaling theory. In equilibrium entrainment conditions integral TKE is considered to react approximately instantaneously to changes of the TKE production. This idea is represented by the convective scaling of the velocity variances (e.g. Eq. 2.72 and Figure 2.5). Thus for the integral values of the TKE we can approximately assume $e \sim z_{\text{il}} w_*^2 = z_{\text{il}} (B_0 z_{\text{il}})^{2/3}$ (Van Heerwaarden and Mellado, 2016, Eq. 28) or similarly $e \sim z_i (B_0 z_i)^{2/3}$. With $B_0 = \text{const}$ and $w_e = \partial z_i/\partial t$ the time derivative of e reads

$$\partial e/\partial t \sim 5/3 B_0^{2/3} z_i^{2/3} w_e. \quad (4.11)$$

To get $\partial e/\partial t$, w_e can be determine with a ZOM (Eq. 2.58). Hence α_e can be readily computed with ZOM quantities as a function of δ/z_{enc} (Eq. 4.10).⁸

However, in this part of our analysis, we are only interested in the stationary properties of the TKE-budget. We tentatively assuming that it influence on integral entrainment is comparably small and therefore pragmatically set $\alpha_e := 0$. This means that we consider the actual integral entrainment rate B_{EZ} (no effect of TKE-tendency included) and the sum of the integral dissipation rate and TKE-tendency

$$\varepsilon_a = \varepsilon_\infty + \frac{-\partial e}{\partial t}. \quad (4.12)$$

As this quantity balances the TKE production term, it is marked by the subscript ‘a’ for ‘antagonistic’. The reason to use ε_a for our characterization is purely technical. For $z_{\text{il}}/L_0 > 5$, the difference between ε_a and ε is rather small, but for our data ε_a shows significantly reduced scatter compared to ε only.

4.1.4 The TKE budget of CBLs with varying shear

4.1.4.1 Entrainment versus shear production

The structure of CBL shear production. Shear production of TKE in CBLs is typically concentrated in two distinct zones, each related to a distinct maximum of wind shear: at the surface and in the EZ (Figure 4.1 (b)). In the lower layer, shear is induced by surface friction, which causes a steady downward flow of momentum. Shear in the upper part of the CBL is caused by the steady entrainment of faster FA air⁹ that is approximately in geostrophic equilibrium. The difference between the momentum flux at the top of the CBL and the momentum flux at the surface induces a stress divergence over the entire CBL, which decelerates the CBL as a whole.

⁸For sheared CBLs δ/z_{enc} should be replaced by δ/z_{il} . The relationship with $B_{\text{EZ}} \sim A(t)$ is given by our entrainment model in chapter 6.2.1 and 6.3.3. w_e can be computed with our ZOM (Eq. 5.12). Finally, it should be possible to complement the scaling for $\partial e/\partial t$ (Eq. 4.11) by additionally accounting for the ZOM shear production (Eq. 5.5).

⁹Faster compared to sub-geostrophic speed of the CBL, which is – as a whole – decelerated by surface friction

Ball (1960) already suggested that turbulence, which is mechanically produced by shear close to the surface, is readily dissipated and does not contribute to entrainment. As shear production in ABLs is the strongest close to the surface, this finding is obviously relevant. Despite Ball's 1960 careful argumentation that refers to field experiments by Taylor (1952), and later observational support by Lenschow (1974), this characteristic feature seems to have been widely overlooked afterwards. We know that it was implicitly used by Sorbjan (2004) and explicitly re-introduced by Conzemius and Fedorovich (2007). However, the vast majority of entrainment models that were evaluated by Conzemius and Fedorovich (2006b) account for shear production at the surface or both shear production at the surface and in the EZ.¹⁰

Conzemius and Fedorovich (2006a, 2007) finally exclude surface-related shear production from their entrainment models (as already shown for the CFM, Eq. 2.94). According to the authors this measure significantly improves model performance. As 'surface-related' they define the TKE shear-production that occurs below the typically pronounced minimum that separates the upper from the lower shear zone (at height z_S , Figure 4.1 (b)). z_S also represents the height of the wind-speed gradient minimum and the height of the inflexion point in the SM wind-profile. Accordingly, one can use a shear-based definition of the surface layer plus mixed layer (between surface and z_S , SSM) and a shear-based entrainment zone (between z_S and z_{iu} , SEZ). The respective integral TKE-shear production for each sublayer is given by

$$S_{SEZ} = \int_{z_S}^{z_{iu}} S dz \quad \text{and} \quad S_{SSM} = \int_0^{z_S} S dz. \quad (4.13)$$

With our data set we have the opportunity to evaluate this concept more directly. On that basis, we prefer a slightly modified definition of the relevant CBL shear layers. Considering the strongly local character of shear production of turbulence, as observed in neutral BLs (e.g. Jonker *et al.*, 2013) but also in the surface layer of CBLs (e.g. Taylor, 1952; Lenschow, 1974), we sharpen Conzemius and Fedorovich's (2006a) idea somewhat. In agreement with Sorbjan (2004) we hypothesize that only TKE shear-production within the actual EZ is relevant for entrainment and that the typically strong shear production in the SL and also the weaker contributions in the upper ML can be neglected, as they are decoupled from the entrainment process.

Hence, analogously to buoyancy production, we subdivide the CBL shear-production of TKE vertically and integrate it over surface layer plus mixed layer (subscript SM) and the EZ separately (Figure 4.1 (b))

$$S_{EZ} = \int_{z_{i1}}^{z_{iu}} S dz \quad \text{and} \quad S_{SM} = \int_0^{z_{i1}} S dz. \quad (4.14)$$

With this subdivision the dimensionless TKE-budget (Eq. 4.5) expands to

$$1 + \frac{B_{EZ}}{B_{SM}} + \frac{S_{SM}}{B_{SM}} + \frac{S_{EZ}}{B_{SM}} + \frac{\Phi}{B_{SM}} + \frac{-\frac{\partial e}{\partial t}}{B_{SM}} + \frac{\varepsilon}{B_{SM}} = 0. \quad (4.15)$$

Relation between entrainment rate and TKE shear production. To get a clear impression of the actual relationships between entrainment and shear production, we plot the dimensionless entrainment ratio $-B_{EZ}/B_{SM}$ as a function of (1)

¹⁰Driedonks (1982) pointed out the uncertainty concerning the relevance of surface- and EZ-shear for the entrainment dynamics. But due to a lack of data, he could not investigate the issue.

dimensionless shear production in the surface layer plus mixed layer S_{SM}/B_{SM} , (2) dimensionless shear production in the entrainment zone S_{EZ}/B_{SM} , and (3) dimensionless shear production in the whole CBL S/B_{SM} . We do this for our complete LES data set in Figure 4.3. Here dimensionless entrainment is displayed along the abscissa

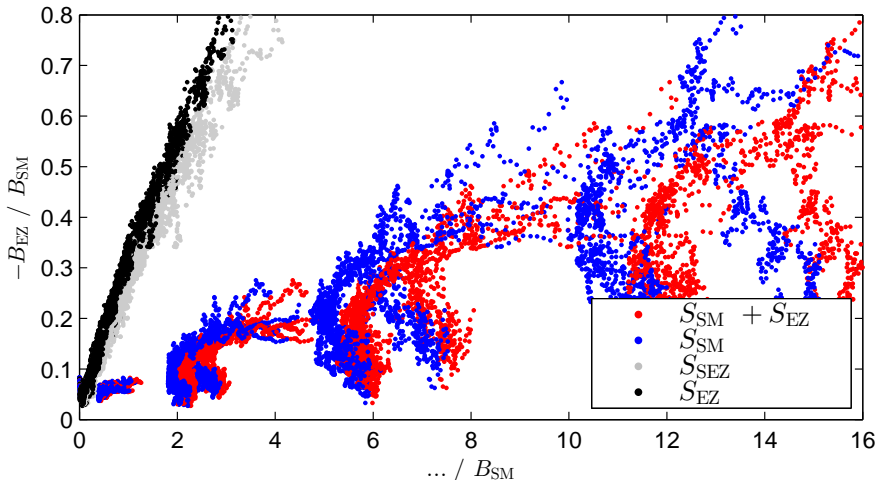


Figure 4.3: Dimensionless entrainment versus TKE shear-production for all LES. Red dots: Shear production in the whole CBL. Blue dots: Shear production in the surface and mixed-layer (SM) only. Black dots: Shear production in the entrainment zone (EZ) only. Gray dots: Shear production in the shear-based entrainment zone (SEZ) only. Shown are instantaneous values for every minute of an LES. Data comprise the early phase and the main phase of the CBL evolution.

and shear production on the ordinate. Between $-B_{EZ}/B_{SM}$ and S_{EZ}/B_{SM} (black dots) we find over the whole range a very well defined, quasi linear correlation, which strongly suggests a direct deterministic relationship. But as soon as surface-related shear production S_{SM} is involved the correlation worsens and single LES runs can be well distinguished as rather independent strongly curved structures (red and blue dots). This clearly suggests that shear production in the surface- and mixed layer does not directly drive entrainment.

Similarly as for S_{EZ} , we find a rather good correlation between S_{SEZ} and entrainment, as shown by the gray dots. However, the correlation is slightly worse, which justifies our preference for the buoyancy-based definition of the EZ and S_{EZ} .¹¹ But it also seems that z_S and the related SEZ do become significant for BLs close to the neutral limit when $z_S > z_{il}$, as we discuss in chapter 7.2.3.

The curved structures that characterize the dependence of $-B_{EZ}$ on S_{SM} , can be explained by the rotational inertial oscillation (IO) of the CBL flow field, caused by the Coriolis force. The time scale of a CBL's IO is of the order of the natural period in the mid-latitudes and with roughly $2\pi/f_c \approx 17.5\text{h}$ (Figure 3.3) at least one order of magnitude larger than turbulent time scales in our CBLs. Hence the

¹¹More important for our choice, however, is the significantly worse agreement with the ZOM representation of entrainment zone shear production, as shown in chapter 5.1.2.2.

IO constitutes an additional external forcing of the CBL wind shear, which has the remarkable property that it influences EZ shear and SM shear differently. Thus, the clear signal of the IO in the relationship between $-B_{EZ}$ and S_{SM} suggest that these quantities are not directly coupled by turbulence, but rather indirectly by the mean-momentum dynamics, which determines shear in the SM as well as in the EZ. The

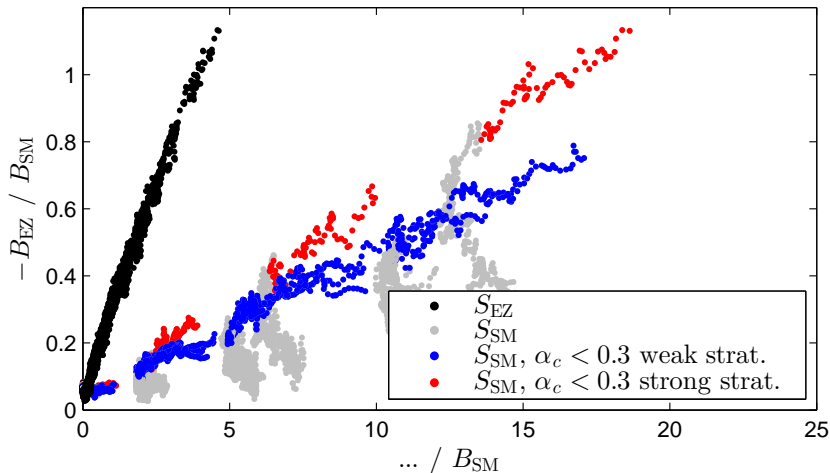


Figure 4.4: Similar as Figure 4.3: Dimensionless entrainment versus integral TKE shear-production. Black dots: Shear production in the entrainment zone only. Grey dots: Shear production in the surface and the mixed-layer (SM). Different to Figure 4.3, the blue and red dots show the SM shear production only on condition that the SM mean wind is reasonably well aligned with the geostrophic wind, i.e. for $\alpha_c = |v/u|$ smaller than 0.3. All cases are shown, but if possible only wide domain runs are displayed. Data comprise both the early phase and the main phase of the CBL evolution.

fact that a rough overall correlation exists between entrainment and S_{SM}/B_{SM} (blue dots), throughout the whole series of LES, seems simply due to an indirect coupling via the momentum budget: for each LES the basic range of both surface shear and EZ shear is given by the shear over the whole CBL (U_g/z_{iu}). Thus the general evolution and range of both shear in the SM and shear in the EZ vary with the choice of U_g . However, if one considers a single LES run (with a particular U_g forcing), there is no simple correlation between S_{SM}/B_{SM} and $-B_{EZ}/B_{SM}$. Hence, Figure 4.3 strongly supports the idea that surface-related shear production of TKE does not contribute to entrainment.

For our data set we can examine the role of the momentum budget for the indirect relationship between SL shear production and EZ shear production by only considering data in the very early stage of the IO, when the mean flow \mathbf{U} is still about parallel to \mathbf{U}_g (e.g. gray markers in Figure 3.3). In those conditions the Coriolis force and the pressure gradient are approximately perpendicular to the flow, which in a first approximations also seems to hold for the momentum tendency. Hence, these forces do not influence the momentum budget in the flow direction (along u_g) and

the budget is mostly governed by a simple balance of forces, given by the decelerating surface stress and accelerating entrainment of momentum (Eq. 2.48, first term on the rhs).¹² This suggests a similarly simple balance between the closely related S_{EZ} and S_{SM} . However, as the flow further develops this simple alignment of forces vanishes and the relationship between surface-stress and momentum-entrainment and consequently also between S_{EZ} and S_{SM} becomes much more complicated.

This reasoning is supported by Figure 4.4. It is similar to Figure 4.3, but here red and blue dots mark all values of $S = S_{SM}$ for which the flow is approximately parallel to \mathbf{U}_g . As criteria we chose an ageostrophic angle¹³ of the mean flow $\alpha_c = |v/u|$ to be smaller than 0.3. For these values we observe a rather good linear correlation between B_{EZ} and S_{SM} , which later disappears when the IO further develops ($\alpha_c \geq 0.3$, gray dots). However, this correlation rather reflects the equally good correlation between S_{SM} and S_{EZ} , which is caused by the correlation between the basic TKE-producing mechanisms. These are the surface stress (and shear) on one hand and momentum entrainment (and EZ shear) on the other, which are both governed by a largely self-similar and self-stabilizing momentum balance in the absence of the pressure gradient force and the Coriolis force in the flow direction (see also the discussion in chapter 7.3.3).

Also note that the good linear correlation between B_{EZ} and S_{SM} in the early periods clearly depends on the FA stratification (red versus blue dots), which, however, is not the case for the relationship B_{EZ} and S_{EZ} . As there is no direct physical linkage between FA stratification and SM turbulence, this feature is again a sign for an indirect coupling between S_{SM} and S_{EZ} via the momentum budget, which determines shear and stresses within the CBL and thereby regulates the distribution of S between S_{SM} and S_{EZ} .

The observed influence of the FA stratification on S_{SM} can be rather easily explained by referring to the ZOM formulation of the momentum budget and TKE-budget. Within the ZOM, buoyancy entrainment is given by $B_{EZ} \sim w_e \Delta b$, momentum entrainment by $w_e \Delta U$, EZ shear-production by $S_{EZ} \simeq w_e \Delta U^2$ (Eq. 2.55) and SM by shear-production $S_{SM} \sim |U|^3$ (Eq. 2.54 with Eq. 2.49). Furthermore, in the particular case of $\mathbf{U} \parallel \mathbf{U}_g$, the CBL mean wind speed U is directly coupled to the entrainment of momentum, as $U = U_g - \Delta U$. Now consider two CBLs with a differently stratified FA but with the same entrainment ratio B_{EZ}/B_{SM} , which also implies the same β . Given the typical evolution, the CBL with the weaker FA stratification is also capped by a weaker inversion Δb (e.g. Eq. 2.59). As a result it grows faster, as $w_e = -\beta/(\Delta b B_0)$. Our data show that for a given level of B_{EZ}/B_{SM} , S_{EZ}/B_{SM} is fixed as well (black points in Figure 4.4). Hence, $\Delta U \simeq \sqrt{S_{EZ}/w_e}$ must be smaller and in turn the CBL mean velocity $U = U_g - \Delta U$ larger. This implies stronger surface shear and surface-stress and thus a larger S_{SM} (blue dots) than for the slower growing CBL with a larger ΔU and smaller U (red dots).

The more general case (gray dots) could be rather elegantly studied by solving a fully prognostic CBL-ZOM, which would combine the entrainment model (NZO) that we develop in chapter 5, with a complete ZOM buoyancy- and momentum-budget,

¹²More precisely, the component of the momentum tendency parallel to \mathbf{U}_g is well > 0 , but also about proportional to the stress divergence. Its impact is therefore similar and comparable for all LESSs.

¹³It measures deviations from the direction of \mathbf{U}_g .

including a surface-stress model¹⁴.

Summary and conclusions. In our set of LES-CBLs we find a direct relationship between EZ shear-production and entrainment, which fully supports the basic approach of Conzemius and Fedorovich (2007). At the same time TKE production in the SM seems to be decoupled from entrainment. Without a further analysis at this point, we assume that this decoupling can be explained by the local character of shear induced turbulence and entrainment and therefore to be representative for well-developed BLs in general.¹⁵ It is also remarkable that this property seem to be completely independent of the composition of the turbulent forcing as our data set covers the range from purely convective CBLs to strongly sheared CBLs, where the total shear production is more than 16 times higher than buoyancy production (red dots in Figure 4.3). As we interpret the results of Jonker *et al.* (2013), also the entrainment dynamics of purely shear-driven BLs are only indirectly coupled to surface shear-production of turbulence via mean momentum transport¹⁶ (discussed in more detail in chapter 7.4).

Figure 4.3 also nicely indicates the basic solution to the problem posed by Moeng and Sullivan (1994), who suggested that only highly non-linear interactions of shear and buoyancy production can explain the dynamics of sheared atmospheric CBLs. This notion is indeed supported by our data (red dots). But Figure 4.3 also demonstrates that the observed ‘non-linearity’ of the relationship is simply caused by the large, essentially uncorrelated contribution of SM shear (blue dot), whereas scaled EZ shear-production (black dots) correlates well and – on the whole – linearly with CBL entrainment. Hence, our data set casts strong doubts on the numerous attempts to interpret mid-latitude ABL growth-dynamics via an extension of surface-layer scaling (Moeng and Sullivan, 1994, section 4(b, c) and citations therein), as long as a correlation between surface layer and EZ dynamics is not enforced by particular conditions (Figure 4.4, red and blue dots).

Finally, we note that Figure 4.3 or 4.4 only displays quantities that have been directly derived from ensemble-averaged turbulence statistics and by integration according to the natural CBL structure that is given by the CBL buoyancy flux. No further assumptions are made.

Non-linear effects. According to Figure 4.3 the relationship between EZ shear and entrainment is well-defined and approximately linear over the whole data range. However, a more detailed zoom (Figure 4.5) reveals a distinct local deviation from

¹⁴For a basic conceptual study, any simple surface drag model, should be sufficient. For an accurate representation of LES-CBL wind-dynamics a well tuned version of the MOS-based drag law, as used in Schröter *et al.* (2013) (see appendix E), combined with a model for directional shear is necessary. According to our experience the model of Arya (1977) works well, if slightly modified constants are used. Furthermore our LESs show a clear additional influence of momentum entrainment on directional shear. Preliminary tests indicate that a rather direct scaling of this effect is possible.

¹⁵This further suggest that in a mature BL the characteristic length scales for entrainment and surface related shear production should be significantly smaller than the CBL depth, as both SL and EZ do not spatially overlap. We come back to this feature in chapter 7.4.

¹⁶But note that for Jonker *et al.*'s (2013) idealized DNS-BLs the surface stress is the only external force. This means that TKE-dynamics, including entrainment can of course be explained by surface shear in all conditions.

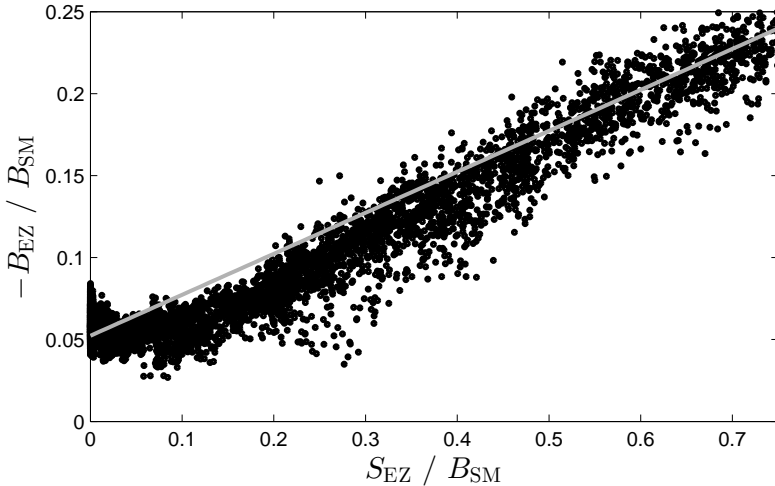


Figure 4.5: Dimensionless entrainment versus shear production in the EZ for all LES. Black dots: LES. Gray line: visual linear approximation.

linearity. We find that for moderate EZ shear-production ($S_{EZ}/B_{SM} < 0.5$) entrainment is significantly smaller than the approximately linear trend for $S_{EZ}/B_{SM} > 0.5$ would suggest (gray line). For weakly sheared CBLs ($S_{EZ}/B_{SM} \approx 0.1$) entrainment is about equal or even reduced compared the purely convective case ($S_{EZ}/B_{SM} = 0$). Such a local reversal of the general shear-enhancement (the latter is indicated by the gray line) has been observed by Fedorovich *et al.* (2001b); Pino and Vilà-Guerau de Arellano (2008) and discussed in Fedorovich *et al.* (2001b) before. Represented by a different but basically comparable ZOM variable, we already showed the same phenomenon in Figure 2.10. The impact on the evolution of CBL depth z_i can also be seen in Figure 3.4, where after 5 hours the significantly sheared CBL with $U_g = 10 \text{ ms}^{-1}$ grows slower than its shear-free counterpart. This effect is even more pronounced for the CBL with $U_g = 5 \text{ ms}^{-1}$, which is constantly shallower than the shear-free CBL (not shown here).¹⁷

4.1.4.2 Dissipation and TKE tendency versus EZ shear production

In this section we shortly present the shear-dependence of the integral dissipation rate. Most results are analogous to, or follow rather directly from our findings in the previous section, but they complete our picture of sheared CBL dynamics. For the purpose of budgeting, it makes sense to subdivide ε in a contribution ε_B that represents dissipation of TKE that was produced by buoyancy and a contribution ε_S

¹⁷In literature such a shear-induced reduction of the entrainment ratio is often associated with a turbulent phenomena called ‘shear sheltering’ (e.g. Hunt and Durbin, 1999). However, it remains unclear if, or to what extent, EZ turbulence of sheared CBLs can be compared to situations for which shear sheltering is actually documented (Fedorovich *et al.*, 2001b). As it turns out, we do not need to evaluate this concept. By simply completing our analysis of the TKE budget, we will automatically find a consistent explanation for the observed shear-induced deviation from a linear EZ-shear dependence of entrainment.

that represents the dissipation of TKE produced by shear. As with the production terms, ε_S can be further subdivided into a contribution related to shear in the surface- and the mixed layer (subscript SM) and one related to shear in the entrainment zone (subscript EZ). Thus

$$\varepsilon = \varepsilon_B + \varepsilon_S = \varepsilon_B + \varepsilon_{S,SM} + \varepsilon_{S,EZ}. \quad (4.16)$$

In the previous section we have demonstrated that for developed CBLs TKE that is produced by shear in the surface and mixed layer (by S_{SM}) does probably not contribute to entrainment. As TKE-spinup is also very small in the SM, it follows that TKE generated by S_{SM} must be dissipated completely within the CBL.¹⁸ Hence S_{SM} and $\varepsilon_{S,SM}$, which typically are very large terms, are in an immediate balance:

$$\varepsilon_{S,SM} \simeq -S_{SM}, \quad (4.17)$$

With respect to our entrainment problem we can therefore define an effective dissipation rate ε_e , which is given by

$$\varepsilon_e = \varepsilon - \varepsilon_{S,SM} = \varepsilon_B + \varepsilon_{S,EZ}. \quad (4.18)$$

The dependence of the above defined parts of ε on the EZ shear production is shown in Figure 4.6. Our whole data-set features a well-defined, quasi-linear, relationship between the CBL dissipation rate (black dots) and shear production in the EZ, as long we do not account for dissipation of surface related shear production (red and blue dots). This is analogous to, and a physical consequence of, what we found for the relationship between shear production and entrainment. Thus Figure 4.6 fully supports the assumption behind Eq. 4.17. Hence, with the focus on the EZ dynamics, we can exclude the contribution of TKE shear-production in the surface- and mixed layer (as well as its subsequent dissipation) from our further consideration. By inserting Eq. 4.16 and the balance, Eq. 4.17, into the budget equation Eq. 4.15 we get

$$1 + \frac{B_{EZ}}{B_{SM}} + \frac{S_{EZ}}{B_{SM}} + \frac{\Phi}{B_{SM}} + \frac{-\frac{\partial e}{\partial t}}{B_{SM}} + \frac{\varepsilon_B + \varepsilon_{S,EZ}}{B_{SM}} = 0. \quad (4.19)$$

With the definition of ε_e (Eq. 4.18) the TKE budget reads

$$1 + \frac{B_{EZ}}{B_{SM}} + \frac{S_{EZ}}{B_{SM}} + \frac{\Phi}{B_{SM}} + \frac{-\frac{\partial e}{\partial t}}{B_{SM}} + \frac{\varepsilon_e}{B_{SM}} = 0. \quad (4.20)$$

In section 4.1.3 we discussed the approximately complementary behavior of dissipation and the entrainment-related TKE spin-up. We now assume that the same reasoning holds for CBLs with additional shear production in the EZ. Thus, accounting for shear we redefine the antagonistic destruction term ε_a (Eq. 4.12) by using ε_e (Eq. 4.18) instead of ε :

$$\varepsilon_a := \varepsilon_e - \partial e / \partial t. \quad (4.21)$$

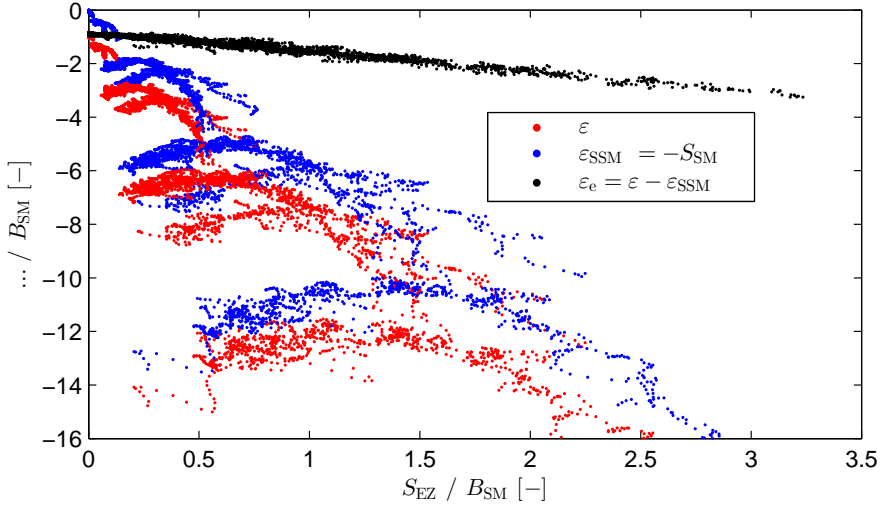


Figure 4.6: Dimensionless dissipation rates versus TKE shear production in the EZ for all LES. Red dots: total dissipation in the whole CBL. Blue dots: Dissipation of shear production in the surface and mixed-layer only. Black dots: Effective dissipation rate: total dissipation rate minus the dissipation rate of shear production in the SM.

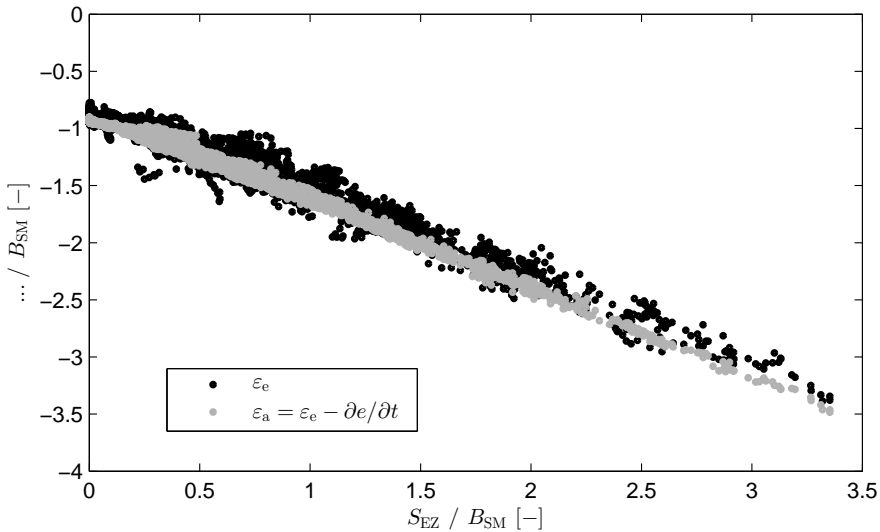


Figure 4.7: Dimensionless effective dissipation rate (black dots) and dimensionless antagonistic TKE-destruction (gray dots) versus shear production in the EZ for all LES.

Figure 4.7 supports this reasoning. Accounting for TKE spinup in ε_a (gray dots) leads

¹⁸A contribution of S_{SM} to the formation of gravity waves at the top of the CBL is also not plausible. See also the following section.

to an even clearer relationship with EZ shear production than for ε_e (black dots, previously also shown in Figure 4.6). However, we suspect that the reduction of scatter is not only caused by the systematic inclusion of the typical temporal evolution of $\partial e/\partial t$ for each LES (as in Figure 4.2), but also by compensating effects of complementary turbulent (or wave-induced, see later) fluctuations of ε_e and $\partial e/\partial t$, which are significantly enhanced by additional shear production. These fluctuations demonstrate the statistical limitation of our LESs. In principle, they are expected to decrease with increasing domain size.¹⁹ The observed complementary reduction of scatter also suggest a direct deterministic coupling between dissipation and TKE spinup, forming the main antagonists to TKE production (see discussion in section 4.1.3).

Generally, we find that ε_a is a simple and rather efficient means to approximately account for systematic contributions of $\partial e/\partial t$ in our data set. For the whole set of LES, Figure 4.7 indicates that in the average and over the whole range of EZ shear $|\varepsilon_a| > |\varepsilon_e|$, which demonstrates the significance of TKE spinup term in the early phase of each LES.

Incorporating ε_a into the integrated TKE-budget gives

$$1 + \frac{B_{EZ}}{B_{SM}} + \frac{S_{EZ}}{B_{SM}} + \frac{\Phi}{B_{SM}} + \frac{\varepsilon_a}{B_{SM}} = 0. \quad (4.22)$$

With respect to the dependence of ε_a on S_{EZ} , our LES data show a quite linear relationship over the whole range of data (Figure 4.7). Remarkably, for $S_{EZ} < 0.7$ we do not find an increase of $-\varepsilon_a$ above the overall linear relationship. Rather we can even recognize a slightly reduced growth of $-\varepsilon_a$ with S_{EZ} . This simply means that the reduced entrainment rate that we observe for weak and moderate EZ-shear (Figure 4.5) is not compensated by an equivalent increase of dissipation. Hence, as the TKE budget is closed we can simply conclude that the remaining wave-loss term ϕ must be important.

4.1.4.3 Shear induced TKE- and momentum drainage via gravity waves

Figure 4.8 shows the dependence of the normalized wave-induced energy-drainage $-\phi$ on the normalized EZ shear-production S_{EZ} for our complete data set. We find that even little shear strongly enhances the wave loss term (black dots) compared to a shear-free CBL. For $0 < S_{EZ}/B_{SM} \lesssim 0.15$ the wave losses grow sharply and approximately linearly from 0.02 to about 0.08. For stronger shear, wave-losses remain rather constant as our data scatters in a band between 0.03 and 0.1. In a region with weak shear the signal is quite sharply defined but for $S_{EZ}/B_{SM} > 0.15$ scatter becomes relatively strong. However, scatter seems to be mostly randomly distributed around a common mean ($-\phi/B_{SM} \approx 0.06$) as can be seen in the similar Figure 4.9, where each single LES is represented by a different color. This indicates that the shown relationship is rather well-defined, but somewhat obscured by the limited statistical representation of the wave structures in our LES. Figure 4.8 also shows that the turbulent part of the integral TKE-flux divergence (red dots) is ≈ 0 (Eq.4.2) and only a finite pressure correlation term (Eq. 4.3), representing wave transport, remains (black dots). This proves that we have correctly integrated the TKE transport terms over the complete turbulent layer.

¹⁹With respect to the potential significance of statistical errors for the forecast of real ABLs we note that our LES domains are already rather large, e.g. 25 km x 25 km for the wide-domain LESs.

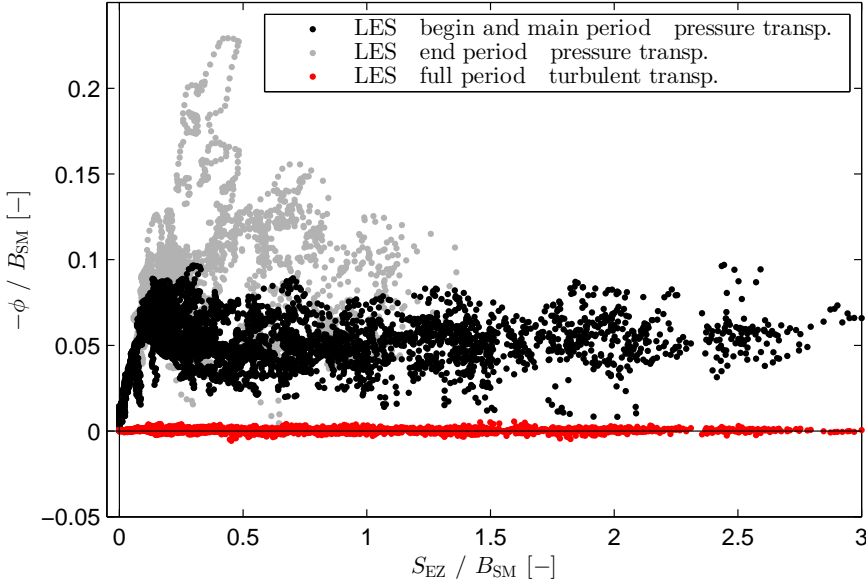


Figure 4.8: Dimensionless losses of fluctuation energy via gravity waves at the CBL top versus dimensionless shear production in the EZ for all LES. Black dots represent all data, except the late simulation phase for LES with moderate shear, which are marked by gray dots. Red dots represent the integrated turbulent transport term.

Grey dots in the same Figure also show the disturbed data from the end phase of many LESs (see chapter 3.3 and Figure 3.1). In this phase the wave-field close to the top of the deep CBLs starts to interact directly with the nearby sponge-layer, which results in a sudden onset of excessive energy drainage, far above the general level that we find for all other data (black dots). These data are excluded from our further analysis.

To get a clearer impression of the behavior of the wave losses at moderate shear, we once more show the shear dependence of $-\phi/B_{SM}$ in the following Figure 4.10. This time however the ordinate displays shear production in terms of a dimensionless velocity scale. As this quantity is very useful also later on, we explicitly call it

$$S_* = \left(\frac{S_{EZ}}{B_{SM}} \right)^{1/3} = \left(\frac{v_*^3}{w_*^3} \right)^{1/3}, \quad (4.23)$$

where $w_* \simeq (2 B_{SM})^{1/3}$ is the convective velocity scale, which has already been introduced (Eq. 2.35). The corresponding velocity scale for the EZ-shear production is

$$v_* = (2 S_{EZ})^{1/3}. \quad (4.24)$$

Figure 4.10 even more clearly (than Figure 4.8) indicates the transition at $S_* \approx 0.5$ between a moderate-shear regime with well-defined growth of wave-losses, and a strong-shear regime where the wave losses scatter around an approximately constant

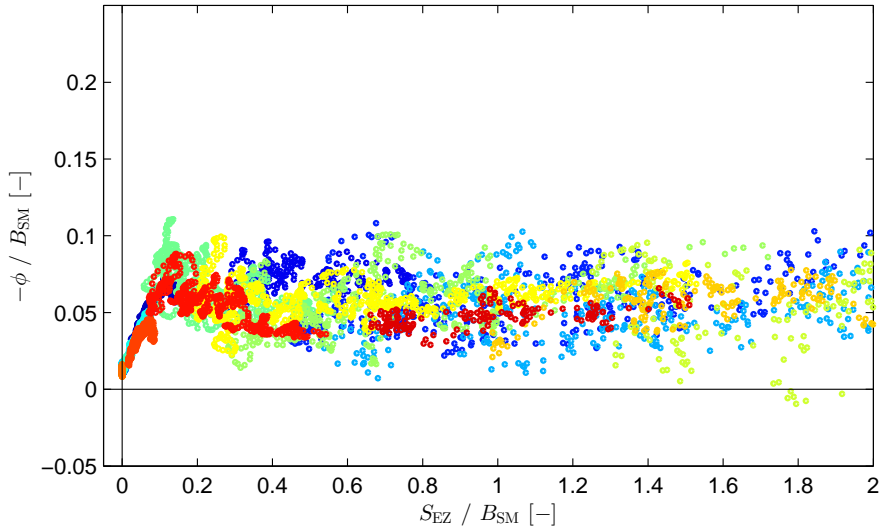


Figure 4.9: Dimensionless energy-losses via gravity waves at the CBL top versus dimensionless shear production in the EZ for all LES-CBLs in the equilibrium entrainment regime. Each LES is represented by a different color.

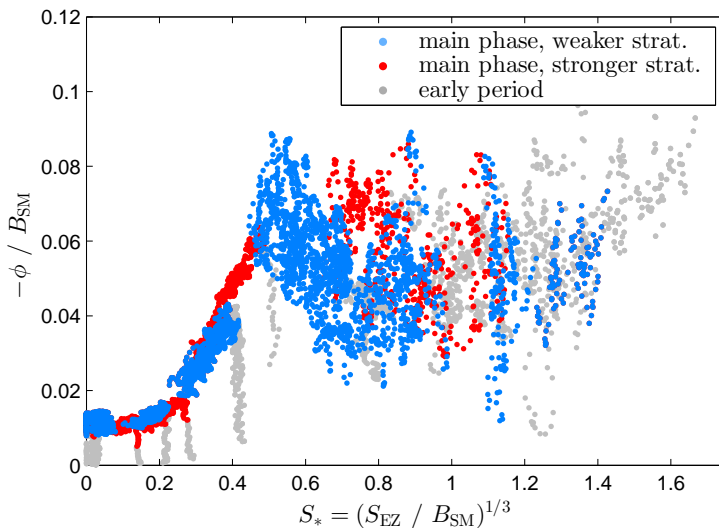


Figure 4.10: Wave energy leakage ϕ normalized by the buoyancy production term B_{SM} as function of S_* .

level. The Figure further shows that the data of CBLs with the stronger (red dots) and the weaker FA-stratification (blue dots) agree rather well, which supports the choice of scales. Data from the early phase of the CBL evolution (gray dots) further show that for weak and moderate shear ($S_* < 0.5$), the maturity of the CBL seems relevant,

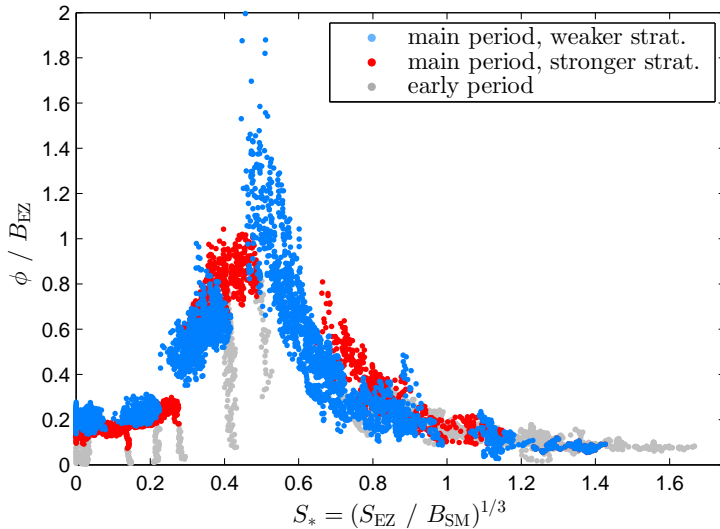


Figure 4.11: As Figure 4.10, but this time ϕ is normalized by the integral entrainment term B_{EZ} .

as $-\phi/B_{EZ}$ does not reach the characteristic level before equilibrium entrainment conditions are met (blue and red dots). For the strong shear, however, we do not see a clear influence of CBL evolution.

Generally, our LESs suggest that wave energy-losses play a significant role in the TKE budget of sheared LES. With respect to our basic question of how to understand and quantify the influence of shear on CBL growth and entrainment, we can specify the significance of ϕ by comparing it with the entrainment term B_{EZ} . Hence we consider the relationship ϕ/B_{EZ} versus S_* . This is shown in Figure 4.11, which is otherwise identical to Figure 4.10. We find that at a peak around $S_* = 0.5$ the wave energy-loss term is about equal to entrainment. And for the whole range of $0.3 < S_* < 0.7$ it is still larger than half the size of entrainment. Hence it is easy to imagine that shear-induced TKE losses via gravity waves have a significant influence on the entrainment rate and may explain the reduction that we observe for moderate shear. We will evaluate this idea further in the following sections.

Another phenomenon that is directly linked to EZ shear and FA gravity waves, is a significant momentum transport downwards from the FA into the CBL. As the stratified FA is not turbulent ($B_z = \overline{w'b'_z}(z > z_{iu}) \approx 0$), the observed momentum flux must represent wave stress. Thus we define

$$\overline{w'U'}_{FA} = \left[\overline{w'u'^2}_{FA} + \overline{w'v'^2}_{FA} \right]^{1/2}, \quad (4.25)$$

which is the magnitude of the momentum flux at the height z_{FA} somewhere in the FA above the turbulent CBL, with, e.g., $z_{FA} \approx 1.2 z_{iu}$.²⁰ The stress divergence in the LES-FA is typically very small. Therefore it does not matter at what height exactly

²⁰The modulus enforces positive values, but for clarity we note that FA momentum transport is generally directed downwards.

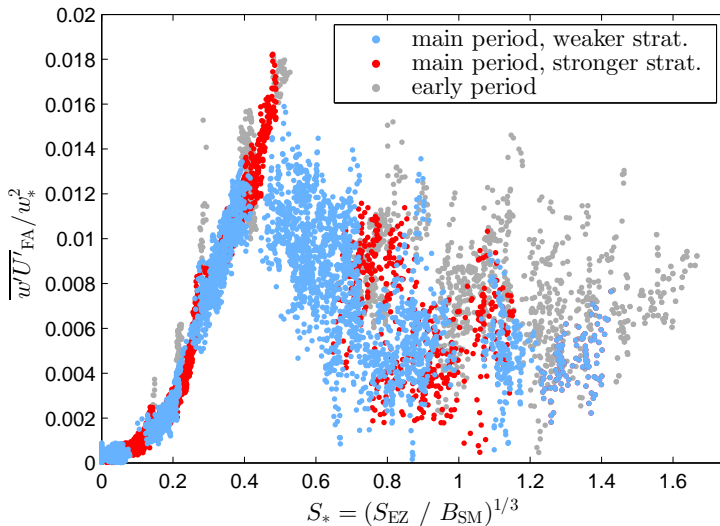


Figure 4.12: Dimensionless wave-stress in the FA as function of the dimensionless TKE shear production in the EZ.

we diagnose the wave-stress from our LES, as long as we are sufficiently far above the turbulent boundary layer.

We straightforwardly assume a basic analogy to the wave-loss term and normalize FA wave-stress by the integral buoyancy production. To get correct dimensions we normalize $\overline{U'w'}|_{\text{FA}}$ with w_*^2 . The resulting dependence on S_* is shown in Figure 4.12. We find a rather similar pattern as for wave energy-losses, with a well-defined sharp increase for moderate shear which peaks at $S_* \approx 0.5$. For stronger shear wave-stress decreases to a constant level of ≈ 0.05 at $S_* \approx 1$. Scatter is strong, but the mean is clearly positive. Physically the scaling with w_*^2 and the well-defined dependence on S_* reflects the fact that the wave momentum-flux is interlinked with the wave energy flux. Therefore it does not, as one might expect, scale well with the entrainment flux of momentum (EZ stress), as, e.g., given by $\overline{w'U'}_{z_i}$ or the ZOM expression $w_e \Delta U$. Also attempts to replace the steering quantity S_* by a measure based on the momentum flux, e.g. $\tau_*^2 = w_e \Delta U / w_*^2$, were not successful.²¹

However, to get an impression of the actual relevance of CBL driven wave-stress in our LESs, it still makes sense to compare it with the entrainment flux and consider its dependence on shear. The relative importance of wave stress, expressed as $\overline{U'w'}_{\text{FA}} / (w_e \Delta U)$ is shown versus S_* in Figure 4.13. It demonstrates that the wave stress can be quite significant for moderately sheared CBLs. For $S_* \approx 0.3$ we find that the wave stress becomes of the order of 40% of the entrainment flux. Note that these values represent CBLs with a pressure forcing of e.g. $U_g = 10 \text{ ms}^{-1}$, a CBL depth $z_i < 1200$, m and a surface heat flux of about 76 Wm^{-2} , which is not atypical for ABLs.

²¹We can further interpret this observation by anticipating the ZOM expression for S_*^3 (see section 5.1.2.2), which reads $S_*^3 \approx 1/2 w_e \Delta U^2 / w_*^3$. Hence $\tau_*^2 = 2S_*(w_* / \Delta U)$, which implies that the factor $w_* / \Delta U$ controls the relationship between the momentum entrainment and wave stress.

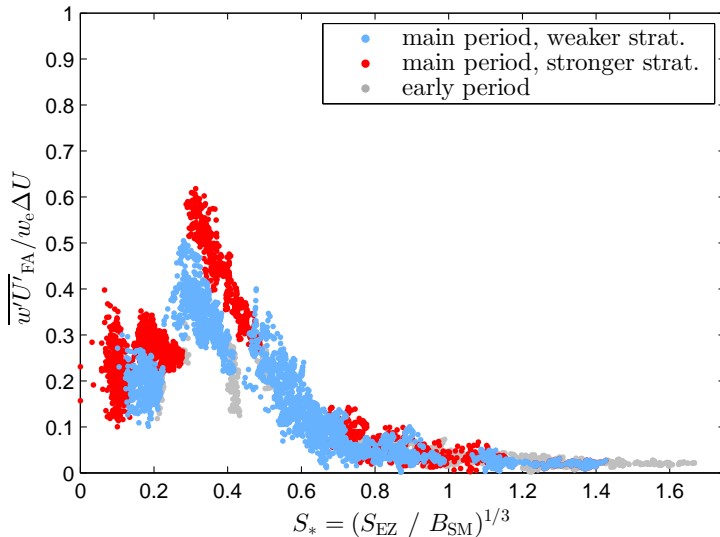


Figure 4.13: Dimensionless wave-stress in the FA versus S_* . Differently to Figure 4.12, the FA wave-stress is normalized by the ZOM entrainment flux of momentum.

Dynamical effects of CBL-induced FA waves in literature. It is remarkable that in the literature on sheared CBLs ϕ as well as $\overline{U'w'_{FA}}$ have either been considered to be negligible or have been ignored due to a lack of trustworthy data or other empirical evidence. For instance, FA wave-transport does not play a role in any of the entrainment models that have been evaluated by Conzemius and Fedorovich (2006b). It is even more remarkable that in all previous LES studies that we are aware of, wave energy-losses of sheared CBLs were generally considered to be negligibly small. However, in none of those studies the insignificance of wave energy-losses for sheared CBLs was actually shown, but merely assumed, referring to literature on non-sheared CBLs (e.g. Stull, 1976b; Fedorovich *et al.*, 2004b). This means that the data used in these studies do not coercively have to contradict our LESs. Rather there are reasons to suspect that the LESs used in these studies would basically agree with our data. Hence, we suppose that if the pressure transport term would have been retrieved, similar wave energy-losses would have been diagnosed for comparable LESs. In this respect the following note may be of interest.

- The LES code used by Pino *et al.* (2003, 2006a,b); Pino and Vilà-Guerau de Arellano (2008) is identical to our code. Figure 7 in Pino *et al.* (2003) even shows a small but positive pressure transport term within the FA, which represents wave-drainage of TKE. Furthermore, Pino and Vilà-Guerau de Arellano (2008) observe a similar reduction of the CBL growth-rate for moderate shear as we do, which points to a similarly significant wave energy-losses.
- Conzemius and Fedorovich (2006a, 2007), using the University of Oklahoma (OU) code (Fedorovich *et al.*, 2004a) for their LESs, focus on strongly sheared

CBLs. For such cases with $S_{EZ}/B_{SM} > 1$ the wave energy-loss may well be significant but it is also about constant (Figure 4.9) and small compared to the entrainment term (Figure 4.11). Thus, if not explicitly considered, the wave energy-loss term might easily be overseen and its contribution attributed to other terms in the TKE budget.

- It seems that LES of sheared CBLs are typically characterized by significant wave stress in the FA. We have reports about such observations for LES-CBLs produced by the code of the National Center for Atmospheric Research (NCAR)²², which was also used by the cited studies of Moeng and Sullivan (1994) and Kim *et al.* (2003, 2006). The same holds for CBLs produced by the OU LES-code, by the PALM LES-code and by the MicroHH LES-code²³.
- The LES-code DALES 3 that we use is very similarly constructed as several other LES-codes and performed well in an inter-comparison study of sheared LES-CBLs (Fedorovich *et al.*, 2004a).

But there are further important arguments that support the significance of our observations. The generation of gravity waves by turbulence in stratified shear-layers seems to be a quite prevalent fluid-dynamical phenomenon. Several studies, based on numerical experiments as well as on real physical flow experiments, show that adjacent to a stratified layer different types of sheared, turbulent flows can systematically induce internal gravity waves (e.g. Strang and Fernando, 2001; Taylor and Sarkar, 2007; Pham *et al.*, 2009). Their dynamical feedback on the flow can be strong and, depending on stability, significantly impact on entrainment (e.g. Strang and Fernando, 2001).

Moreover, shear-induced internal gravity waves and the related energy and momentum transport are an important process in the atmosphere. Besides the well-known and much studied gravity-wave that are induced by flow over orography, also gravity-waves created in a fluctuating, sheared environment are found to be relevant. Most interesting here is the creation of gravity waves by cloud convection (Cumulus and Cumulonimbus convection). Cloud convection often occurs in combination with significant atmospheric shear. It is known that the intrusion of cloud convective plumes into a sheared, stably stratified atmosphere generates gravity waves associated with considerable vertical transport of fluctuation energy and momentum. This phenomenon can frequently be observed for deep convective plumes (tropical thunderstorms) as well as cumulus convection and has been confirmed and investigated by several studies (citations in Song *et al.*, 2003; Beres, 2004). The contribution to the transport of energy and momentum within the atmosphere, both within the troposphere and between troposphere and stratosphere, is significant and therefore parametrized in advanced General Circulation Models (GCMs).

In literature a number of mechanisms for the observed wave dynamics have been proposed, of which two are relevant here. In the most simplistic view, convective clouds in a layer with deviating horizontal velocity were considered to form an obstacle that blocks the flow similarly as studied for orographic undulations, which would result in a standing wave relative to the cloud's velocity. These conceptual 'clouds'

²²Personal communication with Ned Patton (NCAR).

²³This code was used to generate the independent reference case, presented in appendix D

have therefore been denoted as ‘moving mountains’ (Song *et al.*, 2003). However, as the vertical momentum of the cloud seems to be in the order of that of the wave, this explanation was modified and cloud convection more realistically considered as a mechanical oscillator, which enforces waves in the stably stratified atmosphere. If the basically vertically moving clouds enter into a surrounding with a different horizontal velocity, the net contributions of the horizontal fluctuation components become significant, which leads to a net transfer of the cloud’s kinetic energy and momentum into the wave field (Song *et al.*, 2003).

Despite the scale differences in the real atmosphere, the basic similarity between a rising Cumulonimbus cloud and a single penetrating CBL-thermal seems obvious. Hence, we imagine that the above-mentioned mechanism also describes the wave-leakage that we observe above cloud-free, moderately sheared CBLs (see also section 7.4.2) and consider it as a conceptual starting point for further investigations.

Summary. Previous LES studies of sheared CBLs largely ignored the impact of shear on the formation of external gravity-waves at the upper flow boundary and therefore did also not consider the influence of gravity waves on the TKE budget. However, our analysis indicates that gravity-wave transport results in significant leakage of TKE out of the CBL, and an inflow of momentum, if the EZ is moderately sheared and the CBL is well developed. This wave-driven exchange between CBL and FA occurs very persistently in our LES data set.²⁴ Thus, we assume our findings to be basically representative. However, ultimate certainty can only be gained with improved experiments, particularly with future high resolution LES or DNS.

4.1.4.4 Entrainment-zone structure of sheared CBLs

Analogously to non-sheared LES-CBLs (Figure 3.9) we here depict the EZ structure of the sheared CBLs and show its shear-dependence in Figure 4.14. This Figure is rather informative and allows to discuss several aspects of sheared CBLs that guide our further analysis.

For the relative ZOM EZ depth z_i/z_{i1} we find a rather well-defined relationship for the well-developed stages for all of our LES types. z_i/z_{i1} rarely depends on resolution or domain size. During the main phase (equilibrium entrainment regime), the typical constant layering of the CBL only depends on the relative EZ shear S_* . For $z_{i,g}$ some systematic overestimation in the early main phase is probably caused by a too low spatial resolution (as discussed in chapter 3.4.2). Accordingly, deviations from a smooth correlation seem to be more severe in conditions with weak shear, where the EZs are shallower and therefore less well-resolved. For z_{iu}/z_{i1} , which is a less well-defined quantity, these computational distortions are even more pronounced and also noticeable for stronger shear. However, due to the influence of δ on $z_{iu} \sim z_{i,g} + \delta$ we also should not expect the same ideal behavior as for z_i and $z_{i,g}$ (since δ is dependent on the maturity of the CBL).

The EZ structure and the ZOM approach. The well-defined shear dependence of the CBL layering as defined by z_i/z_{i1} means that a ZOM for sheared CBLs exists

²⁴We also find the same pattern in an independent LES with higher resolution (appendix D). See the analysis in the following section and compare Figure D.1 with Figure 4.18.

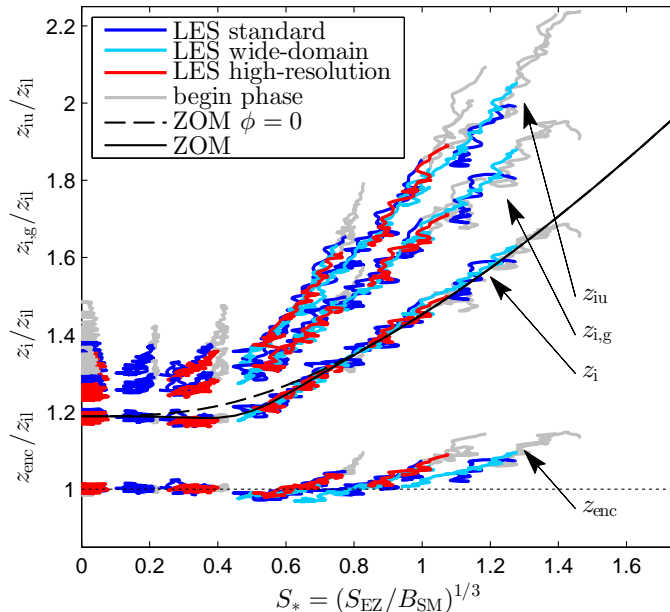


Figure 4.14: Shear dependence of the CBL structure, defined by the height of the minimum buoyancy flux z_i , the height of the maximum buoyancy gradient $z_{i,g}$ and height of the CBL-top $z_{i,u}$. These are all normalized by the depth of the mixed layer $z_{i,l}$, which is given by the height where the buoyancy flux changes sign. Different types of LES, but only cases with the moderate FA stratification are shown.

and that the ZOM entrainment ratio $\beta = z_i/z_{i,l} - 1$ (Eq. 2.57) only depends on S_* . Accordingly, sheared CBLs with $S_* = \text{const}$ would be also characterized by $\beta = \text{const}$. This further implies that the time evolution of the CBL depth would follow the same type of square root growth law that characterizes the non-sheared case (Eq. 2.64), just with a significantly larger growth rate if $S_* > 0.6$.

Hence, using the appropriate ZOM expressions for β and S_* , we could already at this stage try to construct an appropriate ZOM (black line).²⁵ As later shown in chapter 5.4, it turns out that a ZOM is given by a simple linear relationship between β^2 and the integral shear production term S_*^3 (Figure 5.8).

Note that we also find a significant impact of TKE wave-losses on the EZ structure, as indicated by the difference between the solid and dashed black lines in Figure 4.14. In principle, there is no obvious physical reason why one could not also determine the contributions of wave energy drainage within the ZOM framework, which has the advantage of explicitly representing the simpler quasi-stationary character of the equilibrium entrainment regime.²⁶ However, experimentally we found it to be easier to

²⁵Our previous findings and Figure 4.14 strongly suggests that also for a ZOM, the Eulerian partitioning of the buoyancy flux (EP), which is based on $z_{i,l}$ instead of z_i as a length scale for buoyancy production, is crucial.

²⁶As argued before, the uniform ZOM buoyancy profile ‘corrects’ for remaining instationarity that are caused by continuous change of the buoyancy profile of constantly layered CBLs.

first investigate and specify the TKE wave-losses based on the integrated TKE-budget. We therefore continue on the chosen path and first parametrize the TKE-budget of our data set, using the integrated quantities (what we called submodel 1), before we make the transfer to a ZOM in a following step (what we called submodel 2).

Encroachment in sheared CBLs. With enhanced entrainment, encroachment (section 2.5.4) becomes less representative for the SM buoyancy evolution. Particularly for situations with stronger shear, the entrainment ratio far exceeds that of the shear-free CBL and entrainment contributes significantly to SM warming and growth (Figure 2.4, Eq. 2.68). Nevertheless, as long as S_* is constant in time, β is constant as well and the above mentioned relationships hold and encroachment scales z_{enc} and b_{enc} are in principle representative for the CBL (via Eq. 2.64 and Eq. 2.68).

However, mid-latitude ABLs, as represented by our LES-CBLs, are driven by a rather complex shear regime, where S_* continuously decreases. S_* follows a non-trivial course (Figure 4.3), which leads to varying contributions of entrainment to SM buoyancy evolution. As a result, a mature CBL has a ‘complicated’ warming history²⁷ and therefore its instantaneous state, given by b or z_{il} , is not any more well represented by b_{enc} or z_{enc} respectively. This can be clearly seen in Figure 4.14, which not only shows that $z_{\text{enc}}/z_{\text{il}}$ increases above unity for $S_* > 0.5$ but also that each case follows an individual evolution and systematically deviates from a simple correlation with S_* .

On the other hand, even for our strongly sheared case, the contribution of entrainment to SM warming is only significantly enhanced in the earlier half of the LES (as e.g. shown by Figure 2.4, which is a snapshot in the early phase of the strongest sheared case). In the later stages of the LESs these effects are quite moderate and $z_{\text{enc}}/z_{\text{il}}$ becomes roughly unity (Figure 4.14). As indicated by Eq. 2.68 and 2.67, b_{enc}/b or $z_{\text{enc}}/z_{\text{il}}$ should not be very sensitive to the variation of β that we find in our data, although the range is quite substantial ($\beta \approx 0.2 \dots 0.7$). Therefore $z_{\text{enc}}/z_{\text{il}}$ varies rather little within our series of CBLs, even though the variations in the EZ depth are tremendous (Figure 3.4 or 3.6). However, towards more ‘neutral’ cases, the relative importance to entrainment for the CBL buoyancy dynamics further increases, until it becomes the only source for warming in the ‘neutral limit’.

4.2 Parameterizing the integral TKE-budget of sheared CBLs

4.2.1 General considerations

Recapitulation of previous findings. In this section we want to further specify our picture of the TKE dynamics for sheared CBLs. Before continuing our analysis, we shortly recapitulate and discuss the previous findings to provide a clear foundation for our further reasoning. Our main objective is the dependence of the entrainment ratio $-B_{\text{EZ}}/B_{\text{SM}}$ on the composition of the TKE-production. i.e. the relative importance of EZ shear, given by the ratio $S_{\text{EZ}}/B_{\text{SM}} = S_*^3$.

²⁷In its basic form encroachment is defined as the time integral of the surface driven CBL warming (section 2.5.4).

The data analysis in the previous sections revealed a basic linear dependence of entrainment and dissipation on both buoyancy production and shear production. Hence, the effects of both types of forcing, buoyancy and shear, appear to be largely independent. The entrainment dynamics of our LES-CBLs therefore resemble Kolmogorov’s model of idealized turbulence (as expressed by Eq. 2.13). However, in order to ‘recover’ this similarity between idealized isotropic turbulence and the highly anisotropic sheared CBL, it was necessary to identify the relevant TKE-production regions, which are the SM for buoyancy production and the EZ for shear production. Finally, we also observe systematic deviations from the underlying linear scaling behavior, for which we found two different causes.

The first cause is the instationarity of the TKE budget, as represented by TKE-spinup term (section 4.1.3.2). Initially the TKE-tendency is an important term, but upon maturing of the BL the growth rate decreases and with that the entrainment of non-turbulent air that needs to be ‘turbulized’. Hence, relative to other budget terms, the TKE tendency becomes less important.

To specify the basic shear-effects on the dynamics of entrainment and dissipation one would therefore prefer to exclude contributions of TKE-spinup and e.g. consider asymptotically stationary CBLs (with $\delta/z_{il} \mapsto 0$). But experimentally these conditions are difficult to create and in our data set the TKE-spinup term is significant throughout. Thus, to reduce its signal we only consider CBLs in the ‘pragmatic equilibrium-entrainment’ regime²⁸. Here the integral TKE-spinup term is still significant but it does not vary much anymore and is also comparable for all our cases. Furthermore, our results suggest, that the remaining TKE-spinup mostly affects the much larger dissipation term and less so entrainment. Thus, practically, we can assume ‘quasi-stationary’ condition in the following analysis focusing on entrainment. For final clarity we shortly come back to this assumption at the end of this section, before we lift the assumption and explicitly investigate the instationarity and the effect of CBL evolution on the dynamics in the entrainment zone in chapter 6 in detail.

The second cause for a non-linear response of entrainment and dissipation on EZ shear-production is the additional loss of TKE via gravity waves. This process is significant for moderate values of EZ shear (Figure 4.5) only. In contrast, for pure CBLs, TKE wave-losses are generally negligible (chapter 4.1.3), which holds for the purely shear-driven, neutral BL as well (Jonker *et al.*, 2013). Thus wave-losses depend on the composition of the turbulence sources and therefor are the central issue in the following analysis. TKE wave-losses and the deviations from a linear dependence of entrainment on TKE production demonstrate that the production mechanisms of TKE related to buoyancy and EZ-shear are dynamically not fully independent and in fact do interact.

Quantitative approach. To parametrize the shear-dependence of the integral dissipation and entrainment rate of our LESs we retain the common linear scaling approach, which represents an ideal superposition of the contributions of shear and buoyancy. But to account for deviations related to wave-induced energy losses we

²⁸What we called the ‘main period’ of our LES-CBLs (chapter 3.3). Here $\delta/z_{il} \approx 0.05 \dots 0.12$, as specified in chapter 6.

include an additional reduction terms (ϕ_B for entrainment, ϕ_ε for dissipation):

$$-B_{EZ} = c_{B,0} B_{SM} + c_{B,S} S_{EZ} + \phi_B, \quad (4.26)$$

$$-\varepsilon_a = c_{\varepsilon,0} B_{SM} + c_{\varepsilon,S} S_{EZ} + \phi_\varepsilon. \quad (4.27)$$

Here $c_{B,0} \simeq 0.054$ (Eq. 4.7) and $c_{\varepsilon,0} = 1 - c_{B,0} \simeq 0.946$ are the scaled entrainment rate and dissipation for the shear-free CBL as presented in section 4.1.3. $c_{B,S}$ and $c_{\varepsilon,S} = 1 - c_{B,S}$ are constants, that yet have to be determined (recall that the sum of Eqs. 4.26 and 4.27 represents the total scaled TKE-budget). Due to a closed budget

$$\phi_\varepsilon + \phi_B = \phi. \quad (4.28)$$

Given the well-defined dependences of ε , B_{EZ} and ϕ on EZ-shear, S_{EZ} , we can assume the same for both components of ϕ . Thus

$$\phi_\varepsilon = f_1(S_{EZ}) \quad \text{and} \quad \phi_B = f_2(S_{EZ}). \quad (4.29)$$

Apart from the somewhat abstract reference to idealized turbulence in the spirit of Kolmogorov, the choice of a linear relationships plus a correction term (Eqs. 4.26 and 4.27) also seems to be the most obvious and simplistic formulation of the problem from a practical point of view. Below we argue that the observed non-linear pattern can indeed be interpreted as a deviation from a reference flow with simpler linear dynamics.

The sketch in Figure 4.15 summarizes the previous findings of the integral TKE dynamics and shows the suggested scaling (Eqs. 4.26 and 4.27) schematically. As before, all quantities are normalized by B_{SM} . The small panel shows the total TKE production as a function of the shear production. The integral TKE production $B_{SM} + S_{EZ}$, as shown by the area under the gray line, is exactly balanced by the sum of all TKE sink terms, that are shown in the large panel. Here the dissipation rate²⁹, by far the largest term, is represented by the black hatched area and entrainment by the red cross-hatched area. The white area in-between represents the wave energy-losses. In order to illustrate the peculiarity of the shear-dependence of ϕ qualitatively, its shape and magnitude are exaggerate and not drawn to scale. The blue line depicts our linear scaling approach. It separates ϕ in ϕ_B and ϕ_ε .

Note that if we interpret ϕ_B and ϕ_ε as ‘reduction terms’ for B_{EZ} and ε respectively, we then just compare the actual composition of the TKE sink terms to the postulated linear scaling (blue line). This linear scaling would represent a similar, but more simple and archetypal flow, that would not be affected by wave-induced energy drainage. On the other hand, when we consider the TKE budget of our data set, it simply appears that wave energy drainage is a given and essential element of the sheared CBL and thus could be considered as equally characteristic as the other processes.

Except for the convective limit ($S_{EZ} = 0$), where wave activity is negligible, the

²⁹We here use ε_a , which also contains the integral TKE tendency, just for formal reasons as it roughly approximates the stationary limit and enforces a closed budget. However, the small differences with the actual dissipation rate ε_e are not relevant.

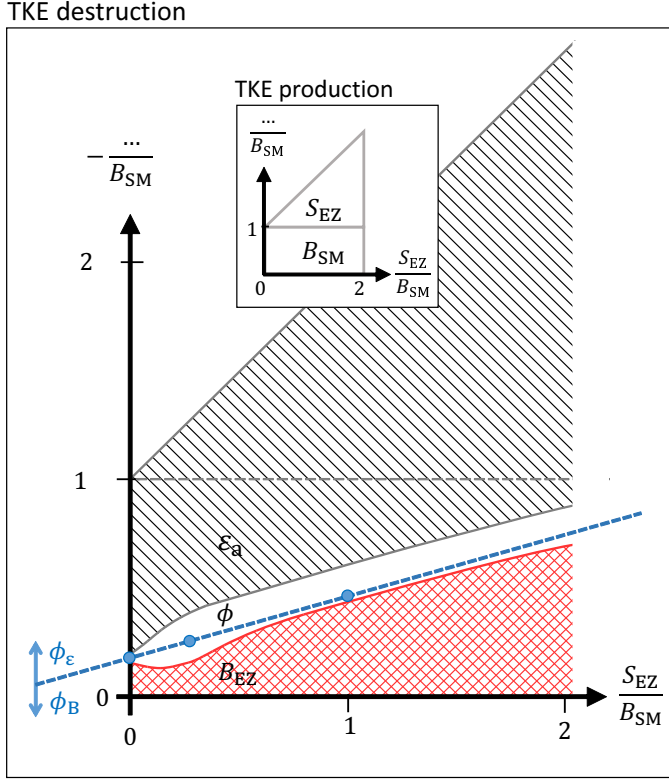


Figure 4.15: Schematic representation of the dimensionless TKE budget. Small panel: TKE production terms. Large panel: TKE loss terms. The blue dashed line represents the traditional linear scaling approach, separating the two components of ϕ .

course of the blue line is unclear.³⁰ If we assume that the occurrence of wave losses only results in a reduction of entrainment and dissipation, and does not redistribute net TKE between both terms, then $-\phi_B \geq 0$ and $-\phi_\varepsilon \geq 0$ and we can at least conclude that the blue line must be located within the white area.

4.2.2 A simplified reference flow: sheared CBLs under a neutral free atmosphere

Necessity of a reference flow. To also empirically justify the concept of a linear scaling and to estimate the respective parameters, one would need to compare our CBLs to a reference flow of which the dynamics would **not** be influenced by wave-

³⁰The neutral limit ($B_{SM} = 0$, $S_* = \infty$), where $\phi = 0$ as well, should offer a second anchor point. But when we made the analysis for this chapter, we did not yet know how to reconcile our approach with the TKE budget of neutral BLs (as e.g. given in Jonker *et al.*, 2013). Particularly, it was unclear how to define S_{EZ} and S_{SM} . Thus we were not really sure, if and how our CBL scaling could be applied in the neutral limit. The actual solution requires some further considerations and is therefore presented separately in chapter 7.3.3.

induced energy losses. At the same time this reference flow should be sufficiently similar to the ‘atmospheric’ type of sheared CBLs under investigation in all other important aspects. As the stable FA stratification is the essential condition for the formation of gravity waves one could consider a sheared CBL under a non-stratified, neutral, FA (NFA) as a potential approximation for such an idealized reference. A neutral FA would prevent the formation of gravity waves at the EZ top and thereby the escape of TKE from the CBL. But to retain a well-defined and confined entraining CBL, a capping inversion at the top of the turbulent layer needs to be present. Thus, inspired by Strang and Fernando (2001) who made an analogous experiment with pure shear-layers, we conducted some LESs of sheared entraining CBLs under a neutrally stratified FA (NFA). After several unsuccessful test simulations, two of these NFA LES turned out to be at least partly successful.

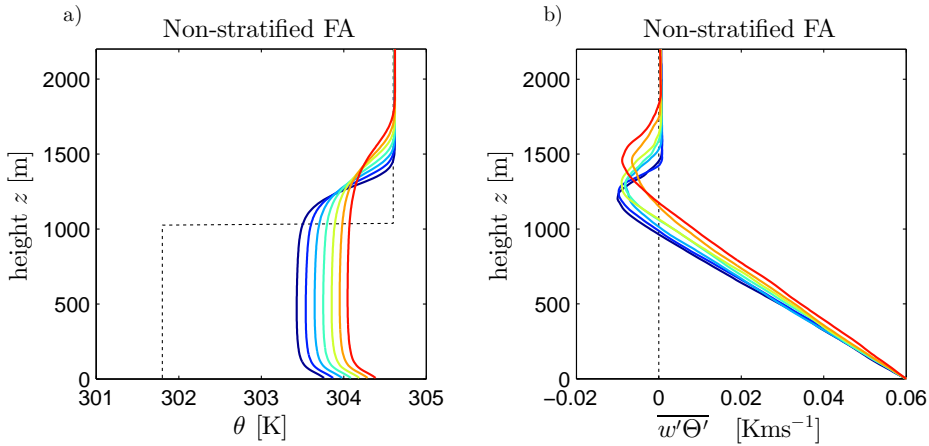


Figure 4.16: LES with neutrally stratified free atmosphere (NFA) and $U_{\text{geo}} = 10 \text{ ms}^{-1}$. a) Half-hourly profiles of potential temperature. Black dotted line shows the initial profile. b) Half-hourly profiles of the kinematic heat flux.

LES-CBLs beneath a neutrally stratified free atmosphere (NFA). The two NFA cases, based on two of the wide-domain LES, are initialized as follows. A step-like, relatively strong, inversion of 3.8 K separates a neutrally stratified upper layer from an equally neutral bottom layer (about 1000 m deep, Figure 4.16). The two NFA cases differ in the pressure forcing, with $U_{\text{geo}} = 10 \text{ ms}^{-1}$ for the first and $U_{\text{geo}} = 15 \text{ ms}^{-1}$ for the second NFA case. Furthermore, the initial wind velocities within the bottom layer are derived from the corresponding ‘atmospheric’ LES-CBLs, when they had reached about the same depth. Also the Coriolis forcing and surface heating agree with the corresponding atmospheric LESs.

With the onset of surface heating, convection fills the bottom layer and a CBL with turbulent EZ around the capping inversion develops. But different to the CBL with a stratified FA, where continuous entrainment maintains a certain inversion strength, the inversion at the top of a NFA-CBL continuously decreases until it finally disappears. At that instant the CBL in the bottom layer completely mixes with the

layer above.

The NFA-setup did not serve its intended role without problems and we needed several attempts to get useful simulations. Even in the initial state with a pronounced inversion, some parcels, probably with a buoyancy in excess of the FA, penetrate the inversion, drain TKE out of the CBL and cause some undesired convective mixing in the FA.³¹ Obviously the probability for such events depends on the distribution of positive temperature deviations in ML-thermals relative to the strength of the inversion. In some conditions these seemed to be rather strong in the spin-up phase of LES turbulence. But finally – and despite the strong transitional character of the NFA LES – we could in both NFA simulations identify a closed period of at least $2^{1/2}$ hours that seemed suitable for our purpose (Figure 4.16).³² During this period the combined TKE losses by pressure fluctuations and turbulent diffusion at CBL top are at least one order of magnitude smaller than the wave-energy loss of comparable simulations with stratified FA.

For these selected periods the buoyancy structure of the NFA CBLs basically agrees with conventional CBLs, as illustrated by Figure 4.16. And apart from the missing wave-loss term, the integral TKE-dynamics of the NFA CBLs mostly resembles the one of the CBLs with a stratified FA. In particular, this also holds for the TKE-tendency (later shown in Figure 4.22). Interestingly, even the relative depth of the upper EZ layer $\delta/z_{i1} \approx 0.06\dots 0.13$ varies in the same range as it does for the conventional CBLs, which indicates a general resemblance of the EZ structure. Hence, based on these similarities of the integral dynamics, we consider both NFA LESs as appropriate experimental approximations for an entraining sheared CBL, that is not affected by TKE drainage at the upper boundary.³³

4.2.3 Scaling the integral TKE budget of sheared CBLs

The scaled TKE-budget including the linear limit. The TKE-sink terms of various LESs with a stratified FA, in combination with both academic NFA-LESs, are displayed in Figure 4.17. The following Figure 4.18 is basically alike, but zooms into the most interesting and variable region of moderate shear, where the influence of TKE wave-losses is relatively strong. The figures are mainly based on LESs with high resolution and large domains, and for all runs with stratified FA the stratification is modest (i.e., $\gamma = 0.03 \text{ Km}^{-1}$).³⁴ The respective lower resolution LESs are displayed in the background with lighter colors. Different to the previous sections, where we focused on the general structures of the TKE composition, we here want to get a more subtle picture and specifically quantify the impact of gravity-waves. Therefore,

³¹Strictly seen, in this case the upper layer ceases to represent the ‘free’ atmosphere. It rather becomes part of a then two-staged CBL. Strang and Fernando (2001) did not have to deal with undesired convective leakage of TKE and buoyancy due to the overshooting of thermals in their tank experiments, as they investigated a free-flow shear-layers without convection.

³²With $w_* \approx 1.2 \text{ ms}^{-1}$ and $z_i \approx 1400 \text{ m}$ this would represent more than 5 convective turnover-times, estimated by $z_i/w_* \approx 20 \text{ min}$.

³³We found significant differences between conventional and NFA CBLs with respect to $\beta = z_i/z_{i1} - 1$ and $\beta_g = z_{i,q}/z_{i1} - 1$. In this respect one should be aware that ultimately the local interfacial turbulence must differ between both flow types. The focus of our comparison, however, is on the basic integral similarity of the TKE dynamics.

³⁴Our weakly sheared LESs with the stronger FA stratification show an unphysical bias, which we attribute to resolution problems. For clarity these data are not considered in the following.

as previously discussed, only data from the quasi-stationary equilibrium-entrainment regime (main period) are considered. Furthermore, to reduce scatter, we filtered the time series by a 30-minute moving average³⁵, a procedure that we will use frequently in the remainder of this study.

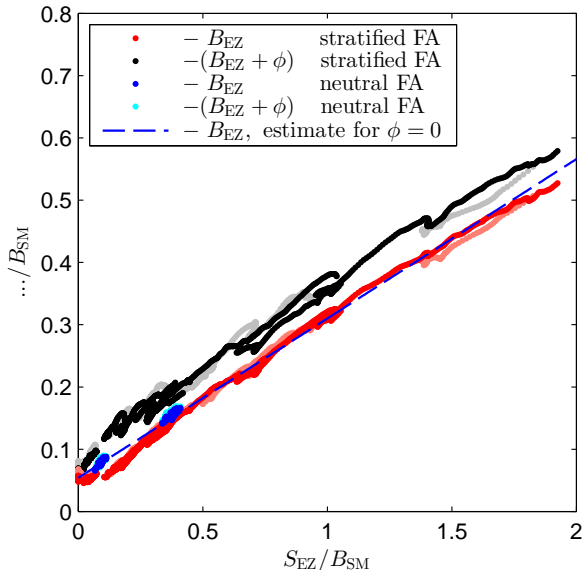


Figure 4.17: Dimensionless TKE-budget terms of various LES versus dimensionless EZ shear production. Presentation as in schematic Figure 4.15. LES data from simulations with a weak FA stratification are shown. Large domain and high resolution LES are shown in bright colors, whereas lower resolution LES are displayed by lighter colors. Time series filtered by a 30-minute moving average.

Arranged as the schematic Figure 4.15, both plots (Figure 4.17 and 4.18) summarize the shear-dependence of the integrated TKE budget, as far as it is relevant for the growth dynamics of our LES-CBLs. Normalized by the buoyancy production, all sink terms are shown as function of EZ shear-production. One can well recognize the significant and characteristic course of the wave-loss term (area between the black and red dots) and of entrainment (area below the red dots). The dissipation rate, which is represented by an area above the black dots, is not of interest here and thus not fully shown.

In addition to the data from the conventional LES-CBLs with stably stratified FA, we plotted the data of the LESs with neutral FA (NFA, blue and cyan dots). As expected, entrainment (area below blue dots) and dissipation (area above cyan dots) are significantly stronger for both NFA cases, as the drainage of fluctuation energy into the FA is close to zero. Therefore, significantly more TKE remains within the CBL and is then consumed by entrainment or dissipated. For both NFA cases TKE-

³⁵An averaging period of 30 minutes is in the order of the convective turnover-time. In this time frame, we expect the integral TKE budget to evolve approximately linearly in equilibrium entrainment conditions.

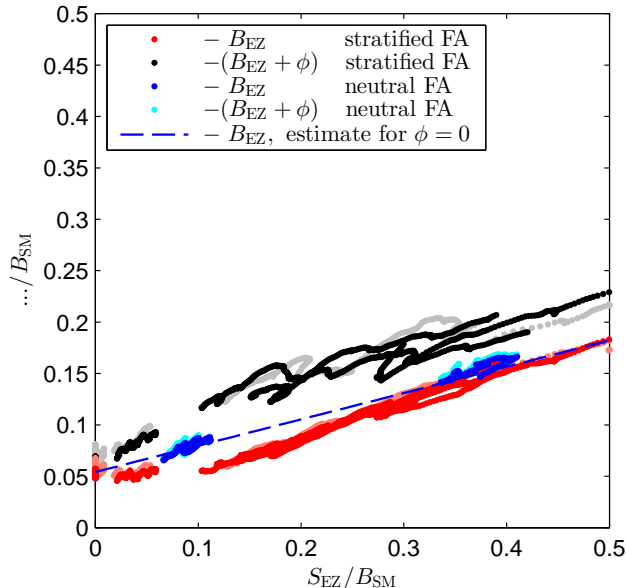


Figure 4.18: Dimensionless TKE-budget terms of varied LES versus dimensionless EZ shear production. Presentation as in schematic Figure 4.15. Shown is a zoom into the plot in Figure 4.17.

losses to the FA are indeed very small, as shown by the strong match between blue (on top) and cyan dots (underneath). As expected, the markers for entrainment of the NFA LES (blue dots) are situated inside the area that represents the TKE wave losses (between the black and red dots). Furthermore we find, that for all LES with very small wave energy-losses – these are the purely connective case (red dots for $S_{EZ} = 0$) and both NFA cases (blue dots) – entrainment indeed seems to form a mostly linear relationship with EZ shear, as indicated by the dashed blue line. These findings agree very well with the idea that, first, the TKE-budget of the NFA CBLs represents a simplified reference for CBLs with stratified FA and, secondly, the deviation from linearity of the shear-dependence of CBL dissipation and entrainment is – at least to a large extent – caused by wave activity and related TKE drainage.

Therefore we finally use the NFA cases as ‘anchor points’ (blue dots, Figure 4.15) to estimate the linear contribution to the variation of the TKE-budget with shear. Although our data give a rather clear general picture of the three TKE budget terms, scatter is still substantial. Furthermore our NFA cases do not cover the region for strong shear production, and there is some uncertainty due to a small but noticeable TKE drainage (difference between blue and cyan dots). For a final estimate of the underlying linear relationship we therefore also use the assumption that the wave-induced reductions terms ϕ_B and ϕ_ϵ are positive. Thus in plots like Figure 4.15, the line must be positioned inside the area that represents ϕ . As shown by the blue dashed line in Figure 4.18 our final solution is consistent, as it corresponds quite well with the three anchor points, given by the convective limit and both NFA cases. To complete

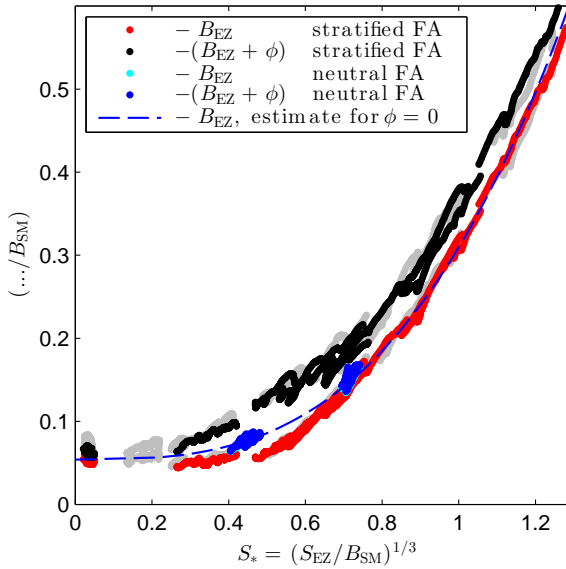


Figure 4.19: Composition of the TKE-budget as function of the dimensionless EZ shear production. Presentation similar as in Figure 4.18, but here the whole data range is shown and the abscissa represents dimensionless velocity-scale S_* . The blue dashed line represent the estimate for the linear scaling approach. Data of LES with low resolution are shown by light-red and gray dots in the background.

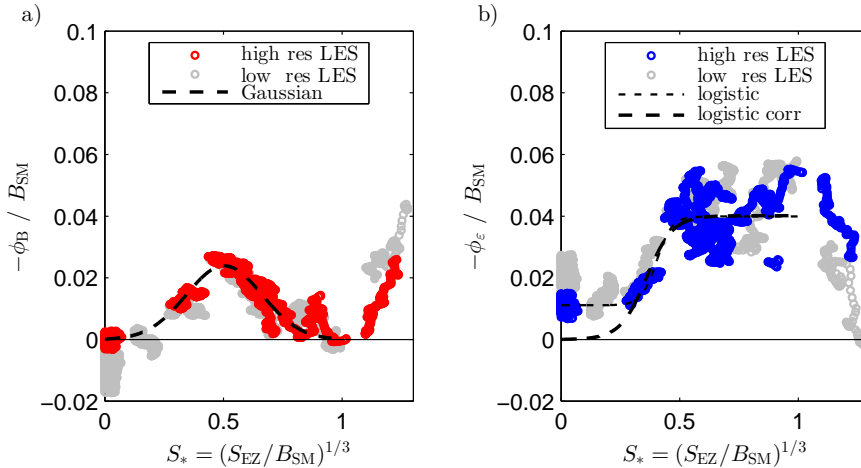


Figure 4.20: Normalized gravity-wave induced reduction terms of entrainment ϕ_B (a) and gravity-wave induced reduction terms of the dissipation rate ϕ_ϵ (b) versus the EZ shear-production velocity S_* . Blue and red dots represent the higher resolution and the larger domain LES. Gray dots represent the low resolution LES.

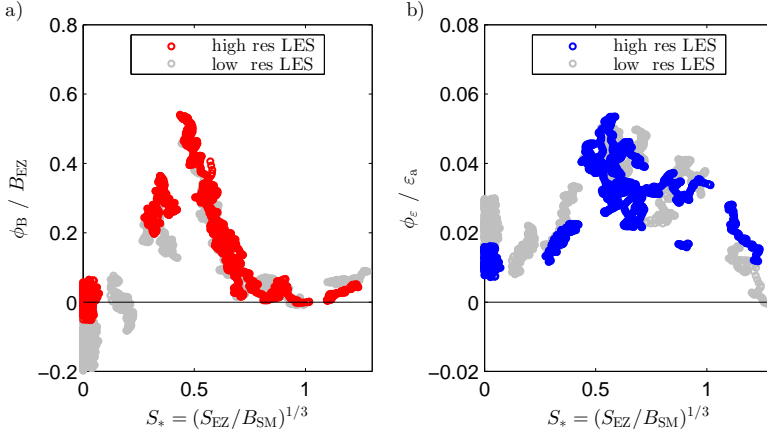


Figure 4.21: Relative impact of gravity-wave related reduction on buoyancy production (a) and dissipation (b). As Figure 4.20, but ϕ_B normalized by entrainment B_{EZ} (a) and ϕ_ε by the antagonistic dissipation rate ε_a , respectively (b). Blue and red dots represent the higher resolution and the larger domain LES. Gray dots represent the low resolution LES.

and refine the picture we additionally present the complete TKE budget once more in the next figure (Figure 4.19). As Figure 4.17, it shows the whole data range, but to better represent the range of moderate shear, the EZ shear production is displayed in terms of the dimensionless velocity scale $S_* = (S_{EZ}/B_{SM})^{1/3}$ (Eq. 4.23). Presented in this way, the shear-dependence of integral entrainment looks roughly similar to Figure 2.10, which shows the CFM quantities \tilde{w}_e (representing an entrainment ratio) versus $\Delta\tilde{U}$ (representing EZ-shear, rather than EZ shear-production). In both figures the structure of the entrainment-shear relationship features a similar depression for moderate shear, when compared to the respective reference model that does not account for TKE wave-losses.

As we have defined the linear part of the relationships, the wave-induced reduction terms for entrainment, ϕ_B , and the dissipation rate, ϕ_ε , can be directly diagnosed from data, as shown in Figure 4.20. Here we display both reduction terms normalized as before. Like in the previous figure, EZ shear-production is given by the dimensionless velocity scale S_* . As already guessed before (Figure 4.5), clear effects on entrainment are noticeable in a range with moderate EZ shear. With the onset of shear, the normalized loss (ϕ_B/B_{SM}) strongly grows and peaks at about $S_{EZ}/B_{SM} = 0.125$ or $S_* = 0.5$, where it reaches about 30% compared to the linear estimate of entrainment (Figure 4.18). However, with further increasing shear it decrease again and becomes very small for strong shear ($S_{EZ}/B_{SM} > 0.5$ or $S_* > 0.8$). As a result of the reduction ϕ_B , entrainment (Figure 4.19, red markers) is not noticeably enhanced by shear up to $S_{EZ}/B_{SM} \approx 0.125$ or $S_* \approx 0.5$ when compared the convective limit. The wave-induced reduction of the dissipation rate ϕ_ε/B_{SM} appears to grow very similarly for moderate shear but settles on a constant level with further increasing shear (Figure 4.19 and 4.20(b)).

For $S_* > 1$ Figure 4.20(a) indicates another strong increase of ϕ_B coupled with a

reduction of ϕ_ε . However, this feature is very probably caused by CBL instationarity or a bias in the data and not physically significant. For strong shear the data only come from the earlier part of the main phase of one single LES. Given the still significant instationarity in this period, the relative size of the various TKE budget terms may deviate somewhat from that in the later stages, which we use as reference for the underlying our linear model. Furthermore, one must be aware of the sensitivity of ϕ_B and ϕ_ε to the statistical and computational uncertainty of our LES and to the estimation of the linear reference. This can be seen by the pronounced differences between the data of high resolution (or wide domain) LES (blue and red markers in Figure 4.19) and the lower resolved standard LES (gray markers).

In any case, in situations with strong shear, the effect of wave-losses seems generally rather small relative to the largely enhanced entrainment rate (see Figure 4.11). Therefore – from a practical point of view – any error in the decomposition of ϕ should then become small as well. To demonstrate this, we plot the relative reduction of entrainment ϕ_B/B_{EZ} versus S_* in Figure 4.21(a). One finds a rather strong reduction of more than 50 % for $S_* \approx 0.5$. But for $S_* > 0.8$ the effects are rather small ($< 5\%$). The relative reduction of the dissipation rate $\phi_\varepsilon/\varepsilon_a$ is depicted in Figure 4.21(b). It appears, that the wave-induced reduction of dissipation peaks later at around $S_* > 0.6$ and decreases less rapidly for $S_* > 0.8$. However, as ε_a is a large term, the relative reduction is generally one order of magnitude smaller than that for entrainment. Our data suggest that it constantly decreases with the increase of S_* . This is in accordance with Jonker *et al.*'s (2013) neutral DNS-BLs ($S_* \mapsto \infty$), whose TKE dynamics is not influenced by gravity-waves.

To complete our line of argumentation we once more consider the significance of the NFA runs. For this purpose we look at the shear-dependence of the normalized TKE tendencies, as depicted in Figure 4.22. For the conventional LES-CBL with a stratified FA, the TKE tendency integrated over the whole CBL is shown with dark-gray dots, the integral tendency in the EZ is shown by light-gray dots and the tendency in the upper EZ layer ($EZ, u : z_{i,g} \pm \delta$ as defined by GM14, section 2.6) is shown by green dots. We find that most of the TKE spinup occurs in the EZ and particularly in the interfacial upper EZ layer, which is mostly affected by the inflow of non-turbulent air. For our data set, the general level of the TKE tendency slightly grows with EZ shear, but much less than entrainment (red markers). The relative importance of the upper EZ for TKE spinup strongly increases with shear (see also Figure 7.3), indicating that mixing in the EZ becomes more local (see also discussion in chapter 7.4.2). However, the most important aspect for the reasoning is the general similarity between the NFA and the conventional LES-CBLs in the EZ (cyan versus dark-gray dots) and in the upper EZ layer (blue versus green dots). These results may not come as a surprise, as the NFA cases are also characterized by similar entrainment and growth rates. But they further illustrate the integral dynamical similarity between both types of CBL and support our approach to use the NFA cases as a simplified reference.

Summary of the data analysis. In this section we further characterized the dependence of the CBL TKE-dynamics on EZ-shear. We could further specify the underlying linear relationship as well as an additional shear-dependent impact of gravity waves that form at CBL top. In this regard, we can identify three distinct regimes:

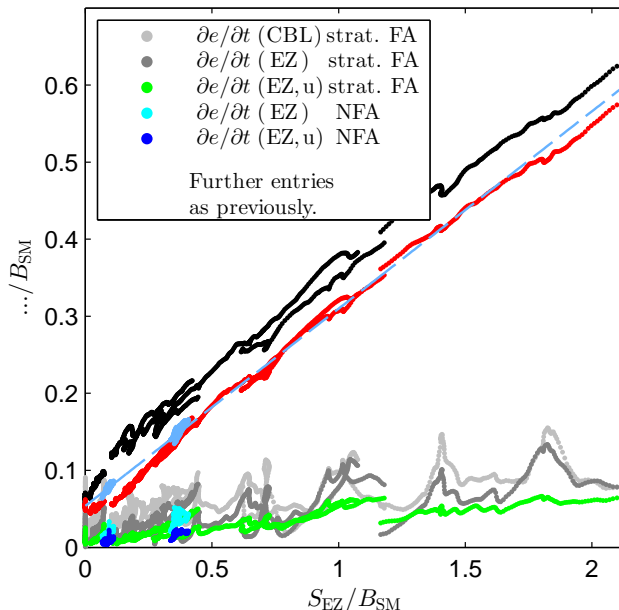


Figure 4.22: Integral TKE tendencies versus S_*^3 . Integrated over the whole CBL (light gray), over the whole EZ (dark gray) and the upper EZ layer ($EZ, u : z_{i,g} \pm \delta$, green). All values normalized by B_{SM} as usual. Wide-domain or high-resolution LES with a stratified FA and the NFA cases are shown separately (cyan and blue, respectively). For comparison also the other terms of the TKE budget are displayed in the same arrangement as in Figure 4.17.

Next to the purely convective reference situation (regime I, $S_{SM}/B_{SM} = 0.0$), where vertical radiation of TKE out the CBL is very small (GM14), we observe for a range of moderate shear (regime II, $0 < S_* \leq 1.0$) a strongly enhanced drainage of TKE, resulting in a significant reduction of dissipation but particularly of entrainment. The reduction of entrainment reaches about 50% at $S_* \approx 0.5$. A further increase of EZ shear production does not result in an increased TKE wave-drainage and for $S_* > 1.0$ (regime III) the impact on entrainment becomes small and insignificant. The wave-induced reduction of dissipation remains about constant with increasing shear when compared to buoyancy production (B_{SM}), but it decreases to insignificance when compared to the total TKE production ($B_{SM} + S_{EZ}$) or the total dissipation. Extrapolated into the neutral limit ($S_{EZ}/B_{SL} \mapsto \infty$) our data suggests that wave effects vanish, which is supported by other data (e.g. Jonker *et al.*, 2013).

In this study we do not aim to investigate the mechanisms that determine the observed wave dynamics in detail, but in chapter 7.4.2 we discuss some ideas that could help to understand the observed pattern of gravity-wave activity. These may be useful for future research.

4.2.4 Pragmatic parametrization of the TKE budget.

To finish this chapter, we complete our parametrization by estimating the respective parameters from our data. First we consider the linear part, which represents a CBL without wave-losses. The constants for the convective contribution $c_{B,0} \approx 0.054$ and $c_{\varepsilon,0} = 1 - c_{B,0} \approx 0.946$ (first term in Eq. 4.26 and 4.27) were already given previously. Our parameter estimation for the proportionality factors that determine the shear contributions (second term in Eq. 4.26 and 4.27) are

$$c_{B,S} \approx 0.256, \quad \text{and} \quad c_{\varepsilon,S} = 1 - c_{B,S} \approx 0.744. \quad (4.30)$$

Our LESs indicate that the dependence of ϕ_B and ϕ_ε on $S_* = (S_{EZ}/B_{SM})^{1/3}$ for $S_* \leq 1.2$, can be rather well represented by a Gaussian and a logistic function, respectively (black lines in Figure 4.20). Thus, as a pragmatic curve fitting for f_1 and f_1 (Eq. 4.29) we suggest

$$f_{\phi_B}(S_*) : \frac{\phi_B}{B_{SM}} = -a_1 e^{-\left(\frac{S_* - a_2}{a_3}\right)^2}, \quad (4.31)$$

$$\text{with } a \approx [0.024 \ 0.50 \ 0.20],$$

$$f_{\phi_\varepsilon}(S_*) : \frac{\phi_\varepsilon}{B_{SM}} = -\left(\frac{b_2}{1 + e^{(b_3(S_* - b_1))}} + b_4\right), \quad (4.32)$$

$$\text{with } b \approx [0.41 \ 0.03 \ 27.50 \ 0.01].$$

To document our findings, we mostly give constants with two non-zero digits. However, due to the data limitations that we discussed before, the physical accuracy as well as the statistical precision is probably significantly lower.

Chapter 5

A 0th-order TKE-model for sheared CBLs

In this chapter we come back to our initial goal and reconsider the 0th-order model (ZOM) representation of sheared CBLs. We derive an improved new 0th-order entrainment model (NZO) by simply rescaling each term in our parameterized TKE-budget (Eq. 4.26) using ZOM quantities (section 5.1). The relationships that result from this rescaling process represent what we introduced as ‘submodel 2’ (chapter 2.7.2). One of our research objectives (research question A-II), was to not only correct but also understand the limitations of the CFM. We therefore introduce the underlying ideas of the CFM in section 5.2. Next, the resulting entrainment rate is evaluated using LES data, and compared to the predictions given by the current state-of-the-art CFM of Conzemius and Fedorovich (2007). Finally, we revisit the concept of equilibrium entrainment, but now in the context of the new ZOM.

5.1 Derivation of a new 0th-order model (NZO)

In this section we first formulate the TKE-budget in terms of ZOM variables, using the insights obtained in the previous chapter. Next, we evaluate the budget terms vis-a-vis our LES data.

5.1.1 Formulation of TKE-budget in terms of ZOM variables

Buoyancy production and consumption. According to the Eulerian partitioning (EP), which we promoted in the previous chapters, the TKE buoyancy terms B_{SM} and B_{EZ} are defined as integrals over the EZ and SM of the **actual** buoyancy flux profile of the CBL (Figure 5.1(c), gray shaded areas). The respective terms for the new ZOM (NZO) can be defined analogously by referring to the idealized linear ZOM flux profile (Figure 5.1(b), gray triangles). To set up the NZO, we simply re-scale the triangular ZOM versions of B_{SM} and B_{EZ} by comparing them to their counterparts based on the full profiles. Using the ZOM quantities that we introduced in

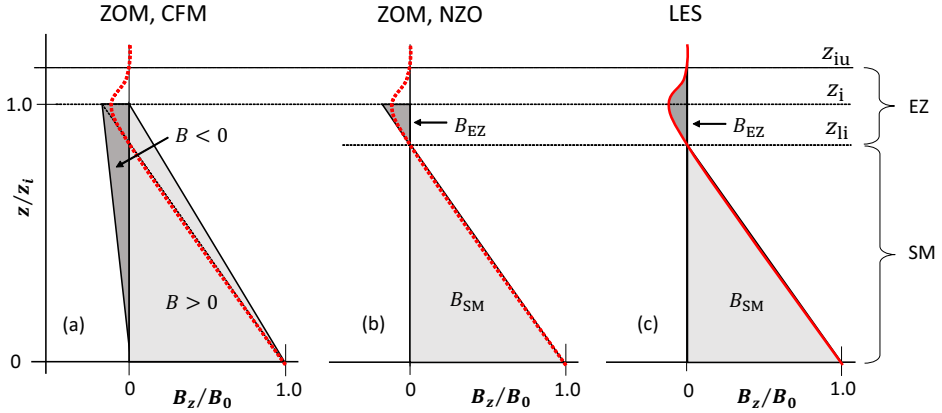


Figure 5.1: Schematic representation of the partitioning of the integrated buoyancy production term B_{SM} and buoyancy consumption term B_{EZ} . (a) Process partitioning (PP) as used in the CFM. (b) Eulerian partitioning (EP) of the NZO. (c) Eulerian partitioning (EP) applied to continuous LES-CBL profile.

chapter 2.5.3, one directly gets

$$B_{SM} = k_{B_{SM}} B_{SM}(NZO) = k_{B_{SM}} \frac{1}{2} B_0 z_{i1} \quad \text{with } k_{B_{SM}} \approx 1, \quad (5.1)$$

$$B_{EZ} = k_{B_{EZ}} B_{EZ}(NZO) = -k_{B_{EZ}} \frac{1}{2} w_e \Delta b (z_i - z_{i1}). \quad (5.2)$$

Here B_0 is the surface buoyancy flux and $-w_e \Delta b$ is the ZOM buoyancy flux at the upper boundary of the ZOM-BL (Eq. 2.47), which is typically denoted as the ZOM ‘entrainment flux’. $k_{B_{SM}}$ and $k_{B_{EZ}}$ are scaling factors, which still have to be determined (see section 5.1.2.1). However, at this point we can already postulate that, due to the linearity of the LES buoyancy-flux profile, we can expect $k_{B_{SM}} \approx 1$.

As the characteristic depth of the ZOM-CBL (SM plus EZ) we use z_i , which represents the height of the strongest entrainment flux. This is the traditional choice for CBL models (e.g. Conzemius and Fedorovich, 2006b). But in the equilibrium entrainment regime the CBL structure is largely self-similar. In principle the height of the maximum buoyancy gradient $z_{i,g}$ could therefore be a possible alternative scale for the ZOM-BL depth.¹ However, for our LESs z_i seems to be a more stable measure that is less affected by simulation uncertainties (Figure 3.9 and 4.14). Moreover, a z_i -based ZOM directly fits the concept of GM14.

An essential difference to previous (PP-based) ZOMs is that the (EP-based) NZO does not rely on z_i as universal turbulence length scale for the buoyancy dynamics. Instead, two length scales are used. The length scale for TKE buoyancy-production is given by the SM depth z_{i1} and the length scale for entrainment (TKE buoyancy-consumption) is given by the ZOM-EZ depth $z_i - z_{i1}$. Hence, the length scale z_i can be interpreted a composite of two separate length scales, each representing an essentially

¹A ZOM-BL depth $z_{i,g}$ has been used in previous studies, e.g. for neutral BLs (Jonker *et al.*, 2013).

different process. As a consequence of the linear buoyancy flux profile (Figure 5.1(b))

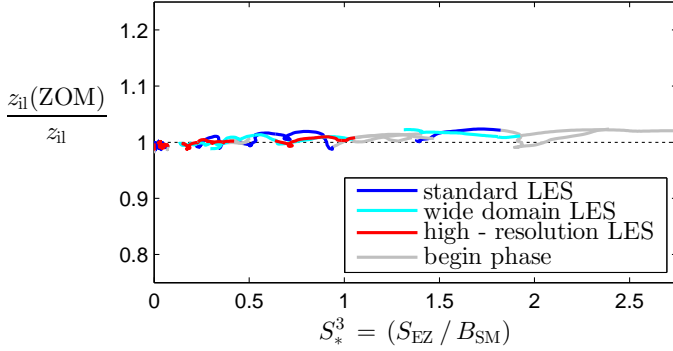


Figure 5.2: Shear dependence of the ratio between $z_{il}(\text{ZOM})$ as the height of the zero crossing of ZOM buoyancy flux and the respective value z_{il} for the actual LES B_z profiles.

and (c)) the CBL structure and the entrainment ratio are directly linked (as discussed in section 2.5.4)

$$\frac{z_i - z_{il}}{z_{il}} = \frac{w_e \Delta b}{B_0} = \beta. \quad (5.3)$$

However, we note that, due to the instationarity of the CBL, the **actual** CBL buoyancy flux profile is not completely linear, even below z_{il} (e.g. Wyngaard and Brost, 1984). This means that in the context of ZOM we implicitly refer to z_{il} as the height of the zero-crossing of the ZOM profile. Using the previous relationship, $z_{il}(\text{ZOM})$ is defined as

$$z_{il}(\text{ZOM}) := \left(\frac{w_e \Delta b}{B_0} + 1 \right)^{-1} z_i \approx z_{il}. \quad (5.4)$$

Figure 5.2 shows the shear-dependence of $z_{il}(\text{ZOM})/z_{il}$ in our LESs. We find that $z_{il}(\text{ZOM})$ is systematically larger than z_{il} . The difference, however, is small and mostly insignificant for our further reasoning. Thus, in the following we usually do not distinguish between $z_{il}(\text{ZOM})$ and z_{il} and only occasionally point out where a distinction matters.

The basic idea behind the NZO is to make use of the self-similar CBL layering in the equilibrium entrainment regime to define a corresponding integral ZOM TKE-budget. Since the layering is the basis for the budget, it implicitly represents an idealized, stationary entrainment regime. The NZO entrainment dynamics therefore differs from the actual entrainment dynamics (section 4.2.3), since the latter is still instationary, even in the equilibrium entrainment regime. However, as our LESs represent CBLs in a similar evolutionary state (mature, but not yet in full equilibrium), their integrated buoyancy dynamics are ‘pragmatically’ quasi-stationary. Therefore, we can expect that the scaling factors $k_{B_{SM}}$ and $k_{B_{EZ}}$ are about constant for our data set or, at most, vary depending on EZ shear.

Shear production. The expression for TKE shear-production in the NZO is mostly identical to the approach of Conzemius and Fedorovich (2007).² The total ZOM shear-production is given by the shear production at the surface and at the upper interface (Eq. 2.55). Excluding surface shear and equating the ZOM approximation of shear production at the upper interface to S_{EZ} we get

$$S_{EZ} = k_S S_{EZ}(\text{NZO}) = k_S \frac{1}{2} w_e \Delta U^2. \quad (5.5)$$

Here $\Delta U = \sqrt{\Delta u^2 + \Delta v^2}$ is the magnitude of the ZOM velocity jump at the upper interface. The factor k_S accounts for any systematic differences between ZOM shear production derived from idealized linear profiles and the values in real CBLs, which exhibit obviously non-linear stress profiles and velocity profiles (Figure 3.2b and 3.2d). Different to Conzemius and Fedorovich (2007), who implicitly assume $k_S \approx 1$, we actually test the relationship and thus here allow $k_S \neq 1$. Given the relatively slow evolution of the CBL mean flow in the equilibrium entrainment regime (Figure 3.2(b) and (d)), we can hope to find k_S to be at least rather constant and, at most, to show a well-defined dependence on S_{EZ} .

The NZO TKE-budget. To obtain the NZO representation of the TKE-budget, we substitute the production terms in our integral TKE-model (decomposed into entrainment (Eq. 4.26) and dissipation (Eq. 4.27)) by the respective ZOM formulations. In the remainder of the thesis we mainly consider entrainment. Thus, we focus on the entrainment model (Eq. 4.26). By inserting the ZOM expressions (Eq. 5.1, 5.2 and 5.5) into Eq. 4.26, we get

$$k_{B_{EZ}} \frac{1}{2} w_e \Delta b (z_i - z_{il}) = c_{B,0} \frac{1}{2} B_0 z_{il} + c_{B,S} k_S \frac{1}{2} w_e |\Delta U|^2 + \phi_B. \quad (5.6)$$

This expression readily reflects the dependence of the entrainment velocity (or growth rate) w_e on EZ shear. Next, using Eq. 5.3, we substitute the ZOM EZ depth $z_i - z_{il}$ by the length scale of the buoyancy production z_{il} , which represents the most basic process of a CBL. This leaves us with z_{il} as the only explicit length-scale.³ Thus, we get

$$k_{B_{EZ}} \frac{1}{2} w_e^2 \Delta b^2 \frac{z_{il}}{B_0} = c_{B,0} \frac{1}{2} B_0 z_{il} + c_{B,S} k_S \frac{1}{2} w_e |\Delta U|^2 + \phi_B. \quad (5.7)$$

Here the term on the lhs is the net ZOM TKE consumption (what we denote as entrainment), the first term on the rhs is the ZOM buoyancy production, the second term is the ZOM shear production at the upper interface and the last term denotes the wave energy losses. This equation already represents the relationship between shear, buoyancy and the CBL growth rate $w_e = f_{ZOM}(\Delta b, \Delta U, B_0, z_{il})$ that we are looking for. It is quadratic in w_e and can be readily solved.

²But it differs significantly from the older EP based model of Stull (1976a), which is based on rather unrealistic assumptions (Conzemius and Fedorovich, 2006b).

³However, z_i is implicitly present, as it defines the ZOM-CBL depth. Thus, for a practical implementation of the NZO, one may prefer an expression based on z_i . The corresponding form of the NZO is given in appendix C.

But before solving the ZOM expression for w_e , we normalize each term with $B_{\text{SM}}(\text{NZO})$ (Eq. 5.1), analogously to the integrated TKE-budget (Eq. 4.22). Thus, Eq. 5.7 becomes

$$\frac{k_{\text{BEZ}}}{c_{\text{B},0}} w_e^2 \frac{\Delta b^2}{B_0^2} = 1 + \frac{c_{\text{B},\text{S}} k_{\text{S}}}{c_{\text{B},0}} w_e \frac{|\Delta U|^2}{B_0 z_{\text{il}}} + \frac{2 \phi_{\text{B}}}{c_{\text{B},0} B_0 z_{\text{il}}}. \quad (5.8)$$

Here the lhs is the dimensionless ZOM entrainment term, unity is the dimensionless buoyancy-production, the second term on the rhs is the dimensionless EZ shear-production, and the 3rd term is the dimensionless wave reduction term. To express the desired relationship between CBL-growth rate and shear in a dimensionless form, we define – for purely formal reasons – the dimensionless entrainment velocity \hat{w}_e and the dimensionless EZ-shear $\Delta \hat{U}$

$$\hat{w}_e = w_e \frac{\Delta b}{B_0} = \beta, \quad \Delta \hat{U}^2 = \frac{|\Delta U|^2}{\Delta b z_{\text{il}}}. \quad (5.9)$$

Note that \hat{w}_e , which we interpret as an entrainment velocity, is identical to the ZOM entrainment ratio β as defined previously, and also to \tilde{w}_e in the dimensionless form of the CFM (Eq. 2.94 or Eq. 5.23 in the following section). $\Delta \hat{U}$ is very similar to the dimensionless CFM shear $\Delta \tilde{U}$ and but differs in the length-scale, as it is defined by z_{il} instead of z_i . Next, we define

$$\hat{\phi}_{\text{B}} = 2 \phi_{\text{B}} / (B_0 z_{\text{il}}) \quad (5.10)$$

as the dimensionless wave reduction term and rewrite Eq. 5.8 as

$$\frac{k_{\text{BEZ}}}{c_{\text{B},0}} \hat{w}_e^2 = 1 + \frac{c_{\text{B},\text{S}} k_{\text{S}}}{c_{\text{B},0}} \hat{w}_e \Delta \hat{U}^2 + \frac{\hat{\phi}_{\text{B}}}{c_{\text{B},0}}. \quad (5.11)$$

Solving for \hat{w}_e we finally get a dimensionless expression for the shear-dependence of CBL-growth and entrainment

$$\hat{w}_e = \frac{c_{\text{B},\text{S}} k_{\text{S}}}{2 k_{\text{BEZ}}} \Delta \hat{U}^2 + \left[\left(\frac{c_{\text{B},\text{S}} k_{\text{S}}}{2 k_{\text{BEZ}}} \Delta \hat{U}^2 \right)^2 + \frac{c_{\text{B},0} + \hat{\phi}_{\text{B}}}{k_{\text{BEZ}}} \right]^{1/2}. \quad (5.12)$$

In the convective and the neutral limit $\hat{\phi}_{\text{B}} = 0$. Thus we find the following limiting behavior. For the purely convective case $\Delta \hat{U} = 0$ and we get $\hat{w}_e = \sqrt{c_{\text{B},0}/k_{\text{BEZ}}} = \beta_0$, which reflects the well-known constant ZOM entrainment ratio. Approaching the neutral limit with $\Delta \hat{U} \gg \sqrt{c_{\text{B},0} k_{\text{BEZ}}} / (c_{\text{B},\text{S}} k_{\text{S}})$, we get an approximately quadratic relationship

$$\hat{w}_e \approx \frac{c_{\text{B},\text{S}} k_{\text{S}}}{k_{\text{BEZ}}} \Delta \hat{U}^2. \quad (5.13)$$

The proportionality factor $(c_{\text{B},\text{S}} k_{\text{S}}) / k_{\text{BEZ}}$ can be interpreted as a critical bulk Richardson number Ri_{U} , which characterizes the neutral limit ($Ri_{\text{U}} \approx 0.17$, based on the values for the constants derived in 5.1.2.1). We discuss this aspect in more detail in chapter 7.2.2.

It is remarkable that the NZO (Eq. 5.12) is also defined for very large $\Delta \hat{U}$ and does not feature the singularity of the CFM that we mentioned in section 2.7.1. However

this is simply a property of the quantity $\Delta\widehat{U}$ in the neutral limit. Here $z_{i1} \mapsto 0$ and therefore $\Delta\widehat{U} \mapsto \infty$. This is different for $\Delta\widetilde{U}$, which remains finite due to a finite z_i (Eq. 5.23). Hence, if we rewrite the NZO in terms of $\Delta\widetilde{U}$, it features the same type of singularity, as shown by Eq. C.6 in appendix C. In chapter 7.2.2 we argue that this behavior is physically well justified and supported by observations.

The wave-loss term in the NZO. The last element of the NZO that we should reconsider is the TKE wave-loss term ϕ_B . We should do this only for practical, not for physical reasons. The NZO framework does not alter ϕ_B in anyway. As we have NZO expressions for B_{SM} , S_{EZ} and therefore S_* , we could re-use our parametrization $\widehat{\phi}_B \simeq \phi_B/B_{SM} = f_{\phi_B}(S_*)$ (Eq. 4.31) for the NZO. However, the implementation of this empirical function into the NZO (Eq. 5.12) would result in a rather complex expression for w_e . This would counteract our intention to build a physically clear and easily interpretable model of the CBL growth. From a conceptual point of view, our analysis has also shown that ϕ_B – although significant for a range of moderate shear – should rather be considered as an additional ‘downstream’ second-tier effect, which modifies a more basic, underlying entrainment regime, but only if a stratified FA is present. It is therefore desirable to preserve the basic structure of the ZOM as defined by the turbulent CBL processes (Eq. 5.7) and include TKE wave-losses in a more additive manner.

To this end, a parametrization of the form

$$\widehat{\phi}_B \simeq f_{\phi_B, \text{NZO}}(\Delta\widehat{U}) \quad (5.14)$$

would be the most simple solution, as then the shear-dependence of both the turbulence dynamics in the CBL and the wave-losses would depend on the same scale $\Delta\widehat{U}$. In fact we can write S_* as

$$S_* = \left[\widehat{w}_e \Delta\widehat{U}^2 \right]^{1/3} \quad (5.15)$$

and therefore $\widehat{\phi}_B \simeq f_{\phi_B}(\widehat{w}_e, \Delta\widehat{U})$. It is also clear that \widehat{w}_e directly depends on $\Delta\widehat{U}$. Thus $\widehat{w}_e = f(\Delta\widehat{U})$, which is the whole idea behind the NZO. In combination with the previous expression one gets

$$f_{\phi_B}(\widehat{w}_e, \Delta\widehat{U}) = f_{\phi_B}(f(\Delta\widehat{U}), \Delta\widehat{U}) \simeq f_{\phi_B, \text{NZO}}(\Delta\widehat{U}). \quad (5.16)$$

This means that the dependence $f_{\phi_B, \text{NZO}}(\widehat{U})$ should be well-defined so that it can replace $f_{\phi_B}(S_*)$ in the NZO.

5.1.2 The NZO TKE-budget terms versus LES

In order to test each element of the NZO, we simply have to evaluate the proportionality constants in the ZOM-definitions of B_{SM} , B_{EZ} and S_{EZ} from our LES data-set as well as find an appropriate estimation for $f_{\phi_B, \text{NZO}}(\Delta\widehat{U})$.

5.1.2.1 NZO buoyancy terms

Figure 5.3 displays the dependence on EZ-shear of the inverse of both NZO scales $k_{B_{SM}}$ and $k_{B_{EZ}}$ as diagnosed from our LES. We find that indeed $k_{B_{SM}} = B_{SM}/B_{SM}(\text{NZO}) \approx$

1 is a good assumption (upper dashed line). However, for higher shear levels we can observe slightly increasing values, which is probably caused by enhanced entrainment. The latter results in an increased instationarity and non-linearity of the buoyancy flux profile close to the EZ. Next, we find that $k_{\text{BEZ}} = B_{\text{EZ}}/B_{\text{EZ}}(\text{NZO}) \approx 1/0.67 \approx 1.49$

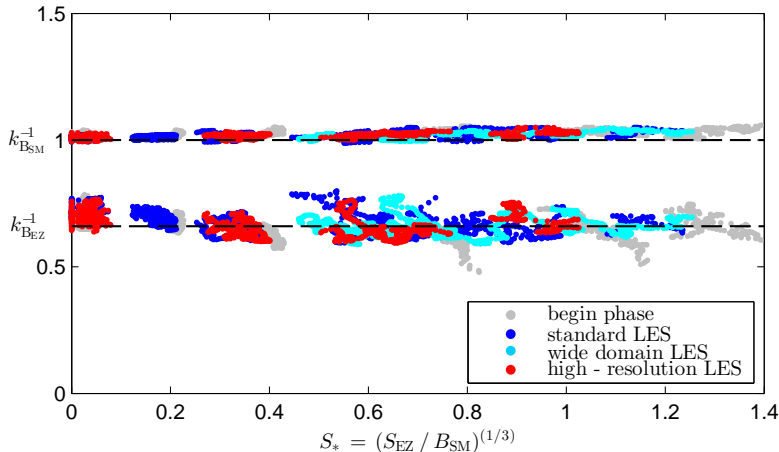


Figure 5.3: Shear dependence of the NZO buoyancy scales. Shown is the dependence of k_{BSM} and k_{BEZ} on S_* as diagnosed by the high-resolution, the standard and the wide-domain LES. All values filtered by a 30-minute moving average.

(lower dashed line). k_{BEZ} seems to be rather constant over the full range of our data set as well. For $S_* = 0$, k_{BEZ}^{-1} is slightly enhanced. With increasing EZ shear it decreases until it settles down at the quoted level for $S_* > 0.4$. We also find systematic deviations from constancy for the early phase of the LES (gray dots), which are particularly noticeable for stronger shear levels ($S_* > 0.25$).

In fact k_{BEZ} is a simple measure for the vertical distribution of buoyancy flux within the EZ (see Figures 5.1b and c). In this respect a systematic reduction of k_{BEZ}^{-1} in the begin phase, implying a larger contribution of the upper part of the EZ, complies with GM14's theory of the interfacial influence on the EZ structure (see chapter 6).

However, we also expect k_{BEZ} to be quite sensitive to simulation errors related to the correct representation of the strong buoyancy gradients at the upper interface. This is most problematic in the early simulation phase, particularly for dominantly convective conditions (very weak EZ shear). Hence, as we already argued before (section 4.1.3), this LES artifact might compensate the early phase reduction of k_{BEZ}^{-1} that we can observe for stronger shear.

5.1.2.2 NZO shear production

Next, we test the ZOM shear production term (Eq. 5.5). Figure 5.4 shows the dependence of normalized ZOM shear production $k_S = S_{\text{EZ}}/S_{\text{EZ}}(\text{NZO})$ on EZ shear production in terms of S_* . We find the relationship to be rather well defined and mostly constant for $S_* \geq 0.5$. For weaker shear we observe a strong variation of k_S

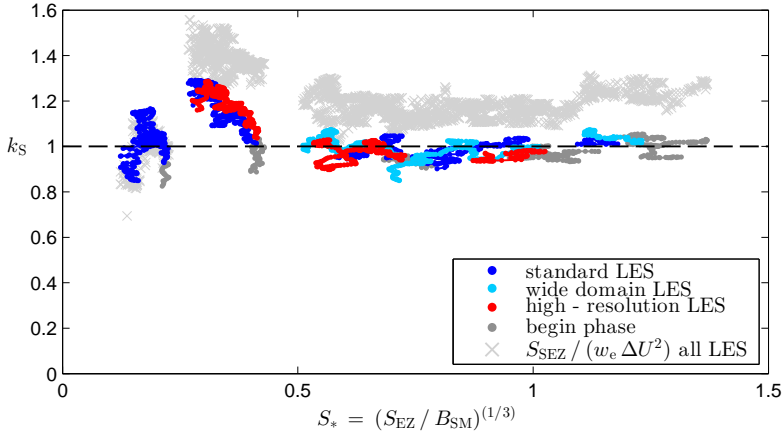


Figure 5.4: Shear dependence of the NZO shear scaling. Shown is the dependence of k_S on S_* as diagnosed from the high-resolution, the standard and the wide-domain LES. Gray crosses show an alternative estimate for k_S using the shear-based definition of the entrainment zone (SEZ). All values filtered by a 30-minute moving average.

with S_* , which are caused by slow changes in the evolution of an LES-CBL. Besides the above mentioned effects related to discretization (significant in the early simulation stage, gray dots), we could well imagine instationarity of the associated FA gravity wave field as a cause for this behavior.⁴ However, with respect to a ZOM entrainment model, the resulting uncertainty of k_S is rather insignificant, as for the particular range of EZ shear ($0 < S_* < 0.5$), S_* is still small in absolute terms and entrainment is about constant and thus rather insensitive to S_* (see Figure 4.19). Thus, pragmatically, we can consider the relationship to be approximately constant over the whole data range, with $k_S \approx 1$ (dashed line), as implicitly assumed by Conzemius and Fedorovich (2007). Still, conceptually the introduction of the parameter k_S makes sense as its value depends on the definition of the ZOM CBL depth. For instance, using the maximum gradient $z_{i,g}$ results in $k_S(z_{i,g}) \neq 1$ (see appendix B, Eq. B.14).

Figure 5.4 also shows our estimates for k_S (gray crosses), using the shear production in the shear-based entrainment zone (SEZ) as a reference (Eq. 4.13), as suggested by Conzemius and Fedorovich (2006a). We find that $k_S = S_{SEZ} / w_e \Delta U^2 \approx 1.2$. Not surprisingly the values are significantly larger than unity (as the integration interval is larger) and show somewhat larger scatter. Nevertheless, they are approximately constant and therefore S_{SEZ} looks like a suitable reference as well. However, our later analysis of the neutral limit (section 7.2.2) suggests that $k_S \approx 1$ is a rather universal property over the whole stability range ($0 \leq S_* \leq \infty$). Hence, for CBLs, we only consider shear within the EZ as relevant for entrainment, which also points to the local character of TKE shear-production in developed CBLs.

⁴The following Figure 5.5(a) shows the compensatory behavior of the wave-loss term at $\Delta \hat{U} \approx 0.5$.

5.1.2.3 NZO TKE-losses via gravity waves

The last element of the NZO that we have to re-evaluate is the TKE wave-loss term ϕ_B . As suggested before (Eq. 5.14), we consider the dependence of the normalized quantity $\hat{\phi}_B \simeq \phi_B/B_{SM}$ on EZ shear, using the dimensionless NZO velocity scale $\Delta\hat{U}$. Figure 5.5(a) shows that this relationship, $f_{\phi_B,NZO}$, is rather well defined, although some additional influence of the CBL evolution can be clearly recognized for several LESs. As indicated by the black dashed line, a Gaussian function seems to fit the data well for $0 < \Delta\hat{U} < 1.5$. For $\Delta\hat{U} > 1.5$ our data show another strong increase (analo-

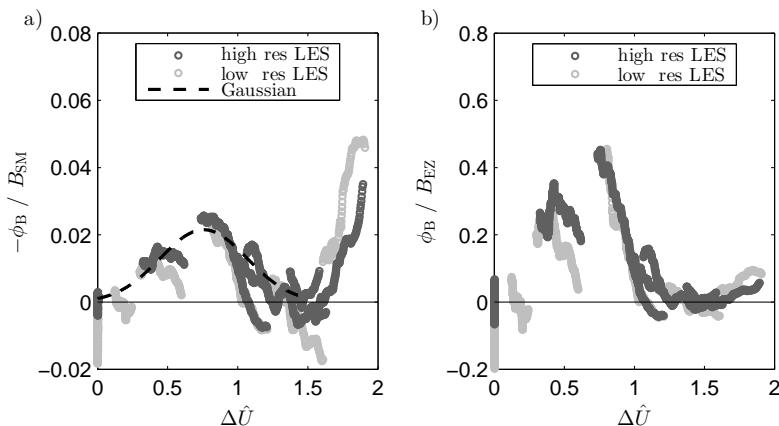


Figure 5.5: Dependency of the normalized wave-induced reduction of entrainment on dimensionless ZOM shear. (a) Normalization by CBL buoyancy production. (b) Normalization by entrainment.

gously to Figure 4.20). However this feature is very probably not physically relevant and compared to the likewise enhanced entrainment, we find it to be rather small, as demonstrated in Figure 5.5(b), which displays ϕ_B normalized by entrainment.⁵ The shown Gaussian function looks like an appropriate estimate of the wave-losses $\hat{\phi}_B$. Thus, as a pragmatic parametrization for the NZO we suggest

$$f_{\phi_B,NZO}(\Delta\hat{U}) : \quad \hat{\phi}_B \approx c_1 e^{\left(\frac{\Delta\hat{U} - c_2}{c_3}\right)^2}, \quad (5.17)$$

$$\text{with } c = [0.023 \ 0.741 \ 0.410].$$

We have now demonstrated that each assumption behind the NZO is rather well supported by our LESs. Therefore we expect the NZO to well predict CBL entrainment and growth, which will be demonstrated in the next section.

⁵See also the analogous discussion for f_{ϕ_B} in chapter 4.2.3.

5.2 The CFM and process partitioning

Structurally the Conzemius-Fedorovich model (CFM, see also section 2.7.1) differs from the NZO in only two aspects: in the neglect of TKE wave-losses and in the ‘process partitioning’ (PP) of the buoyancy terms. Although significant, the TKE wave-losses are not a fundamental issue, as it should be straightforward to complement the CFM by a wave-loss term, analogously to what we suggested for the NZO in the previous section. However, PP reflects a physically different concept, which severely impacts the model properties. Thus, we will focus on this aspect here. The related definition of the buoyancy terms is shown by Figure 5.1(a). Using our notation, the buoyancy production and consumption term of the CFM can be written as

$$B_{\text{SM}}(\text{CFM}) = \frac{1}{2} B_0 z_i, \quad (5.18)$$

$$B_{\text{EZ}}(\text{CFM}) = -\frac{1}{2} w_e \Delta b z_i. \quad (5.19)$$

This concept for determining the buoyancy terms was first formulated by Manins and Turner (1978) and has only later been denoted as ‘process-partitioning’ by Randall (1984). The idea is inspired by the observation that within a CBL regions with buoyancy consumption ($w'b' < 0$) and buoyancy production ($w'b' > 0$) are quite localized but not confined to certain layers and rather distributed over the whole CBL (Wilczak and Businger, 1983). Accordingly, it was suggested to separately account for the positive production of rising thermals in a ‘bottom-up’ contribution and the negative consumption of entraining air parcels in a ‘top-down’ contribution. The contributing regions for both processes expand over the whole CBL depth and are integrated separately. The concept has also been denoted as ‘Lagrangian Partitioning’ (LP Randall, 1984). ‘Process-partitioning’ (PP) can then be interpreted as a further linearization of LP to fit into the ZOM framework (Wilczak and Businger, 1983; Randall, 1984).

We do not question the basic physical sense of a conditional sampling of updrafts and downdrafts, which in many variations has been successfully applied to characterize convective turbulent transport (e.g Wyngaard and Brost, 1984). However, in our opinion, the linking of this concept to a linear model of integral entrainment or dissipation dynamics seems premature and inconsistent. In chapter 7.1 we address this issue once more and present a more basic argument for EP.

As the NZO, the CFM is based on the idea of a linear scaling of the TKE-budget. Using the same constants as Conzemius and Fedorovich (2007) it reads

$$-B_{\text{EZ}}(\text{CFM}) = C_1 B_{\text{SM}}(\text{CFM}) + C_p S_{\text{EZ}}. \quad (5.20)$$

The CFM (Eq. 5.18, 5.19, 5.20 and 5.5) then is given by

$$\frac{1}{2} w_e \Delta b z_i = C_1 \frac{1}{2} B_0 z_i + C_p \frac{1}{2} w_e |\Delta U|^2. \quad (5.21)$$

Normalization with $B_{\text{SM}}(\text{CFM})$ (Eq. 5.18) gives

$$\frac{w_e \Delta b}{B_0} = C_1 + C_p \frac{w_e}{B_0 z_i} |\Delta U|^2. \quad (5.22)$$

Here the lhs is the normalized entrainment term, $C_1 = \beta_0$ is the normalized buoyancy contribution (shear-free entrainment ratio) and the second term on the rhs is the normalized shear contribution to entrainment. With the non-dimensional entrainment rate \tilde{w}_e and EZ-shear $\Delta\tilde{U}$, given by

$$\tilde{w}_e = \frac{w_e \Delta b}{B_0} = \beta_0 \quad \text{and} \quad \Delta\tilde{U}^2 = \frac{1}{\Delta b z_i} |\Delta U|^2, \quad (5.23)$$

we get

$$\tilde{w}_e = \beta = C_1 + C_p \tilde{w}_e \Delta\tilde{U}^2. \quad (5.24)$$

Solving for \tilde{w}_e gives

$$\tilde{w}_e = \frac{C_1}{1 - C_p \Delta\tilde{U}^2}. \quad (5.25)$$

Based on LES, Conzemius and Fedorovich (2007) determined the constants to be $C_1 = \beta_0 \approx 0.2$ (the classical value for the entrainment ratio) and $C_p \approx 0.4$. Note that \tilde{w}_e is equal to the analogue NZO quantity \hat{w}_e . However $\Delta\tilde{U}$ differs from its NZO counterpart as it contains the length scale z_i . Note that Eq. 5.24 implies for $\Delta\tilde{U}$ the restriction

$$\Delta\tilde{U} < 1/C_p^{1/2}. \quad (5.26)$$

Conzemius and Fedorovich (2006b) considered these conditions as unphysical and suspected unaccounted stationarity as a reason. However, in section 7.2 we argue that a limitation of $\Delta\tilde{U}$ is – in principle – physically well justified as it represents the neutral limit of sheared CBLs.

It is worth noting that the PP buoyancy terms $B_{SM}(\text{CFM})$ and $B_{EZ}(\text{CFM})$ are directly defined as ZOM quantities, and thus ZOM quantities are inherent to the CFM. This is different to our derivation of the NZO, where B_{SM} and B_{EZ} are first defined as the integrated ensemble averaged production and consumption terms of the CBL flow (LES in our case), which are then – in a second step – approximated by ZOM expressions (Eq. 5.1 and 5.19). This also means that in the case of the CFM the underlying TKE scaling (Eq. 5.20) defines a relationship between ZOM approximations, involving PP-based assumptions and does not directly reflect ensemble averaged statistical properties, which are independent of any ZOM related assumption (like our EP-based scaling, Eq. 4.26 and 4.27).

We consider this accumulation of assumptions, which cannot be tested independently, as a major design weakness of the CFM and similar PP-based FOMs (1st-order models).

5.3 Comparison of NZO and CFM to LES

In this section we finally evaluate the performance of the EP-based NZO and also compare it with the PP-based CFM. First, we have a short look at the differences between the buoyancy terms, which illustrates the essential difference between both ZOMs. Next, we present a full evaluation of shear-dependent entrainment as modeled by NZO and CFM.

5.3.1 NZO and CFM – comparison of the buoyancy terms

Figure 5.6 displays the shear-dependence of the ZOM estimates of the buoyancy terms B_{SM} and B_{EZ} for the PP-based CFM (grey) and the EP-based NZO (black). The panel on the lhs shows the production term and the panel on the rhs the consumption term. The results of the NZO have been shown before: the shear-dependence of $k_{B_{SM}}^{-1}$ (left panel) and $k_{B_{EZ}}^{-1}$ (right panel), as in Figure 5.3. This time only data from the equilibrium entrainment regime are displayed, without any temporal averaging.

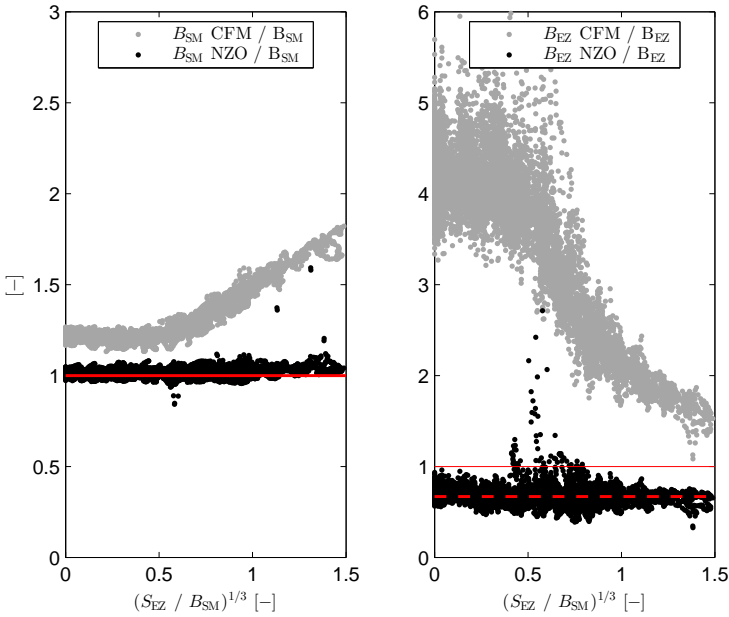


Figure 5.6: Shear-dependence of the normalized ZOM buoyancy terms, as diagnosed from our series of LES. Gray dots represent the PP-based CFM and black dots the EP-based NZO. 1-minute data in the equilibrium entrainment regime are shown.

The purpose of this plot is to illustrate the sensitivity of ZOM buoyancy-partitioning to EZ shear. Although the EP-based and PP-based terms differ, their ratio is constant as long as EZ-shear is constant ($S_* = \text{const}$).⁶ However, as soon as shear varies (and $S_* > 0.5$), the EP-based and PP-based terms react very differently and hence their ratio changes. This is due to the strong variation of the EZ depth with shear, which is addressed by EP, but not by PP.⁷

For a final characterization of the difference between the CFM and the NZO, one best considers the scaled differences between both model formulations with respect to the buoyancy production and consumption term: $(B_{SM}(\text{NZO}) - B_{SM}(\text{CFM})) / B_{SM}(\text{NZO})$ and $(B_{EZ}(\text{NZO}) - B_{EZ}(\text{CFM})) / B_{SM}(\text{NZO})$. These differences depend linearly on \hat{w}_e

⁶For shear-free conditions, this has been mentioned before by several authors (e.g. Stage and Businger, 1981).

⁷Of course, the shown behavior could also be deduced directly from the CFM and NZO model equations.

as shown in appendix C (ΔB_1 and ΔB_2 in Eq. C.2).

5.3.2 NZO and CFM – entrainment velocity

Having all the ingredients together, we can finally compare the shear-dependence of the growth-rate of our LES-CBLs with the predictions of the NZO and the CFM. Figure 5.7 shows the relationship between \hat{w}_e and $\Delta\hat{U}$ for our LES data and both ZOMs.⁸ We find a rather excellent agreement between LES (blue, green and red

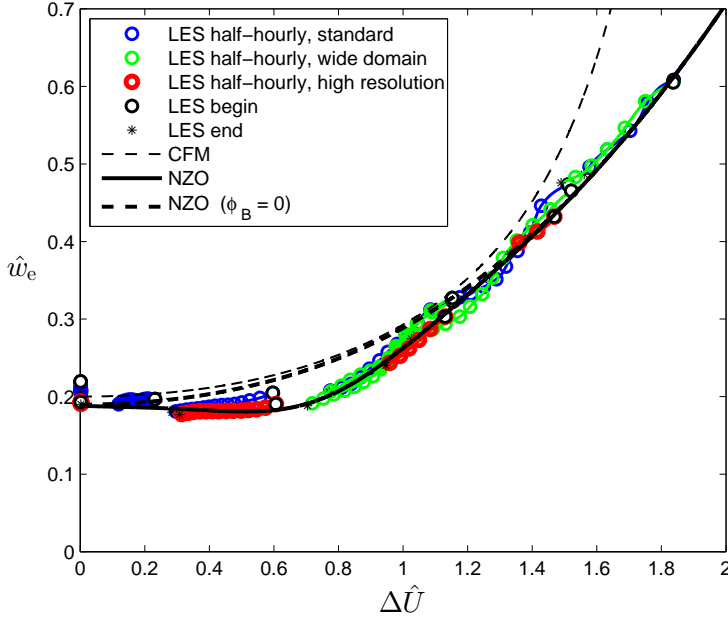


Figure 5.7: Dimensionless entrainment velocity $w_e = \beta$ as function of the dimensionless EZ shear $\Delta\hat{U}$ for our LESs (blue, green, red and black markers), the CFM (thin dashed line), the NZO (thick black line) and the NZO without wave term (thick dashed line).

dots) and the NZO (thick black line). Comparison with the CFM (thin dashed line) demonstrates the systematic improvements that we have incorporated into NZO. For $0 < \Delta\hat{U} < 1.2$ our reanalysis of the integrated TKE-budget, which resulted in an improved TKE-model (Eq. 4.26) comes into effect. Here the difference between the CFM (thin black dashed line) and NZO (or LES) is mainly caused by the inclusion of gravity-wave-induced TKE-losses ϕ_B . This is demonstrated by the thick dashed black line, which represent the NZO without wave-loss term and closely follows the course of the CFM. For $\Delta\hat{U} > 1.2$, when the entrainment has become dominantly shear-driven and the EZ is significantly deeper, the much more realistic EP-based scaling of the NZO results in a systematically improved representation of CBL-growth dynamics.

⁸To directly compare the CFM with the NZO, we had to reformulated the CFM in terms of the NZO quantity $\Delta\hat{U}$, with z_{i1} as length scale, instead of $\Delta\tilde{U}$, which is based on z_1 . The respective expression (Eq. C.3) can be found in appendix C.

5.4 Equilibrium entrainment and the NZO vertical structure

Our derivation of the NZO was based on our empirical model for the integrated TKE-budget of CBLs in the ‘equilibrium entrainment regime’. But with respect to the actual entrainment flux, as, e.g., measured by A_t or B_{EZ}/B_{SM} , our perception of ‘equilibrium entrainment’ is rather approximate and not sharp, and our LES-CBLs are significantly instationary (Figure 3.7 and 3.8). As formulated by GM14 (chapter 2.6), the instationarity of the entrainment flux can be related to the local interfacial dynamics, which evolves during the CBL evolution. In the main phase of our LESs, further changes happen only slowly and therefore all CBLs are in a similar evolutionary state. Accordingly, the integral entrainment ratios in the main phase of our LES scale so well, because they represent similar CBLs. But their state might still differ significantly from the asymptotic, ‘truly stationary’ entrainment regime which is only approached for very mature and slowly growing CBLs (Eq. 2.81, Figure 2.7 and 2.9).

However, the constraint of maturity may not be as limiting as it seems. For a given shear forcing S_* , the natural layering of the CBL, as given by z_i/z_{i1} and $z_{i,g}/z_{i1}$, becomes constant already very early in the CBL evolution and therefore prematurely reflects a property of the asymptotic stationary CBL (Figure 2.7)). This also implies that the remaining instationarity does not affect the CBL layering anymore, but solely the distribution of production and consumption of TKE by buoyancy within the CBL. The NZO is constructed to reproduce this constant layering, by translating it into an equally constant entrainment ratio. We therefore interpret the NZO as a truly ‘quasi-stationary’ idealization⁹ of the still instationary entrainment regime.

Furthermore, this also suggests that from a physical point of view, the derivation of the NZO via the LES-derived TKE-budget and a subsequent parameterization thereof can be seen as an unnecessary detour. Hence, we should be able to alternatively derive the NZO parameters directly, by diagnosing the ZOM estimates of the TKE-budget terms from our LES. As discussed in detail, we found that the – only approximately – stationary integrated TKE-budget widely conforms with a linear scaling based on a superposition of the TKE source terms (Eq. 4.26). As the NZO entrainment ratio represents the quasi-stationary limit of the integral CBL TKE-budget, we have even more reason to assume a linear inviscid scaling behavior in the spirit of Kolmogorov’s concept for high Reynold-number flows. For clarity and as a reference for later use, we demonstrate on our data that indeed the NZO can also be derived based on ZOM estimates of the TKE-budget terms.

Due to the linear buoyancy flux profile (Figure 5.1(b)) the integral entrainment ratio of the NZO, that is TKE buoyancy consumption divided by production, can be expressed as

$$\frac{w_e \Delta b (z_i - z_{i1})}{B_0 z_{i1}} = \left(\frac{z_i - z_{i1}}{z_{i1}} \right)^2 = \left(\frac{w_e \Delta b}{B_0} \right)^2 = \beta^2 = f(S_*), \quad (5.27)$$

Analogously to Eq. 4.26 it can be modeled as

$$\left(\frac{z_i - z_{i1}}{z_{i1}} \right)^2 = \beta^2 = \beta_0^2 + C_S S_*^3(\text{ZOM}) + \hat{\phi}_C. \quad (5.28)$$

⁹As indicated by the uniform buoyancy profile and fully linear flux profiles.

where β_0 is the ZOM entrainment ratio of the shear-free case,

$$S_*^3(\text{ZOM}) = \frac{S_{\text{EZ}}(\text{ZOM})}{B_{\text{SM}}(\text{ZOM})} = \frac{w_e \Delta U^2}{B_0 z_{\text{il}}} \quad (5.29)$$

is the normalized integrated TKE shear production in the EZ and $\hat{\phi}_{\text{C}} \sim \hat{\phi}_{\text{B}} > 0$ represent the relative gravity-wave-driven TKE-losses. As noted before, Eq. 5.27 equally determines both the NZO entrainment ratio and the constant layering of the CBL. Furthermore, with $k_{\text{S}} \approx 1$ and $k_{B_{\text{SM}}} \approx 1$ we find also that

$$S_*^3(\text{ZOM}) \approx \frac{k_{\text{S}}}{k_{B_{\text{SM}}}} \frac{w_e \Delta U^2}{B_0 z_{\text{il}}} = S_*^3 \quad (5.30)$$

is a very good approximation, so that we mostly do not distinguished anymore between $S_*^3(\text{ZOM})$ and S_*^3 in the following.

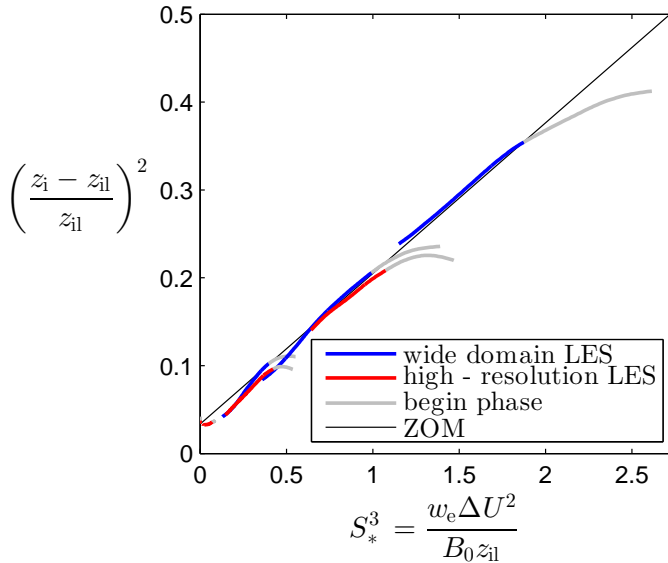


Figure 5.8: Correlation between the NZO integral entrainment ratio β^2 and $S_*^3(\text{ZOM})$.

The dependence of the layering (lhs of Eq. 5.29) on shear ($S_*^3(\text{ZOM})$) as given by our LESs is shown in Figure 5.8. It confirms the validity of the relationship for data in the main-phase (blue and red markers), which represents the constants layering of well-developed CBLs in the equilibrium entrainment regime. The shown information is basically identical with that contained in the earlier Figure 4.14. However here, we determined S_*^3 via the ZOM momentum (Eq. 5.29), which apparently results in much smoother graphs. Going backward in the CBL evolution, the early phase data (gray lines) gradually begin to differ from the scaling, as the high growth rate in immature shallow CBLs still affects the CBL layering. Our data suggest $\beta_0 \approx 0.19$ and $C_S \approx 0.17$. A comparison of the present model (Eq. 5.28) and our previous representation of the NZO (e.g. Eq. 5.8 ff.) shows that the parameters in both

models are related as follows:

$$\beta_0^2 = \frac{c_{B,0}}{k_{BEZ}}, \quad C_S \simeq k_S \frac{c_{B,S}}{k_{BEZ}} = Ri_U \quad \text{and} \quad \hat{\phi}_C = \frac{1}{k_{BEZ}} \hat{\phi}_B. \quad (5.31)$$

Note also that the slope C_S , which expresses the shear-sensitivity of entrainment, equals the critical Richardson number and has a value of $Ri_U \approx 0.17$. This critical Richardson number characterizes the neutral limit of the NZO, which we discuss more in detail in chapter 7.2.2.

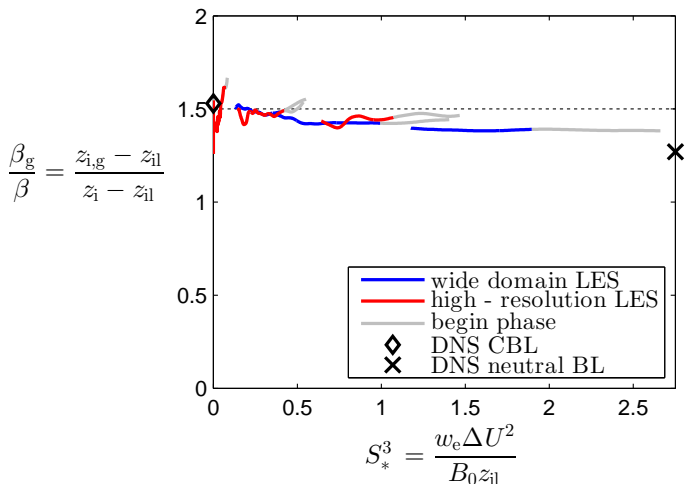


Figure 5.9: Dependency of β_g/β on S_*^3 . For orientation also the values of the shear-free DNS-CBL of Garcia and Mellado (2014) (black diamond) and the neutral DNS-BL of Jonker et al. (2013) (black cross), which represents the limit $S_*^3 \mapsto \infty$, are given.

According to GM14 the constant layering of the CBL structure in the equilibrium entrainment regime also holds for the height of the maximum buoyancy gradient $z_{i,g}$. Therefore one could also use $z_{i,g}$ as a reference height to define a ZOM entrainment ratio $\beta_g = (z_{i,g} - z_{il})/z_{il}$ and expect it to have a similar shear-dependence as β . We will evaluate this idea very shortly here.¹⁰ Our data suggest that the upper EZ structure is modified by the transition from convective to shear-driven turbulence, so that β_g^2 supposedly shows a slightly different dependence on S_*^3 than z_i . This is illustrated by Figure 5.9, which shows the ratio of both entrainment ratios (or equivalently, ZOM EZ depths), $\beta/\beta_g = (z_i - z_{il})/(z_{i,g} - z_{il})$. We should note that, as $z_{i,g}$ relates to the large buoyancy gradient at the interface with the FA, it is probably more sensitive to coarse resolution of the LESs and therefore should come with a higher uncertainty. With moderate EZ shear and large wave losses, β_g varies strongly within a single LES and compared to β scatter remains relatively high. But overall β/β_g shows a rather well-defined dependence on S_* in the main phase of our LESs. For stronger shear, $S_*^3 > 1$, β/β_g starts to settle on a significantly lower level, which characterizes the

¹⁰Furthermore, GM14's DNSs indicate that β_g is more sensitive to the flow's Reynolds number and becomes constant somewhat later in the CBL evolution than β . See GM14's table 2 and Figure 1.

modification of the upper EZ structure by shear driven turbulence. Overall, our LES data basically seem to fit in between the limiting cases given by previous DNS studies (black symbols). The black diamond represents the purely convective DNS-BLs of GM14 with $S_*^3 = 0$ and $\beta/\beta_g \approx 1.53$ (deduced from GM14's table 1) and the black cross represents the purely shear-driven neutral DNS-BLs of Jonker *et al.* (2013) with $S_*^3 \mapsto \infty$ and $\beta/\beta_g \approx 1.27$ (Figure B.1(a) and Eq. B.13, with $\beta/\beta_g = \gamma_{zi}$).

We conclude that the NZO and its scales, z_i or $z_{i,g}$, z_{il} , B_0 , Δb and ΔU should offer a quasi-stationary reference framework that is suitable to rate the remaining CBL instationarity in the equilibrium entrainment regime. We use this idea, when we investigate the local influence of FA stratification on the EZ dynamics in the next chapter.

Chapter 6

Direct interfacial influences on the entrainment zone structure of sheared CBLs

In this chapter we analyze the influence of wind shear on the dynamics of the upper EZ layer at the interface to the stratified FA and its further impact on the overall EZ dynamics. Our practical aim is a set of parameterizations, which characterize the shape of the entrainment- and the buoyancy-profile of sheared CBLs and therefore has to account for both the local interfacial dynamics and EZ shear.

Different to our previous analysis of the quasi-stationary properties in the equilibrium entrainment regime, which are ultimately represented by the NZO, we now focus on the instationary aspects of the CBL dynamics. While the NZO characterizes the quasi-stationary integral dynamics and the 'constant layering' of a CBL, we here consider the actual distribution of the buoyancy dynamics within the EZ of such a 'constantly layered' sheared CBL. Fundamental work on the shear-free CBL by Garcia and Mellado (2014) (GM14), which we already presented in chapter 2.7, shows that the buoyancy distribution in the EZ is directly influenced by the FA stratification. As this influence decreases during the CBL evolution (Figure 2.7) it can therefore also be used as a measure of the CBL's maturity. The questions now is how both the FA-stratification and EZ-shear modify the EZ buoyancy-dynamics and the buoyancy distribution within the EZ. By linking GM14's ideas with our characterization of shear effects, we try to answer this question in the following and finally develop a generalization of GM14's approach for sheared CBLs. Compared to GM14's model, which is based on very detailed examination of the EZ buoyancy structure, our analysis here remains a bit more sketchy, not least because of some limitations of our data set. Nevertheless, the resulting models are able to reproduce the local entrainment dynamics of our sheared LES-CBLs remarkably well. In the convective limit our models fully concur with GM14's findings. For the neutral limit, for which we do not have data, we can at least suggest a plausible solution.

In the next section we first discuss some important differences with regard to set-up and evolution between shear-free and sheared CBLs. Then we introduce some

basic ideas and finally layout the procedure for the following analysis.

6.1 A preliminary evaluation of the problem

As a starting point we hypothesize that the EZ dynamics in a sheared CBL is sufficiently similar to that in a shear-free CBL, so that GM14's model can rather straightforwardly be generalized. Before we show that this notion is supported by our data, we first evaluate some fundamental aspects of sheared CBLs that are crucial for a detailed generalization of GM14's reasoning.

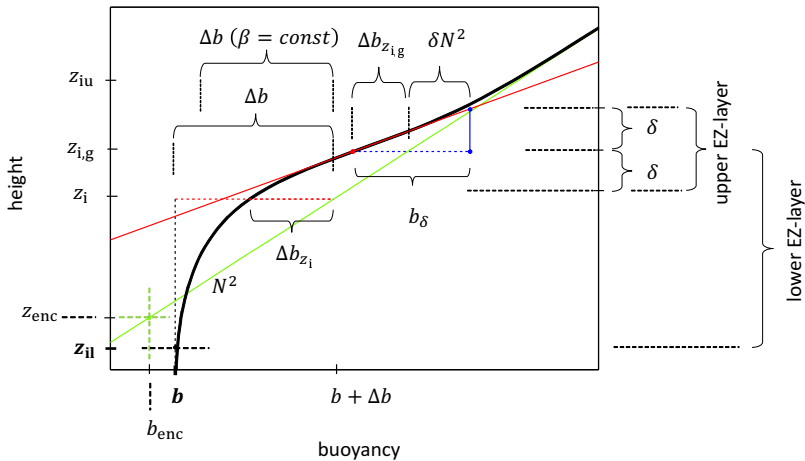


Figure 6.1: Sketch showing the mean buoyancy structure in the entrainment zone of a sheared CBL.

The influence of shear on the CBL structure. An important element of GM14's theory of non-sheared CBLs is the empirical finding (see also Fedorovich *et al.*, 2004b) that during CBL evolution the vertical CBL structure, as defined by any ratio of $z_{i,g}$, z_i and $z_{enc} \approx z_{il}$, becomes constant after a short initial phase, characterizing the quasi-stationary integral properties of equilibrium entrainment regime. The encroachment scales, z_{enc} and the related b_{enc} , represent the quasi-stationary SM, whereas z_i and $z_{i,g}$ the define the closely coupled EZ.

Our data analysis so far has shown that the constant 'natural layering', as given by the ratios of z_i or $z_{i,g}$ and z_{il} , characterizes mature sheared CBLs as well, if one accounts for the influence of TKE shear-production within the EZ (Figure 4.14). Combining this finding with the idea of an 'Eulerian buoyancy partitioning' (EP) implicitly defines a 0th-order model (ZOM), which can be specified via an inviscid scaling (section 5.4, Eq. 5.28 and Figure 5.8). This new ZOM (NZO) defines the shear dependence of the CBL structure (Eq. 5.28), which less specifically simply implies a functional relationships between β and S_* . Thus

$$\beta = \frac{w_e \Delta b}{B_0} = \frac{z_i - z_{il}}{z_{il}} = f_\beta(S_*), \quad (6.1)$$

which is an essential element for the following considerations.

Figure 6.1 displays the mean buoyancy profile and the EZ structure of a strongly sheared CBL. In contrast to the shear-free case (Figure 2.6), where $z_{il}/z_{enc} \approx 1$ and $b/b_{enc} \approx 1$, b is now significantly larger than b_{enc} and z_{il} smaller than z_{enc} .¹ As previously discussed (chapter 4.1.4.4), this means that the encroachment scales are no longer representative for the integral CBL dynamic. Hence, consequently, we modify GM14's approach by replacing the encroachment scales with ZOM related scales, which should represent a solid quasi-stationary reference framework for the sheared CBL interfacial dynamics. This includes the similarly well defined shear dependence of the relative height of the maximum buoyancy gradient, as e.g. given by the β_g/β (Eq. 2.56)

$$\frac{\beta_g}{\beta} = \frac{z_{i,g} - z_{il}}{z_i - z_{il}} = f_{\beta_g}(S_*) , \quad (6.2)$$

which is also shown by our data (Figure 5.9).

An additional scale of the vertical buoyancy structure. However, for our sheared cases, the scaling problem is more complicated than indicated above. In the ideal shear-free case (e.g. GM14) the ZOM scales are not only similar to the encroachment scales but they also directly linked to the background (or FA) stratification via $b/z_{il} \approx b_{enc}/z_{enc} = N^2$ (Figure 2.6), which can be also very intuitively expressed via the characteristic ZOM buoyancy inversion $\Delta b \approx (z_i - z_{il}) N^2$. But for sheared CBLs the contributions of entrainment to the warming of the SM can be significant (Figure 2.4) and therefore this relationship does no longer hold (Figure 6.1). Obviously, a direct measure for the relative arrangement of the EZ and the FA stratifications is

$$\rho_{\Delta b}(t) = \frac{\Delta b(t)}{(z_i(t) - z_{il}(t)) N^2} \quad (6.3)$$

Considering the evolution of the relationship between the FA and the CBL buoyancy structure, e.g. measured by $\rho_{\Delta b}$, one can distinguish between two different cases (as previously discussed in chapter 3.4.2). The first represents an idealized CBL evolution, with a linear initial profile N^2 and a constant β , which also implies a constant S_* . In these conditions, a sheared CBL grows with a square-root law similarly to the shear-free CBL (Eq. 2.60) and in any moment the relationship between N^2 and ZOM-scales², as e.g. Δb , is given by analytical expressions (e.g. Eq. 2.59).

However, for less ideal CBLs such as our LES-CBLs, which experience varying wind shear ($S_*(t) \neq const$)³, the relative position of the FA stratification with respect to the CBL buoyancy structure depends on the specific, arbitrary warming history and therefore defines another dimension of the flow problem.

As an instantaneous measure, one might consider the actual buoyancy structure of a 'real' CBL and compare it with that of an ideal CBL with $N, S_* = const$. E.g. by comparing the actual instantaneous value $\Delta b(t)$ with a reference value, which represent a CBL with the same depth $z_i(t)$, the same linear FA stratification N^2

¹These differences can be illustrated by the sensitivity of the ZOM expressions Eq. 2.64 and Eq. 2.68 to an increase of β from 0.2 to e.g. 2.

²Or the related encroachment scales respectively.

³The same hold for CBLs that grow into a non-linearly stratified FA.

and the same entrainment ratio β , which, however, has remained constant during the previous evolution. Using Eq. 2.59, which describes the ideal CBL, we can compute the respective ratio

$$\rho_{\Delta b, \beta}(t) = \frac{\Delta b(t)}{\Delta b(\beta = \text{const})} = \frac{(1 + 2\beta(t)) z_i(t) N^2}{\beta(t)} \Delta b(t). \quad (6.4)$$

In the main phase of our sheared LES-CBLs, $\rho_{\Delta b, \beta}(t)$ is generally above unity and varies between 1 and 1.2. This means that our CBLs are cooler and the inversion in the EZ is relatively stronger than in the comparable ideal case with $\beta = \text{const}$.⁴

Intermediate conclusions. All above mentioned aspects should be relevant for a detailed generalization of GM14's theory. However we were not able to consistently combine these features with – or integrate them in GM14's parameterizations. Preliminary tests with modifications of GM14's parameterizations, which take the shear dependence of β and β_g into account were rather inconclusive. The limited quality of our data makes it difficult to reproduce the mean buoyancy structure in the upper EZ with the accuracy and precision that seem necessary to re-evaluate GM14's parametrization in detail (Figure 2.8). In addition, our data set only covers a rather small range of $\rho_{\Delta b, \beta}$, yet at the same time it does not offer the advantage of the simplified conditions $\rho_{\Delta b, \beta} = 1$ or $\rho_{\Delta b} = 1$.

Moreover, the following data analysis indicates another aspect, which fundamentally complicates a detailed generalization of GM14's reasoning. When scaling shear effects in the CBL, we basically relied on the assumption of a superposition of buoyancy and shear effects, due to a lack of a more special knowledge about the flow. With respect to the integral TKE dynamics, and the related buoyancy structure this approach seems largely justified (as represented by the NZO). The respective conditions for the local interfacial dynamics are yet basically unclear. The data analysis that we will present below, shows that the impact of the interfacial layer on CBL buoyancy dynamics can be well modeled by an analogous superposition of both turbulence producing mechanisms. This means again that we can use the superposition principle for the TKE budget.

However, to combine the superposition principle directly with GM14's approach, which is based on a scaling of the buoyancy structure, one would first need to define two separate sets of length and buoyancy scales, one for each turbulence producing mechanisms. For a detailed reconstruction of the EZ dynamics analogues to GM14, it would then be necessary to understand, how these separate scales are connected with the mean buoyancy structure. A physically satisfying treatment of this issue would require a clearer conceptual notion about structure, composition and functioning of the combined sheared and convective turbulence (plus respective data), which we do not have and unfortunately cannot further pursue in this study.

But in spite of these limitations, we have clear indications that our LES-CBLs may rather well reproduce the upper EZ dynamics and its coupling with entrainment

⁴This reflects the fact that for each of our sheared CBLs the entrainment ratio is decreasing in time. This is because S_* decreases, which depends on the stress divergence that diminishes with CBL growth. Hence, driven by a stronger entrainment rate in the past, our LES-CBLs have reached a certain depth quicker and therefore have not been able to accumulate as much heat from the surface as a comparable CBL with $\beta = \text{const}$, which had more time to reach the same state.

in an integral sense. For the shear-free case, our data show a clear qualitative agreement with GM14's observations (entrainment ratio A_t in Figure 3.9). More generally, we have argued that for any growing turbulent BL the entrainment of stagnant air should result in the formation of an interfacial zone that is characterized by intermittent turbulence and a strong positive TKE-tendency (TKE spinup), a picture, which basically conforms with GM14's understanding of the upper EZ layer (E.g. their Figure 6(b) and 7). Hence, if we assume that our LESs reproduce the CBL growth regime reasonably well, we can also suspect that the directly dependent interfacial dynamics, as well as the related instationary entrainment regime are captured accordingly.

In other words, we consider both, the instationary entrainment rate (e.g. A_t) and the interfacial layer, as closely related outcomes of the CBL growth dynamics, which we understand rather well and expect to be well represented by our data set. Thus, instead of trying to reconstruct a detailed mechanism based on the EZ buoyancy structure, we directly search for a relationship between the upper EZ dynamics and the instationary entrainment rate A_t . If properly formulated, one could expect to find a comparable simple linkage between both features (analogical to Eq. 2.81) as they are directly related to the growth dynamics, which we can well reproduce with the relative simple quasi-stationary NZO.

Hence, differently to GM14, we approach the problem solely from the perspective of the TKE-dynamics and tentatively consider the buoyancy structure as an outcome. This is in line with our previous focus and offers a natural way to introduce the superposition principle of the shear- and buoyancy-dynamics. As a consequence, we here ignore the detailed intermediate steps of GM14's reasoning. Nevertheless the outcome of our attempts should still fully comply with GM14's basic concept. Note also that the variations of $\rho_{\Delta b, \beta}$ in our data set seem not to affect the validity of the NZO. Therefore we assume that their impact on the buoyancy distribution within the EZ is negligible as well.⁵

The remainder of this chapter is structured as follows: In the next section, we continue with the derivation of proper integral scales, which suit sheared CBLs. Particularly, we suggest a rather intuitive modification to the entrainment rate A_t , which better reflects the CBL integral dynamics, and still matches GM14's shear free case. Afterwards, in the following section 6.3, we eventually characterize the local dynamics of the upper EZ-layer in CBLs with varying shear and then determine its influence on the integral entrainment rate and the EZ buoyancy profile. We close our investigation of the interfacial dynamics with conclusions and short comments on our expectations for the conditions in the neutral limit.

6.2 Integral scales for the quasi-stationary CBL with varying wind shear

As mentioned above, we modify GM14's approach by replacing the encroachment scales with ZOM related scales, on which we elaborate in detail in the following. First of all, as already practiced earlier (e.g. Figure 3.8), we generally use z_{il} instead of z_{enc} as SM length scale. Thus, the relative dept of the upper EZ layer δ , will be

⁵Either because the variations of $\rho_{\Delta b, \beta}$ in our data set are not large enough ($1 < \rho_{\Delta b, \beta} < 1.2$) or due to yet unspecified compensatory effects.

measured as δ/z_{il} instead of δ/z_{enc} . Analogously, one might replace b_{enc} as reference buoyancy scale by the ZOM buoyancy b . However, we find it more intuitive to use the ZOM buoyancy jump Δb , as it represent the EZ inversion more directly.⁶

Next, we consider Δb_{zi} , which is the local buoyancy increment at the height z_i and one of GM14's essential target variables (Eq. 2.89, Figure 6.1). Consistent with our intentions, we normalize Δb_{zi} with Δb . Using the definition of β (Eq. 2.57 and 2.58), the definition of A (Eq. 2.75) and Eq. 2.76 one can directly formulate⁷ the relationship between the local entrainment ratio A_t and the normalized local buoyancy increment $\Delta b_{zi}/\Delta b$ as

$$\frac{\Delta b_{zi}}{\Delta b} \frac{z_i - z_{il}}{z_{il}} = A_t + A_d = A. \quad (6.5)$$

In the case of $S_* = const$ the factor that expresses the CBL structure, $(z_i - z_{il})/z_{il} = \beta$, is constant as well and therefore the difference in the temporal variation of $\Delta b_{zi}(t)/\Delta b$ and $A_t(t)$ only depends on A_d . For $S_* = 0$, GM14 found that $A_d \approx const$, which means that in this case $\Delta b_{zi}/\Delta b$ shows the same type of dependence on CBL maturity (as e.g. measured by δ/z_{il}) as A_t .⁸ In the following, we characterize A_t , A_d and $\Delta b_{zi}(t)/\Delta b$ for $S_* > 0$.

6.2.1 The integral entrainment ratio A_S

In Eq. 2.81, γ_0 represents the asymptotic value of A_t for $\delta/z_{enc} \mapsto 0$ and $-\gamma_1(\delta/z_{enc})$ the instantaneous deviation from it. For our further analysis we keep this basic structure of GM14's model, but for convenience rename the variables and write more generally

$$A_t = A_{t,\infty} + \Delta A_t, \quad (6.6)$$

where $A_{t,\infty}$ is the asymptotic stationary limit and $\Delta A_t = f(\delta/z_{il})$ the instantaneous deviation from it. This logic not only applies for A_t but generally for A . Hence, we write

$$\begin{aligned} A &= A_t + A_d \\ &= A_{t,\infty} + \Delta A_t + A_{d,\infty} + \Delta A_d. \end{aligned} \quad (6.7)$$

Here $\Delta A_d \approx const \approx -0.02$ for the non-sheared CBL (GM14's Figure 9).

Our data analysis so far has shown that the integral entrainment ratio $-B_{EZ}/B_{EZ}$ scales basically linearly with the normalized TKE shear production in the EZ, $S_*^3 = S_{EZ}/B_{EZ}$ (red line in Figure 4.17). Any deviations from linearity are expected to be

⁶Equally one could use the buoyancy jump Δb_m , which is defined by the ZOM layer average value $b_m = \frac{1}{z_i} \int_0^{z_i} b_z dz$, with $\Delta b_m = b_{ini}(z_i) - b_m$. But then one has to take into account that

$$\beta = \frac{w_e \Delta b}{B_0} = \frac{w_e \Delta b_m}{B_0} - A_d,$$

where A_d is the shape contribution to the entrainment ratio A , as defined earlier (Eq. 2.78).

⁷This is analogous to GM14's step to reach their Eq. 50 and 51.

⁸Compare with GM14's similar expressions, given by Eq. 2.90 and 2.81.

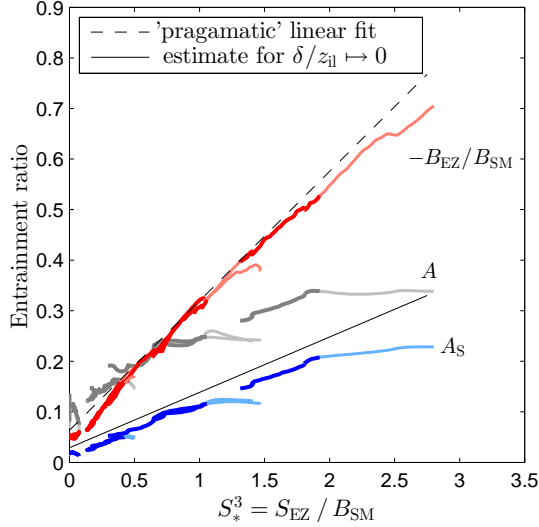


Figure 6.2: Dependence of $-B_{EZ}/B_{SM}$, A and A_S on the TKE shear-production in the EZ, S_*^3 . For clarity only wide-domain and high-resolution LES are shown. Dark colors represent the later phase of the LES. Light colors the early phase. Thin black lines show the respective linear fits used in this study: The dashed line approximates $-B_{EZ}/B_{SM}$ in the pragmatically perceived 'equilibrium entrainment regime'. The closed black line shows our estimates for the actual stationary asymptote $A_{S,\infty}$, with $\delta/z_{11} \mapsto 0$.

caused by local turbulent interaction with the stratified FA, which can be related to two different phenomena. The first one, which we have previously characterized (chapter 4.2) is the loss of fluctuation energy (TKE) via gravity waves, which are created in a regime of weak to moderate shear ($0 < S_*^3 < 1$). The second phenomena, which we examine in the following is the direct interfacial impact of FA stratification on upper EZ turbulence. A plot of $-B_{EZ}/B_{EZ}$ versus S_*^3 , as shown by the red lines in Figure 6.2, reveals both features: Wave effects result in significant reduction of the entrainment ratio for weak shear. The influence of a deep upper EZ layer is particularly noticeable for entrainment ratios in the early phase of CBL evolution (the light colors), which are significantly reduced compared to the overall linear trend (dashed black line), which represents the LES-CBLs in a later stage of evolution, with deeper CBLs and relative shallower upper EZ (smaller δ/z_{11} and smaller TKE spinup). Consequently, we would associate the linear trend with the asymptotic state for deep, mature CBLs with small δ/z_{11} . However, we note that the data close to the linear trend line represent CBLs in a similarly advanced stage of evolution, where δ/z_{11} only changes slowly in time (analogously to the interval marked by the thick blue line in Figure 2.9 for the shear-free CBL), which nevertheless may be significantly lower than the actual asymptote for $\delta/z_{11} \mapsto 0$.

For the entrainment ratio A we would expect a comparable dependence on S_*^3 . But as shown by the gray lines in Figure 6.2, the overall variation of A with S_*^3 deviates significantly from linearity. The reason is that A is formulated as ratio of local fluxes.

In contrast to $-B_{EZ}/B_{EZ}$, A does not represent integral quantities. However, a linear dependence of entrainment on TKE production terms (given by $S_*^3 = v_*^3/w_*^3$) is only expected to occur for proper spatial integrals of the entrainment and buoyancy production⁹. In the shear-free case the ratio of EZ- and SM depth, which represent the respective integral length scales, is constant. It can pragmatically be absorbed in parameters and A is therefore an appropriate measure. However the presence of shear in the EZ does not only increase the intensity of the characteristic entrainment flux B_{z_i} but also the depth of the EZ (Figure 4.14), which therefore becomes important. This feature is best summarized by the NZO, where the product of both, the characteristic flux ratio and the ratio of the integral depths, are necessary for an inviscid scaling. As both equal β (Eq. 5.27), this result in the linear dependence of β^2 on S_*^3 (Eq. 5.28).

Inspired by these findings, we suggest a simple solution: To account for the shear-driven deepening of the EZ, we construct a new integral entrainment ratio A_S , by multiplying A with $(z_i - z_{il})/z_{il} = \beta$, which is a representative measure for the relative EZ-depth of the ZOM framework (Eq. 5.27).¹⁰ Or in other words, we effectively multiply the entrainment flux in the numerator with the EZ lengths-scale $(z_i - z_{il})$ and the surface buoyancy flux in the denominator with the SM length-scale z_{il} and get integral entrainment ratio

$$A_S = A\beta = A \frac{z_i - z_{il}}{z_{il}} = A_{t,S} + A_{d,S}. \quad (6.8)$$

By substituting A further with Eq. 6.5, we also obtain

$$A_S = \frac{\Delta b_{z_i}}{\Delta b} \left(\frac{z_i - z_{il}}{z_{il}} \right)^2. \quad (6.9)$$

Using the definition for A_t and A_d (Eq. 2.77 and 2.78) the full expressions for $A_{t,S}$ and $A_{d,S}$ read:

$$A_{t,S} = A_t \frac{z_i - z_{il}}{z_{il}} = - \frac{B_{z_i}}{B_0} \frac{(z_i - z_{il})}{z_{il}} \quad (6.10)$$

$$A_{d,S} = A_d \frac{z_i - z_{il}}{z_{il}} = - \frac{z_i - z_{il}}{z_{il}} \frac{1}{B_0} \frac{d}{dt} \int_{z_i}^{z_{iu}} (b_z - b_{ini}(z)) dz. \quad (6.11)$$

A_S or $A_{t,S}$ and $A_{d,S}$ respectively have two desirable, closely connected properties. (1) The first property is given by the fact that $(z_i - z_{il})/z_{il} = \beta$, which represents the NZO¹¹, is an appropriate scale for the quasi-stationary characteristics of the sheared CBL structure in the equilibrium entrainment regime. This means that in the composite quantity $A_t\beta = A_{t,S}$ the ratio of length scales β is merely a stationary factor that does not affect the instationary properties of the local entrainment ratio A_t , which are therefore retained. The same logic holds for $A_d\beta = A_{d,S}$. (2) The

⁹This represents the most basic type of inviscid scaling of high Reynolds number turbulence in the spirit of Kolmogorov (see chapter 2.2).

¹⁰In effect, difference between A and A_S represents the difference between 'process partitioning' (PP) and 'Eulerian partitioning' (EP). As demonstrated earlier, the former is unsuitable for sheared CBLs.

¹¹Note also that the we use z_{il} (ZOM) (Eq. 5.4) in the following, which slightly improves data representation by our models.

second property follows directly from the ability of the NZO to accurately reproduce the shear-dependence of the entrainment ratio with shear, as it implies that $(z_i - z_{il})/z_{il} = \beta$ represents the correct ratio of length scales to determine of the integral entrainment ratio with varying shear. Hence, different to A , we expect A_S to adhere to an underlying linear inviscid scaling, analogous to $-B_{EZ}/B_{EZ}$ or β^2 .

This notion is supported by the darker blue lines in Figure 6.2, which show that our data for A_S indeed exhibit a rather linear dependence on S_*^3 in the later simulation stage of our LES-CBLs (compared to A , gray lines).¹² In the earlier CBL evolution A_S is systematically smaller than in the later stages, as shown by the light blue lines. The deviation from an asymptotic state (estimated by the black line), which we call $\Delta A_{S,\infty}$, seems to be clearer defined and more pronounced than for $-B_{EZ}/B_{EZ}$ (red lines), which strongly encourages a further analysis of A_S .¹³

As with $-B_{EZ}/B_{EZ}$, the basic linearity in the dependence on A_S on S_*^3 indicates the approximate quasi-stationary properties of our data set, which represents CBLs in a comparable stage of development. The observed relationship, however, remains distorted by instationary effects and the actually underlying inviscid scaling would only refer to the truly stationary contributions to A_S , which is represented by the asymptotic value $A_{S,\infty}$ (Eq. 6.6). Thus, analogously to the similarly quasi-stationary NZO (Eq. 5.28), we have good reasons to suggest the scaling

$$A_{S,\infty} = A_\infty \frac{z_i - z_{il}}{z_{il}} = c_{[A_S,B]} + c_{[A_S,S]} S_*^3. \quad (6.12)$$

Here the constant $c_{[A_S,B]}$ determines the buoyancy contribution to entrainment and the constant $c_{[A_S,S]}$ the shear-driven one. Just as A (Eq. 6.7), we subdivide A_S in the components

$$\begin{aligned} A_S &= A_{S,\infty} + \Delta A_S \\ &= A_{t,S,\infty} + \Delta A_{t,S} + A_{d,S,\infty} + \Delta A_{d,S} \end{aligned} \quad (6.13)$$

With Eq. 6.12 we can also assume that each component of $A_{S,\infty}$ scales linearly with S_*^3 . Thus

$$A_{t,S,\infty} = c_{[A_{t,S},B]} + c_{[A_{t,S},S]} S_*^3, \quad (6.14)$$

and

$$A_{d,S,\infty} = c_{[A_{d,S},B]} + c_{[A_{d,S},S]} S_*^3. \quad (6.15)$$

¹²In GM14's model for A , the dependence on the CBL structure β is absorbed in the constants. However as the CBL structure varies with shear, we find the incorporation of β into the new representative measure A_S more intuitive.

¹³As discussed in chapter 3.4.2, our values of B_{EZ} seem systemically biased, due to a too low spatial resolution of the upper EZ. Particularly in the begin phase of our LESs, but also in the earlier main phase, the upper EZ is too deep and the B_{EZ} therefore too large. Hence we expect A (or A_S respectively), which is diagnosed in the central EZ at z_i , to be a more robust measure, which better represents the actual variations of entrainment.

As before $c_{[A_t,S,B]}$, $c_{[A_t,S,S]}$, $c_{[A_d,S,S]}$ and $c_{[A_d,S,B]}$ are constants. Again, the subscript B signifies the buoyancy-driven contribution and S the shear-driven one. Equations 6.13 - 6.15 also imply that the parameters for the asymptotic total flux $A_{S,\infty}$ (Eq.6.12) are given by the sums

$$\begin{aligned} c_{[A_S,B]} &= c_{[A_t,S,B]} + c_{[A_d,S,B]}, \\ c_{[A_S,S]} &= c_{[A_t,S,S]} + c_{[A_d,S,S]}. \end{aligned} \tag{6.16}$$

To illustrate the reasoning above, the shear dependence of A_t , $A_{t,S}$ and $A_{d,S}$ and the linear scaling for $A_{t,S,\infty}$ and $A_{d,S,\infty}$ of our best LESs are depicted in Figure 6.3. Full colors signify mature CBLs in the equilibrium entrainment regime (main period) and light colors the conditions before (early period). The considerable difference $\Delta A_{t,S}$ between the $A_{t,S}$ of our LES (red markers) and our estimate for $A_{t,S,\infty}$ (black lines) indicates how far away our LES-CBLs actually still are from stationary conditions. However, except for the early period of the CBLs with strong shear, $\Delta A_{d,S}$ is rather small, which agrees with GM14's finding for the shear-free case.

With GM14's DNS-based specifications for $\gamma_0 = A_{t,\infty} \simeq 0.12$, $A_d \simeq const = -0.02$ and the CBL layering $(z_i - z_{il})/z_{il} \simeq 0.174$ (their table 2),

$$c_{[A_t,S,B]} = \gamma_0 \frac{z_i - z_{il}}{z_{il}} \simeq 0.021 \quad \text{and} \quad c_{[A_d,S,B]} = A_d \frac{z_i - z_{il}}{z_{il}} \simeq -0.0035 \tag{6.17}$$

can be directly estimated for $S_* = 0$. However, as noted earlier (section 3.4.2), the values that we can derive from our best LES, $A_{t,\infty} \approx 0.15$, and the CBL structure factor, $\beta = (z_i - z_{il})/z_{il} \approx 0.19$, are both somewhat larger and still vary throughout the CBL evolution. Thus, our data rather give

$$c_{[A_t,S,B]}(\text{LES}) \approx 0.029 \quad \text{and} \quad c_{[A_d,S,B]}(\text{LES}) \approx -0.0038. \tag{6.18}$$

In principle, $c_{[A_t,S,S]}$ and $c_{[A_d,S,S]}$ could be estimated directly by data of very mature CBLs that are close to the asymptotic state.¹⁴ However, our fast growing CBLs are far from that state. Hence, our estimates $c_{A_t,S,S} \approx 0.135$ and $c_{A_d,S,S} \approx -0.022$ fall out from the following data analysis, which simultaneously addresses $\Delta A_{t,S}$ and $\Delta A_{d,S}$.

6.2.2 Scaling the local buoyancy increment Δb_{zi} for $S_* > 0$

According to GM14, the local buoyancy increment at Δb_{zi} (Figure 6.1, Eq. 2.89) characterizes the buoyancy profile in the central EZ well (Figure 2.7). Its evolution, as described by Eq. 2.90, also determines GM14's model for the evolution of A_t . GM14's model for $\Delta b_{zi}/b_{enc}$ (Eq. 2.90) also determines GM14's model for the evolution of A_t . With Eq. 6.5 we already have introduced an alternative normalization of Δb_{zi} , using Δb instead of b_{enc} , and the explicit relationship with A_t and A_d , which, however,

¹⁴Experimentally, these limiting conditions are difficult to approach as they imply extremely small growth-rates. Thus, the CBLs must be very deep and/or the turbulent forcing very weak and/or FA stratification very strong. Each of these conditions is difficult to reproduce.

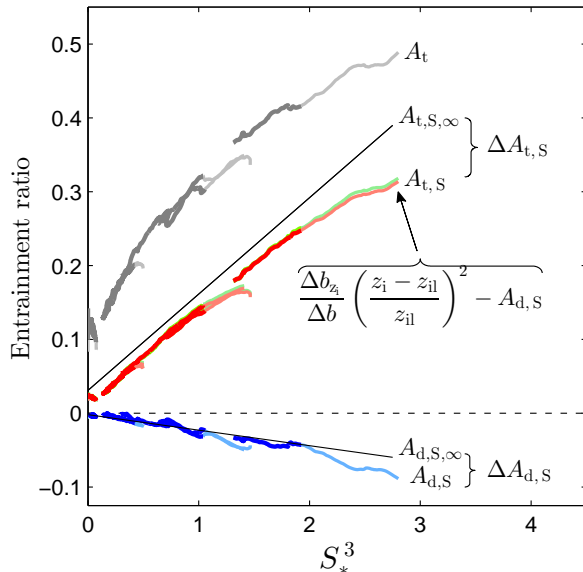


Figure 6.3: Dependence of various quantities on S_*^3 . Red lines represent $A_{t,S,\infty}$ directly and green lines the lhs of Eq. 6.19. Darker colors represent the later phase of the LES, light colors the early phase. Black lines indicate our estimation for $A_{t,S,\infty}$ and $A_{d,S,\infty}$, respectively. For clarity only wide-domain and high-resolution LES are shown.

still fully conforms with GM14's approach. Inserting Eq. 6.8 into Eq. 6.9, directly gives the respective relationship between the integral entrainment ratio $A_{t,S}$ and the normalized buoyancy jump $\Delta b_{z_i}/\Delta b$:

$$\frac{\Delta b_{z_i}}{\Delta b} \left(\frac{z_i - z_{il}}{z_{il}} \right)^2 - A_{d,S} = A_{t,S}. \quad (6.19)$$

The dependence of the lhs of Eq. 6.19 on S_*^3 is shown in Figure 6.3 by the green lines. The good agreement with $A_{t,S}$ (red lines) supports our approach. A slight disagreement that is restricted to a short period in beginning of the early LES phase (light colors) with strong shear ($S_*^3 > 2.3$) may reflect numerical uncertainties in the estimation of the z_i and the time-derivative in A_d in these conditions.

6.3 Influence of shear on interfacial turbulence, entrainment and the EZ buoyancy structure

In this section we first analyze and characterize the dynamics of the upper EZ-layer in CBLs with varying wind shear. With these results we then determine the influence of the upper EZ-dynamics on entrainment, as given by $A_{t,S}$ and $A_{d,S}$, and on the buoy-

ancy profile, as represented by $\Delta b_{zi,g}$ and Δb_{zi} , which both measure the deformation of the initial buoyancy profile (Figure 6.1).

6.3.1 Shear dependence of the eddy penetration depth δ

It is well known that TKE-dynamics in shear-driven, high Reynolds-number flows are typically determined by local scales (see also section 7.2). The flow conditions in a purely shear-driven stable BL, which grows into a stably stratified FA, strongly resemble those in a similarly stratified EZ of a sheared CBL. Observations (e.g. Conzemius and Fedorovich, 2006a) indicate that these commonalities also result in similar flow dynamics¹⁵, which therefore inspires our reasoning in the following.

The TKE dynamics of purely shear-driven neutral BLs scales very well with the length scale u_*/N (Jonker *et al.*, 2013). Although the surface friction velocity u_* may rather be interpreted as a measure of the characteristic integral TKE shear production, u_*/N signifies local processes as it is independent of BL depth.¹⁶ By expressing the EZ shear-production S_{EZ} in terms of the velocity scale v_* (Eq. 4.24) we can construct the length scale v_*/N , which much resembles $w_*/N \sim \delta$ (Eq. 2.73) and therefore could be associated with the influence of stratification on mechanically produced turbulence at the upper EZ interface¹⁷.

If one considers an ‘eddy’, which is created by shear in the EZ, e.g., in the area of strongest shear production (Figure 4.1), one can presume that with a certain probability its momentum is directed upwards into the FA. The penetration depth δ_S will depend on its initial vertical velocity (A) and the FA stratification (B), as it will be decelerated by buoyancy forces, when entering the inversion. The latter process will also depend on the initial buoyancy of the eddy (C).

Completely analogously to convective plumes, (A) should statistically depend on the intensity of the TKE production, thus on v_* . Analogously to the penetration of a convective plume, (B) is given by N . Concerning (C) one may consider the local balance of TKE shear-production and entrainment, which typically characterizes shear flows beneath a stratification and which is often expressed in terms of a constant ‘critical bulk Richardson number’ (Jonker *et al.*, 2013, and section 7.2.2). Such a balance indicates a dynamic self-control of the capping inversion, which would imply that v_*/N can be associated with a characteristic buoyancy difference between the intruding eddies and their surroundings. Without elaborating this idea further, we here, in a basic analogy to the free convective case, directly suggest a shear driven contribution to the upper EZ length scale

$$\delta_S = c_{\delta,S} (v_*/N), \quad (6.20)$$

with $c_{\delta,S} \approx const.$ If we, once more, make the most simplistic assumption that

¹⁵For details see our chapters 7.2.2, 7.2.3 and 7.4.2, where we investigate this issue and show that certain ‘critical Ri’s, which are a typical feature of stable shear flows, also govern the EZ of sheared CBLs.

¹⁶This seems reasonable if one can rely on a straight self-similarity of velocity- and stress profiles, as shown by Jonker *et al.*’s (2013) DNSs. For stable BLs with a more complicated wind profile, e.g. with a Coriolis forcing, the local character of both the TKE and the momentum dynamics should be better represented by the local stratification and a locally defined ‘friction velocity’, e.g. by $S_z^{1/3}/N_z$.

¹⁷To stress the consistency of our considerations, we remind the reader that both velocity scales of CBL TKE-production can be also expressed by the ZOM quantities: $v_*^3 \simeq w_e \Delta U^2$ and $w_*^3 \simeq B_0 z_{il}$.

convective and shear-driven turbulence superimpose¹⁸, the characteristic length scale for the upper EZ of sheared CBL would be

$$\delta = \delta_B + \delta_S, \quad (6.21)$$

where δ_S is given by Eq. 6.20 and the convective contribution is given by

$$\delta_B = c_{\delta,B} (w_*/N), \quad (6.22)$$

which equals GM14's model of δ for the non-sheared CBL (Eq. 2.73). $c_{\delta,B}$ and $c_{\delta,S}$ are constants, with $c_{\delta,B} \simeq 0.55$ as proposed by GM14 and $c_{\delta,S} \approx 0.02$ according to our LES data.

With the definition of δ (Eq. 2.69, Figure 6.1) we can diagnose δ/z_{i1} directly from the buoyancy profile of our LES. The correlation between diagnosed and modeled

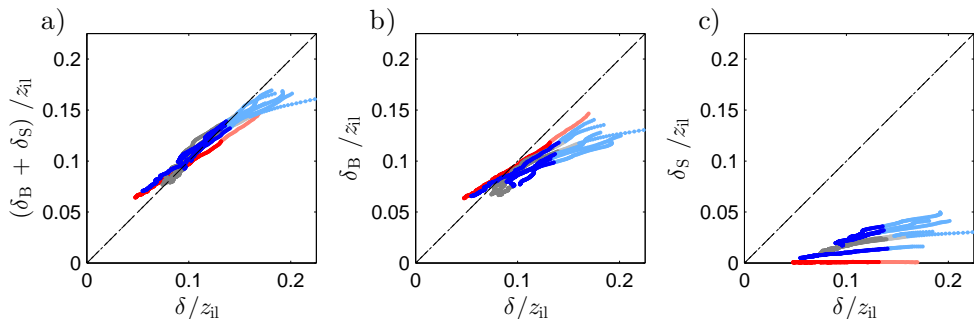


Figure 6.4: Correlation between diagnosed (Eq. 2.69) and modeled δ for a series of LES. δ modeled with buoyancy- and shear-driven contributions $\delta_B + \delta_S$ (a), with buoyancy-driven contributions δ_B only (b) and with shear-driven contributions δ_S only (c). Red markers represent the shear-free CBLs, blue markers the strongly sheared ones ($S_*^3 > 0.4$) and gray markers the moderately sheared CBL ($0.1 < S_*^3 < 0.4$), which lose a significant amount of TKE via gravity waves. For each case, light colors represent the early evolutionary phase and dark colors the later main phase. Only high resolution and wide domain LESs with moderate FA stratification are shown.

values for δ of our series of LES with widely varying shear are shown in Figure 6.4. Here red markers represent the shear-free CBLs, blue markers the strongly sheared ones and gray marker the moderately sheared CBL, which – via gravity waves – drain a significant amount of TKE into the FA. For each case, light colors represent the early LES phase and dark colors the later main phase, with mature CBLs. Figure 6.4(a) supports our reasoning as data of all cases align rather well with the suggested model (Eq. 6.21). Both the convective and the shear-driven contribution are important, as demonstrated by Figure 6.4(a) and (b), where δ is plotted either versus δ_B or δ_S only,

¹⁸A further idea in this context: As long as an organized convective structure is present in a sheared EZ, the strongest shear and TKE-shear production in the upper EZ should spatially correlate with the impinging thermal updrafts, as these transport slow, surface born air masses, with a pronounced velocity deficit $\Delta U' \sim U_g - U_{\text{thermal}} > 0$. See also chapter 7.4.1 and our discussion of regime II in chapter 7.4.2.

which in each case results in a much wider spread and systematic deviation from equality.

Stronger errors are noticeable for CBLs in or close to free convection (red marker and some gray markers), for both small δ/z_{il} and large δ/z_{il} . However, in these conditions the scaling equals the one of GM14, which is very well supported by their high quality data. Any deviations are therefore clearly a sign of a systematic bias of our LESs, which are most pronounced in the convective limit (see section 3.4.2). Due to significantly deeper EZs this issue appears to be much less severe for the sheared LES-CBLs in the later simulation phase (Figure 6.4(a), dark blue markers). We also observe a systematic underestimation of the modeled δ/z_{il} for $\delta/z_{il} > 0.15$. As these values represent shallow, strongly sheared CBLs in the early phase of the LESs (light blue markers), their physical representativity is again doubtful and the observed deviations are very likely influenced by the low spatial resolution. Interestingly, however, also in this phase the various LESs still agree quite well. Furthermore, according to GM14, we must also be aware of basic limitations of our approach. For larger δ/z_{il} (e.g. > 0.15) the CBLs touch the transitional 'weak stratification regime' (with a relatively thick EZ) in the early stage of CBLs formation as described by GM14. Here the CBL depth is still of the order of the convective Ozmidov scale L_0 ($z_{il}/L_0 < 10$) and therefore the influence of the FA stratification is still relatively weak. Thus, the assumptions for the GM14's scaling are not fully met anymore, which, e.g., seems to result in a reduced c_δ (GM14's Figure 8(a)). Moreover, in this early stage CBLs do not feature 'equilibrium entrainment' conditions, which should affect the CBL layering, as indicated by the gray markers in Figure 5.8.¹⁹ But due to the low data quality in the early simulation phase, we do not further try to interpret the visible deviations.²⁰

It is worthy of note that the TKE-drainage due to gravity-waves has no noticeable impact on δ , as shown in Figure 6.4(a) by the good agreement between gray and blue markers. This finding is plausible, if we assume that the kinetic energy outflow by gravity waves is induced by the systematic horizontal component of the impinging thermal plumes, when they are slightly sheared ($0.1 < S_* < 0.9$). The drainage of kinetic energy would therefore not affect the initial intrusion of a plume, which represents the characteristic depth δ , but primarily the horizontal fluctuations and also the subsequent mixing.²¹ Hence, we imagine that it is particularly the loss of kinetic energy in horizontal fluctuations that reduces mixing, possibly by reducing the mixing efficiency of the plumes' return movement. TKE wave-losses therefore well affect the TKE budget of the fully turbulent part of EZ, which is represented by the lower EZ layer. This we demonstrated before e.g. in Figure 4.14 and 4.18.

¹⁹According to GM14, the transition between the weak- and the strong stratification regime happens at $z_{il}/L_0 \simeq 10$. With Eq. 2.92 we can determine the corresponding limit $\delta/z_{il} \approx 0.12$, which also marks the limit above which our data start to deviate from the proposed scaling (Figure 6.4(a), gray markers).

²⁰Nevertheless, the systematic behavior indicates the possibility of a rather straight extension of the proposed scaling to the earlier phase, before the 'equilibrium entrainment' regime (GM14's 'intermediate regime') is reached. See also GM14's appendix A.

²¹See also our discussion of regime II in section 7.4.2.

6.3.2 Significance of δ , b_δ and the EZ buoyancy fluctuations

Above we have demonstrated the validity of expression Eq. 6.21. It shows that both shear and buoyancy provide the energy for the penetrating eddies that form the upper interfacial EZ layer of our LES-CBLs. According to GM14, the characteristic depth δ of the upper EZ is an appropriate quantity to scale the influence of the upper EZ on integral entrainment. However for a CBL with varying shear δ is not sufficient, if one assumes that also the properties of the upper EZ layer turbulence vary with shear. Thus, we expect that the composition of the turbulence sources, i.e. the ratio of shear- and buoyancy-driven turbulence production is important for the actual properties of upper EZ 'turbulence' and its connection with the lower EZ. We can demonstrate

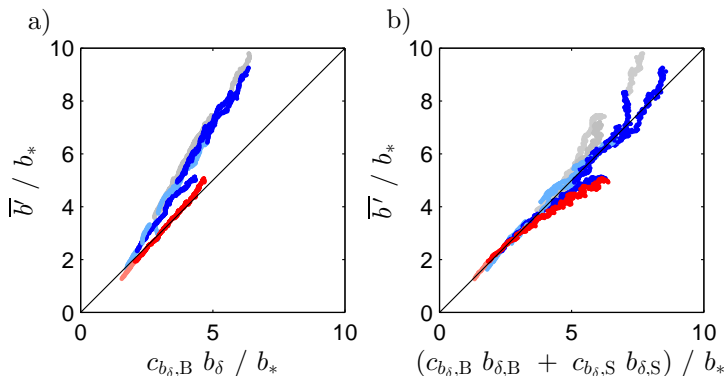


Figure 6.5: Modeled versus observed values of the characteristic buoyancy fluctuations $b'(z_{i,g})$ (rms or standard deviation). All values normalized by convective buoyancy scale $b_* = B_0/w_*$. In (a) the modeled values are proportional to b_δ , as found by GM14 for the non-sheared CBL. In (b) the values are modeled as superposition of a convective and a shear-induced buoyancy scales $b_{\delta, B}$ and $b_{\delta, S}$, which are estimated via Eq. 6.24. Colors as in the previous Figure 6.4.

this idea by considering the upper EZ buoyancy scale b_δ , which is readily defined by Eq. 2.70 or by $b_\delta = N^2 \delta + \Delta z_{i,g}$ (Figure 6.1). According to GM14, b_δ is very good scale for the maximum buoyancy variance in the EZ, $b'(z_{i,g})$, which occurs very close to $z_{i,g}$ (Figure 2.5 (c)) and signifies the buoyancy structure of the intermittent upper EZ. Thus, GM14 found $b_\delta = c_{b_\delta, B} b'(z_{i,g})$, with $c_{b_\delta, B} \simeq 0.55$. Figure 6.5(a) shows the correlation between $c_{b_\delta, B} b_\delta$ and $b'(z_{i,g})$, both normalized by convective scale b_* (Eq. 2.36, Figure 2.5). As in the previous Figure, data from the wide domain and high resolution LESs are shown, using the same color code. We find that the shear-free case (red markers) agrees well with GM14's parametrization. The sheared cases (blue markers), however, clearly follow a different regime, which demonstrates that δ and b_δ , respectively, are not representative for the combined convective and shear-driven turbulence in the upper EZ. Therefore it seems natural to consider $b'(z_{i,g})$ as a composition of a buoyancy and a shear-driven contributions instead. Accordingly, we define an effective buoyancy scale for the upper EZ of a sheared CBL as the sum

of a buoyancy and shear related contributions:

$$b_{\delta,BS} = b_{\delta,B} + b_{\delta,S}. \quad (6.23)$$

In line with the definition of b_δ (Eq. 2.70) one could estimate these contributions to be

$$b_{\delta,B} = \frac{\partial b}{\partial z}(z_{i,g}) \delta_B \quad \text{and} \quad b_{\delta,S} = \frac{\partial b}{\partial z}(z_{i,g}) \delta_S. \quad (6.24)$$

It is unclear how to diagnose δ_B and δ_S from data. However, we can model them with Eq. 6.22 and 6.20. As $b_{\delta,B}$ and $b_{\delta,S}$ represent turbulence with different qualities, we associate each of them with a separate contribution to the EZ buoyancy variance. Hence, we supplement GM14's original parametrization with an additional term, which accounts for the shear-driven contribution to buoyancy variance. This gives

$$b'(z_{i,g}) = c_{b_{\delta,B}} b_{\delta,B} + c_{b_{\delta,S}} b_{\delta,S}, \quad (6.25)$$

where $c_{b_{\delta,B}}$ and $c_{b_{\delta,S}}$ are constants. $c_{b_{\delta,B}} \simeq 0.55$ is given by GM14 and $c_{b_{\delta,S}} \approx 1.4$ estimated from our data. For $v_* = 0$ the expression reduces to GM14's scaling. By inserting Eqs. 6.24 in Eq. 6.25 one gets the expression

$$b'(z_{i,g}) = \frac{\partial b}{\partial z}(z_{i,g}) (\kappa_B \delta_B + \kappa_S \delta_S), \quad (6.26)$$

with, $\kappa_B = c_{\delta,B} c_{b_{\delta,B}}$ and $\kappa_S = c_{\delta,S} c_{b_{\delta,S}}$. Figure 6.5(b) shows the correlation between diagnosed $b'(z_{i,g})$ and values parametrized by Eq. 6.26, Eq. 6.22 and 6.20 for our data set. Overall, we find a reasonable agreement over the full range of values, which nearly spans an order of magnitude. But the data also show some systematic deviations from the model, which surprisingly mostly occur in the later main phase of the LESs. For the shear-free case (red dots), these can be clearly related to simulation issues, as the shown parametrization is well supported by GM14's DNSs. We have no clear idea about the cause for these deviations. They might be an early indication for the undesired disturbance of the CBL by the sponge layer, which affects the discarded late phase of our LESs (Figure 3.1).

6.3.3 Interfacial effects on entrainment

To determine the influence of the upper EZ on the integral EZ, GM14 demonstrated step by step that the normalized EZ buoyancy scales b_δ/b_{enc} , $b_{z_{i,g}}/b_{\text{enc}}$, b_{z_i}/b_{enc} and, consequently, the entrainment rate A can be modeled as sum of a stationary constant value and an instantaneous deviation, which linearly depends on the relative thickness of the upper EZ, δ/z_{enc} . The only new aspect that we add to this conceptual framework is EZ-shear, which adds a further dimension to the problem. But we assume that if shear effects are properly considered, GM14's basic arguments are similarly valid for sheared CBLs.

Integral reference scales. With respect to the integral properties of the CBL, we take shear into account by replacing the encroachment scales with the similar but more

versatile ZOM scales and by reformulating the entrainment ratio A as the physically more appropriate integral quantity $A_S = A_{t,S} + A_{d,S}$ (introduced in section 6.2.1). So if wind shear is present, the stationary characteristics of the mature CBL, which are the 'constant layering', the asymptotic state of the EZ buoyancy-flux profile, as, e.g., represented by entrainment rate $A_{t,S,\infty}$, and the related EZ buoyancy profile all become a function of S_* . Hence, we assume that for any S_* GM14's approach (e.g. Eq. 2.81) can be retained and the actual EZ dynamics can be dissected in a asymptotic stationary limit and a deviation, which is caused by the local influence of the stratified FA. To determine this influence, we have to consider the additional impact of shear on the local interfacial dynamics, for which we developed a concept in the previous section.

Local turbulence dynamics. According to GM14 the characteristic length scale δ is an appropriate quantity to scale the upper EZ and its influence on the EZ structure and dynamics. However, in the previous section we argued that for a CBL with varying shear the upper EZ layer has not a uniform quality. Therefore, it should not be sufficiently characterized by δ alone. But, if represented by individual length scales δ_B and δ_S , the contributions of both turbulence creating processes to the upper EZ's dynamics seem to superimpose well, as just demonstrated by the parametrization of the characteristic EZ buoyancy variance $b'(z_{i,g})$ (Eq. 6.26).

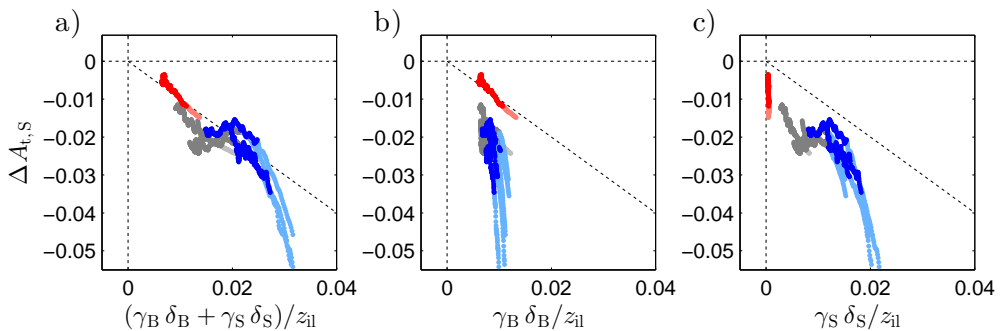


Figure 6.6: Correlation between diagnosed and modeled $\Delta A_{t,S}$ for a series of our LES with varying shear. $\Delta A_{t,S}$ modeled with buoyancy- and shear-driven contributions (a), with buoyancy-driven contributions only (b) and with shear-driven contributions only (c). Red markers represent the shear-free CBLs, blue markers the strongly sheared ones ($S_*^3 > 0.4$) and gray markers the moderately sheared CBL, which lose a significant amount of TKE by wave-losses ($0.1 < S_*^3 < 0.4$). For each case, light colors represent the early phase of LES and dark colors the later phase with mature CBLs. Only high resolution and wide domain LESs with moderate FA stratification are shown.

$A_{t,S}$ versus upper EZ dynamics. Finally, we combine all the above mentioned aspects and directly consider the impact of the upper EZ on the entrainment ratio $A_{t,S}$, which is the main objective of this chapter. In full analogy to GM14 (Eq. 2.81) we suggest that $\Delta A_{t,S}$, which is the reduction of integral entrainment due to influence

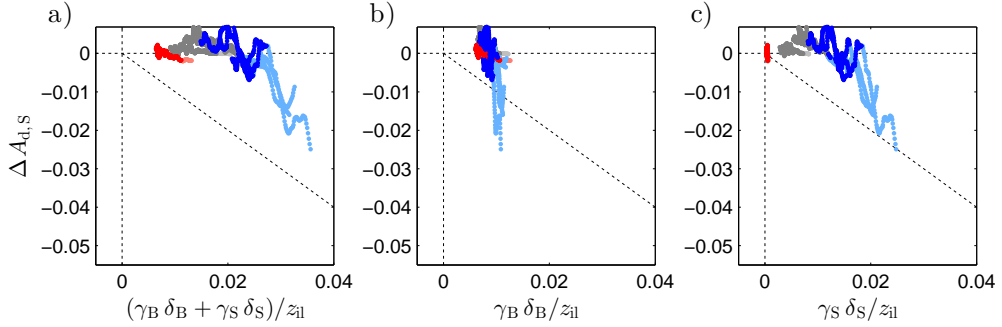


Figure 6.7: As Figure 6.6, but displaying the correlation between diagnosed and modeled $\Delta A_{t,S}$. Colors as in the previous Figure 6.6.

of the upper EZ layer, scales with a linear combination of the local length scales

$$-\Delta A_{t,S} = \gamma_B (\delta_B/z_{il}) + \gamma_S (\delta_S/z_{il}). \quad (6.27)$$

Our physical interpretation of this expression is mostly identical to GM14's interpretation of the shear-free case (section 2.6), except that the information of the EZ structure is now absorbed in the entrainment ratio $A_{t,S}$ and the interfacial layer is now formed by two different entities (virtual 'sub-layers'), representing the buoyancy- and the shear-induced dynamics. To stress the formal similarity with GM14 (Eq. 2.81), one could also define an 'effective' upper EZ lengths scale $\delta_{\text{eff}} \neq \delta$:

$$\delta_{\text{eff}} = \gamma_B \delta_B + \gamma_S \delta_S \quad (6.28)$$

so that

$$\Delta A_{t,S} = -\delta_{\text{eff}}/z_{il}. \quad (6.29)$$

With $A_{t,S} = A_{t,S,\infty} + \Delta A_{t,S}$ (Eq. 6.13) the whole local entrainment term $A_{t,S}$ is given by

$$A_{t,S} = A_{t,S,\infty} - \delta_{\text{eff}}/z_{il}, \quad (6.30)$$

where $A_{t,S,\infty} = f(S_*)$ (Eq. 6.12).

To directly express the shear dependence of $\Delta A_{t,S}$, one also can rewrite Eq. 6.28 as a function of S_* , using $v_*/w_* = S_*$ (Eq. 4.23), Eq. 6.20 and 6.22:

$$\Delta A_{t,S} = -\gamma_B \frac{\delta_B}{z_{il}} \left(1 + \frac{\gamma_S c_{\delta S}}{\gamma_B c_{\delta B}} S_* \right). \quad (6.31)$$

Here the expression in brackets represents a steering factor, which accounts for the impact of EZ shear on $\Delta A_{t,S}$ of a pure CBL.

With GM14's data for $S_* = 0$, one gets $\gamma_B = \gamma_1(z_i - z_{il})/z_{il} \simeq 0.054$, with $\gamma_1 \simeq 0.31$ and $(z_i - z_{il})/z_{il} \simeq 0.174$. However, our best LES conforms with significantly larger values for $(z_i - z_{il})/z_{il} \approx 0.19$ and $\gamma_1 \approx 0.5$ so that $\gamma_B \approx 0.095$. With respect to the shear contributions, our LESs suggest $\gamma_S \approx 0.54$.

The resulting correlation between modeled and diagnosed $\Delta A_{t,s}$ is shown in Figure 6.6. It is organized like the previous Figure 6.4. Figure 6.6(a) shows that the suggested scaling (Eq. 6.27) basically works, as the data from the purely convective (red) and sheared CBLs (blue) align rather well. Figure 6.6(b) and (c) demonstrate that for a successful scaling of our data indeed both shear-driven and convective contribution are relevant. In (b) only the convective contribution (first term in Eq. 6.27) and in (c) only the shear-driven contribution (second term in Eq. 6.27) is considered. Both variants results in a systematic misalignment of the data points.

For the non-sheared case the proposed model equals GM14's scaling. Apart from the too large parameters, also the slight misalignment for the respective data in (a) and (b) can therefore be attributed to LES problems. Stronger, but still remarkably well-defined, systematic deviations from the identity line occur again for strongly sheared LESs in the early simulation phase (light blue dots). However, in the early phase the assumed equilibrium-entrainment- and constant-layering-conditions (Eq. 5.28, Figure 5.8, gray lines) are not yet met. Moreover, due to the comparably low resolution of the shallow and strongly sheared CBLs, these LES are probably significantly biased. But it is worth noting that the sign and the gradual increase of the deviation (observed values higher than model values) concur with GM14's observation for purely convective CBLs in the same range of $\delta/z_{il} > 0.12$ (See GM14's Figure 9 for $z_{enc}/L_0 < 10$).

To define the beginning of the CBL main phase, we used the constant natural layering as criteria, which we simply diagnosed by visual inspection, as illustrated by Figure 5.8. Due to the smooth evolution of the CBL structure, the exact choice of the transitional point is rather approximate. We find that the chosen points all fulfill the conditions $0.15 < \delta/z_{il} < 0.11$, which suggest that GM14's criterion $\delta/z_{il} < 0.12$ also holds for our sheared CBL. Indeed, all our results can be well reproduced, if this criterion is met.

A further remarkable finding is that $\Delta A_{t,s}$ for the weakly sheared LES-CBLs (gray markers) are significantly lower than the model estimate. This makes sense as these data represent CBLs that are affected by significant drainage of TKE, a process that is not considered in the proposed model. Hence this observation also supports our general stance to distinguish between the local interfacial effects on turbulent mixing and the formation of gravity-waves.²²

$A_{d,s}$ versus upper EZ dynamics. Figure 6.3 shows the shear dependence of the main-phase data of $A_{d,s}$. It basically represents a line (dark blue markers). Only small deviations from that line occur during the evolution of a single LES. This indicates that also for sheared CBLs $A_{d,s} \approx A_{d,s,\infty}$ and therefore $\Delta A_{t,s} \approx 0.0$ as found by GM14 for the shear-free CBL. From our data, we estimate the slope of the linear shear dependence of $A_{d,s,\infty}$ (Eq. 6.15, Figure 6.3) as $c_{[A_{d,s,S}]} \approx -0.022$.

For a direct comparisons with $\Delta A_{t,s}$, we plot $\Delta A_{d,s}$ versus the same parameterizations (Eq. 6.31) in Figure 6.7, which is also constructed in the same way as the previous Figure 6.6. We find that $\Delta A_{d,s}$ scatters slightly around zero for most of the

²²This raises questions about the relationship between both processes. In particular, how do the TKE wave-losses and wave-drag develop during the CBL evolution? Due to relatively large scatter and high uncertainty, we did not find clearer indications in our data. Thus, in this study we do not further investigate this rather subtle issue, which seems to require a better data base.

data range, indicating the rather constant change of the upper EZ buoyancy profile in the equilibrium entrainment regime, as represented $A_{d,S,\infty}$ (Eq. 6.15). Significant, but apparently systematic deviations occur for strongly sheared CBLs in the early evolutionary phase (light blue markers). This is not surprising as in the early phase the CBL's 'layering' is not yet constant, and the effect of profile-shape changes are supposedly much more significant. But then the data quality is also low, which may enhance this effect.

For conditions with weak shear and significant gravity-wave driven leakage of TKE (gray markers), we find somewhat positive values for $\Delta A_{d,S}$. With respect to the integral entrainment ratio, this would partly compensate the systematic negative shift that we found for $A_{t,S}$, indicating a characteristic TKE re-distribution within the EZ. However, as we showed in detail before, the net-effect of TKE-leakage on entrainment for low S_* remains significant (chapter 4.2.3).

6.3.4 Interfacial effects on the buoyancy structure

To finalize our analysis, we shortly consider the impact of the interfacial dynamics on the EZ buoyancy-structure. Unlike GM14, who use the buoyancy structure as basis for the derivation of the entrainment model, we here tend to consider the EZ buoyancy-profile shape rather as a consequence of the CBLs interfacial dynamics, as discussed in the beginning of this chapter. As GM14, we here consider the influence of CBL maturity on the buoyancy profiles at the characteristic heights $z_{i,g}$ and z_i , which represent the upper and the central EZ (Figure 6.1).

$b_\delta/\Delta b$ and $\Delta_{z_{i,g}}/\Delta b$ versus the upper EZ dynamics. The essential local buoyancy scale of the upper EZ is b_δ , which we already characterized as a composite quantity $b_{\delta,BS}$ (Eq. 6.23, and 6.24). At this spot we are interested in its relationships with the overall CBL buoyancy structure, as measured by the NZO buoyancy jump Δb . Analogously to Eq. 2.84, we suppose that also for the sheared case the ratio $b_\delta/\Delta b$ depends on the relative depth of the interfacial layer. Similarly as before, we assume that for sheared CBL the ratio $b_\delta/\Delta b$ scales with vertical CBL structure or the 'layering' of the CBL respectively, so that we define the respective shear-insensitive quantity $b_{\delta,S}/\Delta b$ (subscript S). But as b_δ is situated at $z_{i,g}$, we this time should choose $(z_{i,g} - z_{i1})/z_{i1} = \beta_g$ instead of β . Hence

$$\frac{b_{\delta,S}}{\Delta b} = \frac{b_\delta}{\Delta b} \frac{z_{i,g} - z_{i1}}{z_{i1}}. \quad (6.32)$$

However as β_g roughly equals 1.35β (Figure 5.9) our results only slightly change if we use the simpler and better defined NZO quantity β instead.²³ As previously, we dissect $b_\delta/\Delta b$ in a stationary limit (subscript ∞) and an instationary deviation

$$\frac{b_{\delta,S}}{\Delta b} = \frac{b_{\delta,S,\infty}}{\Delta b} + \Delta \frac{b_{\delta,S}}{\Delta b}. \quad (6.33)$$

Assuming β_g/β to be approximately constant or to depend only linearly on S_*^3 respectively, one can also expect the asymptotic $b_{\delta,S,\infty}/\Delta b$ to depend roughly linearly

²³As a potential further improvement the actual relationship $\beta_g/\beta = f(S_*)$ could be taken into account (Figure 5.9). For this, however, one should use better data set.

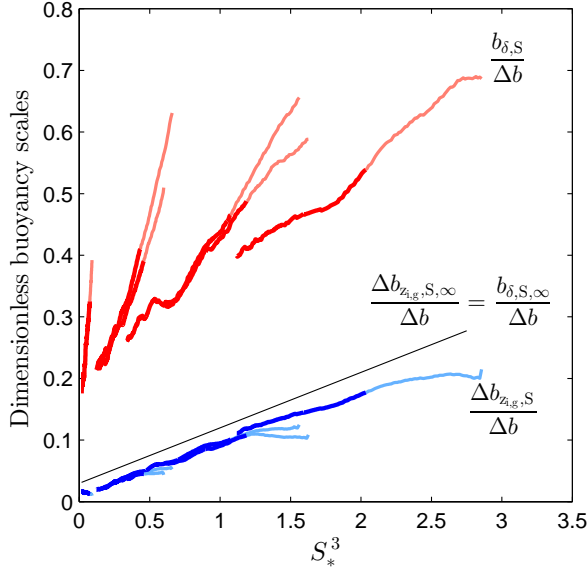


Figure 6.8: Dependence of the characteristic buoyancy scales b_δ and $\Delta b_{z_{i,g}}$ on S_*^3 . Darker colors represent the later mature phase of the LES, light colors the early phase. The black line indicates our estimation for both asymptotic relationships for $\delta/z_{i1} \rightarrow 0$. For clarity only wide-domain and high-resolution LES are shown.

on S_*^3 . Hence

$$\frac{b_{\delta,S,\infty}}{\Delta b} \approx c_{[b_{\delta,S},B]} + c_{[b_{\delta,S},S]} S_*^3. \quad (6.34)$$

Our data suggest that $c_{[b_{\delta,S},B]} \approx 0.03$ and $c_{[b_{\delta,S},S]} \approx 0.09$ (Figure 6.8, black line).

The deviation from the asymptotic value, $\Delta(b_{\delta,S,\infty}/\Delta b)$, as shown by the difference between the black line and red lines in Figure 6.8, should represent the actual impact of the finite upper EZ depth, which for $\Delta(b_{\delta,S}/\Delta b)$ should result in an increase (Figure 6.1). Again, we assume that the influences of convection- and shear-driven dynamics superimpose. Hence in analogy to Eq. 2.84 we suggest

$$\Delta \frac{b_{\delta,S}}{\Delta b} = (\xi_B \delta_B + \xi_S \delta_S) / z_{i1}. \quad (6.35)$$

With $\xi_B = 2.2$ and $\xi_S = 3.7$, this parametrization represents our data well, as demonstrated in Figure 6.9(a), which is constructed analogously to Figure 6.6(a), etc. For each LES the diagnosed quantities agree very well with the modeled values. Systematic deviation only occur for early-phase data (light colors), when equilibrium-entrainment conditions (e.g. necessary for Eq. 6.34) are not fulfilled yet and, as it seems, for moderate EZ-shear, when wave-losses are significant and the observed values are slightly lower than the modeled ones (gray markers). This agrees with the idea that for the same eddy penetration depth δ less energy is available for mixing and the subsequent deformation of the buoyancy profile.

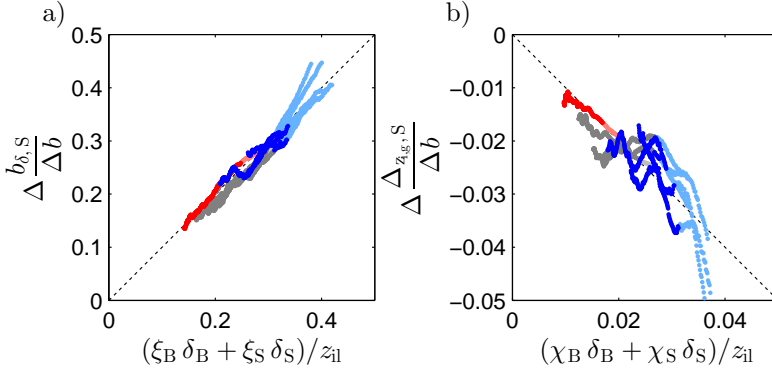


Figure 6.9: As Figure 6.6(a), but here (a) displays the correlation between diagnosed and modeled $\Delta(b_{\delta,S} / \Delta b)$ and (b) the correlation between diagnosed and modeled $\Delta(\Delta b_{z_{i,g},S} / \Delta b)$.

Note that one can interpret Eq. 6.35 as an empirically well justified approximation of a 'true' analogy of GM14's similar model. The latter is based on explicit regularities with respect to relationship between EZ buoyancy structure and FA stratification, which are difficult to reconstruct and evaluate for our cases, as discussed in the beginning of this chapter.

As $b_\delta = \Delta b_{z_{i,g}} + \delta N^2$ (Figure 6.1), b_δ and $\Delta_{z_{i,g}}$ are closely related and directly depend on δ . However with respect to the mentioned uncertainties, particularity with relationship $\delta N^2 / \Delta b$ and δ / z_{il} in our setup²⁴, we cannot directly compute an explicit expression for $\Delta_{z_{i,g}} / \Delta b$ versus δ / z_{il} , as it is possible for GM14's setup (Eq. 2.87). Hence, as an approximation, we directly propose an analogous form of Eq. 2.87. Following the previous procedure, we define the dimensionless quantity $\Delta b_{z_{i,g},S} / \Delta b$ for sheared cases (subscript S) as

$$\frac{\Delta b_{z_{i,g},S}}{\Delta b} = \frac{\Delta_{z_{i,g}}}{\Delta b} \frac{z_{i,g} - z_{il}}{z_{il}}, \quad (6.36)$$

using again as β_g as a scale.²⁵ The shear dependence of $\Delta b_{z_{i,g},S} / \Delta b$ is shown by the blue markers in Figure 6.8.

Following our previous approach $\Delta b_{z_{i,g},S} / \Delta b$ can be dissected in an asymptotic contribution $\Delta b_{z_{i,g},S,\infty} / \Delta b$, which should scale with S_*^3 and a deviation $\Delta(\Delta b_{z_{i,g},S} / \Delta b)$,

²⁴Or in other words, the basic ZOM structure $N^2(z_i - z_{il}) / \Delta b$ is not clearly specified, as expressed by a varying $\rho_{\Delta b, \beta}(t)$ (Eq. 6.4) in our data.

²⁵Note that this choice is probably a quite approximative simplification, which is difficult to evaluate with our data. For instance, empirically, we find that the model Eq. 6.39 also works, if β^2 is used as a scale in Eq. 6.36 instead of β_g . This could make sense, because similarly as Δb_{z_i} , $\Delta b_{z_{i,g}}$ measures the deformation of the initial buoyancy profile that is caused by the turbulent flux. According to Eq. 6.9, a multiplication with β^2 would create a resemblance with the normalized integral flux A_S , which is successfully represented by a model of the type Eq. 6.39. Thus, a scaling of $\Delta b_{z_{i,g}} / \Delta b$ with β^2 would stress a similarity with Δb_{z_i} or A_S respectively, whereas a scaling with β_g would express a similarity with b_δ .

which represents the direct local effects of the FA stratification. Thus

$$\frac{\Delta b_{z_i, g, S}}{\Delta b} = \frac{\Delta b_{z_i, g, S, \infty}}{\Delta b} + \Delta \frac{\Delta b_{z_i, g, S}}{\Delta b}. \quad (6.37)$$

From the asymptotic conditions $\delta \mapsto 0$ follows $b_\delta \mapsto \Delta b_{z_i, g}$ (Figure 6.1). Hence

$$\frac{\Delta b_{z_i, g, S, \infty}}{\Delta b} = \frac{b_{\delta, S, \infty}}{\Delta b}. \quad (6.38)$$

Thus also $\Delta b_{z_i, g, S, \infty}/\Delta b$ is represented by Eq. 6.34 and the black line in Figure 6.8. Analogously to Eq. 2.87 we finally propose

$$\Delta \frac{\Delta b_{z_i, g, S}}{\Delta b} = -(\chi_B \delta_B + \chi_S \delta_S) / z_{i1}. \quad (6.39)$$

With $\chi_B \approx 0.15$ and $\chi_S \approx 0.50$, the diagnosed and modeled values correlate rather well as shown in Figure 6.9(b), despite significantly higher scatter than for $b_\delta/\Delta b$.

Δb_{z_i} versus upper EZ dynamics. The buoyancy jump at Δb_{z_i} is explicitly coupled with $A_{t, S}$ and $A_{d, S}$ (Eq. 6.19 and Figure 6.3). Hence, its dependence on the interfacial dynamics is directly given by the parametrization for $A_{t, S} + A_{d, S} = A_S$. For clarity and completeness we here shortly present the respective expressions.

With Eq. 6.8 and 6.9 (or Eq. 6.19) we define the relevant normalized buoyancy jump at z_i

$$\frac{\Delta b_{z_i, S}}{\Delta b} = \frac{\Delta b_{z_i}}{\Delta b} \left(\frac{z_i - z_{i1}}{z_{i1}} \right)^2 = A_{t, S} + A_{d, S} = A_S. \quad (6.40)$$

As this quantity equals $A_S = A_{t, S} + A_{d, S}$, we can therefore directly refer to the respective parameterizations. Accordingly, $\Delta b_{z_i, S}/\Delta b$ can be resolved into an asymptotic contribution and an instantaneous deviation. The asymptotic contribution, as represented by the sum of the black lines in Figure 6.3, is given by

$$\frac{\Delta b_{z_i, S, \infty}}{\Delta b} = A_{t, S, \infty} + A_{d, S, \infty} = c_{[\Delta b_{z_i, S, B}]} + c_{[\Delta b_{z_i, S, S}]} S_*^3, \quad (6.41)$$

with

$$c_{[\Delta b_{z_i, S, B}]} = c_{[A_{S, B}]} \quad \text{and} \quad c_{[\Delta b_{z_i, S, S}]} = c_{[A_{S, S}]}, \quad (6.42)$$

which are specified further by Eq. 6.16. As demonstrate before, in the equilibrium entrainment regime the instationary part of $A_{d, S}$ is about zero ($\Delta A_{d, S} \approx 0$, Figure 6.3). Thus the instationary reduction of $\Delta b_{z_i, S}/\Delta b$ equals $\Delta A_{t, S}$ and can therefore be modeled with Eq. 6.27 by

$$\Delta \frac{\Delta b_{z_i, S}}{\Delta b} = \Delta A_{t, S} = -(\gamma_B \delta_B + \gamma_S \delta_S) / z_{i1}. \quad (6.43)$$

Accordingly, the significance of this relationship for our data has already been demonstrated in Figure 6.6.

6.3.5 Scaling of direct interfacial influences in the neutral limit

Unfortunately, our data set does not contain near neutral or fully neutral BLs, with $B_0 \mapsto 0$, so that we cannot directly investigate the full stability range. But in agreement with our basic reasoning in section 6.3.1, we suppose that also in purely shear-driven BLs an interfacial upper EZ layer exists, whose dynamics is equally characterized by the eddy presentation depth δ , which in this case equals δ_S (Eq. 6.20). However, an obvious problem is the normalization with z_{il} , as in or close to the neutral limit with $z_{il} \mapsto 0$ and $\delta/z_{il} \mapsto \infty$, which means that z_{il} cannot anymore represent the SM (the surface-layer plus ‘mixing-layer’). Based on data in literature, we argue soon below (chapter 7.2) that in or close to the neutral limit the SM depth is well represented by the height of the minimum shear z_S .

Another issue is that at the neutral limit any entrainment ratio becomes meaningless ($B_0 \mapsto 0$). But as we show soon below, also in neutral limit the concept of an integral EZ can be defined and corresponds with the integral shear-production $S_{EZ} \mapsto S_{SEZ} \approx 1/2v_*^3$. Hence S_{SEZ} can be used to normalize any measure of entrainment, which would defines a Richardson number. As a result we also find that the NZO remains physically representative in the neutral limit.

Hence, without further proof, we here hypothesize that also close to the neutral limit our representation of the upper EZ-dynamics remains valid, if we (1) replace z_{il} by z_S as soon as $z_{il} < z_S$, and (2), replace $A_{t,S}$, $A_{d,S}$ and β by respective Richardson numbers.²⁶

Preliminary conclusions. With the above results we have finalized the characterization of both the stationary and the instationary contribution to CBL entrainment for our set of LES-CBLs with widely varying shear. We managed to explain the observed temporal and spatial variation of the entrainment flux and the related variations of the EZ buoyancy-profile to a very high degree, using rather simple but physically well justified models, which provide substantial improvements compared to previous concepts. Practically, these models enable the construction of the buoyancy- and the buoyancy-flux-profile in the EZ, for any value of EZ shear, in any stage of the evolution of a mature CBL.²⁷ This means that, within the limitations given by our data set, we have reached all essential objectives of our research project.

²⁶Assuming an ideal barotropic BL with no Coriolis forcings, similar to the setup of Jonker *et al.* (2013).

²⁷Analogously to Figure 2.7, which depicts the non-sheared case.

Chapter 7

Discussion

In this chapter we discuss several yet unclear aspect of our analysis, which mostly go beyond our basic research questions. We also touch issues that we cannot fully solve within this thesis. However, by examining a wider context, we try to find a final notion of sheared CBLs, which is as consistent as possible. So in some parts, our considerations in the following lead to further results, in other parts, they remain speculative.

First, we reconsider the historical debate about the relevance of ‘Process Partitioning’ (PP), the similar ‘Lagrangian Partitioning’ (LP) and ‘Eulerian Partitioning’ (EP) (Randall, 1984) and finally come up with a rather basic argument for the latter. Next, we consider the neutral limit of the NZO (section 7.2) and the implications of the fact that TKE dynamics in neutral BL’s is very local (section 7.3). Finally, we once more consider the structure of CBLs with varying shear (section 7.4).

7.1 Empirical evidence and simple arguments for Eulerian Partitioning

Summarizing our empirical findings, the practical weakness of PP for sheared CBLs lies in the fact that it defines inappropriate length-scales for both buoyancy production and entrainment. The length scales used do not account for the strong variation of EZ depth with shear.¹ Hence, although PP and EP give comparable (proportional) entrainment ratios for purely convective CBLs (constant CBL structure), the PP estimate of entrainment starts to diverge once the CBL is sheared to various degrees (varying CBL structure). We have shown that using EP entrainment can be considered as a linear combination of buoyancy-driven entrainment and shear-driven entrainment. Given that the difference between PP- and EP-entrainment is shear-dependent, PP clearly does not conform with the assumed superposition of buoyancy and shear-driven entrainment.

This suggests that the superposition principle, which reflects properties of ideal turbulence (Eq. 2.10), can be used as a basic criterion to decide about the most ap-

¹This is also reflected by the common stance that ZOMs do not represent a finite EZ. However, using EP, this idea is unfounded.

appropriate concept for buoyancy partitioning (EP, LP or PP) of CBLs. As it seems, this simple idea is absent in literature. The main reasons for this might have been a lack of appropriate data, uncertainty regarding the determination of the shear contributions, and finally a certain focus on cloud-topped BLs. Thus, the debate mostly centered around indirect arguments and indirect evaluations of the partitioning principles in cloud layers, whose general properties significantly differ from well developed ‘dry’ CBLs (e.g. Randall, 1984; Stage and Businger, 1981). So, besides our empirical results, are there also more fundamental arguments for EP?

Randall (1984) already carefully reviewed arguments pro and contra EP, PP and LP, that had been brought forward by others (Manins and Turner, 1978; Stage and Businger, 1981; Wilczak and Businger, 1983) and discussed some physical inconsistencies of LP and the similar PP. His criticism boils down to the argument that both LP and PP account for ‘irrelevant’ background production and consumption’, caused by small-scale eddies, which – in effect – cancel. All ‘relevant contributions’, that represent the ‘principal circulations’, are expected to equal the net buoyancy flux, which actually defines EP. In our understanding, this argument simply implies that LP and PP contradict Kolmogorov’s picture of high Reynolds-number turbulence dynamics, as they intermingle large-scale and inertial-subrange-scale turbulence, which results in an overestimation of buoyancy production and consequently of consumption (entrainment)

The disagreement corresponds with the fact that – by definition – LP- and PP-defined buoyancy terms represent subsamples of the turbulent ensemble, whereas EP is based on averages over the full ensemble (approximated by sampling in all homogeneous directions). The latter is a requirement of Kolmogorov’s approach and reflects an integral view on turbulence.² The emphasis on ensemble properties of turbulence is particularly relevant here as our analysis of turbulence dynamics is entirely based on the turnover of TKE, which, intrinsically, is an ensemble averaged quantity. Hence, the agreement with Kolmogorov’s concept for the inviscid scaling of high Reynolds-number turbulence, which we could confirm empirically, seems the most basic argument for EP.³

However, in the case of e.g. a cumulus-cloud layer the conditions seem quite different. Here turbulence and TKE production are concentrated in the rising clouds, whereas the subsiding environmental air is non-turbulent. Hence the whole cloud layer is highly intermittent (partly turbulent) throughout and so differs fundamentally from idealized homogeneous turbulence, but also from a developed dry CBL. Thus, to model cloud layers it obviously makes sense to apply ‘conditional sampling’ and

²As we understand, Kolmogorov basically refers to integral properties (which means ensemble statistics) and scales of a turbulent flow: e.g. “Here L and U denote the typical length and velocity for the flow in the whole” (Kolmogorov, 1941), which agrees with our analysis and the presentation in chapter 2.2. This does also not contradict Kolmogorov’s further concept of ‘local isotropy’, which is assumed to hold for sufficiently small regions in a turbulent flow.

³Note that we do not suggest that turbulence modeling should be restricted to such integral approaches. To the contrary: We think that a process-oriented focus on conditional subsamples of the turbulent ensemble, as, e.g., successfully applied in plume mass-flux models (e.g. Siebesma and Cuijpers, 1995; Siebesma *et al.*, 2007), are physically quite intuitive for convection. Moreover, we think, that a detailed analysis of updrafts and downdrafts, particularly their spatial distribution and their budgets (e.g. inspired by Schumann and Moeng, 1991) would be a very natural and promising approach for continuation of this study, to gain a more detailed understanding of the CBL structure and the entrainment process.

consider separate ensembles of the turbulent cloudy updrafts ('bottom-up') and the sinking environment ('top-down') (e.g. Siebesma and Cuijpers, 1995). For a mixed layer model of cloud layers, PP would therefore appear as the most sensible approach (e.g. Stage and Businger, 1981; Stevens, 2002).⁴

7.2 The neutral limit of sheared CBLs

In our analysis we have so far only considered data of purely convective BLs and convective BLs with added shear. Purely shear-driven 'neutral' BLs became only relevant as a theoretical limiting condition, which, however, we could not test with our data set. Here we address the topic again and try to evaluate to what extent our entrainment model – both the TKE-scaling and its ZOM representation – may be valid purely shear-driven BLs. For this purpose we use results from the DNS study of Jonker *et al.* (2013) to serve as a suitable basis and reference to frame our results in the neutral limit.

7.2.1 DNSs of neutral BLs as reference base

Using the DNS (direct numerical simulation) technique, Jonker *et al.* (2013) investigated the dynamics of neutral, purely shear driven BLs that grow into a linearly stratified quiescent FA. Fine computational grids and a rather long simulation time resulted in high Reynolds-number BLs with an inviscid, quasi-stationary growth regime, similar to our CBLs. But the experimental set-up is even more idealized than ours. The flow is solely driven by a constant surface-stress and lacks a pressure-gradient or a Coriolis forcing. Different to our LES-CBLs, the BL growth-regime and the BL structure can therefore directly be modeled (scaled) with the external parameters N , u_* , and t (see appendix B). However, despite the differences, the idealized experimental setup turns out to conform well with our LES data, with regard to the entrainment dynamics. The reason for this is the following.

Our sheared LES-CBLs are driven by a horizontal pressure gradient and a Coriolis forcing. In combination with surface friction these induce an anharmonic inertial oscillation (IO), which result in a rather complex time evolution of wind-shear in the EZ. But in effect, this time evolution is not relevant for our considerations, as entrainment only depends on the instantaneous state of the CBL. Within the range of our data set, the further **direct** influence of the Coriolis force on the EZ momentum dynamics and, hence, on the local TKE shear production is negligible and therefore also not considered in our analysis.⁵ This means that our entrainment models essentially represent CBLs in non-rotating flows. These can be CBLs that, e.g., are driven by a constant uniform pressure forcing, are initialized with a uniform velocity in which the BL develops, or are driven by an imposed, slowly varying or constant surface stress (as in Jonker *et al.* (2013)).⁶

⁴However, as we understand, some basic issues with mixed layer model of cloud topped BLs are still unsolved (e.g. Randall, 1984; Stevens, 2002).

⁵But for CBLs that are much deeper or much more shear driven than our LES-CBLs, a significant impact of the Coriolis force on the EZ wind-profile has to be expected. This should reduce and finally limit the shear-driven contribution to entrainment.

⁶A uniform pressure gradient merely causes a uniform acceleration everywhere in the flow. There-

Thus we can expect Jonker *et al.*'s (2013) DNS-BLs to produce the neutral limit ($B_s \mapsto 0$) of the CBL entrainment dynamics that we have identified and analyzed in the previous chapters. In the remainder of this section we therefore discuss Jonker *et al.*'s (2013) findings and compare, and try to align, them with our results. Practically, this means that we use Jonker *et al.*'s (2013) scalings and their entrainment law to interpret the universal profiles (their Figure 5 and 8) and to derive the respective ZOM quantities and integral TKE-budget terms. With these, we can then estimate the respective constants for our models. Details of the derivation can be found in appendix B.

7.2.2 The NZO in the neutral limit

Considering the NZO in the neutral limit (Eq. 5.7 with $B_0 = 0$), we find each term well defined. As the wave-loss term ϕ_B becomes insignificant, the NZO is reduced to the balance of the weighted shear production and entrainment (buoyancy consumption) term

$$k_{\text{BEZ}} \frac{1}{2} w_e \Delta b (z_i - z_{i1}) = c_{\text{B,S}} k_S \frac{1}{2} w_e |\Delta U|^2. \quad (7.1)$$

However, as both terms depend on it linearly, w_e is no longer specified. In the limiting neutral case, the NZO TKE dynamics only depends on properties of the EZ or the upper BL boundary respectively, which is rather counterintuitive with respect to the pretense of representing the dynamics of a ‘boundary layer’. Obviously the NZO offers an incomplete representation of the problem, but it remains physically meaningful and can be evaluated.

In the neutral limit $\beta = w_e \Delta b / B_0 \rightarrow \infty$ (Eq. 5.3), the buoyancy-driven SM disappears ($z_{i1} \rightarrow 0$), thus the EZ fills the whole boundary layer and ‘touches the ground’. z_i becomes the only length-scale and thus represents CBL and EZ depth simultaneously. Likewise, BL shear-production can be interpreted as ‘EZ’ shear-production. As a consequence, the neutral case (Eq. 7.1) defines a minimum condition for the EZ or BL depth respectively. With $z_{i1} = 0$ we get

$$z_i = \frac{c_{\text{B,S}} k_S |\Delta U|^2}{k_{\text{BEZ}} \Delta b}. \quad (7.2)$$

A physical interpretation is straightforward. For a given EZ velocity jump (TKE shear-production (Eq. 7.1, rhs), the EZ (or the BL respectively) requires a minimum depth to ensure enough TKE consumption to keep the budget in balance (Eq. 7.1, lhs). Thus, Eq. 7.2, reflects the typical shear-related deepening of the EZ, which now acts as a limit for the whole BL.

for it does not influence the turbulent field directly but only **indirectly**, as it increases the velocity difference between the mean flow and the surface and so enhances shear-induced surface stress. Thus, for the BL a uniform constant pressure forcing is effectively nothing more than a surface-stress forcing with a particular time evolution. This means that one can create the same type of turbulent BL by replacing the moving fluid over a resting surface with a resting fluid over a moving surface. In numerical experiments, one can simplify this setup even further and artificially impose a surface-stress, that would mimic a moving surface. As long as the temporal variation of this forcing is slow enough to allow quasi-stationary conditions it does not change the general typology of the turbulent flow. Finally, choosing surface stress to be constant ($u_* = 0$) leads to the same experimental setup as (Jonker *et al.*, 2013).

Moreover, to characterize the conditions in the neutral limit, one can also rewrite the above NZO-expression as a definition for a characteristic (or critical) bulk Richardson number Ri_U .

$$Ri_U = \frac{\Delta b z_i}{|\Delta U|^2} = \frac{c_{B,S} k_S}{k_{BEZ}}. \quad (7.3)$$

Using our values for the scaling parameters $c_{B,S}$, k_S and k_{BEZ} , one gets

$$Ri_U(\text{LES}_c) = \frac{c_{B,S} k_S}{k_{BEZ}} \approx \text{const} \approx 0.17. \quad (7.4)$$

Here ‘LES_c’ in brackets denotes the convective LES-BLs. A constant Ri_U has frequently been observed in shear flows and can be considered as a consistent property of mature, neutral BLs. According to Jonker *et al.* (2013, adapted notation) ” ... *the flow will strive to make Ri_U constant. If Ri_U drops below this value, then turbulence will be enhanced leading to higher values of h and Δb , thus restoring Ri_U . A high value of Ri_U would reduce turbulence and therefore also Ri_U ”.*

Thus BL growth dynamics and entrainment are actually controlled by the inversion and shear at the upper boundary. But as shown by Jonker *et al.* (2013, discussion in their section 5) for a complete quantification of the dynamics, the reference to surface shear-stress is necessary. As surface-stress is the essential process to produce shear (and hence forces turbulence) this is a logical necessity. Later on, we try to sketch a more instructive picture of the relationship between entrainment and surface forcing.

For empirical evidence, we compared our LES estimate for Ri_U with the value we can diagnose from Jonker *et al.*’s (2013) DNS results. The necessary calculations are shown in appendix B (Eq. B.15). These yield

$$Ri_U(\text{DNS}_n) \approx 0.19, \quad (7.5)$$

which roughly agrees with our LES estimate $Ri_U(\text{LES}_c) \approx 0.17$. Within our data set $Ri_U(\text{LES}_c)$ does not vary significantly, so there is no obvious physical reason for the remaining difference. But from a another, independent and high resolution LES (appendix D), we estimate $Ri_U \approx 0.19$, which agrees well with the DNS estimate and clearly hints at a slight bias in our LES, probably caused by a too coarse or too anisotropic grid.

Note that a constant Ri_U is not only significant for the neutral limit, but more generally controls the shear-driven contribution to NZO entrainment. This is indicated by the fact that Ri_U equals C_S (Eq. 5.31), which is the sensitivity of β^2 to S_*^3 in the NZO TKE-budget (Eq. 5.29) (the slope of the graph in Figure 5.8). Thus, apart from the wave-loss effects, the NZO straightforwardly represents any sheared CBL as a superposition of a pure CBL, with a constant entrainment ratio β^2 , and a neutral BL, with entrainment dynamics controlled by $Ri_U = \text{const}$.⁷ In the the next section we evaluate if this simple idea also applies to the integral TKE budget.

Finally, for completeness we note that the CFM (Eq. 5.21) is defined by exactly the same physical conditions in the neutral limit, which gives

$$Ri_U(\text{CFM}) = \frac{\Delta b z_i}{|\Delta U|^2} = C_p = \text{const} \approx 0.4. \quad (7.6)$$

⁷For completeness we note that the NZO EZ dynamics can also be expressed as the sum of the critical Richardson number Ri_U (Eq. 7.3) and a stability correction. For details see appendix A.

However, the value of 0.4 for $Ri_U = C_p$ given by Conzemius and Fedorovich (2007) is about two times the actual size, which reflects the fundamental problem of the CFM to capture the CBL dynamics over a wider range of shear (Figure 5.7). But physically, $Ri_U(\text{CFM}) = \text{const}$ is commensurate with observations and the NZO in the neutral limit. Thus, in contrast to Conzemius and Fedorovich (2007), we find that a maximum value for $\Delta\tilde{U}$ is physically well justified, as in the neutral limit $\Delta\tilde{U} = 1/\sqrt{Ri_U(\text{CFM})}$.

7.2.3 The integral TKE-budget in the neutral limit

In this section we will determine the integral TKE budget and extract the parameters k_{BEZ} (Eq. 5.2) and $c_{\text{B,S}}$ (Eq. 4.26) in the neutral limit. Our analysis will be based on the DNS study of Jonker *et al.* (2013), in particular on their BL growth-law and the related universal scaling of the BL structure (Figure B.1).

TKE-budget for the full neutral BL. By determining the NZO buoyancy consumption from Figure B.1(c) (via Eq. B.18) we can diagnose the entrainment shape-parameter in the neutral limit, $k_{\text{BEZ}}(\text{DNS}_n)$, to be ≈ 1.44 (via Eq. B.20), which is similar to what we get from our sheared LES-CBLs ($k_{\text{BEZ}} \approx 1/0.67 \approx 1.49$, Figure 5.3). Apparently, this integral quantity is rather robust over the whole stability range.⁸ But we also know that k_{BEZ} is not universal, as it depends on the maturity of the BL, which might somewhat differ between our LES-CBLs and Jonker *et al.*'s (2013) neutral DNS-BLs⁹. We also must take into account the remaining uncertainties due to the moderate resolution of our LESs.

Next we consider $c_{\text{B,S}}$, the sensitivity of entrainment to shear. In the neutral case it should equal the ratio between integral TKE shear production and entrainment (originally defined by Eq. 4.26 with $B_{\text{SM}} = 0$), hence $c_{\text{B,S}}(\text{neutral BL}) = -B_{\text{EZ}}/S_{\text{EZ}}$, which defines the inverse of an integral flux Richardson number, analogous to Ri_U . In principle, $c_{\text{B,S}}$ can be directly diagnosed from the integration of B_z and S_z , which are both given as profiles over the entire BL (Figure B.1(c) and (d)). According to our estimate¹⁰ $c_{\text{B,S}}(\text{DNS}_n)$ is below 0.1, which is significantly smaller than the value for $c_{\text{B,S}} \approx 0.256$, that we diagnose from our LES-CBLs. In turn, this would imply $k_{\text{S}}(\text{DNS}_n) > 2.7$ (via Eq. B.22 or Eq. 7.3 and 7.5), which is drastically larger than unity, as found for our LES-CBLs.

Hence, it appears, as if shear-production within the neutral DNS-BL is less ‘efficient’ than in the EZ of our CBL-LES, as a significantly higher shear-production is necessary to generate the same amount of entrainment. The discrepancy is not only present for the integral value, but throughout the whole BL, as at any height in

⁸Even though the EZ buoyancy structure varies systematically as shown in Figure 5.9.

⁹We did not further analyze the instationarity of Jonker *et al.*'s (2013) DNS-BLs, but their Figure 7 indicates that in the later half of the BL evolution, the ratio between TKE tendency and the buoyancy term (entrainment) has become significantly smaller than in our LESs, where $-(\partial e/\partial t)/B_{\text{EZ}}$ remains mostly larger than ≈ 0.15 (e.g. Figure 4.22, gray versus red markers). Hence, their DNS-BLs should be less influenced by TKE-spinup and so come somewhat closer to the asymptotic stationary limit. This would rather imply a slightly larger k_{BEZ} than for our LESs.

¹⁰Due to the still relatively low Reynolds number of the DNS-BLs, the viscosity-affected surface-layer is rather deep and SL turbulence therefore significantly weaker than in real atmospheric BLs. To avoid these viscous effects we only integrate over the upper 90% of the BL (Eq. B.21) and so get $c_{\text{B,S}}(\text{DNS}_n, 0.1 z_{i,g}) \approx 0.10$. The actual value for a whole neutral BL must be even lower.

the neutral BL $-B_z/S_z$ is significantly smaller than $c_{B,S}$ of our sheared CBLs. Due to the very small TKE-transport term and the consequently local character of the TKE-balance between production, consumption and dissipation, the redistribution of TKE between the lower and the upper BL must be very small as well (see Jonker *et al.*'s (2013), Figure 8).

To explain this apparent discrepancy between sheared CBLs and neutral BLs, one can easily argue that our comparison is inconsistent. In the neutral case the ‘TKE consuming region’, the EZ as we defined it previously, extends from the BL top until the surface. Thus the EZ would comprise both the shear production close to the upper interface, which we expect to ‘actively’ drive entrainment, and surface-related shear production, which we previously found to be ‘inactive’ with respect to entrainment and therefore was explicitly excluded from our scalings. Thus, we suspect that the low value for $c_{B,S}(\text{DNS}_n)$ (computed according to Eq. B.21) is the result of a balancing error, as – in contradiction to our actual intention – we have possibly lumped together ‘active’ and ‘inactive’ portions of TKE shear production.

Thus the question is if – in analogy to the CBL – we could find a way to identify an upper sublayer of the BL, where TKE shear-production directly drives entrainment and a lower sublayer, where TKE shear-production does not feed entrainment.

A shear-based definition of the EZ in neutral BLs. Searching for a criterion to separate between zones of influence for TKE shear-production at the upper- and lower-boundary in a purely shear-driven BL, it seems quite natural to consider the height of minimum shear, z_S (i.e. the inflection point of the wind profile). Thus we come back to the idea of a shear-related BL-structure, as suggested by Conzemius and Fedorovich (2006a) and discussed in chapter 4.1.1 (Figure 4.1 (b)). Accordingly, the neutral BL would consist of a ‘shear-driven’ SM (SMS), which extends from 0 to z_s and a ‘shear-driven’ EZ (SEZ), which extends from z_s till z_{iu} (Eq. 4.13). With the SEZ as the relevant integral shear layer, we can now redefine $c_{B,S}$ in the neutral limit as

$$c_{B,S}(\text{SEZ, neutral}) = - \frac{\int_0^{z_{iu}} B_z dz}{\int_{z_S}^{z_{iu}} S_z dz} = - \frac{B_{EZ}}{S_{SEZ}} \approx \text{const.} \quad (7.7)$$

For Jonker *et al.*'s (2013) neutral DNS-BLs, we find that $z_s \approx 0.5z_{ig}$ (Figure B.1, with $h = z_{ig}$). From the dimensionless profiles, we read $c_{B,S}(\text{SEZ, DNS}_n) \approx 0.25$. This is quite close to the value $c_{B,S} \approx 0.256$, which we diagnosed from our LES (chapter 4.2.4), based on the buoyancy-based definition of the EZ (using z_{il} rather than z_S). Furthermore, we find that S_{SEZ} of the neutral BL is well approximated by the ZOM TKE shear production $w_e \Delta U^2$, as we diagnose $k_S(\text{SEZ, DNS}_n) \approx 1.04$. With the given uncertainty this equals unity, as found for our set of LESs and the independent higher resolution LES (appendix D). Both findings strongly support our concept.

These results suggest that somewhere in the transition from a strongly sheared CBL to a neutral BL z_S replaces z_{il} as the lower boundary of the relevant shear zone in the EZ. We have no data to investigate this transition in detail. But we imagine that at a certain point the sheared EZ becomes so deep that it extends into the ‘inactive’, decoupled surface shear-production layer. Thus as soon as $z_S \geq z_{il}$, we could expect the SEZ to become the relevant shear zone for integral entrainment.

Hence, with z_S as the lower boundary of the upper shear layer, we find that the composition of the integral TKE-budget of a neutral BL-DNS is very similar to that of our sheared CBLs, as expressed by the constants $c_{B,S}$ and k_S . This finding complements the rather good agreement with respect to the ZOM TKE-budget, as given by the constant Ri_U and $k_{B,EZ}$. In summary, the data presented in this thesis, in combination with the data of Jonker *et al.* (2013) suggest that the proposed scalings are significant for the whole stability range of quasi-stationary BLs.

Once more we note that $c_{B,S}$ and $k_{B,EZ}$ are not fully universal, as both, via B_{EZ} , depend on the BL maturity and the influence of TKE-spinup. But for equally developed BLs these quantities are similar and appear to be independent of shear. In the equilibrium entrainment regime, the NZO quantities $Ri_U \simeq 0.19$ and $k_S \simeq 1$ are constant. This means that also the ratio $c_{B,S}/k_{B,EZ} \simeq 0.19$ is constant and independent of TKE-spinup.

7.2.4 Conclusions

Our data analysis clearly indicates that the integral TKE-budget of sheared CBLs, if appropriately decomposed by accounting for the natural partitioning of the buoyancy production (EP) and for the decoupling of surface shear, basically complies with a linear inviscid scaling law over the whole stability range, from pure convection to the neutral limit. With respect to the basic underlying dynamics this holds for both the NZO and the actual integral TKE-budget.¹¹ To our knowledge such rather ideal and simple behavior has never actually been demonstrated before, although it must have been frequently assumed.

It is the simplicity of the EP- and NZO framework, that strongly facilitates the identification and representation of further aspects of the EZ dynamics, such as the local interfacial influence and the TKE wave-losses.

Our interpretation of shear-driven entrainment as a rather localized phenomenon, that is restricted to the upper BL, might seem uncommon compared to typical other scaling approaches of neutral BLs. The latter are usually based on surface-stress, which is indeed the initial cause for turbulence (e.g. Jonker *et al.*, 2013). But according to our interpretation, surface-stress is only an **indirect** driver for entrainment, as we try to further illustrate in the following section. In this respect our concept consistently combines and extends the existing ideas of a constant Ri_U in the neutral BLs (Jonker *et al.*, 2013, and references herein), the decoupling of surface- and EZ-shear in CBLs (Conzemius and Fedorovich, 2007, and references herein) and EP (Lilly, 1968; Randall, 1984).

Finally, we stress that the characteristic quantities $c_{B,0}$, $c_{B,S}$, $k_{B,EZ}$, k_S and likewise β_0 and $Ri_U = C_S$ (Eq.5.31) represent integral statistical properties. As they are based on correct ensemble means, they conform with Kolmogorov's representation of high Reynolds number turbulence and as such characterize the self-similarity of 'similar' turbulent BL-flows, that are all bounded by a stratified FA. In our opinion, any further interpretation is quite problematic. For instance, these integral scales should not be suitable to characterize other, in particular, more local properties of turbulence, which

¹¹TKE spinup and the TKE wave-losses should be considered as separate interfacial processes, which only under particular conditions cause noticeable deviations from the underlying linear behavior.

differ fundamentally between purely convective and purely sheared turbulence.

Implicitly we were already confronted with the question of shear-dependent variation of local turbulent properties before, e.g., when observing the characteristic wave-loss regime for weakly sheared convective EZs. Moreover we explicitly discussed local properties of the upper interfacial EZ (chapter 6.3). We address this topic once more in the following.

7.3 Locality of turbulence in neutral BLs and its implications

7.3.1 Interfacial length scale

The highly local character of turbulence in shear-driven SBLs is a known and well studied phenomena (e.g. Wyngaard, 2010, chapter 12.1). For the particular case of a neutral, quasi-stationary BL, Jonker *et al.* (2013) showed that the vertical TKE-transport term is very small within the whole BL (e.g. their Figure 8), except for a small region around $h = z_{i,g}$, which is also strongly affected by TKE spinup. This shallow sublayer obviously represents the neutral limit of GM14's interfacial upper EZ layer (as studied in chapter 6.3). But in the bulk of the BL, the TKE-budget is characterized by a local balance between shear-production and dissipation plus entrainment. This is also what we observe within the EZ of sheared CBLs (as later shown in Figure 7.2, for $S_* > 0.5$) and which is very different from convective turbulence, where a strong net upward transport of TKE is a dominant feature.

The locality of the neutral BL turbulence can also be expressed by corresponding turbulent lengths scales. As already mentioned in chapter 6, Jonker *et al.* (2013) demonstrated the validity of the characteristic length scale $h_* = u_*/N$, which is based on external parameters¹². Comparing h_* with the BL dept $h = z_{i,g}$ measures the relative locality of the BL turbulence, and implicitly also the maturity of the BL.¹³ With our perspective on BL entrainment, the use of the interfacial lengths scale δ or more specifically δ_S (Eq. 6.20) would also be a logical choice and δ_S/h at the same time an appropriate measure of BL maturity. But as $z_s = \frac{1}{2}h$ and z_s effectively replaces the SM depth z_{i1} in the neutral limit (section 7.2.3), we finally propose the quantity δ_S/z_s , which represents the neutral limit of δ_S/z_{i1} , which we used to quantify the local interfacial dynamics of CBLs (chapter 6). But what does this locality mean for the interpretation of the integral BL TKE-dynamics? And how can we align it with our findings?

7.3.2 Coupling between upper and lower half of the neutral EZ

A straightforward superficial interpretation of a constant $c_{B,S}(\text{neutral}) = -B_{EZ}/S_{SEZ}$ suggests that entrainment, even though it is spread over the whole BL, is only driven

¹²Note the formal similarity with GM14's L_0 , Eq. 2.91.

¹³As an example, the DNS data that we refer to here (Figure B.1) represent BLs with $h_*/h < 0.2$, as $h_*/h = 1/\sqrt{Nt}$ and $Nt \approx 40...160$. These BLs are characterized by a constant layering (Figure B.1) and therefore represent the equilibrium entrainment regime.

by the shear in the upper BL (SEZ). However, as the TKE transport is zero, TKE produced in the SEZ can obviously not drive the entrainment flux in the lower EZ.¹⁴ In fact, we already know that entrainment throughout the whole BL is caused by local shear production. Then, if it is not turbulent transport of TKE that connects the upper and lower half of the EZ, what can be responsible for the integral characteristics of the neutral BL? It must be the profiles of mean shear and turbulent momentum transport, as those features create local TKE shear production. Both mean shear and turbulent momentum transport are induced and maintained by surface stress and are both coupled via the momentum- and the stress-budget. Together they determine the local transfer of the flow's mean kinetic energy (MKE) into TKE (e.g. Stull, 1988, chapter 5.4, page 169) and at the same time provide the global coupling between the upper and lower half of the EZ.

This interpretation suggests, that one could close the NZO (Eq. 7.1) in the neutral limit by introducing an integral scaling for the momentum flux (stress) dynamics. Such a 'closure' can very easily be demonstrated by using Jonker *et al.*'s (2013) setup. Here one finds that the momentum flux profile is self-similar in a rather direct manner (their Figure 5(d), compare also Figure B.1(b) and (d)), which simply means that the ZOM entrainment flux at z_i (or $z_{i,g}$) and the surface stress u_*^2 are proportional. Hence

$$w_e \Delta U \sim u_*^2. \quad (7.8)$$

Inserting into Eq. 7.1 with $z_{i1} = 0$ gives

$$w_e \sim \frac{u_*^2 \Delta U}{z_i \Delta b}. \quad (7.9)$$

This expression represents the NZO entrainment model for an ideal neutral BL.¹⁵

Thus, to summarize the basic principles, the neutral BL's TKE-dynamics can be described as a layering of local budgets, each determined by local shear production and entrainment. These local budgets are interactively but indirectly coupled via the mean buoyancy and velocity profile, which in the absence of transport, very sensitively control the vertical distribution of the TKE-dynamics.¹⁶ This is fundamentally different to a CBL, where basic integral properties of the turbulent dynamics are established by TKE transport.

7.3.3 Entrainment and momentum dynamics in a neutral BL

We can use the above thoughts to try to explain how the entrainment over the whole neutral BL depth (B_{EZ}) could be controlled by turbulence that is produced at the upper interface (e.g. by S_{SEZ}), despite the local character of the TKE dynamics. As with the example of the critical Richardson number (see the quote in section 7.2.2)

¹⁴In turn, the analogous conclusions can be made with respect the surface-based scaling of Jonker *et al.* (2013), as, due to the lack of TKE-transport, entrainment at the upper half of the layer is obviously not driven by TKE produced at surface.

¹⁵The corresponding proportionality constant can be directly computed (e.g. via Eq. B.6 and B.11). Note that Eq. 7.9 fully conforms with Jonker *et al.*'s (2013) scaling approach and can therefore also be considered as a particular formulation of their entrainment model.

¹⁶Note that these concepts are well-known, but to our knowledge rarely discussed to understand the **integral** dynamics of BLs, including sheared CBLs.

we consider the reaction of the BL dynamics to a deviation from the quasi-stationary state.

Imagine an episode with enhanced entrainment, which results in a warming and acceleration of the upper BL. This has two effects. The warming increase the stratification towards the lower BL and thereby tends to suppress turbulence, momentum flux and shear production. However, at the same time the acceleration of the upper BL increase shear in the lower part of the BL, and thereby enhances stress and TKE shear-production. As shear production is much stronger in the lower BL and further increases towards the surface¹⁷, we can expect the second effect to dominate. Hence, the increase of shear production and the enhanced buoyancy gradients enhances the buoyancy (entrainment) flux also in the lower BL. So any event of enhanced entrainment at the BL top results in similarly enhanced buoyancy entrainment in the lower EZ, which ensures a smooth distribution of buoyancy over the whole BL. After an episode with reduced entrainment, the reaction of the lower BL is inverse, and less TKE production is needed to maintain a sufficient buoyancy flux in the lower BL. Thus, the upper BL shear-production controls the lower BL buoyancy-entrainment indirectly via momentum entrainment.

The conceptual issue here is that on one hand the basic idea of ‘entrainment’ is that of a local process close to a free-flow boundary. On the other hand, we use the common definition of ‘entrainment’ as buoyancy consumption, which in the neutral BL extends over the whole BL. To reconcile these apparently contradictory¹⁸ notions we suggest the following picture for the conditions in a neutral CBL.

As we consider ‘entrainment’ as an interfacial process, induced by local shear production of turbulence, we suggest that ‘active entrainment’ is indeed restricted to the upper part of the BL. But the feedback of surface shear to the ‘active’ entrainment of momentum in the upper BL ensures a positive response of the entrainment flux (buoyancy consumption) in the lower BL. One could therefore denote this mechanism as ‘reactive entrainment’. Thus, one finds that the continuous downward flux of momentum (or mean kinetic energy, MKE), which couples the upper and lower entraining regions, is the essential mechanism that determines the integral appearance of the neutral BL.

7.3.4 The character of the integral length scale $\sim z_S$

For final clarity, we once more rephrase the above concept to comment on the character of integral length scales associated with z_S . Due to the local character of BL turbulence dynamics the transition between ‘active’ upper and ‘reactive’ lower entrainment should be rather continuous. Thus z_S should not represent an actual boundary between regions with different turbulence properties but rather define characteristic lengths scales for the integral BL behavior ($\sim z_S$ for a ‘neutral’ mixed layer’ and $\sim (z_{i,g} - z_S)$ for the ‘neutral’ EZ), which are ensured by the mean momentum dynamics. In this regard the inflection point of the mean wind profile at z_S should be

¹⁷In a neutral BL the local flux Richardson number continuously decreases with height.

¹⁸For clarity we note that these ‘contradictions’ are not an issue of physics but a result of the attempt to tie ‘entrainment’ to a single term in the TKE-budget. As discussed before, also the TKE-spinup term, which directly represents the local interfacial dynamics of the upper EZ, would have been a contender. But this choice would have resulted in other peculiarities, as TKE-spinup continuously decreases towards zero during BL evolution.

significant, as it specifies the reaction of TKE shear-production to momentum entrainment. Above z_S enhanced momentum entrainment results in a linearization of the EZ wind profile and thus a reduction of maximum EZ shear. But below z_S positive momentum entrainment increases the curvature of the wind profile, thus increasing the maximum shear at the surface. Taking the non-linear response of TKE shear production into account this results in an overall reduction of shear production in the upper BL and an increase in shear production close to the surface.

This is essentially different from a CBL, where the entrainment process is a result of the upward transport of TKE, which leads to a direct coupling between the surface and the upper boundary dynamics.¹⁹

7.4 The structure of turbulence shear-production in CBLs

In our quasi-stationary sheared LES-CBLs²⁰, the presence of a rather deep SM restricts the EZ to the upper portion of the CBL. Wind shear is concentrated in the surface layer (SL) and the EZ, as indicated by a pronounced minimum of TKE shear production at z_S (Figure 4.1 (b)). As a result, TKE shear production in the SM appears to be ‘decoupled’ from entrainment throughout the evolution and the full stability range of our data, as we demonstrated in section 4.1.4.1.²¹

Using the considerations from the previous section, we address this issue again and discuss possible mechanisms that could explain the observed decoupling. Afterwards we focus once more on the sheared CBL-EZ, discuss its variability and thereby try to synthesize all our findings.

7.4.1 Decoupling between entrainment and TKE shear-production in the surface- and mixed-layer

Due to the spatial separation between the regions of mean shear in the SL and the EZ (Figure 7.1(a)), it seems intuitive and not surprising that TKE shear production in the SM seems not to affect the entrainment process in the distant EZ. However, different to the neutral BL, the convective, vertical upward flux of TKE (dashed arrows) is strong in a CBL. So the question arises, why TKE that is mechanically produced (i.e. by shear) in the SM (or the SMS) is not transported upwards. Or, if it is transported upwards, why does it not contribute to entrainment? The mechanism that we describe in the following could provide an answer.²²

¹⁹Using a ‘conventional’ coordinate system that is fixed with the surface, we find that in a sheared BL, entrainment of momentum and mean kinetic energy (MKE) from the faster free flow (FA) is an energy source for the BL mean flow and hence a source for TKE shear-production. In the absence of a pressure gradient (or a body force) it is actually the only source. But as momentum- and MKE-entrainment are ultimately a reaction of the flow to surface stress, a sheared BL is commonly considered as a ‘surface driven’ phenomenon, in spite of the energy supply from above.

²⁰Even in the CBLs with strong overall shear production and $(S_{SM} + S_{EZ})/B_{SM} > 15$.

²¹Decoupling is present in all our usable data, including the early periods (see Figure 4.4).

²²It seems difficult to evaluate these questions with our data-set directly, as one would need to distinguish and trace TKE depending on its source. Hence, one would need a concept to define separate budgets for TKE that is produced by buoyancy and TKE that is produced by shear. This seems not to be a trivial issue.

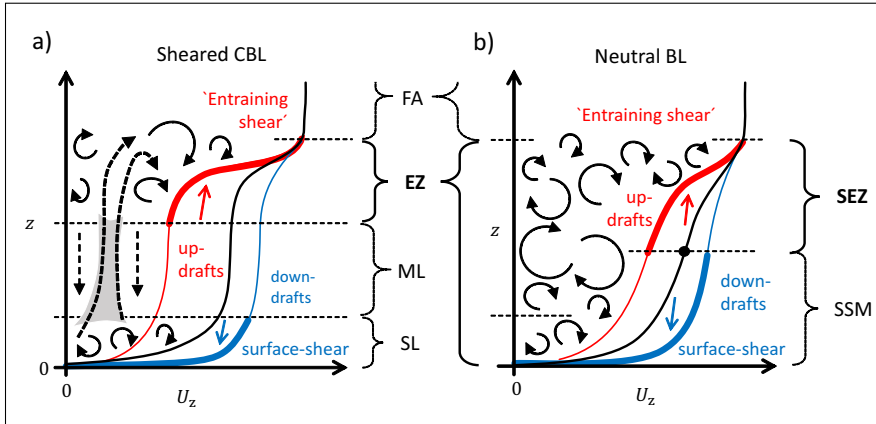


Figure 7.1: Schematic sketch of the wind profiles and the turbulent structure of a sheared CBL (a) and a neutral BL (b). Solid black arrows indicate shear-driven turbulence and local transport of momentum. Dashed black arrows signify convection and non-local transport of TKE and momentum. The mean wind velocity of turbulent and convective updrafts (red arrows) are shown by the red profiles. These are associated with shear production of turbulence at the upper boundary that actively contributes to entrainment. The mean wind velocity of turbulent downdrafts (blue arrows) are shown by the blue wind profiles. These are associated with shear production at the surface, which is shielded from entrainment.

To begin with, we consider a mature, moderately sheared CBL (e.g. sketched in Figure 7.1(a)). Taking the depth of the shear zone in the SM and the EZ as an indicator, the characteristic length scales of the turbulence produced by shear must be small compared to the CBL depth, which roughly equals the scale of convection (dashed arrows). This means that eddies produced by shear in the SL (curved arrows) would be rather small and short lived compared to the large convective plumes (dashed arrows), which are essentially responsible for the upward transport and convective entrainment. So one can expect that in a deep CBL, mechanical turbulence, which was produced in the SL, might have been subjected to significant decay and dissipation, before it reaches the EZ. In the common spectral view on turbulence, one could further argue that SL shear-production creates relatively small-scale eddies. So even if they reach the EZ, they would rather feed the inertial subrange of EZ turbulence than contribute to the larger energy-containing eddies in the EZ, which are ultimately driving entrainment.²³

This pattern of a scale separation between SL turbulence produced by shear and

²³The rather abstract idea of a one-way energy flow through the ‘turbulent cascade’, which is inspired by Fourier-decompositions of the turbulence fields, is often used in boundary layer meteorology. However, such an ‘energy cascade’ can actually not clearly be found back in the physical space, and the coupling between the large production scales and small dissipating scales seems much more complex and interactive (Tsinober, 2001, Chapter 5.3). So instead, one might rather interpret the mentioned scale separation somewhat differently and consider the small scale turbulent motions that are created by shear in the SL as ‘disconnected’ from the relevant large convective structures, which drive entrainment and consist of both large-scale and ‘connected’ small-scale motions.

large scale convection and the associated spatial decoupling can be further illustrated by taking the structure of BL momentum transport into account. Here one finds that relatively slow air is concentrated in updrafts and fast air in downdraft as schematically shown by the red and blue profiles in Figure 7.1. In a CBL, with developed convective structures, slow warm SL air is concentrated in thermal updrafts, which are subjected to strong shear, when colliding with the fast FA air in the upper EZ. Thus thermals seem to feed the TKE shear production in the EZ (correlation between EZ shear and thermals). In turn, downdrafts (i.e. the subsiding cool environment of the thermals), have a relatively high horizontal momentum as they are enriched with FA properties. In regions, where these downdrafts reach the ground, the flow is subjected to relatively strong wind shear and therefore strong shear production of turbulence. However, before the so produced TKE can be transported upwards, the related turbulent air mass first has to form a thermal or laterally transfer its TKE into an emerging thermal. Thus, for a moving air parcel, we can expect a maximum spatial and temporal distance between the EZ dynamics and SL shear production.

A further particular quality of convective momentum transport becomes apparent in the upper SM. Here a strong momentum flux is maintained without ‘local’ mean shear (Figure 3.2(b) and (d)), which is commonly denoted as ‘non-local’ transport (e.g. Brown and Grant, 1997). Compared to the neutral BL, non-local transport results in rather upright wind profiles and hence in a further concentration of shear in the SL and the EZ (Figure 7.1).

If one increases the portion of TKE shear-production in the CBL, the SM depth decreases and the EZ depth increases. Due to enhanced shear and reduced convection, the suggested scale separation should become less pronounced as well. But at the same time, the TKE transport in the upper SM decreases as well, and the shallower SM and the deepened EZ both become dominated by shear-driven, local TKE dynamics. So we imagine that surface-related TKE shear-production remains detached from entrainment throughout the whole stability range. For weakly sheared CBLs scale-separation prevents an effective TKE transfer into the EZ, whereas close to the neutral limit TKE transport is simply small. Between the limiting states a combination of both mechanisms may be effective with varying intensity, depending on stability.

Ultimately, both mechanisms should depend on a sufficient locality of shear production within the BL, a property, which can be associated with a certain maturity of the BL, and might not hold for very shallow BLs in a very early state, when a strong shear production of turbulence is concentrated in a shallow layer. Due to a lack of data we can only speculate about a proper criterion that signifies the onset of the observed decoupling. A minimum value of the length scale h_*/z_{ig} (Jonker *et al.*, 2013) as a measure for the neutral BL’s maturity, could be a starting point. Again one might analogously consider the problem from the perspective of entrainment, which would suggest a critical minimal value for e.g. δ_S/z_i .²⁴

Finally, we expect that for any CBL in the equilibrium-entrainment regime entrainment is decoupled from SM-shear production. This conclusion is based on the finding that **all** our usable data show such a decoupling, but only a **subsample** are in the state of equilibrium entrainment, viz. the later stages of our LES-CBLs. Moreover, our analysis in chapter 6 indicates that the equilibrium-entrainment regime

²⁴Or, as $\delta_S \sim v_*/N$ is more characteristic for the upper EZ, an analogous length scale that represents the whole EZ may be more suitable. For instance, $\Delta_S = v_* / [(\Delta b / (z_i - z_{i1}))^{1/2}]$.

implies a significant locality of TKE shear-production within in the EZ, which should be sufficient to ensure the same for the whole CBL. Hence, the requirements for equilibrium-entrainment seem to be much more restrictive than the ones for a decoupling between entrainment and SL shear.

7.4.2 Shear-induced variation of the EZ turbulence regime and the generation of gravity waves

In chapter 4.2 we have investigated in detail the shear dependence of the integral TKE budget in the EZ. In the transition from the purely convective to the dominantly shear-driven CBL ($0 \leq S_* \leq 1$) we found a significant and characteristic variation of the TKE wave-drainage terms ϕ_B and ϕ_ε , which we interpret as an indicator for a systematic, but ‘non-linear’, change of the turbulent regime (Figure 4.19). Here we address this phenomenon once more and discuss some further aspects, which could help to better understand the nature of the transition. For this purpose, we consider four additional plots (Figure 7.2 to 7.5). Each of them shows the vertical variation of a quantity within the EZ and its dependence on EZ shear. Figure 7.2 shows the vertical distribution of the TKE transport term ϕ_z normalized by the EZ-mean entrainment flux, which equals $-B_{EZ}/(z_{iu} - z_{il})$. The height, which is displayed on the ordinate, begins at the bottom of the EZ at z_{il} and is normalized by the ZOM EZ depth $z_i - z_{il}$. For spatial orientation, the central EZ and the EZ top are marked by z_i (red dots) and $z_{i,g}$ (blue dots) respectively. As usual, the EZ shear-production in terms of S_* is shown on the abscissa. Figure 7.3 is constructed alike but displays the vertical distribution of the TKE tendency $\partial e_z/\partial t$, again normalized by the mean entrainment flux. The following plots use the same layout, but show the slab-averaged flux Richardson number Ri_f (Figure 7.4) and the gradient Richardson number Ri_g (Figure 7.5).

In the following we reconsider again the non-linear response of the EZ dynamics on shear. Based on the integrated TKE budget we already identified four different regimes:

Regime I ($S_* = 0$): It represents the non-sheared, free-convective CBL. EZ dynamics are driven by distinct thermals, that vertically penetrate into the stably stratified FA. Hereby they initiate local oscillations in the stably stratified FA that might spread as gravity-waves and transport momentum and kinetic energy. Horizontally traveling waves are initiated without any directional preference and thus cancel, if averaged over the ensemble. The remaining TKE losses due to the vertical component of gravity waves are rather small for mature CBLs²⁵, as also shown in various experiments before (e.g. GM14).

Regime II ($0 < S_* \leq 1$): It marks the transition from a convection-dominated to a shear-dominated entrainment regime if one considers the integral CBL TKE-dynamics, as, e.g., represented by S_* . Most significant for regime II is the presence

²⁵Stull (1976b) developed a detailed analytical model to estimate TKE wave-losses in a shear-free CBL. If we understand his reasoning correctly, the author also suggests that a large fraction of the gravity-waves spectrum is trapped within the EZ, as their frequency is higher than N , which represent the upper limit for wave-propagation in the FA.

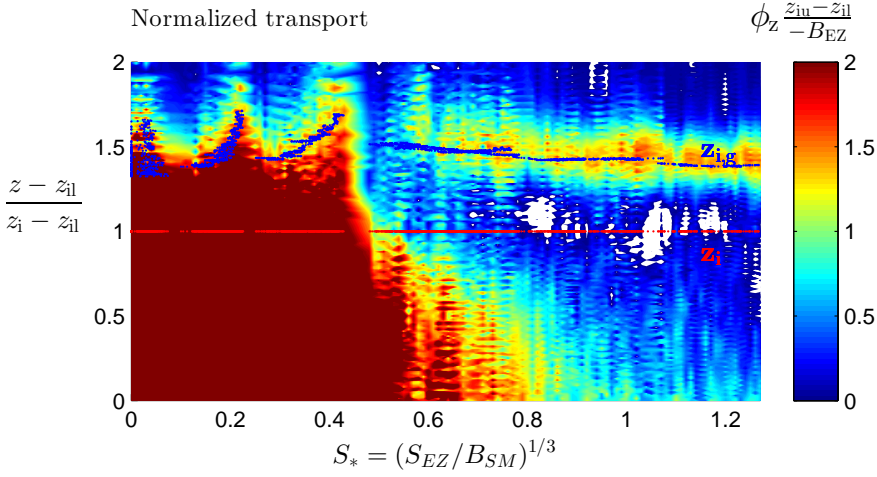


Figure 7.2: Vertical distribution of the local (slab-averaged) TKE transport in the EZ and its dependency on the integrated EZ shear-production. The TKE transport term is normalized with the EZ-averaged buoyancy flux $B_{EZ}/(z_{iu} - z_{il})$. The height z is shown on the ordinate and is normalized by the EZ depth $z_i - z_{iu}$. Overall EZ shear production on the abscissa is given as the characteristic velocity scale S_* . The white areas represent negative values.

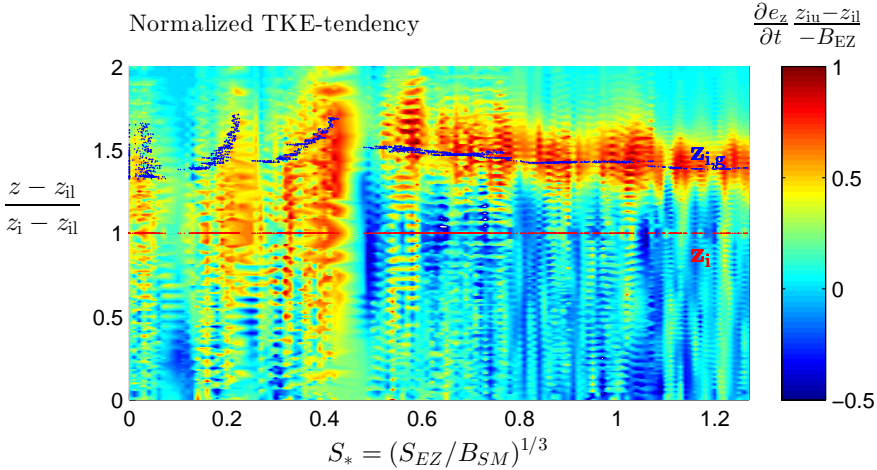


Figure 7.3: Vertical distribution of the local (slab-averaged) TKE-tendency (TKE spin-up) in the EZ and its dependency on the integrated EZ shear-production. TKE-tendency is normalized with the EZ-averaged buoyancy flux $B_{EZ}/(z_{iu} - z_{il})$. The height z is shown is normalized by the EZ depth $z_i - z_{iu}$. EZ shear production is given as the characteristic velocity scale S_* .

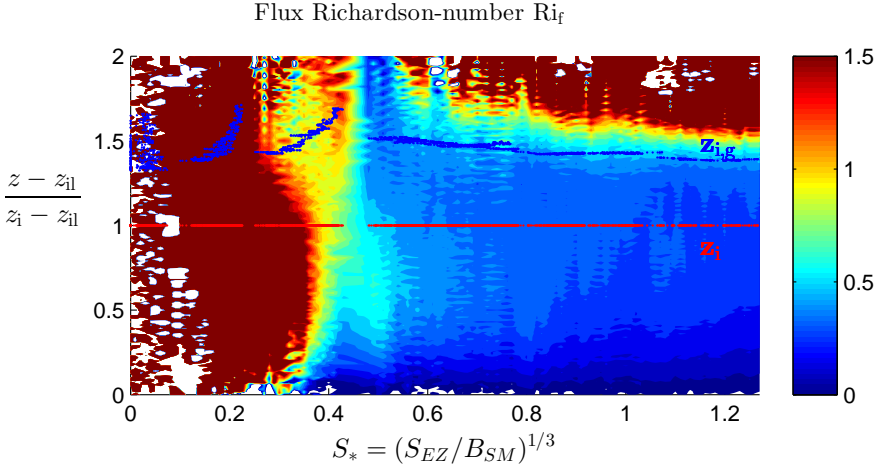


Figure 7.4: Vertical distribution of the local (slab-averaged) flux Richardson number Ri_f in the EZ and its dependency on the integrated EZ shear-production. The height z is normalized by the ZOM EZ depth $z - z_{il}$. EZ shear production is given as the characteristic velocity scale S_* .

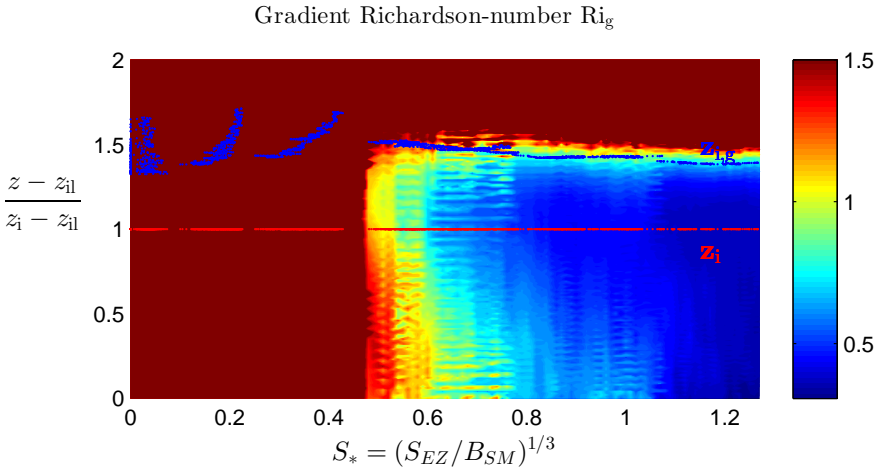


Figure 7.5: Vertical distribution of the local (slab-averaged) gradient Richardson number Ri_g in the EZ and its dependency on the integrated EZ shear-production. The height z is normalized by the ZOM EZ depth $z_1 - z_{il}$. EZ shear production is given as the characteristic velocity scale S_* .

of a finite wave-loss term ϕ_B , which results in a reduction of entrainment compared to a CBL with no wave-losses (Figure 4.19 and 4.20). If one considers the local TKE-dynamics within the EZ, as e.g. represented by the local flux Richardson number $Ri_f = -B_z/S_z$, regime II can be further subdivided: As shown in Figure 7.4 Ri_f becomes unity in the range of $S_* \approx 0.4..0.5$ throughout the EZ, representing the

actual transition between local buoyancy dominance (red) to shear dominance (blue). The distribution of the gradient Richardson number Ri_g gives a very similar picture, as shown in Figure 7.5. Thus regime II consists of a convection-dominated regime II,B for $0 < S_* \leq 0.5$ or $Ri_f \geq 1$ and a shear-dominated regime II,S for $0.5 < S_* \leq 1.0$ and $Ri_f < 1$.

Regime II,B ($0 < S_* \leq 0.5$): With the onset of shear in the EZ, the thermals enter an environment of faster flowing FA air in the upper EZ. As a result, they are accelerated in the horizontal direction and their trajectories (upward and downward) become tilted. This also means that the thermals hit the FA with a preferential horizontal momentum component against the flow direction and induce correspondingly oriented local gravity waves. Due to the preferred horizontal direction, they do not cancel statistically. Thus the systematic horizontal component of the impinging thermals is the cause for the correlation between vertical velocity and pressure fluctuations and between vertical and horizontal velocity fluctuations, which result in a net upwards flux of wave energy and a downward flux of momentum (Figure 4.12).

The maximum of energy leakage (relative to entrainment) occurs at $S_* = v_*/w_* \approx 0.5$ (Figure 4.10, 4.10 and 4.19). Under these conditions the trajectory of the thermals are strongly deflected by EZ shear, but the convective plume structure seems still largely preserved.²⁶ This would suggest that for the large penetrating thermals the vertical velocity is still mostly driven by convection, and therefore $\sim w_*$, whereas the horizontal velocity deviation of the plumes is caused by shear, which suggest a characteristic value $\sim v_*$. Hence, for $S_* = v_*/w_* \approx 0.5$ both velocity scales would be of the same order of magnitude. Thus convection and the shear-driven structures are supposed to ‘resonate’, which might signify the conditions for maximum wave-losses of TKE and momentum.

As discussed before, the TKE-drainage into the wave-field, seems mostly to be fed by the largest energy-containing convective plumes, which are the dominant source for EZ turbulence. As a consequence of the TKE-drainage, the portion of the available energy for both entrainment and dissipation is reduced.

At the upper interface of the thermals, entering the quicker but barely turbulent FA, local shear levels can reach critical values, so that Kelvin-Helmholtz (KH) waves can form, break and decay, which enhances local turbulent production. For weakly sheared CBL the scale of these local KH-waves is supposed to be significantly smaller than that of the entraining turbulence (Stull, 1988, page 476, Figure 11.31) and therefore their decay should not significantly contribute to entrainment.

Regime II,S ($0.5 < S_* \leq 1$): With S_* around 0.5, we imagine that the KH-unstable zones at the top of the plumes have significantly grown, approaching the size of the overturning plumes themselves. Hence, with a further increase of S_* beyond 0.5, we imagine the entire plume tops to become KH-unstable when entering the upper EZ. The recurring sequence of large-scale KH-billow formation, breaking and decay intensifies. The continuous creation of turbulent regions in the wake of the plumes result in a growth of the turbulent layer. Thus turbulent shear production becomes significant and finally leads to a significant enhancement of entrainment. At the same time the quick fracturing of the overshooting thermals reduces the formation of larger gravity waves and the wave-energy drainage ϕ_B diminishes until it has disappeared

²⁶Unfortunately, we did not store the 3-dimensional data-fields of a respective LES. Probably these would have enabled us to evaluate this and similar other questions directly.

for $S_* \approx 1$.²⁷

Thus in the range $0.5 < S_* \leq 1$ the convective structure of the EZ dissolves and the EZ turbulence becomes increasingly shear-driven. Our data suggest that the transition between convection-dominance and shear-dominance (change between regimes II,B and II,S) starts rather abruptly at the CBL top and then quickly extends downwards. Figure 7.2 shows that up to $S_* \approx 0.5$ the relative intensity of the TKE-transport term is large throughout the EZ (red and yellow), which is typical for convection. But for $S_* \approx 0.5$ TKE transport in the upper EZ, below $z_{i,g}$ becomes small (blue), which characterized the shear-driven local TKE-balance in a mature neutral BL. With a further increase of shear, this layer of shear-driven local turbulence continuously deepens (blue area). For $S_* \approx 1$, it fills most of the EZ. The same pattern can be deduced from the vertical distribution of the TKE spinup (TKE-tendency), as shown in Figure 7.3. In the convective state ($S_* < 0.5$) the spin-up process is spread over the whole upper and central EZ, (red and yellow areas) reflecting the TKE transfer within deeply intertwined structure of rising, highly turbulent, thermals and sinking non-turbulent FA air. For $S_* > 0.5$ TKE spin-up is restricted to a rather shallow layer at the interface to the FA (around $z_{i,g}$), where turbulence is maintained via TKE transport from below (Figure 7.2).²⁸ Such a narrow layer with significant TKE spin-up and positive TKE-transport is typical for a purely shear-driven neutral BL (Jonker *et al.*, 2013, Figure 8). Hence, for $0.5 < S_* < 1.0$ (regime II,S) the EZ-dynamics already largely resembles that of a neutral BL. But convective turbulence is still important and contributes to entrainment significantly.

Our qualitative view on the interaction of convection and EZ-shear agrees with the findings of Kim *et al.* (2003), who observed the formation of large KH-‘billows’ in the area directly downstream of ‘cool’ thermals (their Figure 11 and 12), using LESs, that are quite similar to ours. The authors do not characterize the flow conditions associated with KH-waves, but based on boundary-conditions and forcings, we estimate their relevant LES-CBLs to be in the range $S_* \approx 0.5 \dots 1.5$.

A critical value of the gradient Richardson number $Ri_g \approx 0.25$ has often been used as a predictor for KH instabilities and the onset of turbulence in a laminar shear flow (e.g. Stull, 1988, page 176). However, even in less sheared conditions (i.e. $Ri_g > 0.25$), we would expect KH instabilities to occur at the top of penetrating thermal updrafts. This is related to the fact that Ri_g is based on slab averages, as shown in Figure 7.5, and thus not representative for local flow conditions at the top of the thermals. Ri_g should therefore not be suitable to predict the local occurrence of KH instabilities in a moderately sheared EZ of a CBL.

²⁷One should clearly distinguish between the creation of energy-leaking, internal gravity waves in a stratified shear layer, which is always caused by an external forcing, e.g. orography or convection, and KH-billows, which are a shear driven phenomenon, that does not result in a leakage TKE, but in production of TKE. An interesting point is that for moderately sheared EZs, convection can be linked with both phenomena. The combination of organized penetrating plumes and EZ shear results in a rather efficient production of gravity waves ($S_* \leq 0.5$). But at the same time, the very efficient vertical momentum transport by the plumes should also result in locally elevated levels of shear at the top and windward side of the plumes, which for $S_* > 0.5$ should result in increasingly instable regions.

Note also that for both processes the ‘well organized’ character of convective plumes is relevant and not their ‘turbulent’, chaotic properties.

²⁸This layer corresponds well with GM14’s instationary interfacial upper EZ, see chapter 6.

Regime III ($S_* > 1.0$): It represents the shear-dominated EZ for $S_* > 1.0$. Different to the regime II,S, ϕ_B is finally zero again. Thus entrainment can be completely determined by the linear scaling of the TKE shear production. Regime III is distinguished from the neutral limit (regime IV) by the fact that still $w_* > 0$ and that – according to our data – the wave-loss term ϕ_ε , representing the reduction of dissipation due to the wave-drainage of TKE, is still finite. For the range $S_* > 0.5$ (regime II,S and III) we find ϕ_ε to be proportional to buoyancy production and to be significant, with $\phi_\varepsilon \approx 0.04 B_{SM}$ (Figure 4.20(b)). We have no clear idea about a cause for or a mechanism behind this term. As it is not related to entrainment, it seems not to be driven by the largest energy containing eddies. From a spectral point of view, it might therefore be related to turbulence in the inertial subrange. Speculatively, one could still attribute ϕ_ε to the ongoing vertical pulses of the buoyancy-driven plumes, whose intensity and characteristic size may now be exceeded by the scales of the shear-driven turbulence, as represented by the strongly deepened EZ (Figure 4.14). The characteristic size of the remaining convection, however, is still related to the ML, which has relatively decreased in size.

Regime IV ($S_* \rightarrow \infty$): It represents the neutral limit of a our sheared CBLs. As $w_* = 0$ and $\phi_\varepsilon = 0$ it equals the naturally neutral BL, as discussed in section 7.2. The self-regulation of the flow, as represented by the constant Ri_U (Jonker *et al.*, 2013, section 7.2.2) maintains a turbulent regime with a continuous dynamic instability throughout the BL. Fluctuating unstable regions with a noticeable formation of KH-billows may be still be present²⁹ at the interface between eddies and the FA. However, they should be restricted to the shallow intermittent upper EZ/BL-layer around $z_{i,g}$.

²⁹But we have no reports about that.

Chapter 8

Summary and perspectives

8.1 Summary of the most relevant findings

In this thesis we characterized the dynamics and structure of turbulent boundary layers (BLs) that are driven by both shear and buoyancy. Particularly, we focused on the question, how the combination of shear and buoyancy influences BL growth and entrainment. These hybrid BLs, or sheared convective boundary layers (CBLs) as we call them, are a core subject of boundary-layer meteorology as they represent typical daytime BLs. Yet, there is still no consensus about their actual behavior and functioning. Physical understanding seems patchy and common concepts and models are inconsistent and regularly show significant deviations from observations. This even holds for the most basic cases of mature, horizontally homogeneous and rotation-free BLs under a linearly stratified free atmosphere (FA), on which we focused here.

For a coherent view on these issues and a comprehensive understanding of the shear-dependence of the integral TKE- and growth-dynamics of CBLs, we investigated a series of LES of sheared CBLs in detail. Here we summarize our findings. First, we consider the suspected, but previously unproven linear dependence of entrainment on shear in the entrainment zone (EZ). Second, we consider the additional non-linear shear-effects on entrainment, These are related to local processes at the interface between the EZ and the overlying FA. We conclude this chapter with an outlook that outlines open issues and directions for further research.

8.1.1 The integrated TKE-budget and a 0th-order model for quasi-stationary sheared CBLs

Linear scaling of the integral TKE-budget of sheared CBLs. As our first major result we found that the integral entrainment and dissipation rate of sheared CBLs can – to first order – very well be represented by a linear combination of integral TKE buoyancy- and shear-production (research question A.I, submodel 1). Such an ideal linear behavior corresponds with the general idea of a Kolmogorov-type of inviscid scaling and seemed therefore likely. But due to physical ambiguity in the interpretation of the CBL structure it had never been consistently demonstrated before and had therefore even been disputed (e.g. Moeng and Sullivan, 1994). The

linear dependence of the entrainment ratio on shear production in the (EZ) can only be observed (Figure 4.3, black markers) if the integral buoyancy TKE-production and the TKE-consumption (i.e. entrainment) are defined by the structure of the mean buoyancy flux (Figure 4.1(a)).

This so called 'Eulerian Partitioning' (EP, Figure 5.1(a) or (c)) of the buoyancy TKE-production ensures that ensemble averages of the turbulent field are considered. Therefore it corresponds with the general idea of a Kolmogorov-type of inviscid scaling. Despite its manifest physical consistency, EP has been widely ignored in previous studies on sheared CBLs. Instead, those favored the so-called 'process-partitioning' (PP, Figure 5.1(a)). PP-based buoyancy terms implicitly represent subsamples of the turbulence ensemble. As a result, background contributions in the inertial sub-range do not cancel each other, which leads to an overestimation of both the effective integral buoyancy production and the entrainment term. Hence, PP does not conform with Kolmogorov-type of inviscid scaling. For CBLs this issue becomes apparent when shear varies, as due to local shear-enhancement the depth of the EZ varies as well.

Furthermore, we found that the EP-based CBL structure is also relevant to scale TKE shear-production. We showed that in mature CBLs only shear within the EZ contributes to entrainment (Figure 4.1(b)), and that the much larger shear-production in the surface layer plus mixed layer (SM) is irrelevant for entrainment (Figure 4.3, black versus blue markers). This significant feature has frequently been overlooked. Our data suggest that the EP-based EZ is the relevant entraining shear-layer, which refines Conzemius and Fedorovich's (2006b) earlier approach of a shear-based EZ. The consistent decoupling of surface-driven shear production and entrainment is suspected to be caused by a combination of (1) a scale separation between turbulence in the EZ and turbulence in the surface-layer under predominantly convective conditions and (2) the locality of the TKE budget under shear-dominated conditions.

An improved ZOM as quasi-stationary projection of the TKE-budget. Another initial goal of our study (research question A.II) was an explicit rescaling of the integral TKE-budget in terms of a 0th-order model (ZOM). Based on this rescaling approach (submodel 2) we could identify and correct the systematic deficiencies of previous ZOMs and construct a new ZOM (NZO), which very well reproduces the CBL growth dynamics of our LES-CBLs (Figure 5.7). As it represents the 'equilibrium entrainment regime' of mature CBLs, the NZO can be interpreted as a model for the shear-dependence of the CBL's constant layering. At the same time it also represents an accurate, fully linear, quasi-stationary projection of the CBL's integral TKE-dynamics (Figure 5.8), which, however, remains locally instationary (Figure 2.7, for a non-sheared CBL). Finally, in the neutral limit the NZO reduces to a constant bulk Richardson number Ri_U .

Validity of both linear TKE-models over the full stability range. To extend our data analysis to the neutral limit, we referred to Jonker *et al.*'s (2013) DNS study of neutral BLs under a stratified FA. These are commensurate with the neutral limit of our barotropic sheared CBLs. As in previous studies, the authors found that entrainment in neutral BLs is governed by a critical bulk Richardson number Ri_U , which corresponds to the neutral limit of the NZO. The good quantitative agreement between $Ri_U \approx 0.17...0.19$ as diagnosed from our LES-CBLs and the value of $Ri_U \approx$

0.19 as given by the neutral DNS-BLs strongly suggests that the NZO is indeed valid over the full stability range.

Additionally, we analysed the integral TKE budget in the neutral limit (Eq. 4.26). As buoyancy production becomes insignificant close to the neutral limit, the relevant EZ shear-layer must be redefined. Instead of the buoyancy-based EZ, the shear zone above the inflection point of the wind profile becomes the relevant layer (as previously suggested by Conzemius and Fedorovich, 2006b). We denote this layer as the shear-driven EZ (SEZ, Figure 4.1(b)). With this redefinition of the layer structure of the sheared CBL, we demonstrated that the linear model of the integral TKE budget could be extended to the neutral limit.

8.1.2 Deviations from the linear characteristics due to local interfacial processes

Due to two distinct local processes at the upper interface between the entrainment zone and the stratified FA, we observe systematic and significant deviations from the underlying linear shear-dependency of the TKE-dynamics. The first process is the direct local influence of FA stratification on turbulence in the intermittent upper part of the EZ. The second process is the turbulence-driven formation of gravity waves at the stratified interface, which result in a leakage of TKE out of the CBL into the stratified FA.

Direct influence of the FA stratification on the EZ dynamics. The direct influence of the FA stratification on the upper EZ, which can be linked to the CBL's instationarity, has recently been studied in detail for non-sheared CBLs by Garcia and Mellado (2014, GM14). With our data we show that their model for the interfacial influence on the EZ dynamics can well be extended to sheared CBLs (research question B).

Our generalized model is based on two elements. The first is a redefined, shear-dependent stationary reference framework, that allows to rate the local effects. For this purpose the NZO is a natural choice. The second element is based on GM14's concept for the formation and dynamics of the interfacial upper EZ layer, extended to take into account the impact of EZ-shear (Figure 6.4). According to our data this extension can be achieved by a superposition of convective and shear-driven contributions, each represented by a separate characteristic penetration depth. Our model for the EZ-structure can well reproduce the influence of shear on entrainment (Figure 6.6) and the EZ buoyancy structure (Figure 6.9) in the equilibrium entrainment regime. The generalized EZ model is supposed to cover the full stability range as well. But due to a lack of data we cannot test it in the neutral limit.

As the model for the EZ-structure is defined relatively to equilibrium entrainment conditions, which are represented by the NZO, our parametrization of FA-stratification effects on entrainment can directly be incorporated into a ZOM (e.g. the NZO).

Shear dependence of the gravity-wave-driven TKE-drainage. Based on observations of shear-free CBLs and neutral BLs, previous studies assumed that the

impact of turbulence-induced FA gravity-waves on the TKE budget is also negligible for sheared CBL. However, to the contrary, our data show that the drainage of TKE via gravity-waves can be significant and systematically depends on EZ shear. TKE wave-losses are strongest for moderately sheared CBLs, where velocity scales for EZ shear- and buoyancy-production are of the same order ($S_* \approx 0.5$, Figure 4.10), conditions for which the local $Ri_g \approx 1.5$ (Figure 7.5).

In order to quantify the effect of wave-losses on entrainment, we need not only quantify these wave-losses but also partition them between entrainment and dissipation. For this partitioning we compare our atmospheric LES-CBLs to conceptual CBLs with a neutrally stratified FA (NFA). This idealized setup prevents the formation of gravity waves and therefore represents the undisturbed dynamics without wave-losses (blue marker in Figure 4.18). The idealized simulations indeed confirm that with the exclusion of gravity-wave losses both entrainment and dissipation scale linearly with EZ shear production. From this result we can determine which part of the wave-losses affects entrainment (the difference between the actual entrainment and the linear model). Subsequently, these wave-loss reduction terms can be parameterized via simple curve fitting (Figure 4.20) and integrated into the NZO (Figure 5.7).

8.2 Perspectives

Here we present and discuss a number of directions for a potential continuation of the research of this thesis. We grouped our ideas in five categories, which could be loosely associated with a series of partly independent steps for a line of research (not coercively in temporal order) to come to a further improved understanding of ABL entrainment dynamics. We note that some of these ideas are quite preliminary and need further reflection and scrutiny based on current literature.

The first (1) step would consist in the creation of an improved data base (in terms of simulation quality) to verify and sharpen the results of this thesis. Next (2) we might stretch our analysis to earlier phases of the BL development, but still do so within the general framework of this thesis. In a further step (3) one could increase the complexity of the investigated BLs in order to approach the conditions in real ABLs. Such investigations should be complemented (4) with a refined analysis, that could take a closer look at the EZ structure. Such efforts could finally result in refined and more detailed understanding of the entrainment process, as well as of the formation of gravity waves, using alternative modeling concepts. At the same time (5) one should consider potential applications and implications for atmospheric modelling at all scales, while at the same time look at the connection with other issues in a wider meteorological context.

Improved data base. Before dealing with new issues, it seems advisable to put the findings of this thesis on a more solid basis by evaluating them once more with an improved data set. Such an evaluation would mostly entail a testing of the assumptions behind the NZO (chapter 5) and the EZ-structure model (chapter 6), and the determination of reliable values for the respective constants. A proper data base would consist in a series of DNSs or high resolution LESs. A combination of both techniques might be an economical approach, e.g. a small series of computationally

expensive corner-stone DNSs that are interpolated by a set of less expensive LESs. In first instance we would prefer the simple experimental set-up of (Jonker *et al.*, 2013) combined with a constant buoyancy surface flux. This would eliminate the additional complexity of the effect of system rotation on the wind field. Such a basic data set could be later complemented according to further requirements.

Early phase dynamics. First of all, it seems a logical step to extend our analysis to the earlier phases of the CBL evolution, when δ/z_{zi} (or δ/z_S) > 0.15 . This phase is quite relevant for ABLs, e.g. during typical morning transitions. Under these conditions, the layering of the BL structure additionally depends on the evolutionary state (as indicated by the gray lines in Figure 5.8). However, we expect that also under these conditions δ/z_{zil} (or δ/z_S) remains a characteristic scale that could be used to determine the CBL structure. A relationship $\beta = f(\delta/z_{zil})$ would define an extension of the NZO. In this context also the dependence of the wave-losses on the evolutionary state of the CBL (Figure 4.8, gray versus colored markers), which we mostly ignored in our analysis, should be determined and investigated in more detail.

Added complexity to approach real-life boundary layers. Another research trajectory would deal with the dynamics of sheared CBL that are subject to more complex forcings and boundary conditions, thus resembling real ABLs more strongly¹ More complex sheared CBLs could e.g. include a height-dependent pressure gradient (baroclinicity, e.g. as in Conzemius and Fedorovich, 2006a), a Coriolis forcing or a height-dependent stratification of the free atmosphere.

As mentioned before, the addition of a Coriolis forcing results in an inertial oscillation (IO), which adds another time scale to the mean momentum dynamics. A typical feature is the occurrence of directional shear. In our data set directional shear only affected the ML and therefore had no discernible effect on entrainment. However, for near-neutral BLs, directional shear is supposed to occur within the EZ and therefore affects the integral entrainment dynamics (e.g. Wyngaard, 2010, Figure 11.4). The instantaneous impact of the IO depends on the oscillatory state, which is determined by much earlier conditions and the oscillation history. It would be interesting to see to what extent this variability can be accounted for with a simple integral framework like the NZO.² A switch to a multilayer column model might finally become necessary.

Another issue that is common in real ABLs is the impact of a non-linear FA stratification, e.g. enhanced inversions above a less stratified residual layer. Such an arrangement would result in a significant variation of $\rho_{\Delta b}$ (Eq. 6.3). We mentioned the potential issues in chapter 6, but these transitional effects could be studied more systematically and included in the formulation of the NZO and the EZ-structure model.

Spatial structure of BL turbulence and FA gravity waves. There are still several open questions with respect to the composition and the spatial structure of

¹The selection of such modification should be influenced by the relevance for applications.

²Note that the considerations of Zilitinkevich and Esau (2002) seem to be based on approximate equilibrium solutions of the IO. However, one can easily show that the mean velocity field of a typical growing ABL is constantly and significantly out of its inertial equilibrium. With respect to a typical diurnal cycle of the ABL mean wind velocity, see, e.g., Thorpe and Guymer (1977).

CBL flows. To address them, one may next visualize and carefully inspect the three-dimensional fields of BL turbulence as well as the FA gravity waves (e.g. GM14's Figure 2 and 6). Such an unfiltered visualization of the actual flow may well inspire further investigations. Due to lack of data, we could not use this basic source of information in our study.

A broader topic that we have in mind is a selective analysis (using conditional sampling (e.g. Schumann and Moeng, 1991)) of updrafts and downdraft, focusing on their properties and their budgets of buoyancy and momentum. The aim would be to further specify the actual working of entrainment dynamics, as well as the transfer of momentum and TKE into gravity waves. Using the NZO framework, these budgets of basic types of CBLs can probably be well scaled. A model for the updraft and downdraft budgets could next be used to build more complex multi-layer mass-flux models of sheared CBLs, similar to those developed for pure CBLs (Siebesma *et al.*, 2007; Cheinet, 2003).³ Such models should be more flexible and therefore work better in complex conditions (e.g. with the additional vertical variations of shear due to baroclinicity) and allow a closer connection with a cumulus cloud layer. Improvements in this respect could be useful for GCMs, that use mass-flux models for the CBL representation (e.g. the ECMWF model⁴.)

A further topic would be a characterization of the horizontal structure of CBL turbulence and the related FA wave field. A very prominent feature in sheared CBLs is the formation of large-scale convective rolls.⁵ According to previous studies the occurrence and intensity of these CBL rolls basically depends on SM stability, as measured by SL-similarity-theory based measure $(-z_i/L)$.^{6,7} However, it is easy to imagine that also EZ shear and entrainment contribute to the roll formation, particularly in the immature CBLs, when momentum entrainment can be strong. According to Salesky *et al.* (2017) this issue is still unclear. The characterization of the EZ dynamics, that we develop in this thesis could be quite helpful to identify a potential impact of the EZ on the formation of convective rolls in an appropriate data set.⁸ In turn, one could also expect that well-developed convective rolls, which extend over the whole CBL and are aligned with SM shear, influence the structure of the EZ. This should be particularly relevant for CBLs in the mid-latitude as these may exhibit an inertial oscillation (IO). The IO typically causes strong differences in the direction of shear between SM and EZ (i.e. directional shear, Figure 3.3). In this respect it remains remarkable that we could not notice any direct influence of the directional shear between SM and EZ on the entrainment dynamics of our LES-CBLs. This raises more question about the specific nature of the relationship and interactions between the spatial structures of turbulence in the SM and the EZ and turbulence-driven FA

³Note that according to De Roode *et al.* (2000) mass-flux approaches remain analogous to Reynolds averaged models.

⁴European Centre for Medium-Range Weather Forecasts, ECMWF.

⁵If cloud condensation in the upper BL occurs, the top of these rolls is marked by characteristic cumulus cloud streets.

⁶Where $L = -u_*^3/(\kappa B_0)$ is the Obukhov length with the 'Von Kármán constant' $\kappa \simeq 0.4$.

⁷The physical significance of this roll-structure lies in the fact that it minimizes the disturbance (shear and momentum exchange) between slow thermal updrafts and quicker downdraft, which means that it preserves the large convective structures (thermals) in a sheared environment. As this roll structure uniquely combines shear and convection it forms best in moderately sheared CBLs with $(-z_i/L) \approx 3$ (Salesky *et al.*, 2017, Figure 7).

⁸Where e.g. $(-z_{i1}/L)$ (or very similarly S_{SM}/B_{SM}), S_* and δ/z_{i1} vary independently.

gravity-waves.

In this context it is worth noting that the horizontal scale of convective rolls tends to grow continuously and independently of their vertical scales. For scalars, it is known that an enhanced growth of horizontal scales in CBLs is typically caused by entrainment (in particular when the entrainment ratio differs significantly from that of buoyancy, e.g. De Roode *et al.*, 2004). A final characterization of this feature in relation to the CBL momentum structure (e.g. rolls) seems still missing.⁹

Finally, it would be worthwhile to study sheared CBLs with a forced subsidence (vertical velocity) regime. This would result in horizontal flow divergence and a horizontal heterogeneity of the mean flow, including resulting momentum advection, an aspect that is relevant in real ABLs (e.g. Wyngaard, 2010, chapter 11.2.3.2).¹⁰ The homogeneous case and the NZO would offer a reference framework to characterize inhomogeneous flows.

Meteorological application and implications. With the view on more direct and practical applications of our findings we want to mention two aspects.

The most direct practical outcome of our research is the simple integral representation of sheared CBLs, as represented by the NZO and the EZ-structure model. These enable a very efficient and direct evaluation and comparison of various types of data related to horizontally homogeneous CBLs within the studied parameter space. This not only holds for LES and DNS, as we demonstrated in the previous chapters in detail, but basically for any other observational dataset or CBL model. This could be directly used for a comprehensive evaluation of various boundary-layer parameterization schemes in GCMs (as, e.g., used for numerical weather prediction).

The other aspect concerns the significant CBL gravity-wave interactions that we observed and characterized for moderate EZ shear ($S_* \approx 0.5$). These interactions lead to TKE-losses, resulting in a reduced entrainment rate, and wave-drag, causing a momentum transfer between the FA and the CBL.

As far as we know, these effects are not explicitly considered in GCMs. The neglect of wave-losses should — in principle — result in systematic errors in the development of CBLs. However with respect to a more integral performance of GCMs, we do not expect that such errors will have a strong impact on the forecast potential, as they may well be compensated by other errors, or by a tuning of existing CBL parametrizations.

The contribution of the systematic and unaccounted CBL wave-drag could be more relevant. The reason would be that slightly sheared CBLs with $S_* \approx 0.5$ might occur quite frequently in the atmosphere¹¹ and therefore could create a background wave-drag for the FA. Locally these effects should be much weaker than the wave-drag that is caused by orography and cloud convection (which are parametrized in advanced GCMs), but due to its frequent occurrence, it might be significant on a global scale. This idea agrees with the finding that, e.g., the ECMWF-model atmosphere lacks a sufficient coupling between the ABL and the troposphere above, a deficiency that

⁹But any further research on this issue should be coordinated with the profound and partly unpublished work of Harm Jonker and Stephan De Roode (both TU Delft) about horizontal scales in cloudy BLs.

¹⁰In a LES or DNS such CBLs could be realized by a external sinusoidal forcing of the vertical mean velocity at the upper domain boundary. This could also be combined with heterogeneous surface heating.

¹¹Particularly, if one assumes similar conditions in CBLs with a low cloud coverage.

cannot be related to convective processes.¹² The unnoticed background wave-drag of very common fair-weather CBLs might explain this feature. Using our LES result (Figure 4.12) and standard output fields of a global weather model, one could easily estimate the global impact of fair weather CBL wave-drag.¹³ These values could then be compared with the mentioned drag bias and e.g. with the wave-drag induced by other relevant processes, such as cloud convection and orography.

¹²According to an oral presentation by Anton Beljaars (then ECMWF), ca. 2011 at Wageningen University.

¹³With the model outputs one determines S_* and w_* for every point on the global grid. By fitting a curve to Figure 4.12, one gets a relationship $\overline{U'w'}|_{\text{FA}} = f(S_*, w_*)$ so that wave-drag $\overline{U'w'}|_{\text{FA}}$ can be estimated for each location and globally integrated afterwards.

Appendix A

The critical Richardson number for CBLs, $Ri_{U,B}$

The NZO can be written as a EZ bulk Richardson number $Ri_{U,B}$, which equals the sum of the critical EZ bulk Richardson number Ri_U plus a stability correction. By normalizing the NZO TKE budget Eq. 5.6 with the EZ shear production term $S_{EZ} = 1/2 k_S w_e \Delta U^2$ and assuming $\phi_B = 0$ on gets:

$$\frac{\Delta b(z_i - z_{il})}{\Delta U^2} = \frac{c_{B,S} k_S}{k_{BEZ}} + \frac{c_{B,0}}{k_{BEZ}} \frac{B_0 z_{il}}{k_S w_e \Delta U^2} \quad (\text{A.1})$$

Here the term on the lhs is the EZ bulk Richardson number $Ri_{U,B}$, the first term on the rhs equals the constant critical EZ Richardson number $Ri_U \approx 0.17$ (Eq. 7.4) and the second terms is proportional to the ratio of integral buoyancy- and shear-production, which can be denoted as the integral production Richardson number

$$Ri_P = \frac{B_0 z_{il}}{k_S w_e \Delta U^2} = \frac{B_{SM}}{S_{EZ}} = \frac{1}{S_*^3}. \quad (\text{A.2})$$

Hence the NZO equals

$$Ri_{U,B}(\text{NZO}) = Ri_U + \frac{c_{B,0}}{k_{BEZ}} Ri_P. \quad (\text{A.3})$$

In the equilibrium entrainment regime the factor $c_{B,0}/k_{BEZ}$ is supposed to be constant. In the neutral limit $S_* \mapsto \infty$ or $Ri_P \mapsto 0$ and therefore $Ri_{U,B}(\text{NZO}) \mapsto Ri_U = \text{const.}$

Appendix B

The NZO in the neutral limit: Reanalysis of Jonker *et al.*'s (2013) DNS results

To diagnose the NZO parameters from the DNSs of Jonker *et al.* (2013), we digitalized their plots of scaled flow profiles (their Figure 5 and 8), as reproduce in our Figure B.1).¹ In this appendix we interpreter these dimensionless profiles, using the associated empirical BL growth-law. The evolution of the flow can be rather directly determined by the external parameters, which is the constant linear stratification of the undisturbed fluid N^2 and the friction velocity u_* , which is set to be constant as well. The latter is an important detail, which determines the quite characteristic BL evolution and the related growth-law of the BL depth $h(t)$. However, we do not focus on the temporal evolution and only use Jonker *et al.*'s (2013) growth-law to interpret the characteristic state of turbulence as represented by profiles of buoyancy b_z , velocity u_z , TKE shear-production S_z and buoyancy-consumption B_z and their respective ZOM representation, which are shown in dimensionless form in Figure B.1 (subscript EZ,h or EZ).

With the condition $u_* = const$, Jonker *et al.* (2013) empirically found that the evolution of the BL depth h strictly follows a square-root law (their Figure 4b) given by

$$h(t) = z_{i,g}(t) = \gamma \frac{u_*}{N} \sqrt{Nt}, \quad \text{with } \gamma \simeq 1.0, \quad (\text{B.1})$$

which is the essential base for their scaling. Here h is defined as the height of the maximum gradient (which we denoted as $z_{i,g}$ before). The difference between h and the total dept of the turbulent layer z_{iu} is rather small. The respective ZOM averages (subscript h) shall therefore well represent averages over the whole flow. Thus the

¹Reading errors are supposed to be insignificant.

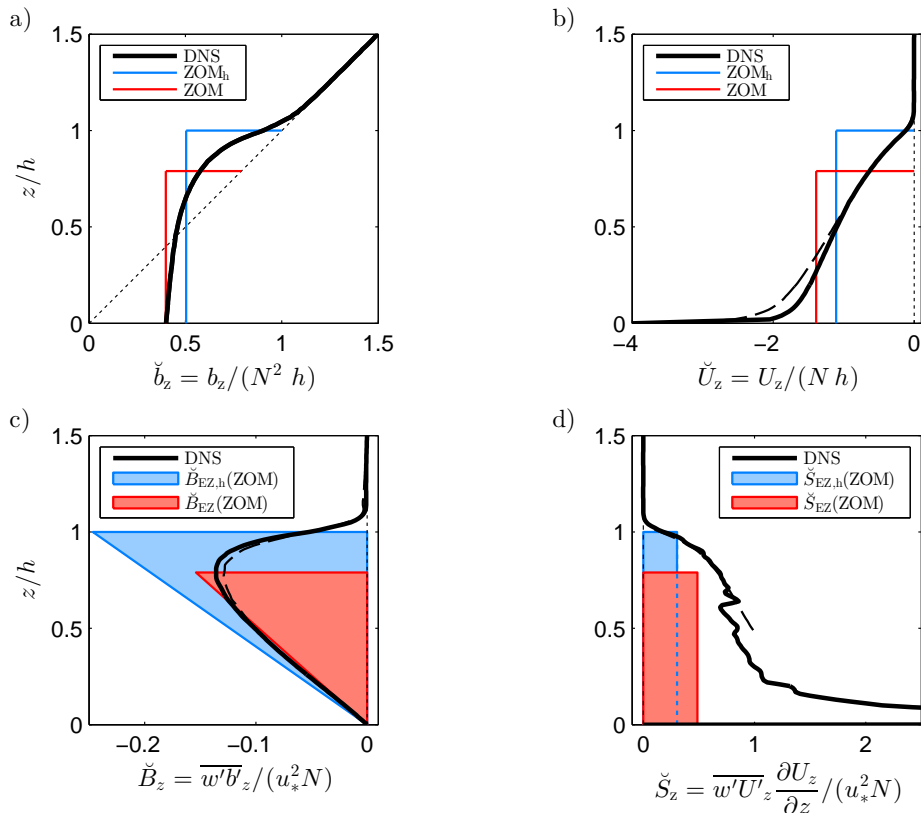


Figure B.1: DNS-results of neutral boundary layers by Jonker et al. (2013). Self-similar profiles (solid black lines), related ZOM based on h (blue) and ZOM quantities based on z_i (red) are displayed. (a) buoyancy, (b) horizontal velocity, (c) buoyancy production of TKE (d) shear production of TKE. For (a) and (b) the ZOM profiles are displayed. (c) and (d): The integrated ZOM TKE term for the upper interface is displayed as closed area. (d): The shape of the shear production is arbitrarily shown as a rectangle. Flow profiles scanned and digitalized from Jonker et al. (2013), solid black line: their Figure 5, black dashed line: their Figure 8. Differences between solid and dashed black lines indicate remaining uncertainties in the profiles, mostly due to transitional and viscous effects.

ZOM jumps at the upper interface are given as

$$\Delta U_h = -U_h = -\frac{1}{h} \int_0^h U_z dz \quad \Delta b_h = \frac{1}{h} \int_0^h b_z dz. \quad (\text{B.2})$$

From the chosen experimental setup and the observed growth-regime follow quite simple rules for the Δb_h and Δu_h : As we do not have any buoyancy source in the system, the total amount of buoyancy stays constant and therefore the buoyancy jump

at the top Δb_h is always given by (see geometry in Figure B.1(a), gray dotted line):

$$\Delta b_h = b_z(h) - b_h = \frac{N^2 h}{2}. \quad (\text{B.3})$$

As stress divergence is the only force that acts on the BL flow, the mass flow $hU = -\Delta(hU)$ of the layer is given by the time integral of

$$\frac{\partial(hU_h)}{\partial t} = u_*^2. \quad (\text{B.4})$$

Thus

$$\Delta U_h = 0 - U_h = -\frac{u_*^2 t}{h}. \quad (\text{B.5})$$

Here we substitute t with $t = Nh^2/u_*^2$ as given by the growth-law Eq. B.1 and simply get

$$\Delta U_h = Nh. \quad (\text{B.6})$$

Consequently, $N^2 h$ and Nh are appropriate scales to normalize buoyancy and momentum respectively (Jonker *et al.*, 2013, their Figure 5) as shown in Figure B.1(a) and (b). Here black lines represented the profiles of the dimensionless (marked by \checkmark) buoyancy $\checkmark b_z$ and the dimensionless wind velocity $\checkmark U_z$, with

$$\checkmark b_z = \frac{b_z}{N^2 h} \quad \text{and} \quad \checkmark U_z = \frac{U_z}{Nh}. \quad (\text{B.7})$$

With Eq. B.3 and B.6, one can directly determine a critical (characteristic) bulk Richardson number $Ri_{U,h}$ of the flow:

$$Ri_{U,h} := \frac{h\Delta b_h}{\Delta U_h^2} = \frac{1}{2}. \quad (\text{B.8})$$

The entrainment velocity $w_{e,h}$ is defined by the time derivative of the growth law $h(t)$ (Eq. B.1)

$$w_{e,h} = \frac{\partial h}{\partial t} = \frac{u_*}{2} \left(\frac{N}{t} \right)^{1/2}, \quad (\text{B.9})$$

To express $w_{e,h}$ only with state variables, one again substitutes t by $t = Nh^2/u_*^2$ (Eq. B.1) and get

$$w_{e,h} = \frac{u_*^2}{2Nh} = \frac{1}{2\sqrt{2}} \frac{1}{\sqrt{Ri_*}}, \quad \text{with } Ri_* = \frac{N^2 h^2}{2u_*^2}. \quad (\text{B.10})$$

With $w_{e,h}$ we can determine the integrated ZOM entrainment $B_{\text{EZ},h}(\text{ZOM}) = 1/2 w_{e,h} \Delta b_h h$ and the upper boundary shear production $S_{\text{EZ},h}(\text{ZOM}) = 1/2 w_e \Delta U_h^2$ (as for the NZO). Division by $u_*^2 Nh$, defines the respective normalized quantities $\checkmark B_{\text{EZ},h}$ and $\checkmark S_{\text{EZ},h}$, (again marked by \checkmark), as shown in Figure B.1c and d (blue bounded areas). By further inserting the expression for Δb_h (Eq. B.3) and ΔU_h (Eq. B.6) we get

$$\checkmark B_{\text{EZ},h}(\text{ZOM}) = \frac{w_{e,h} \Delta b_h h}{2u_*^2 Nh} = \frac{\Delta b_h h}{4N^2 h} \simeq \frac{1}{8}, \quad (\text{B.11})$$

and

$$\check{S}_{\text{EZ},h}(\text{ZOM}) = \frac{w_{e,h}\Delta U_h^2}{2u_*^2Nh} = \frac{\Delta U_h^2}{4N^2h^2} \simeq \frac{1}{4}, \quad (\text{B.12})$$

For comparison with the NZO we have to rescale all ZOM quantities to the respective depth z_i (denoted by red lines and areas in Figure B.1). From the DNS profiles we read

$$\gamma_{zi} = \frac{h}{z_i} \approx 1.27. \quad (\text{B.13})$$

Furthermore

$$w_e = \frac{w_{e,h}}{\gamma_{zi}}, \quad \Delta b = \frac{\Delta b_h}{\gamma_{zi}}, \quad \Delta U = \Delta U_h \gamma_{zi}. \quad (\text{B.14})$$

From $Ri_{U,h}$ (Eq. B.8) the respective z_i based critical Richardson number Ri_U can be computed as

$$Ri_U = \frac{B_{\text{EZ}}(\text{ZOM})}{S_{\text{EZ}}(\text{ZOM})} = \frac{Ri_{U,h}}{\gamma_{zi}^4} \approx 0.19. \quad (\text{B.15})$$

The respective NZO TKE terms can be determined as

$$B_{\text{EZ}}(\text{ZOM}) = \frac{1}{2}w_e\Delta b z_i = \frac{B_{\text{EZ},h}}{\gamma_{zi}^3} \quad (\text{B.16})$$

and

$$S_{\text{EZ}}(\text{ZOM}) = \frac{1}{2}w_e\Delta U^2 = S_{\text{EZ},h} \gamma_{zi}. \quad (\text{B.17})$$

Using again the scale u_*^2Nh , we get the respective dimensionless quantities \check{B}_{EZ} and \check{S}_{EZ} :

$$\check{B}_{\text{EZ}}(\text{ZOM}) = \frac{\check{B}_{\text{EZ},h}}{\gamma_{zi}^3} \approx 0.061 \quad (\text{B.18})$$

and

$$\check{S}_{\text{EZ}}(\text{ZOM}) = \check{S}_{\text{EZ},h} \gamma_{zi} \approx 0.32. \quad (\text{B.19})$$

These are shown in Figure B.1(c) and (d) as the red-bounded areas.

From the data presented in Figure B.1 we can now estimate the NZO parameters. For k_{BEZ} , which represents the ratio between actual and ZOM entrainment, can be computed as

$$k_{\text{BEZ}}(\text{DNS}_n) = \frac{\int_0^{z_{iu}} \check{B}_z dz}{\check{B}_{\text{EZ}}(\text{ZOM})} \approx 1.44. \quad (\text{B.20})$$

Here z_{iu} is the top of the turbulent layer. To diagnose the shear parameters $c_{B,S}$ and k_S one must be aware that the mentioned Reynolds-number independence is only fully realized in the upper half of the DNS flow. The lower part of the flow do not fully comply with the inviscid scaling. The resulting spread of the flow profiles is indicated by the difference between the black solid and dashed lines in Figure B.1b. These undesired viscous effects are supposed to results in $\Delta U_h/Nh \approx 1.1$ (Figure B.1b, blue line), which is somewhat larger than the predicted unity (Eq. B.6). To get an interpretable values for $c_{B,S}$ and k_S , we therefore follow (Jonker *et al.*, 2013) integrate the BL over upper portion of the BL from z_x to z_{iu} , for various z_x . For the neutral BL DNS these are given by:

$$c_{B,S}(\text{DNS}_n, z_x) = \int_{z_x}^{z_{iu}} \frac{\check{\check{B}}_z}{\check{\check{S}}_z} dz \quad (\text{B.21})$$

a respective value for k_S could be analogously defined as

$$k_S(\text{DNS}_n, z_x) = \frac{\int_{z_x}^{z_{iu}} \check{\check{S}}_z dz}{\check{\check{S}}_{EZ}(\text{ZOM})}, \quad (\text{B.22})$$

Or, for $z_x = 0$, $k_S(\text{DNS}_n)$ can be simply computed via $Ri_U = c_{B,S} k_S/k_{BEZ}$ (Eq. 7.3).

Appendix C

Mutual rescaling of the CFM and the NZO

To directly compare the CFM with the NZO, it makes sense to rescale the CFM using the EP- or the NZO scales z_{il} or $\Delta\hat{U}$ respectively. In turn, for typical applications, it seems convenient to rewrite the NZO using CBL depth z_i as the only scale, which also implies the use $\Delta\tilde{U}$ instead of $\Delta\hat{U}$.

The CFM in terms of $\Delta\hat{U}$. With $z_i = z_{il} + (z_i - z_{il})$ one can write the CFM (Eq. 5.21) as

$$\begin{aligned} & \frac{w_e}{2} \Delta b z_{il} + \frac{w_e}{2} \Delta b (z_i - z_{il}) = \\ & C_1 \frac{B_0}{2} z_{il} + C_1 \frac{B_0}{2} (z_i - z_{il}) + C_P \frac{w_e}{2} |\Delta U|^2. \end{aligned} \quad (\text{C.1})$$

Using the ZOM geometry (Eq. 5.3), normalizing with the NZO buoyancy production $1/2 B_0 z_{il}$ (Eq. 5.1) and using the definition for \hat{w}_e and $\Delta\hat{U}$ we get

$$\hat{w}_e^2 + \underbrace{\hat{w}_e}_{\Delta B_1} = \underbrace{C_1 \hat{w}_e}_{\Delta B_2} + C_1 + C_P \hat{w}_e \Delta\hat{U}^2. \quad (\text{C.2})$$

Disregarding the different value of the constant parameters, this expression is structurally identical with the NZO (Eq. 5.11), except for two additional terms, ΔB_1 and ΔB_2 , which represents the difference between PP as used in the CFM and EP in the NZO. Interestingly, this 'error term' $\Delta B = \Delta B_1 - \Delta B_2$ is simply linear in \hat{w}_e , whereas the whole equation is quadratic. This means that also the CFM is defined for the full range of EZ shear, if the latter is measured in terms of $\Delta\hat{U}$ using z_{il} as integral length scale. Solving for \hat{w}_e one gets the expression

$$\hat{w}_e = \frac{C_P \Delta\hat{U}^2 + C_1 - 1}{2} + \left[\frac{(C_P \Delta\hat{U}^2 + C_1 - 1)^2}{4} + C_1 \right]^{1/2}, \quad (\text{C.3})$$

which is displayed in Figure 5.7 (dashed black line).

The NZO in terms of $\Delta\tilde{U}$. Analogously, we can also rescale the NZO, using CFM- or PP-scales respectively. These are based on the Deardorff-length z_i , which implies $\Delta\tilde{U}$ as measure for shear and the buoyancy production $B_{\text{SM}}(\text{CFM}) = 1/2B_0z_i$. The ZOM geometry (Eq. 5.3) can also be expressed as

$$z_{i1} = \frac{z_i}{\frac{w_e\Delta b}{B_0} + 1} = \frac{z_i}{\tilde{w}_e + 1}. \quad (\text{C.4})$$

Normalizing the NZO budget equation (Eq. 5.6) with the CFM buoyancy production, substituting z_{i1} with Eq. C.4 and using the definitions for $\Delta\tilde{U}$ and \tilde{w}_e (Eq. 5.23) we finally get

$$\begin{aligned} \tilde{w}_e = & \frac{c_{\text{B,S}} k_{\text{S}} \Delta\tilde{U}^2}{2 (k_{\text{B,EZ}} - c_{\text{B,S}} k_{\text{S}} \Delta\tilde{U}^2)} \\ & + \left[\frac{1}{4} \left(\frac{c_{\text{B,S}} k_{\text{S}} \Delta\tilde{U}^2}{k_{\text{B,EZ}} - c_{\text{B,S}} k_{\text{S}} \Delta\tilde{U}^2} \right)^2 + \frac{c_{\text{B,0}} + \phi_B}{k_{\text{B,EZ}} - c_{\text{B,S}} k_{\text{S}} \Delta\tilde{U}^2} \right]^{1/2}. \end{aligned} \quad (\text{C.5})$$

As $\Delta\tilde{U}$ now appears in the denominator, Eq. C.5 poses a restriction for $\Delta\tilde{U}$, similarly as for the CFM.

$$\Delta\tilde{U} < \left[\frac{1}{Ri_{\text{U}}} \right]^{1/2} = \left[\frac{k_{\text{B,EZ}}}{k_{\text{S}} c_{\text{B,S}}} \right]^{1/2} \approx 2.4. \quad (\text{C.6})$$

This value represent the neutral limit, which is in equilibrium entrainment conditions characterized by a constant bulk Richardson-number Ri_{U} , with $Ri_{\text{U}} \approx 0.17$ for our LESs (chapter 7.2.2). The limiting value $\Delta\tilde{U} < 2.43$ fits well to Jonker *et al.*'s (2013) neutral DNS-BLs, which suggest $\Delta\tilde{U} < 2.30 \approx [1/Ri_{\text{U}}]^{1/2}$, with $Ri_{\text{U}} \approx 0.19$. However quantitatively these limiting condition cannot be reproduced by the CFM as here $\Delta\tilde{U} < [1/C_{\text{p}}]^{1/2} \approx 1.58$, which implies an unrealistically large value for $Ri_{\text{U}} \approx C_{\text{p}} \approx 0.4$

Note also that Eq. C.5 represents the directly 'applicable' form of the NZO, that could directly be implemented in a typical ZOM-code, using CBL depths z_i as representative length scale, which also determines the ZOM budgets for momentum and temperature, moisture and the concentration of trace gases, etc..

Appendix D

TKE budget of an independent LES-CBL

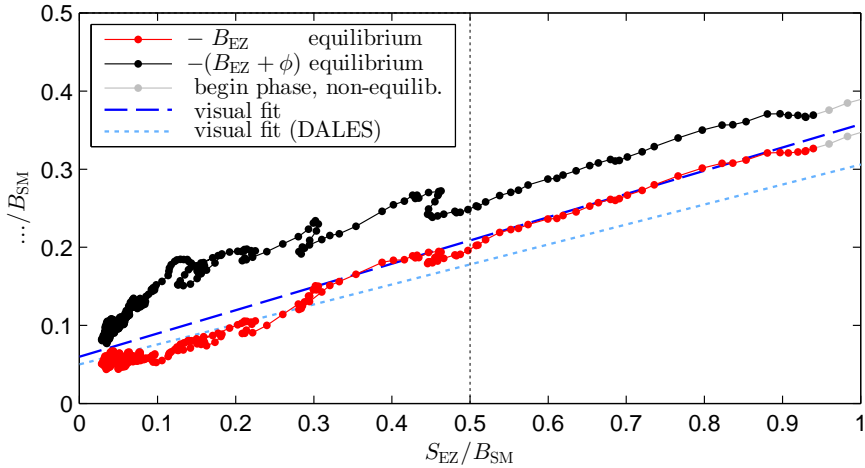


Figure D.1: Dimensionless TKE-budget terms versus dimensionless EZ shear production of the MHH-LES. Presentation analogous to Figure 4.17 and 4.18. Gray dots mark the begin phase. All data represent instantaneous values for every 5 minutes filtered by a 30-minute moving average.

To get a further impression of the experiential and physical significance of our DALES LES, we made use of the possibility to compare the TKE budget and its sensitivity to EZ shear with that of alternative LES-CBL. This LES was conducted in 2014 by Chiel van Heerwaarden (then PMI, Hamburg), who is also the author of the computer code, which is called MicroHH 1.0 (MHH hencefort). For details see Van Heerwaarden *et al.* (2017). The basic setup of our MHH-LES equals that of the wide domain DALES run with $u_{geo} = 15 \text{ m s}^{-1}$, but was performed on a significantly larger grid of $1024 \times 1024 \times 512$ grid points. The domain width (25.6 km x 25.6 km)

is similar whereas the larger domain height of 6400 m (versus 3600 m) enabled a simulation of 30 h physical time. During the simulation the CBL finally reached a height of 2600 m (versus 1600 m for our DALES runs) and passed through a wide range of varying EZ shear. The vertical grid spacing was about the same (12.5 m instead of 12 m) but horizontal resolution was half of the DALES counter part (25 m instead of 50 m), resulting in a more balanced grid-box ratio of $\Delta z/\Delta x = 1/2$ (instead of $\Delta z/\Delta x = 1/4.17$ of our DALES runs).

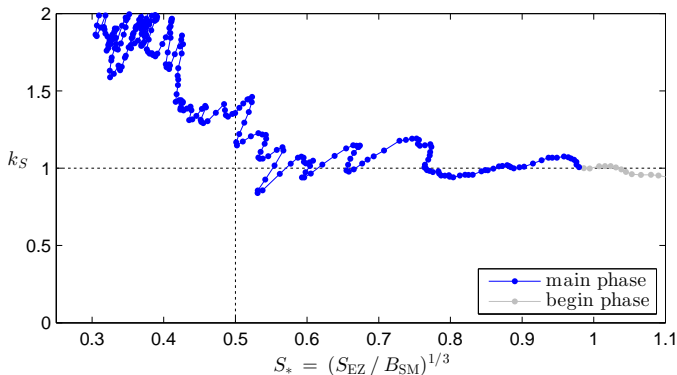


Figure D.2: Shear dependency of the NZO shear scaling. Shown is the dependency of k_S on S_* as given by the MHH-LES. All values filtered by a 30-minute moving average.

TKE-budget versus EZ shear. Figure D.1 shows the shear dependency of the composition of the dimensionless TKE-budget analogous to Figure 4.17 and 4.18. The dashed blue line is a visual fit to the data, that represents the linear scaling, as discussed in detail in section 4.2. We find basically the same pattern with the distinct wave-induced energy losses (regimes II and III), which supports our results.

The agreement is not only qualitative, but mostly also quantitative, with the noticeable exception that entrainment is generally more sensitive to shear, resulting in a steeper linear relationship than observed for the DALES runs (dashed blue line versus dotted blue line), suggesting $c_{B,S}$ (MHH) ≈ 0.3 rather than $c_{B,S}$ (DALES) ≈ 0.256). We suspect the higher resolution and particularly the more even ratio between vertical and horizontal grid sizes to cause the difference, which may reproduced shear-induced turbulence better, than the flat grid boxes of the DALES runs. However we must also take the very long simulation time into account which results in much more mature and stationary CBLs for $S_*^3 > 0.3$ and therefore comparable stronger entrainment than for the DALES LES-CBLs, as indicated by the different fitting lines. Therefore we can better quantify the difference between both data sets by considering shear-sensitivity of the ZOM TKE budget as shown below.

Dimensionless integral quantities k_S and Ri_U . As for our DALES-LESs we consider the shear dependency of $k_S = S_Z/(w_e \Delta U^2)$ as shown in Figure D.2. For $S_*^3 >$, where $\phi_B \approx 0$ we find that $k_S \approx 1$, which agrees with our LESs (Figure 5.4).

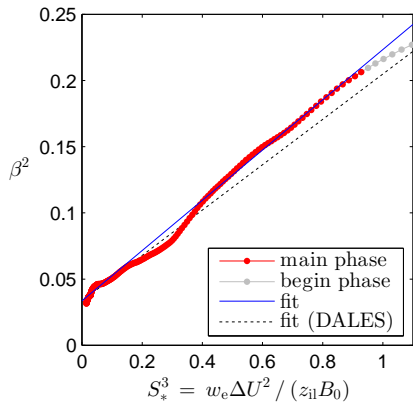


Figure D.3: Correlation between the ZOM integral entrainment β^2 and S_*^3 for the MHH-LES. All values filtered by a 30-minute moving average.

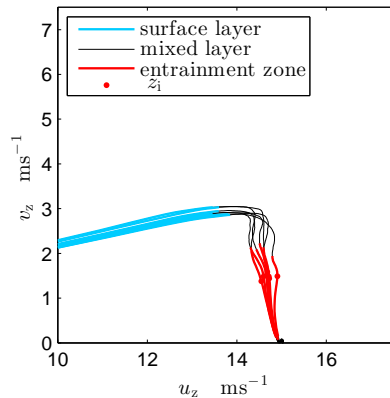


Figure D.4: Hourly hodographs of the instantaneous wind profile of the MHH-LES. Shown are the 17-30 hour of the simulation, when $S_* < 0.4$.

Plotting the ZOM quantities β^2 versus S_*^3 in Figure D.3 we find a largely linear relationship for $S_*^3 >$, which confirms the NZO (Eq. 5.28). The slope of the line, that represent the sensitivity of entrainment to shear, equals the critical Richardson number Ri_U , that characterizes entrainment in neutral limit (Eq. 5.31 and 7.4). From the figure we read $Ri_U \approx 0.19$, which equals the value given by Jonker *et al.*'s (2013) DNSs of neutral BLs.

Appendix E

Inertial Oscillations and surface stress in the CBL

Abstract

Investigating the influence of surface friction on the Inertial Oscillation (IO) of an extratropical, non-growing, convective boundary-layer (CBL), we paid particular attention to the stability-dependent interactive coupling of shear-induced turbulence and turbulent friction, which leads to a non-linear relationship between friction and velocity. We showed that in contrast to common perception, IO damping is controlled not only by friction but also by the dependence of friction on velocity. Furthermore, we found that surface friction not only causes damping but also modifies the restoring force. Using these basic principles, we studied the oscillatory properties (equilibrium, periodicity and damping) of the CBL by means of a model based on Monin-Obukhov surface-layer similarity (MOS) and the mixed-layer approximation. We found that the model complies with a Quadratic Surface stress-velocity relationship (QS) in the neutral limit, and a Linear surface Stress-velocity relationship (LS) in the proximity of the free-convective limit. Dynamically, the LS leads to a harmonic oscillation with a constant periodicity and exponential damping of the IO. However, the QS displays rather complex anharmonic behaviour; in comparison with the LS it produces a 50% stronger overall damping and a 100% larger contribution to the restoring force. Considering CBLs of arbitrary stability, we found that the MOS stress-velocity relation can be very well approximated by a much simpler linear combination of the LS and the QS which, respectively, represent the convective and the shear-induced contributions to friction. This enabled us to link the set of the external parameters (surface roughness, surface buoyancy flux and boundary layer depth) to a set of three effective parameters: the equilibrium velocity, the convective friction constant, and the neutral

This chapter was published as Schröter *et al.* (2013). For the interested reader we note that since the publication of this paper, we have made significant progress with the further characterization of the IO of moderately sheared CBLs. We developed a rather comprehensive concept, which also accounts for the contributions of directional-shear and momentum entrainment. Furthermore we switched to a fully analytical representation of the IO by considering the wind-vector dynamics in the 'phase space' instead of relying on empirical properties of some particular temporal solutions, as we did in this paper. But these results are not anymore part of this thesis.

friction constant. Together with the Coriolis coefficient, these parameters completely determine the IO.

E.1 Introduction

The horizontal mean wind in the planetary boundary layer (PBL) is exposed to surface friction, and its speed and direction therefore deviate from the flow in the free atmosphere above the PBL. Furthermore, observations of the PBL wind (speed and direction) in the mid-latitudes are often characterized by wide temporal variations on a time-scale of hours, i.e. well beyond turbulent time-scales (e.g. Buajitti and Blackadar, 1957; Thorpe and Guymer, 1977; Steeneveld *et al.*, 2008b). These wind variations cannot be normally attributed to a single cause, as all atmospheric drivers may fluctuate on time-scales of the same order of magnitude. The atmospheric drivers are the mean pressure gradient, the intensity of PBL turbulence (which controls turbulent friction) and the advection of mean momentum. Over land, however, the PBL wind velocity variations are typically dominated by a pronounced diurnal cycle (Baker, 2010), mainly caused by the alternation of daytime heating and night-time surface cooling, which leads to a pronounced diurnal cycle of turbulence and associated surface friction, particularly under clear skies.

Above heterogeneous terrain, horizontal gradients of diurnal changes in heating and cooling can also induce meso-scale thermal circulations, such as sea-breeze systems or mountain-valley-breeze systems. These may alternately modify the pressure field, thereby contributing to the diurnal wind variation (e.g. Peagle and Rasch, 1973; Baas *et al.*, 2010).

Another feature of the PBL flow outside the tropics is its oscillatory behaviour, which is basically caused by the Coriolis force. The latter acts as a restoring force and induces (in the absence of other forces) a steady circular rotation of the wind vector, called the Inertial Oscillation (IO) (Kundu and Cohen, 2004). The concept of an IO is usually used to explain the jet-like acceleration of the upper part of stable PBLs at night, when turbulent friction becomes very small (e.g. Blackadar, 1957; Thorpe and Guymer, 1977; Beyrich and Klose, 1988; Steeneveld *et al.*, 2008a; Van de Wiel *et al.*, 2010). However, observations (Thorpe and Guymer, 1977; Byun and Arya, 1986) reveal that rotational oscillations of the mean wind vector also occur in typical daytime convective boundary layers (CBLs). Despite strong turbulent surface friction, damping of the wind seems to be rather small in the CBL. This can also be seen in Large-Eddy Simulations (LES) of such boundary layers. For cloudless CBLs see Pino *et al.* (2006b) and Conzemius and Fedorovich (2006a), and for shallow cumulus convection see Siebesma and Cuijpers (1995).

The significance of the IO lies in the fact that the natural period in the mid-latitudes of approximately $2\pi/f_c \approx 17.5$ h (Stull, 1988, p. 525) is of the same order of magnitude as typical diurnal variations in PBL forcings (turbulent friction and others). Assuming that damping is not excessive, the PBL wind field can then resonate with the periodic forcings, which keep the wind field constantly out of balance. As a result, the trajectory of the wind vector continuously follows an oscillatory pattern, as has been demonstrated by a number of studies (e.g. Buajitti and Blackadar, 1957; Thorpe and Guymer, 1977; Tan and Farahani, 1998). We can therefore take the IO to be an inherently significant property of the PBL wind, even though the actual wind

does not show a pure IO, as it is masked by interactions with other processes (e.g. Dutton, 1976, p. 297).

The concept of IO can be extended to include all processes that contribute to the momentum budget in addition to Coriolis and pressure forces. It turns out that one can consider the PBL wind field as a forced damped oscillator (Thorpe and Guymer, 1977; Shapiro and Fedorovich, 2010). Indeed, this idea of an extended inertial oscillator has proven to be a useful tool for the qualitative and quantitative interpretation in several model studies. These studies represent relatively complex cases, e.g. with temporal and spatial variation of turbulence (e.g. Sing *et al.*, 1993), momentum advection due to isobaric curvature (Tan and Farahani, 1998) and terrain-induced diurnal pressure variations (Peagle and Rasch, 1973).

Many of the quantitative studies of the IO are based on analytical models. These typically describe harmonic oscillations and thus provide us with explicit relationships between model parameters and oscillatory properties such as equilibrium, damping and periodicity. In nearly all cases, the analytical models rely on the use of idealised linear turbulence models, in which turbulent diffusivities or turbulent friction factors have to be treated as external forcing, either constant in time and/or space (Shapiro and Fedorovich, 2010), or with a prescribed temporal (Buajitti and Blackadar, 1957) and spatial dependence (Buajitti and Blackadar, 1957; Sing *et al.*, 1993). In physical terms, this means that we neglect the shear-dependent contribution to turbulence production and thus the feedback of wind speed on turbulent friction. However, the interactive coupling (negative feedback) of shear-induced turbulence and turbulent friction is typically an important mechanism in boundary layer flows.

With respect to the mean flow in a PBL, the above mechanism results in non-linear dependence of surface friction on flow velocity. This is because friction is directly dependent on shear and on the transport coefficient (transport efficiency), which also depends on shear. The study of Byun and Arya (1986) can be regarded as an notable step in this direction. They investigated the evolution of momentum and the oscillatory character of a CBL with the aid of a Mixed-Layer (ML) model. Besides a linear drag relationship, Byun and Arya (1986) also considered a quadratic drag law for their determination of oscillatory properties (equilibrium and damping) of the CBL mean wind vector. Although not done by Byun and Arya (1986), the quadratic drag law can be interpreted as accounting for the above-mentioned shear-velocity feedback.

The primary question to be addressed in this paper is, if and how the concept of the IO can be helpful to understand the dynamics of a PBL-model, which accounts for shear production of turbulence (and hence is based on a non-linear relationship between velocity and friction). Inspired by Byun and Arya (1986), we reinvestigate the oscillatory characteristics of a CBL wind field. By so doing, we systematically take shear-turbulence feedback into account and consider the combined contributions of buoyancy and shear to turbulent friction. We thus also take into account the variation of stability during an IO and its effect on the IO properties. Like Byun and Arya (1986), we use a mixed-layer model and consider an idealized horizontally homogeneous setup, with no advection and constant forcing. However, we deviate from Byun and Arya (1986) in a number of important respects:

- Like Garratt *et al.* (1982), we combine the mixed layer with a surface layer, which follows Monin-Obukhov surface layer similarity (MOS). This enables us

to account for the combination of convective and shear induced instability.

- We define the IO via the 2nd-order expression of the momentum budget, which enables us to identify the role of various terms in the oscillator.
- For an anharmonic IO, we determine the dynamic properties – damping and periodicity – with the help of an analogous harmonic parametric oscillator. This results in a complex but coherent picture of damping and periodicity and the relation of these to the CBL flow characteristics.

Apart from the friction at the surface, the flow in a CBL also experiences an exchange of momentum over the interface between the turbulent layer and the free atmosphere flow at the upper boundary, known as entrainment. Assuming a well-mixed layer, both processes – surface friction and momentum entrainment – can be considered as being driven by both CBL convection and local shears in the surface layer and the entrainment zone, respectively (Conzemius and Fedorovich, 2006a; Pino and Vilà-Guerau de Arellano, 2008). This suggests that the shear dependence of turbulent surface friction and entrainment can be characterized in a similar way (Conzemius and Fedorovich, 2007). However, shear at the surface and in the entrainment zone are interdependent (in both direction and magnitude). Typically they are not aligned, and in combination with non-linear shear-stress relationships at each boundary, this leads to rather complex behaviour of the vertical stress divergence during an IO. In order to address this complexity, we have split the problem, and in this paper we consider only the influence of surface friction. The combination of surface friction and entrainment will be addressed in a later publication.

The remainder of this paper is structured as follows below: In the next section we introduce and discuss the 2nd-order differential equation for the momentum budget of an advection-free PBL. This represents the oscillator form of the PBL wind field and is the theoretical basis for our subsequent analysis. In section 3 we introduce and analyse a surface-stress model for a non-growing CBL. Considering the basic role of atmospheric stability, we find that the behaviour of this stress model is asymptotically bounded; approaching the free convection limit, the stress model tends to a Linear Stress relationship (LS) and in the neutral limit it complies with a Quadratic Stress relationship (QS).

Hence we can reformulate our research question in a preliminary step as: how does the strength of surface stress and its dependence on velocity – either linear or quadratic – affect the IO of the CBL? Answering this question in section 4, we formally address a problem that was already dealt with by Byun and Arya (1986) who compared the two drag laws, although without relating them to atmospheric stability.

Thus in this paper we also review some of the findings of Byun and Arya (1986), which we interpret in the context of an extended oscillator analysis. In section 5 we finally address the central question of this paper and characterize the general stability-dependency of the CBL wind oscillator. It turns out that the general friction-velocity relationship of the CBL with arbitrary stability can be very accurately replaced by a linear combination of its stability asymptotes, which we investigated in section 4. This new finding then provides us with a clear concept that illustrates the influence of stability-dependent surface stress on the IO.

E.2 Governing equations

E.2.1 Reynolds-averaged momentum budget

Assuming horizontal homogeneity, no advection and using the geostrophic assumption (e.g. Dutton, 1976), the Reynolds-averaged budget for horizontal momentum in the orthogonal coordinates x,y and z is given as

$$\frac{\partial u}{\partial t} = + f_c v - f_c v_g - \frac{\partial \overline{w'u'}}{\partial z}, \quad (\text{E.1})$$

$$\frac{\partial v}{\partial t} = - f_c u + f_c u_g - \frac{\partial \overline{w'v'}}{\partial z},$$

A B C D

$$\text{with } + f_c u_g = -\frac{1}{\rho} \frac{\partial p}{\partial y} \quad \text{and} \quad - f_c v_g = -\frac{1}{\rho} \frac{\partial p}{\partial x},$$

where u,v are the components of the horizontal ensemble-averaged wind vector in the direction of x,y , and u_g,v_g the components of the geostrophic wind vector. f_c denotes the Coriolis parameter, p the pressure and ρ is air density. Then term A is the momentum tendency, terms B and C are sources of momentum, and term D is the divergence of the turbulent momentum fluxes. The pressure gradient force (term C) is the only source of total momentum and the Coriolis-force (term B) redistributes momentum between the two components, but does not add or remove total momentum to the system.

Note that in this paper, a wind velocity vector is either designated by its components u and v or by \mathbf{U} .

E.2.2 The momentum budget as oscillator

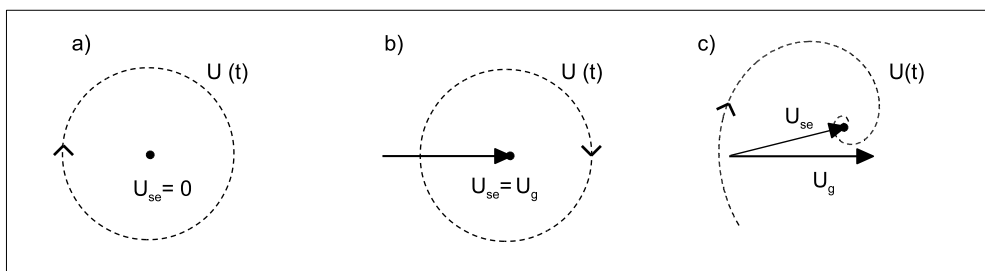


Figure E.1: Schematic of basic cases of inertial oscillations of the PBL mean wind with $f_c > 0$. $U(t)$ denotes the trajectory (dashed line). Case (a): no pressure forcing - no turbulent friction. Case (b): finite pressure forcing - no turbulent friction. Case (c): finite pressure forcing - finite turbulent friction. U_g is the geostrophic wind vector. U_{se} denotes the vector of the equilibrium velocity.

By further differentiating the momentum budget and eliminating some terms we can directly derive the 2nd-order expression of motion. With $-\nabla_z F_u$ and $-\nabla_z F_v$ representing the vertical divergence of the turbulent momentum fluxes we obtain

$$\frac{\partial^2 u}{\partial t^2} + \frac{\partial \nabla_z F_u}{\partial t} + f_c^2 u + f_c \nabla_z F_v = u_g f_c^2, \quad (\text{E.2})$$

$$\frac{\partial^2 v}{\partial t^2} + \frac{\partial \nabla_z F_v}{\partial t} + f_c^2 v - f_c \nabla_z F_u = v_g f_c^2,$$

$$\frac{\partial^2 \phi}{\partial t^2} + 2\gamma\omega_0 \frac{\partial \phi}{\partial t} + \omega_0^2 \phi = \text{const.} \quad (\text{E.3})$$

I II III IIIb IV

With regard to this system of equations (Eqs. (E.2)), we can already detect some features of the PBL wind dynamics, which we will encounter later on the basis of a particular CBL model. If we focus strictly on terms I, III and IV, we see that Eqs. (E.2) are homogeneous in terms I, III and IV and in agreement with the universal harmonic oscillator equation, which is given for an arbitrary variable ϕ by Eq. (E.3). Here, ω_0 is the undamped angular frequency and γ is the damping ratio. Therefore we can formally interpret (for $f_c \neq 0$) the Reynolds-averaged momentum budget as an oscillator (possibly anharmonic). Here, term I is the 'inertia' of the oscillator, term III the 'restoring force' and term IV a constant, which determines the equilibrium. Terms II and IIIb represent the as yet unspecified contribution of the turbulent stresses to the oscillation. As it forms the basis for further reasoning, we shortly discuss Eqs. (E.2) via three basic cases, as displayed in Figure E.1.

In case (a) the geostrophic forcing and stress divergence are zero, and term II, IIIb and IV are therefore also zero. The wind field (Eq. (E.2)) hence forms an undamped harmonic oscillator (Eq. (E.3), with $\gamma\omega_0 = 0$). The wind vector performs a circular rotation around the origin called the 'Inertial Motion' of a rotating system (Kundu and Cohen, 2004) or 'Inertial Oscillation'. The inertia of the flow (term I) is only determined by the restoring Coriolis term (term III), which is the intrinsic agent that makes the planetary wind budget an oscillator.

In case (b) an additional pressure force (finite term IV) results in a circular oscillation around the finite geostrophic wind. The dynamics of the system still equals an undamped rotational oscillation. It represents e.g. the nocturnal oscillation of the decoupled and quasi stress-free residual layer wind as investigated by e.g. Blackadar (1957) and Thorpe and Guymer (1977).

In case (c), which is meteorologically more relevant, all variables including the stress divergence $\nabla_z F_{\mathbf{U}}$ are finite. Term II primarily represents the as yet unspecified influence of stress divergence on the wind oscillation. But we can interpret term II as a damping term, if it, or the $\nabla_z F_{\mathbf{U}}$ it contains, can be expressed as a monotone function of the velocity, $f_m(\mathbf{U})$. As the turbulent stresses in a PBL generally depend on the magnitude of shear, and shear in turn is related to the wind velocity, it is likely that such a monotone function $-\nabla_z F_{\mathbf{U}} = f_m(\mathbf{U})$ exists. In this paper we do not further investigate the general case (Eq. (E.2)), but specifically explore the form of this monotone function for the vertically-averaged mean flow in a CBL (section E.3.1)

with help of a mixed-layer model (section E.3.2).

Assuming that such a monotone velocity-stress relationship $f_m(\mathbf{U})$ does exist, we can also point out three features of the oscillator equation, which will later become important:

- The cross-dependency between the u and v components in term IIIb indicates that such a damped oscillator may have a complicated non-homogeneous form.
- Inserting $f_m(\mathbf{U})$ in term II, which is the time derivative of $\nabla_z F_{\mathbf{U}}$, means that we have to consider the chain rule. In consequence, damping does not only depend on the temporal derivative of the velocity $\partial(\mathbf{U})/\partial t$ as for a harmonic oscillator, but also on the derivative of $f_m(\mathbf{U})$, $\partial f_m(\mathbf{U})/\partial \mathbf{U}$. As long as $f_m(\mathbf{U})$ is not linear $\partial f_m(\mathbf{U})/\partial \mathbf{U} = f(\mathbf{U})$, which means that damping also depends on the velocity itself. On the other hand this suggests that term II also contributes to the restoring force.
- The appearance of $f_m(\mathbf{U})$ in term IIIb indicates that term IIIb may also contribute to the restoring force of the oscillator (which will be also discussed in section E.4.1), and in this way also influences the position of the equilibrium.

We tentatively conclude that for a given pressure and Coriolis forcing and a monotonic velocity-stress relationship $f_m(\mathbf{U})$, the PBL mean wind vector oscillates. As it is damped, the wind vector approaches an equilibrium value on a 'spiral-like' trajectory (Figure E.1 c).

E.3 Convective boundary layer model

E.3.1 CBL momentum budget

As the purpose of this paper is to study the influence of surface friction on the CBL flow, here we ignore entrainment and discuss only non-growing CBLs ($dh/dt = 0$). Physically this case approximates a situation where the CBL top is capped by a very strong temperature inversion, so that the CBL growth and momentum entrainment is weak in spite of ongoing surface heating and sensible heat entrainment. More precisely, our case resembles the academic setup of a CBL, which is capped by a stress-free rigid lid, an approach that has frequently been used to exclude entrainment effects in large-eddy simulations (Brown and Grant, 1996, 1997).

Assuming horizontal homogeneity and no advection the CBL-averaged momentum budget reads

$$\begin{aligned} \frac{\partial u}{\partial t} &= + f_c v - f_c v_g - \frac{\overline{w'u'_h} - \overline{w'u'_s}}{h}, \\ \frac{\partial v}{\partial t} &= - f_c u + f_c u_g - \frac{\overline{w'v'_h} - \overline{w'v'_s}}{h}, \end{aligned} \tag{E.4}$$

A
B
C
D

where u and v denote the CBL-mean velocity and h the depth of the CBL. $\overline{w'\mathbf{U}'_s}$ is the surface stress and $\overline{w'\mathbf{U}'_h}$ the stress at PBL top. The designation of the terms is analogous to Eq. (E.1).

We treat the boundary layer strictly as a turbulent layer and therefore define the boundary layer top as the lowest height at which the momentum flux becomes zero (and thus $\overline{w'\mathbf{U}'_h} = 0$), which in the academic analogue equals the height of the rigid lid.

E.3.2 CBL stress model

In order to simulate the CBL mean wind with Eq. (E.4), we need a closure for the turbulent surface stress, e.g. $\overline{w'\mathbf{U}'_s} = f(\mathbf{U})$. Typically mean wind profiles of neutral PBLs are strongly sheared and characterized by a distinct turning of wind direction with height. However, observations (e.g. Holtslag, 1984) and LES (e.g. Deardorff, 1972; Moeng and Sullivan, 1994) suggest that already moderately unstable CBLs feature significant convective transport, which leads to a rather uniform mixed layer wind field in a barotropic environment. Convective mixing also strongly reduces the turning of the wind direction with height within the CBL so that the angle between surface stress and mixed layer velocity (α_*) becomes small (Arya, 1977). Thus, under already moderately convective conditions a simple mixed-layer model is supposed to reproduce CBL mean wind quite well. Therefore we base our further analysis on a profile-surface-stress relationship for the CBL similar to Garratt *et al.* (1982) which, in spite of its relative simplicity, is quite realistic and performs well (Brown *et al.*, 2006).

According to this model, the lower 10% of the CBL is considered as the surface layer (SL) with a depth of h_{SL} as shown in Figure E.2. In the SL the wind profile follows Monin-Obukhov similarity (MOS) theory. The value $h_{\text{SL}}/h = 0.1$ is frequently used in the literature (e.g. Garratt *et al.*, 1982). However, note that the findings here do not depend on the exact value of h/h_{SL} . The upper 90% of the CBL is assumed to be well mixed with a uniform horizontal wind velocity, which also implies that the turning of wind with height is assumed to be insignificant and surface stress is well aligned with the CBL mean velocity.

Unlike Garratt *et al.* (1982), we do not deal with entrainment and associated shear close to the upper boundary. Hence, the CBL-averaged mean wind speed $|\mathbf{U}|$ is given by

$$|\mathbf{U}| = \frac{1}{h} \int_{z_0}^{h_{\text{SL}}} |\mathbf{U}_{\text{SL}}(z)| dz + \frac{h - h_{\text{SL}}}{h} |\mathbf{U}_{\text{SL}}(h_{\text{SL}})|, \quad (\text{E.5})$$

$$\text{with } |\mathbf{U}_{\text{SL}}(z)| = \frac{u_*}{\kappa} \left\{ \ln \left(\frac{z}{z_0} \right) - \Psi_m \left(\frac{z}{L} \right) + \Psi_m \left(\frac{z_0}{L} \right) \right\}.$$

Here z is height, z_0 is roughness length, $U_{\text{SL}}(z)$ is height-dependent velocity in the Surface Layer, u_* is friction velocity, L Obukhov-length, and Ψ_m is the integrated Businger-Dyer flux-gradient relationship for momentum Paulson (1970).

Garratt *et al.* (1982) do not clearly specify the conditions under which their model can be considered as valid. But referring to large-eddy simulations (e.g. in Moeng and Sullivan, 1994; Brown *et al.*, 2006; Kim *et al.*, 2006), we assume for, say, $-h/L \geq 3$ that the CBL is sufficiently well mixed and $\alpha_* < 3^\circ$, and thus that the surface stress

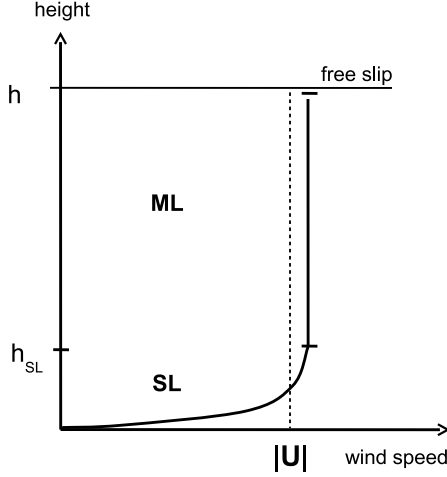


Figure E.2: Schematic wind profile of the CBL model; ML: mixed-layer, SL: surface layer, h : CBL depth, h_{SL} : surface layer depth.

is sufficiently well aligned with the layer mean velocity. These values also agree well with the CBL model of Arya (1977) (Eqs. 28-31 in Byun and Arya (1986)). Note that according to Brown *et al.* (2006), the model of Garratt *et al.* (1982) is able to reproduce LES with $-h/L$ as low as ≈ 2 . Hence, in our further analysis, the mean wind velocity of developed CBLs within a wide range of stabilities will be well-represented based on Eq. (E.5).

Equation (E.5) not only gives the CBL-mean velocity but also provides a relationship between the CBL mean wind velocity and surface stress (expressed by u_*). Hence, we call Eq. (E.5) ‘MOS-based Stress-velocity relationship’ (MOSS). We can also formulate the MOSS as a drag law:

$$\begin{aligned} \overline{w'\mathbf{U}'_s} &= -C_d |\mathbf{U}| \mathbf{U} \\ \text{or} \quad u_*^2 &= C_d |\mathbf{U}|^2. \end{aligned} \quad (\text{E.6})$$

Here C_d is a drag coefficient, which is given by

$$\begin{aligned} C_d \left(\frac{h}{L}\right) &= -\frac{h^2 \kappa^2}{\left\{ \int_{z_0}^{h_{\text{SL}}} \chi(z) dz + (h - h_{\text{SL}}) \chi(h_{\text{SL}}) \right\}^2}, \\ \text{with} \quad \chi(z) &= \left\{ \ln \left(\frac{z}{z_0} \right) - \Psi_m \left(\frac{z}{L} \right) + \Psi_m \left(\frac{z_0}{L} \right) \right\}. \end{aligned} \quad (\text{E.7})$$

For the following it is important that we can consider surface buoyancy flux ($\overline{w'\theta'_v}$)_s to a good approximation as an external forcing (of the CBL), independent of velocity. In a typical daytime situation the magnitude of ($\overline{w'\theta'_v}$)_s is controlled first by the available energy at the surface and second by the partitioning of the energy between sensible heat flux and latent heat flux. The available energy is typically dominated by the radiative forcing. Furthermore, for typical combinations of available energy and

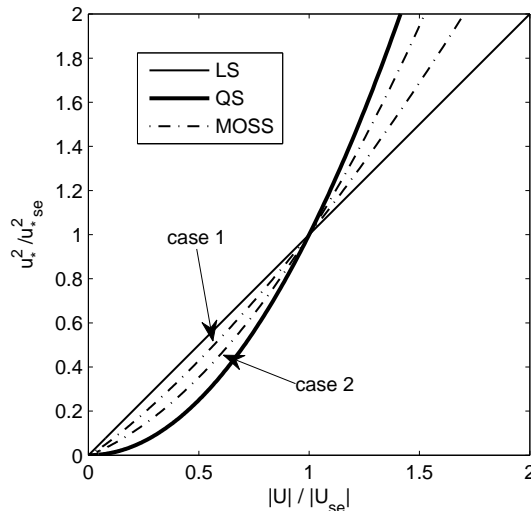


Figure E.3: Surface stress - wind speed relationship for non-growing CBLs with $h = 600$ m, $z_0 = 0.1$ m. Two different cases (dotted lines) are given for the MOSS: case 1: $(\overline{w'\theta'_v})_s = 0.3$ K m s $^{-1}$, $|\mathbf{U}_g| = 2$ m s $^{-1}$; case 2: $(\overline{w'\theta'_v})_s = 0.065$ K m s $^{-1}$, $|\mathbf{U}_g| = 6$ m s $^{-1}$. The LS (thin line) and the QS (thick line) represent the free convective and the neutral limits of the MOSS.

surface resistance, the energy partitioning is rather insensitive to the aerodynamic resistance and hence to wind velocity as well (Jacobs and De Bruin, 1992). With a given h , z_0 and $(\overline{w'\theta'_v})_s$ the MOSS implies, that stability and surface stress only depend on the wind velocity.

Figure E.3 shows the relationship between the CBL mean wind speed and surface stress for two different CBL flows. In the strongly convective case 1, the flow is bounded by $h = 600$ m, $z_0 = 0.1$ m and forced with $(\overline{w'\theta'_v})_s = 0.3$ K m s $^{-1}$, $|\mathbf{U}_g| = 2$ m s $^{-1}$ and $f_c = 10^{-4}$ s $^{-1}$. The more neutral (moderately convective) case 2 is derived by increasing $|\mathbf{U}_g|$ to 6 m s $^{-1}$ and reducing $(\overline{w'\theta'_v})_s$ to 0.065 K m s $^{-1}$. The reader should not be puzzled by the scaling we apply in Figure E.3; it is sufficient to know that $|\mathbf{U}|$ and u_* are scaled using their respective values in the equilibrium state ($|\mathbf{U}_{se}|$ and $u_{*,se}$), which will be dealt with in detail in section E.4. According to this, the two cases are also classified by their stability in the equilibrium state, expressed by the dimensionless parameter $-h/L_{se}$, where L_{se} is the Obukhov-length in the equilibrium state. For case 1 $-h/L_{se} = 224$ and for case 2 $-h/L_{se} = 7.9$. Thus both cases span a wide range of convective instabilities.

As expected, the stress-velocity relation appears to be monotonic. More importantly, however, we can recognize a strong stability dependency such that when the CBL becomes more neutral (case 1 \rightarrow case 2), the relationship between the CBL wind speed and stress becomes less linear.

Though the MOSS is not valid for neutral PBLs, we can in a purely formal manner consider the neutral limit of the MOSS. For $h/L = 0$ the stability correction Ψ_m

becomes zero and C_d approaches a constant value

$$C_{dq} = C_d\left(\frac{h}{L} = 0\right) = \frac{\kappa^2 h^2}{\left\{h_{SL} - z_0 - h \ln\left(\frac{h_{SL}}{z_0}\right)\right\}^2}. \quad (\text{E.8})$$

This means that in the neutral limit the MOSS follows a Quadratic Stress law (QS), represented by the thick line in Figure E.3.

But with respect to the opposite case of the CBL approaching the hypothetical free-convection limit ($-h/L_{se} \rightarrow \infty$), Monin-Obukhov similarity theory as used in the MOSS is not physically meaningful (Beljaars, 1994). Thus we cannot deduce the respective asymptotic drag law from MOSS. However even for very convective conditions (far more convective than case 1), we still observe the above mentioned regularity and find that with an increase of convective instability the drag relationship slowly but steadily approaches linearity (Figure E.3, see also discussion of the free convection limit in section E.5.1). Thus by simply extrapolating this regularity to the convective limit, we assume that CBL surface friction for $-h/L_{se} \gg 1$ is governed by a Linear Stress law (LS), represented by the thin line in Figure E.3). The limiting QS and LS are then given by

$$\overline{w'\mathbf{U}'_s} = -C_{dq} |\mathbf{U}| \mathbf{U}, \quad \text{for } -h/L_{se} = 0, \quad (\text{E.9})$$

$$\overline{w'\mathbf{U}'_s} = -C_{dl} \mathbf{U}, \quad \text{for } -h/L_{se} \rightarrow \infty, \quad (\text{E.10})$$

where $C_{dq} = \text{const}$ (Eq. E.8) is the dimensionless quadratic drag coefficient and $C_{dl} = \text{const}$ is a linear stress factor with the dimension of a velocity.

Note that both limiting drag laws have a formal asymptotic character though for different reasons. In the physically well-defined neutral limit ($h/L = 0$) the assumption of a well-mixed layer no longer holds, and the whole PBL wind profile is sheared. Furthermore, we can expect a distinct turning of the wind direction with height and therefore dissimilarity between the drag law of the u and v component. In contrast, in close proximity of the free convection limit the assumption of a well mixed wind profile is assumed to hold well, but in this case either wind velocity and surface stress have to become insignificantly small or the buoyancy flux unrealistically large ($\rightarrow \infty$).

However, as asymptotes of the MOSS, both the LS and the QS are physically meaningful in the sense that they agree well with the common concept of turbulent diffusion in the neutral and free convection limits (Stull, 1994): in the neutral case turbulent friction is shear-induced, as is expressed by the proportionality of the exchange factor $-C_{dq} |\mathbf{U}|$ to the horizontal velocity scale $|\mathbf{U}|$. In the free convection limit turbulence is solely driven by the vertical buoyancy flux and turbulent diffusivity is independent of the horizontal mean wind. Thus we expect that C_{dl} , which has the dimension of a velocity, scales well with a characteristic vertical convective velocity. Accordingly, we can relate the LS and the QS directly to different types of turbulent friction without considering the rather hypothetical limiting states of the MOSS (see section E.5 and Appendix E.7.2). This turns out to be very useful for the interpretation of realistic cases (section E.5).

To estimate C_{dl} , one can construct a convective drag coefficient (C_{dq}^{conv}) analogous to C_{dq} (Appendix E.7.1) and in this way indeed interpret C_{dl} as the product of this convective drag coefficient and a convective velocity scale. However a further

Table E.1: List of models and their abbreviations:

Principle	Stress law	CBL Model
Monin-Obukhov (MOS)	MOSS	MOSM
Linear	LS	LM
Quadratic	QS	QM
Combination	CS	CM

characterisation of C_{d1} or C_{dq} beyond the fact that they are constant (or independent of U respectively), is not crucial for our further reasoning. Rather, it is important that the QS and the LS form an envelope for a monotonic continuum of all possible drag relations given by the MOSS (Eq. (E.6)). In other words, the two stress laws seem to capture the range of non-linearity of the MOSS, from the quadratic neutral to more linear convective regimes. Therefore we can take the first step to approach our goal of understanding the influence of surface stress on the IO by studying only the impact of the two limiting stress laws. This means that we insert both, the QS and the LS, in the momentum budget (Eq. (E.4)). We then obtain two different models for the CBL wind, which we call the ‘Linear Model’ (LM) and the ‘Quadratic Model’ (QM). In the remainder of this study, we consequently consider the different stress laws always as integrated parts of the related CBL model (see Table E.1).

Analogous to what we observe for the drag laws, we assume that the behaviour of these two models frames the behaviour of the general CBL wind model (MOSM), which we likewise obtain by inserting the MOSS (Eq. (E.6)) into the momentum budget (Eq. (E.4)). The stress-velocity relationships in Figure E.3 can easily give us the impression that the more complicated, but realistic MOSS, could well be approximated by a linear combination of the QS and the LS. For its simplicity, such an idea would be quite appealing. We test and discuss this in detail in section E.5.

E.4 Limiting cases of the CBL wind oscillations

E.4.1 The convective limit – oscillator properties of the linear model

By inserting the LS (Eq. E.10) in the velocity-budget equation, we obtain the linear model (LM), which forms a system of non-homogeneous linear differential equations (Byun and Arya, 1986):

$$\begin{aligned} \frac{\partial u}{\partial t} - f_c v + r_1 u &= -f_c v_g, \\ \frac{\partial v}{\partial t} + f_c u + r_1 v &= +f_c u_g. \end{aligned} \quad (\text{E.11})$$

Here $r_1 = C_{d1}/h$ (with the dimension T^{-1}) is the linear friction factor of a CBL with depth h .

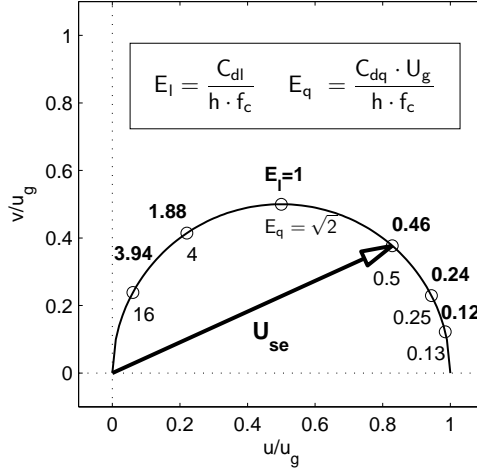


Figure E.4: Static equilibrium velocity vector \mathbf{U}_{se} for a non-growing CBL as a function of the linear E_1 and the geostrophic Ekman number, denoted as circle of equilibrium vectors (CEV). Here \mathbf{U}_{se} for $E_q = 0.5$ is shown as an example. Small circles mark \mathbf{U}_{se} for distinct values of E_1 (bold) and E_q (thin). The u -component is aligned with \mathbf{U}_g and both axes are normalized with $|\mathbf{U}_g|$.

Equilibrium

Setting the time derivatives in Eq. (E.11) to zero defines the equilibrium velocity \mathbf{U}_{se} . Analogously to the geostrophic Ekman number E_q (Byun and Arya, 1986), one can express the equilibrium in terms of a dimensionless ‘linear’ Ekman number E_1 , which we define by $E_1 = C_{dl}/(h f_c) = r_1/f_c$. Aligning the coordinate system with the geostrophic wind \mathbf{U}_g we obtain

$$\frac{u_{se}}{u_g} = \frac{1}{1 + E_1^2}, \quad \frac{v_{se}}{u_g} = \frac{E_1}{1 + E_1^2}. \quad (\text{E.12})$$

The Ekman number represents the relative CBL stress-divergence with respect to Coriolis forcing. As we can see \mathbf{U}_{se} depends on the linear Ekman number, as well as on the geostrophic forcing. In this way \mathbf{U}_{se} is only determined by h , C_{dl} , f_c and \mathbf{U}_g , which determine the boundaries and the forcing of the flow, and does not depend on time. Therefore we also call it ‘static equilibrium’ (subscript se). Note that this is expected to be different for a growing CBL, where $h = h(t)$ and the equilibrium becomes a function of time and the growth rate.

From Figure E.4 we can see that for very large E_1 (shallow CBLs and large C_{dl}) the static equilibrium is close to zero. For small E_1 (deep CBLs and small C_{dl}) the static equilibrium is close to the geostrophic wind vector. Eliminating E_1 in equation E.12 gives the relationship between u_{se} and v_{se}

$$\frac{v_{se}}{u_g} = \sqrt{-\left(\frac{1}{2} - \frac{u_{se}}{u_g}\right)^2 + \frac{1}{4}}. \quad (\text{E.13})$$

As shown in Figure E.4, Eq. (E.13) represents a half circle in vector space, which

we name circle of equilibrium velocity (CEV). So if E_1 moves from 0 (frictionless) to infinite (infinite friction), the respective equilibrium velocity moves (according to Eq. (E.12) and (E.13)) on a circular line between $(|\mathbf{U}_g|, 0)$ and $(0, 0)$ around the centre $(|\mathbf{U}_g|/2, 0)$. The maximum ageostrophic flow is reached with $E_1 = 1$ and a cross-isobar angle of 45° .

The oscillator equation of the LM – damping and periodicity

In order to display the oscillation alone, we align the coordinate system with the equilibrium velocity and call the deviation from the equilibrium velocity $\mathbf{U}_d(t) = \mathbf{U}(t) - \mathbf{U}_{se}$. By differentiation and subsequent elimination we directly obtain the oscillator equation of $\mathbf{U}_d(t)$, which forms a harmonic oscillator for both components as

$$\frac{\partial^2 u_d}{\partial t^2} + 2r_1 \frac{\partial u_d}{\partial t} + (f_c^2 + r_1^2) u_d = 0, \quad (\text{E.14})$$

$$\frac{\partial^2 v_d}{\partial t^2} + 2r_1 \frac{\partial v_d}{\partial t} + (f_c^2 + r_1^2) v_d = 0.$$

i ii iii

Note that the dynamic characteristics of the oscillation (Eq. (E.14)) are independent of the geostrophic forcing and depend only on the Coriolis parameter f_c and the turbulent friction factor r_1 . The amplitude of both components is damped by a constant damping factor $2r_1 = 2\gamma\omega_0$ (compare with term II in Eq. (E.3)). Furthermore, we find that turbulent friction is not only present in the damping term (term ii) but also in the restoring term (term iii), and therefore contributes to the undamped angular frequency ω_0 . From Eq. (E.14) we read

$$\omega_0 = \sqrt{f_c^2 + r_1^2}. \quad (\text{E.15})$$

This is different from the formal analogue of e.g. the simple linearly damped mass-spring-oscillator (Eq. (E.3)), where friction only contributes to the damping and does not affect the restoring force. Recall that the damped angular frequency ω of any harmonic oscillator is generally given by

$$\omega = \omega_0 \sqrt{1 - \zeta^2}, \quad \text{with } \zeta = \frac{r_1}{\omega_0}. \quad (\text{E.16})$$

Using this for the LM and inserting Eq. (E.15) in Eq. (E.16) gives

$$\omega_1(r_1) = \sqrt{(1 - \zeta) (f_c^2 + r_1^2)} = f_c, \quad (\text{E.17})$$

$$\text{with } \zeta = \frac{r_1^2}{f_c^2 + r_1^2} < 0.$$

Hence the damped angular frequency ω_1 of the LM is always f_c and independent of r_1 . This means that by changing the friction in the LM, the restoring force of the LM oscillator is adjusted in such a way that first, the LM is never over-damped ($\gamma < 1$)

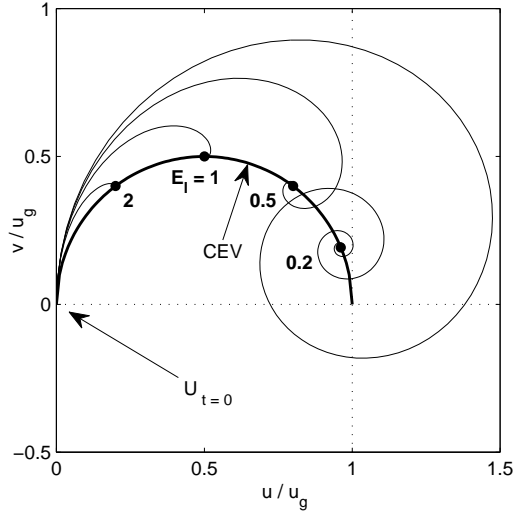


Figure E.5: Trajectories of the mean wind velocity vector $\mathbf{U}(t)$ according to the LM for a set of different linear Ekman numbers E_1 . The trajectories are all initialized in the origin. The thick line denotes the ‘circle of equilibrium vectors (CEV)’. Black dots mark the equilibrium velocity vector \mathbf{U}_{se} for distinct values of E_1 . The u -component is aligned with \mathbf{U}_g and both axis are normalized with $|\mathbf{U}_g|$.

and second, the angular frequency is constantly f_c . For the mid-latitudes, where $f_c \approx 10^{-4} \text{ s}^{-1}$, this leads to a constant period of $T_1 = 2\pi/f_c \approx 17.5 \text{ h}$. The analytical solution, which can be found in e.g. Byun and Arya (1986) also expresses these findings: $\mathbf{U}_d(t)$ rotates with a constant angular frequency of f_c around \mathbf{U}_{se} , while the amplitude $|\mathbf{U}_d(t)|$ decreases in time exponentially at a rate of r_1 . Figure E.5 displays several simulations of the LM in the u, v -plane, which summarize the behaviour of the LM. The trajectories show how, with decreasing E_1 , the damping of the IO decreases and the equilibrium approaches \mathbf{U}_g .

E.4.2 The neutral limit – oscillator properties of the quadratic model

Analogous to the LM, we obtain the quadratic model (QM) by inserting the quadratic stress law (Eq. (E.10)) in the momentum budget (Eq. (E.4)):

$$\begin{aligned} \frac{\partial u}{\partial t} - f_c v + r_q |\mathbf{U}| u &= -f_c v_g, \\ \frac{\partial v}{\partial t} + f_c u + r_q |\mathbf{U}| v &= +f_c u_g, \end{aligned} \quad (\text{E.18})$$

with $|\mathbf{U}| = \sqrt{u^2 + v^2}$.

Here we call $r_q = C_{dq}/h$ the quadratic friction factor (r_q has the dimension L^{-1}), where the QM forms a non-homogeneous, non-linear differential equation system

(Byun and Arya, 1986).

Equilibrium

As in the linear model, we can explicitly derive the static equilibrium velocity for the quadratic model from Eq. (E.18). Byun and Arya (1986) show that this relation can be expressed in terms of the geostrophic Ekman number E_q , which is given by $E_q = C_d |\mathbf{U}_g|/f_c h$. In a coordinate system aligned with the geostrophic wind the expression for the equilibrium velocity U_{es} reads

$$\frac{u_{se}}{u_g} = \frac{-1 + (1 + 4E_q^2)^{1/2}}{2E_q^2}, \quad (\text{E.19})$$

$$\frac{v_{se}}{u_g} = \frac{[-1 + (1 + 4E_q^2)^{1/2}]^{3/2}}{2\sqrt{2}E_q^2}.$$

Eliminating E_q , we find that the equilibrium velocity moves on the same circular line as the LM (Eq. (E.13)). This is readily understandable, as in the equilibrium state we can replace the QM by an analogous LM (Byun and Arya, 1986). This also holds for the MOSM (or any other model which complies with a drag law according to Eq. (E.6)), as it has the same form as the QM. Thus, in order to oscillate around the same equilibrium, the LM, the QM and the MOSM must be adjusted to each other as

$$r_l = r_q |\mathbf{U}_{se}| = \frac{C_d}{h} |\mathbf{U}_{se}|. \quad (\text{E.20})$$

Note that we have already used this kind of scaling in section E.3.2, in order to compare stress-velocity relations in Figure E.3.

The oscillator equation of the QM – damping and periodicity

The 2nd-order system of differential equations (the oscillator equations) for the quadratic model are given by

$$\frac{\partial^2 u}{\partial t^2} + 2r_q |\mathbf{U}| \frac{\partial u}{\partial t} + (f_c^2 + r_q^2 |\mathbf{U}|^2) u + r_q \frac{\partial |\mathbf{U}|}{\partial t} u = \epsilon_u, \quad (\text{E.21})$$

$$\frac{\partial^2 v}{\partial t^2} + 2r_q |\mathbf{U}| \frac{\partial v}{\partial t} + (f_c^2 + r_q^2 |\mathbf{U}|^2) v + r_q \frac{\partial |\mathbf{U}|}{\partial t} v = \epsilon_v,$$

i ii iii iiib iv

$$\text{with } \epsilon_u = f_c r_q |\mathbf{U}| v_g + f_c^2 u_g,$$

$$\text{and } \epsilon_v = f_c r_q |\mathbf{U}| u_g + f_c^2 v_g.$$

This system of equations is similar to the one of the LM, but due to the presence of $|\mathbf{U}|$ it remains non-homogeneous. Term ii resembles the damping term and term iii the restoring term in the LM. Therefore one can understand $r_q |\mathbf{U}(t)|$ as the locally equivalent linear friction factor of the QM and consider terms ii and iii as the ‘harmonic’ contributions to the oscillation. A term iiib also occurs; as it is linear in u (and v respectively) it contributes to the restoring force. However, it also contains the time derivative of $|\mathbf{U}|$ and hence contributes to damping as well. In fact terms ii and iii have a similar hybrid character, as they depend not only on the time derivative but also on the velocity itself. This implies that they contribute to damping as well as to the restoring force of the oscillation. Finally, term iv is no longer constant but is proportional to $|\mathbf{U}|$. Thus it also contributes to the restoring forces. This means that we can no longer distinguish between damping and restoring terms as in a harmonic oscillator. We can therefore expect more complex oscillatory behaviour, which we characterize best by comparison with that of the ‘well behaved’ harmonic LM. An analytical solution of the QM is not readily found, so we rely on numerical solutions (Runge-Kutta method).

With respect to the dynamic behaviour of the QM, Byun and Arya (1986) distinguished between cases with finite geostrophic forcing and hypothetical cases with zero geostrophic forcing. In this paper we simply consider the meteorologically relevant case with finite geostrophic wind. For this case Byun and Arya (1986) stated that the QM generally damps more efficiently than the LM. We wish to refine this picture and more precisely characterize the differences between the two models. We therefore consider the following exemplary simulations: the quadratic model is set up with a constant $E_q = 0.5$, which represents a realistic CBL in the middle latitudes ($f_c = 10^{-4} \text{ s}^{-1}$) with $C_{dq} = 0.003$, $h = 600 \text{ m}$ and a considerable geostrophic forcing of $|\mathbf{U}_g| = 10 \text{ ms}^{-1}$. The linear model is scaled to the same equilibrium velocity (Eq. E.20), which implies that $E_l = 0.46$. Both models are initialized with two different velocities, which are symmetric with respect to the equilibrium velocity. Somewhat arbitrarily, but convenient for our further reasoning, we initialise the wind field with $\mathbf{U}(t_0) = 2 \mathbf{U}_{se}$ for one simulation (S^+) and with $\mathbf{U}(t_0) = 0$ for another (S^-). In a case with $|\mathbf{U}_g| = 10 \text{ ms}^{-1}$, this imbalance seems rather large so one might regard the two cases as outer limits compared to real CBL wind field imbalances.

Figure E.6 shows the trajectories of the two simulations for both models (QM: thick lines, LM: thin lines). Figure E.7 displays the temporal development of the amplitude $|\mathbf{U}_d(t)|$ for the same simulations. For both simulations, S^- and S^+ , we actually find that the QM is always closer to equilibrium, and thus damps more intensely. For an initial period in the S^- simulation, however, the differences are rather small and both models follow a similar trajectory.

In both plots we also see that the damping behaviour of the QM depends on the initial condition (or rather on the actual position in the vector space). In contrast, the relative damping of the LM is always exponential and independent of its initial state, which means that the two different trajectories of the LM for S^- and S^+ are rotated, but have identical shapes. The less smooth, angular graphs of $|\mathbf{U}_d(t)|$ show that the quadratic model features a rather unsteady damping over time, although the spiralling of the trajectories looks fairly smooth. Moreover, we find that the damping of the two simulations of the QM diverges mostly in the beginning, but then tends to synchronize after about 10 h (Figure E.7).

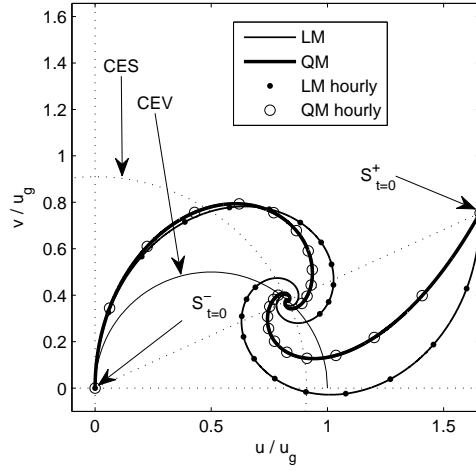


Figure E.6: Trajectories for simulations $S^- S^+$ of the QM (thick line) and the LM (thin line). Hourly values for the first 11 hours are marked with dots (LM) and circles (QM). The coordinate system is aligned with the geostrophic wind. CEV denotes the ‘circle of the equilibrium velocities’ and CES is the ‘circle of equal stress’ for the LM and the QM.

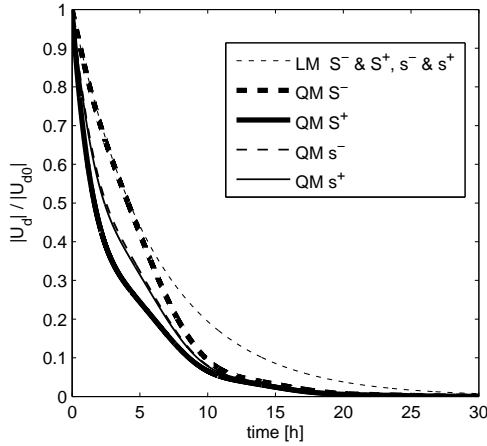


Figure E.7: Temporal evolution of the relative amplitude of the IO $|\mathbf{U}_d|/|\mathbf{U}_{d0}|$ for the LM and the QM. The examples shown are simulations S^+ and S^- (as well as later simulations s^+ and s^-).

In order to understand the damping behaviour of the QM, in a first instance we follow the reasoning of Byun and Arya (1986), who directly associated damping with the friction. We characterise the difference in friction between QM and LM by forming

the ratio of the QS and the LS

$$R_\tau = \frac{C_{dq}}{C_{dl}} \frac{|\mathbf{U}(t)|}{|\mathbf{U}(t)|} \frac{|\mathbf{U}(t)|}{|\mathbf{U}(t)|}. \quad (\text{E.22})$$

Referring to the CBL momentum budgets, we can interpret R_τ as the ratio between the linear friction factor of the LM and the analogous linear friction factor of the QM, $r_q |\mathbf{U}(t)|$. With Eq. E.20 we get

$$R_\tau = \frac{r_q}{r_l} \frac{|\mathbf{U}(t)|}{|\mathbf{U}_{se}|} = \frac{r_q}{r_l} \frac{|\mathbf{U}(t)|}{|\mathbf{U}_{se}|} = \frac{1}{|\mathbf{U}_{se}|} |\mathbf{U}(t)|. \quad (\text{E.23})$$

Considering the oscillator equation for each model (Eq. (E.21) and Eq. (E.14)), we immediately see that R_τ also equals the ratio of the terms ii. So if one expects that R_τ explains the differences in damping, one assumes that only the harmonic contribution of the oscillator (term ii) is relevant. Note that Eq. (E.23) is quantitatively identical but simpler than the similar expression given by Byun and Arya (1986, their Eq. (22)).

R_τ simply depends linearly on $|\mathbf{U}(t)|$. Hence in vector space, lines of equal R_τ form concentric circles around the origin. One distinct circle, which is defined by $|\mathbf{U}(t)| = |\mathbf{U}_{se}|$ represents all wind vectors for which the stress of the LM and the QM are equal. We therefore name it ‘Circle of Equal Stress’ (CES). As displayed in Figure E.6 the CES separates the vector space in two areas. Inside the CES $R_\tau < 1$ and the QM experiences lower friction than the LM. Outside the CES the situation is reverse. So when the wind rotates around U_{se} , which is situated on the CES, the QM experience alternately higher and lower friction than the LM, which – according to Byun and Arya (1986) – would consequently lead to alternately higher and lower damping. Looking at the trajectories, we can recognize this feature at the beginning of the S^- simulation, where the linear and the quadratic models are relatively similar: the trajectories start inside the CES, where the quadratic model hence follows a wider curvature and departs from the linear trajectory. Once it has passed the CES, however, it is in the area of higher stress and thus starts to turn more strongly towards the equilibrium and finally crosses the linear trajectory. By the same logic, the variation of R_τ also seems to explain the less smooth decrease of $|U_d|$ in time (Figure E.7).

Nevertheless it is unclear how the variation of R_τ comes to result in the generally stronger damping of the QM, which after 10 h is about the same for both simulations (Figure E.7). The first 10 hours of simulation S^- indicate that the periods when $R_\tau > 1$ seems to have a stronger impact on the oscillations than the periods when $R_\tau < 1$.

The concentric distribution of R_τ in the wind vector space, which is particularly represented by the circular shape of the CES ($R_\tau = 1$), suggests a reason: assuming that the angular velocity of the oscillation does not vary too much, the curvature of the CES would imply that a random trajectory of the QM must spend more time in the area of high drag. This in turn would lead to the stronger overall damping that we observe for both S^- and S^+ .

But the limitation of this argument can be directly seen when the QM is close to U_{se} . For this purpose we consider the simulations s^- and s^+ (Figure E.8), which are identical to S^- and S^+ except for being initialised close to the equilibrium with

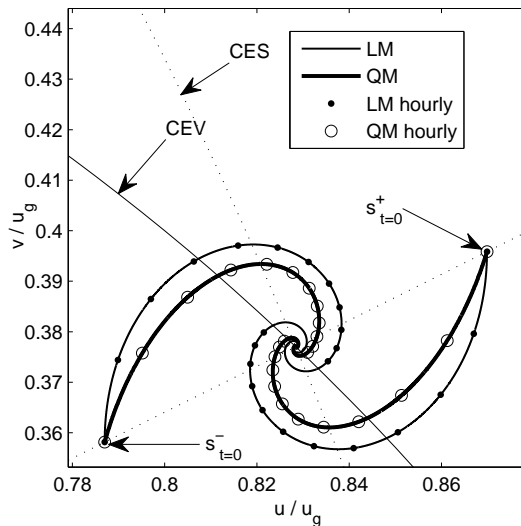


Figure E.8: As Figure E.6, but for simulations s^- and s^+ .

$\mathbf{U}_{t=0} = 0.8 \mathbf{U}_{se}$ and $\mathbf{U}_{t=0} = 1.2 \mathbf{U}_{se}$ respectively. We find that the two different trajectories of the QM are almost point-symmetrical and damp about as smoothly as the LM (Figure E.7). This is still what we would expect: since \mathbf{U}_d is small, $\mathbf{U}(t)$ varies only slightly and is always close to \mathbf{U}_{se} . Therefore the friction of the QM also deviates only very little from that of the LM ($R_\tau \approx 1$). Furthermore, the CES now resembles a straight line, which separates the vector space nearly symmetrically. But from all this, we would not expect a significantly stronger damping of the QM. However it does exist and can be seen in Figures E.8 and E.7.

We thus find that for the QM the magnitude of instantaneous friction is a relevant mechanism, although it cannot solely explain the particular damping. Analogously, we expect similar difficulties when we attempt to explain the influence of friction on the periodicity of the damped system. Hence, we are obliged to adopt a more rigorous approach to determining the oscillatory behaviour of the QM.

E.4.3 Parametric oscillator analysis of the QM

As the LM is harmonic, we can explicitly derive damping and periodicity from the oscillator equation and the solution. However, as the oscillator equation of the QM cannot be cast in a ‘harmonic form’ and as we do not have a closed-form solution, this is not possible for the QM. But we can determine any particular solution $\mathbf{U}(t)$ numerically where one can diagnose actual damping and periodicity very well at each moment t . This means that we treat the QM as a ‘parametric harmonic oscillator’ and diagnose the effective linear damping factor $D_{\text{eff}}(t)$ and the restoring factor $P_{\text{eff}}(t)$

from a numerical solution according to

$$\frac{\partial^2 u_i}{\partial t^2} + D_{\text{eff}}(t) \frac{\partial u_i}{\partial t} + P_{\text{eff}}(t) (u_i - u_{\text{se},i}) = 0, \quad (\text{E.24})$$

I II III IV

where $u_i(t)$ (with $i = 1, 2$) denotes the instantaneous velocity vector and $u_{\text{se},i}$ the equilibrium velocity vector. As we have two equations (one for each component), we can solve this equation system for the two unknowns D_{eff} and P_{eff} at every moment t . As the parametric oscillator is harmonic, we can give it the form of the LM-oscillator (Eq. (E.14)) and therefore express D_{eff} and P_{eff} in terms of effective friction factors $r_{\text{eff,D}}$ and $r_{\text{eff,P}}$:

$$D_{\text{eff}} = 2r_{\text{eff,D}} \omega_c, \quad P_{\text{eff}} = \omega_{0,\text{eff}}^2 = r_{\text{eff,P}}^2 \omega_c^2 + f_c^2. \quad (\text{E.25})$$

Note that $r_{\text{eff,D}}$ and $r_{\text{eff,P}}$ are independently derived from the damping factor and the restoring factor respectively, so we have no reason to assume that they are equal. We now compare the effective friction factor with the actual value (term II in Eq. E.24 versus term ii in Eq. E.21) and define the dimensionless damping factor

$$R_{D,\text{loc}} = \frac{r_{\text{eff,D}}}{r_{\text{q}} |\mathbf{U}(t)|}. \quad (\text{E.26})$$

The subscript ‘loc’ denotes that $r_{\text{eff,P}}(t)$ and $r_{\text{q}} |\mathbf{U}(t)|$ are both local values along the trajectory. Similarly, we can also form the ratio with the ‘global’ equilibrium value $r_{\text{q}} |\mathbf{U}_{\text{se}}|$

$$R_D = \frac{r_{\text{eff,D}}}{r_{\text{q}} |\mathbf{U}_{\text{se}}|} = \frac{r_{\text{eff,D}}}{r_1} = \frac{D_{\text{eff}}}{D_1}. \quad (\text{E.27})$$

As $r_{\text{q}} |\mathbf{U}_{\text{se}}| = r_1$, this ratio equals the ratio of the effective damping factors (subscript D) of the QM and the LM. Now the question is, if $R_{D,\text{loc}}$ and R_D can help to identify general properties in the dynamics. Using the example of simulation S⁺, Figure E.9 (a) shows the temporal behaviour of $R_D(t)$ (thick line) and $R_{D,\text{loc}}(t)$ (thin line). For comparison, the ratio of the stresses for the LM and the QM, $R_\tau(t)$ is also displayed. We can see that both $R_D(t)$ and $R_{D,\text{loc}}(t)$ are oscillating with diminishing amplitude around a fixed value of 3/2, which we can regard as the attractor of both and which we denote as \tilde{R}_D . Such behaviour of $R_{D,\text{loc}}(t)$ means that the damping of the QM is 50% stronger than one would expect when friction alone is taken into account. Rather, the behaviour of $R_D(t)$ demonstrates that the overall damping of the QM is 50% stronger than that of the LM, although the ratio of friction $R_\tau(t)$ varies around and approaches unity (dashed line). It seems that the temporal variation of $R_D(t)$ (thick line) roughly correlates with the variation of $R_\tau(t)$ (dashed line), at moments when the trajectory crosses the CES and $R_\tau(t) = 1$, $R_D(t)$ appears to be quite close to \tilde{R}_D . However, this correlation is not good for $|\mathbf{U}_d(t)| \approx |\mathbf{U}_{\text{se}}|$ and hence $R_\tau(t)$ does not fully account for the dynamics of either D_{eff} or R_D . Thus with respect to the QM oscillator (Eq. (E.21)), we conclude that instantaneous friction, represented by term ii, contributes to the overall magnitude as well as to temporal variations in damping, but does not do so alone, as is the case for the harmonic LM. Obviously,

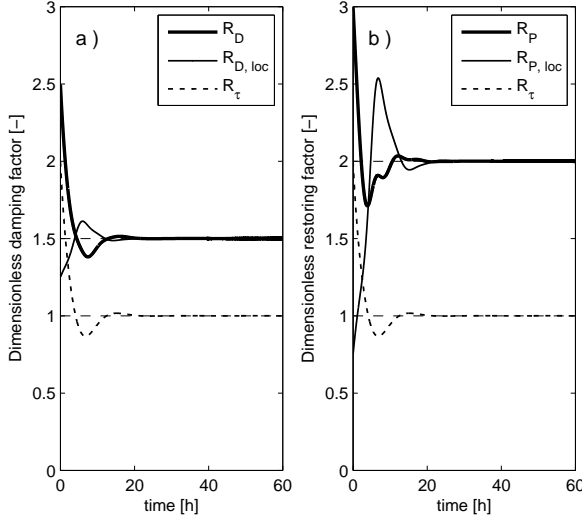


Figure E.9: a) Temporal evolution of R_D and $R_{D,loc}$ for simulation S^+ . b) Temporal evolution of R_P and $R_{P,loc}$ for simulation S^+ . For comparison, the temporal evolution of $R_\tau(t)$ is plotted in both panels.

the contributions of the other ‘hybrid’ terms in the oscillator equation (Eq. (E.21)) are important.

Recalling the discussion of the general wind oscillator (section E.2.2, case (c)) we can usually assume that this is the case for any significantly non-linear stress-velocity relationship. In this case, the internal derivative $\partial f_m(\mathbf{U})/\partial \mathbf{U}$ is not constant and will result in hybrid terms in the oscillator equation.

Further testing (not shown) indicates that \hat{R}_D is independent of any of the model parameters (r_q , f_c and U_g) and always $3/2$. It thus represents a basic property of the QM. As we do not have an explicit expression for $\mathbf{U}(t)$ we find it difficult to prove the general case. However, for small $|\mathbf{U}_d|$ we can demonstrate that $R_D(t) = 3/2$ for selected but arbitrarily small values of $|\mathbf{U}_d|$ (see Appendix E.7.3).

In order to characterize the periodicity of the QM, we similarly define the ratio of the restoring factors $P_{\text{eff}} = \omega_{0,\text{eff}}^2$ and $P_1 = \omega_0^2$, which equals the natural (undamped) angular frequency of the QM and the LM respectively. However, instead of forming the ratio directly, we first subtract the square of the damped circular frequency of the LM, $\omega_1 = f_c$, and define the dimensionless restoring factor R_P

$$R_P(t) = \frac{P_{\text{eff}} - \omega_1^2}{P_1 - \omega_1^2} = \frac{\omega_{0,\text{eff}}^2(t) - \omega_1^2}{\omega_0^2 - \omega_1^2}. \quad (\text{E.28})$$

This enables us to interpret R_P as the ratio of the influences of ‘harmonic’ friction on the restoring term. This is explicitly articulated by the fact that by using Eq. (E.25), we can express R_P as the ratio of the linear friction coefficients squared:

$$R_P(t) = \frac{\omega_{0,\text{eff}}^2(t) - f_c^2}{\omega_0^2 - f_c^2} = \frac{r_{\text{eff},P}^2(t)}{r_1^2}. \quad (\text{E.29})$$

Analogous to the damping ratio, we can also define $R_{P,\text{loc}}(t)$, using the local friction of the QM $r_q^2 |\mathbf{U}(t)|^2$ as a base instead of r_1^2 . From our numerical solutions we find that $R_P(t)$ as well as $R_{P,\text{loc}}(t)$ oscillate around the fixed value $\tilde{R}_P = 2$, which is generally reached at the limit $|U_d| \rightarrow 0$ (Figure E.9 (b)). Once again, this value appears to be independent of the model parameters. It represents a basic property of the QM, which we again attribute to the hybrid terms in the oscillator budget.

Since the parametric oscillator of the QM is harmonic, we can apply Eq. (E.16) and calculate the time-dependent damped angular frequency of the QM as

$$\omega_q(t) = \omega_{0,\text{eff}} \sqrt{1 - \left(\frac{r_{\text{eff,D}}^2}{\omega_{0,\text{eff}}^2} \right)}. \quad (\text{E.30})$$

Referring to Eq. (E.27) and Eq. (E.29), the effective values are given by

$$\omega_{0,\text{eff}}^2 = R_P r_1^2 + f_c^2, \quad r_{\text{eff,D}} = R_d r_1.$$

Inserting these in Eq. (E.30) gives

$$\omega_q(t) = \sqrt{(R_P - R_D^2) r_1^2 + f_c^2}. \quad (\text{E.31})$$

By using the characteristic values $\tilde{R}_D = 3/2$ and $\tilde{R}_P = 2$ we get the characteristic damped angular frequency $\tilde{\omega}_q(t)$:

$$\tilde{\omega}_q = \sqrt{-\frac{1}{4} r_1^2 + f_c^2}. \quad (\text{E.32})$$

For the simulations S^+ and S^- , r_1 is $\approx 4.55 \cdot 10^{-5} \text{s}^{-1}$. This results in $\tilde{\omega}_q = 0.974 f_c$, which means that $\tilde{\omega}_q$ is 0.974 of that of the LM, and on average the QM rotates 2.6% more slowly than the LM. Thus the overall impact of the nonlinearity of the QS on the periodicity is quite limited.

E.5 CBL wind oscillations and the general stability dependence

In section E.3.2 we demonstrated that the quadratic stress law (QS) and the linear stress law (LS) form the neutral and free convection limits of the general stress law (MOSS). Assuming monotony, we hypothesised that this regularity is conserved when the stress laws are inserted in the wind velocity budget equation. Thus, we analogously regarded the oscillatory behaviour of the LM and the QM as the limits of the oscillatory behaviour of the MOSM. In section E.4 we subsequently analysed the LM and the QM, making use of their formal simplicity. We therefore still have to show that this hypothesis actually holds and that the dynamic properties of the MOSM are generally framed by the asymptotic behavior of the LM and QM. Moreover, in order to complete our analysis, we finally have to characterize the general MOSM oscillator, which covers the full range of stability. We do both straightforwardly and elegantly by deriving a direct relationship between the MOSM and its stability asymptotes, the LM and QM.

E.5.1 MOSM versus combination model

Inspired by Figure E.3, we also surmised that the MOSS could be well approximated by a linear combination of the LS and the QS, which we call combination stress law (CS).

Before we will test this idea, however, it is helpful to briefly recapitulate and justify the setup that leads to Figure E.3. In the perspective of section E.3.2, Figure E.3 features the three stress laws (LS, QS, MOSS). However, it represents yet more: as the stress laws are scaled to the equilibrium, Figure E.3 also contains information about CBL dimensions, the geostrophic forcing and the Coriolis parameter. In this way Figure E.3 rather displays the sensitivity of the surface stress to the wind velocity imbalance for all three CBL models, which is the perspective that results when we regard the CBL wind as an oscillator.

All three models are oscillators and only differ in how they formulate the stress law. Thus the terms ‘stress law’, CBL ‘model’ and ‘oscillator’ are closely related, and in the remainder of this paper we therefore always treat a stress law as an integral part of the related model (Table E.1).

For a single case Figure E.3 can therefore be constructed as follows: first one numerically determines the equilibrium velocity \mathbf{U}_{se} and the equilibrium drag coefficient $C_d(|\mathbf{U}_{se}|)$ of the MOSM for a given parameter set z_0 , h , \mathbf{U}_g , f_c and $(\overline{w'\Theta'_v})_s$. Thereafter one determines the parameters of the LM and QM. One can consider the LM and the QM as neutral and convective limits of the specific case and determine C_{dq} and C_{dl} according to Eq. E.8 and Eq. E.41 (Appendix E.7.1). Note that then the equilibrium states of the LM and the QM differ from that of the MOSM, which is taken into account by dimensionless axes. However, alternatively, one can also use the analogous LM and QM, which are defined by the same equilibrium as the MOSM (Eq. E.20). Then with $C_d(|\mathbf{U}_{se}|)$ being the MOSM-drag coefficient in the equilibrium, the drag parameters of the analogous LS and the QS are

$$C_{dq} = C_d(|\mathbf{U}_{se}|) , \quad C_{dl} = C_d(|\mathbf{U}_{se}|) |\mathbf{U}_{se}| . \quad (\text{E.33})$$

Plotting the velocity stress relationships of all three models gives equivalently Figure E.3.

Derivation of the combination model

As a linear combination of the LS and the QS, the CS takes the following form:

$$u_*^2/h = r_{cl} |\mathbf{U}| + r_{cq} |\mathbf{U}|^2 = (r_{cl} + r_{cq} |\mathbf{U}|) |\mathbf{U}| , \quad (\text{E.34})$$

where $r_{cl} = C_{cl}/h$ is the linear friction factor and $r_{cq} = C_{cq}/h$ the quadratic friction factor of the CS (subscript c for combined). Inserting the CS in the budget equation provides us with the Combination Model (CM). However, both parameters of the CS still have to be determined. As the CM needs to combine properties of the LM and the QM, it is clear that r_{cl} and r_{cq} are constants as well and must be defined by the same boundaries and forcing as our reference, the MOSM. Consequently, assuming that the CS is a good approximation of the MOSM, we should be able to derive r_{cl} and r_{cq} from the MOSS.

In order to do so, we linearise both stress laws by dividing by $|\mathbf{U}|$. In this way we actually consider the effective linear friction factor $r_{1,\text{eff}} = u_*^2/(h|\mathbf{U}|)$ as a function

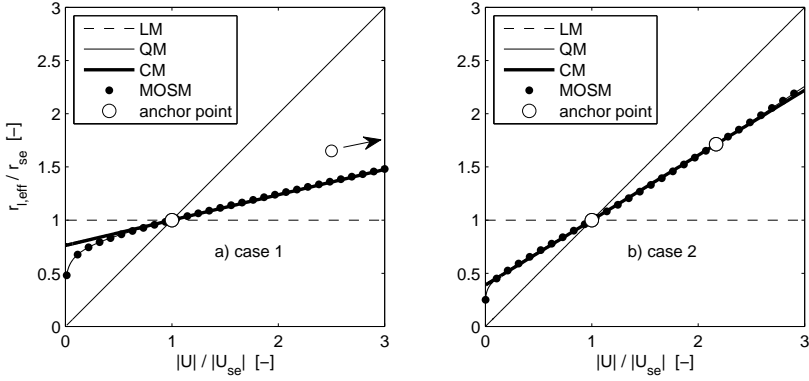


Figure E.10: Relationship between the effective linear friction factor and velocity of the three analogical models for (a) the strongly convective case 1 and (b) the weakly convective case 2. Cases as presented in figure E.3. Case 1 is further characterised by $-h/L_{se} = 224$ and $|\mathbf{U}_{se}| = 1.83 \text{ ms}^{-1}$. Case 2 is further characterised by $-h/L_{se} = 7.9$ and $|\mathbf{U}_{se}| = 5.6 \text{ ms}^{-1}$. Second anchor points were determined with $\Delta_U = 6 \text{ ms}^{-1}$.

of the velocity, which for the CS reads $r_{1,\text{eff}} = r_{\text{cl}} + r_{\text{cq}} |\mathbf{U}|$ (Eq. (E.34)). This means that r_{cq} and r_{cl} comprise the slope and the intercept of a linear relationship. We now depict $r_{1,\text{eff}}$ versus $|\mathbf{U}|$ for the MOSM, LM and QM in Figure E.10, which resembles Figure E.3 but with the ordinate also divided by $|\mathbf{U}| h$. As in Figure E.3, we scale each axis with its respective equilibrium value. For clarity we plot case 1 (highly convective) and case 2 (moderately convective) in two different panels. The LM (convective limit of the CM) appears as a constant value and the QM (neutral limit of the CM) as a straight line with slope of 1 through the origin. Remarkably, the MOSM (black dots) behaves quite linearly as well, with a slope and an intercept between those of the LM and the QM.

Only in a range of low wind speeds do noticeable discrepancies from a straight line occur, these being most visible for case 1. But bearing in mind the scaling with $|\mathbf{U}_{se}| = 1.83 \text{ ms}^{-1}$, a significant non-linearity occurs only for very low wind speeds in the range below $|\mathbf{U}| \approx 1 \text{ ms}^{-1}$. Low wind speeds imply that the SL turbulence state is close to the free-convection limit, where local MOS is no longer realistic (discussed in more detail below). Furthermore, for situations with calm winds, even relatively large errors in the friction term are small in the absolute sense. Hence, any subsequent erroneous contribution to the momentum budget is also assumed to be very small and to have only minor effect on the dynamics.

To determine the parameter of the CS, we need to fit a straight line to the curve of the MOSS. As low wind speeds are less relevant to our problem and also because we find that the MOSS is fairly linear for moderate to high wind speeds, we simply use two 'anchor' points (small circles) in the area of higher wind speeds to obtain a linear approximation of the MOSM. The first anchor point is the equilibrium ($|\mathbf{U}_{se}|, C_d(|\mathbf{U}_{se}|)$), which is chosen to be equal for the CM and the MOSM.

A reasonable value for the second anchor point is given by the typical wind speed

imbalance Δ_U for the case of interest. Hence, we simply take $(|\mathbf{U}_2|, C_d(|\mathbf{U}_2|))$ with $|\mathbf{U}_2| = |\mathbf{U}_{se}| + \Delta_U$ as the second anchor point. However, since the MOSM behaves quite linearly, the fit is supposed to be good and relatively insensitive to the actual choice of Δ_U . We might therefore also simply estimate a general value that is representative of planetary CBLs, which we would roughly guess to be around ≈ 2 to 5 ms^{-1} . Accordingly, the slope and intercept, which define the coefficients r_{cq} and r_{cl} of the CM, are given by

$$C_{cq} = r_{cq} h = \frac{C_d(|\mathbf{U}_{se}| + \Delta_U) - C_d(|\mathbf{U}_{se}|)}{\Delta_U/|\mathbf{U}_{se}|}, \quad (\text{E.35})$$

$$C_{cl} = r_{cl} h = C_d(|\mathbf{U}_{se}|) - C_{cq}(|\mathbf{U}_{se}|) |\mathbf{U}_{se}|.$$

Generally speaking, the agreement between the MOSM (black dots) and the CM stress relationship (thick line) is surprisingly good for both the moderately convective case 2 and the strongly convective case 1, which covers the range between the neutral (QM) and the free convection limit (LM) rather well. Note that with 6 ms^{-1} we use a rather high value for Δ_U in order to demonstrate the validity of the CM for a wide range of velocities.

Hence we can conclude that Eq. (E.34) and Eq. (E.35) represent a quite accurate transformation from the relatively complicated stress relationship of the MOSM – complicated in the perspective of the wind oscillator equation – to the simple stress law of the CM.

It can be shown that the CS agrees also well with the CBL drag-models of Arya (1977) and Zilitinkevich *et al.* (1992). Moreover, it is noteworthy that the CS (Eq. (E.34)), as used in the CM, has the same shape as the surface flux parametrization proposed by Stull (1994). But unlike Stull (1994), who determined the necessary empirical coefficients directly from observations, we derived the CS indirectly from MOS and the empirical Businger-Dyer stability functions using the complete MOSM. However, a more detailed comparison of the CS and the parametrization proposed by Stull (1994) is beyond the scope of this paper.

Physical interpretation of the CM

The physical interpretation of the CM (and the CS) is straightforward. The identical form of the CM and the QM in the neutral limit suggests that we can understand the ‘neutral friction factor’ $r_{cq} |\mathbf{U}|$ as the shear-induced contribution to friction (compare with Stull (1994)). In turn, the similarity between the CM and LM in the free convection limit suggests that the ‘convective friction factor’ r_{cl} represents the convective contribution to friction. This idea agrees well with our picture of convective turbulent diffusion. As convective turbulence is driven by the vertical buoyancy flux, its intensity is independent of the horizontal mean wind. Hence, analogous to C_{dl} , we expect that $C_{cl} = r_{cl} h$ scales well with a characteristic convective velocity (Appendix E.7.2). In turn, the neutral turbulent contribution to friction, $C_{cq} |\mathbf{U}| = r_{cq} h |\mathbf{U}|$, is – analogous to C_{dq} – shear-induced, as is expressed by its proportionality to the horizontal velocity scale $|\mathbf{U}|$.

However the analogy between C_{cl} and C_{dl} , or C_{cq} and C_{dq} does not imply that they are equal. The CM approximates the MOSM only at one point in the parameter space

and in the restricted (though relevant) range in the velocity space. Thus, despite good local agreement there is no reason to assume that for an arbitrary case the parameters of the CM equal C_{dq} and C_{dl} (Appendix E.7.1), which represent rather estimates for the asymptotic boundaries of the MOSM (see also Appendix E.7.2).

Considering \mathbf{U}_{se} as a characteristic velocity of the CBL-oscillator, we can therefore define a characteristic stability parameter for the CM-oscillator by forming the ratio of the convective and the neutral stress factor (or friction factor respectively):

$$\zeta_{CM} = \frac{C_{cl}}{C_{cq} |\mathbf{U}_{se}|} = \frac{r_{cl}}{r_{cq} |\mathbf{U}_{se}|}. \quad (\text{E.36})$$

Similar to the MOS-derived ratio, $-h/L$, $\zeta_{CM} = 0$ represents the neutral case and $\zeta_{CM} = \infty$ the free convection limit. We can also define another stability measure F_{CM} , which has the advantage of ranging between 0 and 1:

$$F_{CM} = \frac{r_{cl}}{r_{cl} + r_{cq} |\mathbf{U}_{se}|} = \frac{r_{cl}}{r_{se}} = 1 - \frac{r_{cq} |\mathbf{U}_{se}|}{r_{se}}. \quad (\text{E.37})$$

F_{CM} expresses the relative contribution of convection to the total friction $r_{se} = r_{cl} + r_{cq} |\mathbf{U}_{se}|$ in the equilibrium. Thus we call this the relative convective friction factor. It will be of good use later on.

The CM in the free convection limit

Although we have already demonstrated its practical irrelevance, the physical interpretation of the discrepancy between the MOSM and CM close to the free convection limit is interesting. For the MOSM we use empirical stability functions that were derived from single-point observations close to the surface. They imply that if the wind speed becomes very small, u_* and the effective friction factor (or any linear exchange-factor) become very small as well and approach zero (Figure E.10 (a)). However, these observations have a rather local character compared to our setup, where we consider the convectively turbulent PBL with a horizontal length scale of the order of several kilometres. For this scale it is well known that convective thermals create surface wind fluctuations, which even in the case of zero mean wind speed lead to significant variations of local surface shear stress (Beljaars, 1994). By using scalar averages these can be quantified and result in a finite domain-averaged \tilde{u}_* (Akylas *et al.*, 2003), which would translate into a finite representative Obukhov-length and thus a finite linear exchange factor. Large-scale models, which typically rely on MOS, therefore include a free convection correction (e.g. Beljaars, 1994). However, similar to the parametrization of Stull (1994), the concept of the CM already takes the free convection limit into account in its design and thus features a finite linear exchange factor r_{cl} (finite intercept in Figure E.10). In this respect, we can consider the CM as intrinsically more realistic than the MOSM.

E.5.2 Oscillator properties of the CM and the MOSM

As demonstrated above, the the MOSM is rather well-approximated by the simpler CM. This is very suitable for the final step of our investigation in which we want to determine the influence of stability on the IO for the whole stability range of the MOSM.

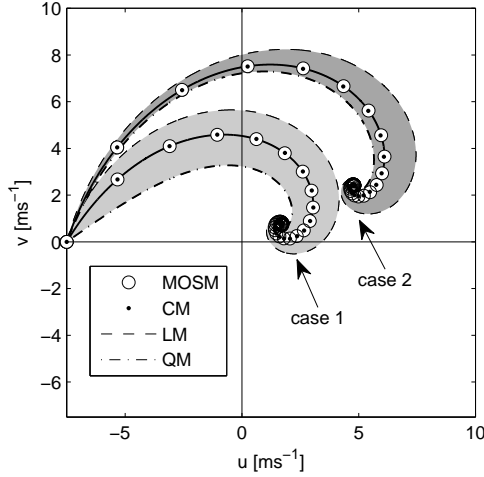


Figure E.11: Trajectories of the wind velocity vector for simulations of the strongly convective case 1 and the weakly convective case 2, initialized with $u_{t=0} = -7.5 \text{ ms}^{-1}$ and $v_{t=0} = 0 \text{ ms}^{-1}$. The shaded areas depict the velocity space between the analogous LM and the analogous QM.

Velocity trajectories of the CM and the MOSM

Figure E.11 displays the trajectories of the MOSM and the CM for two exemplary simulations, which are set up according to case 1 and case 2 respectively.

The simulations are initialized with a large imbalance in order to demonstrate the performance of the CM over a wide velocity range. The choice of initial velocities also ensured that the CBL remained reasonably well mixed during the whole simulation ($-h/L \geq 3$). As expected, the trajectories of the MOSM and the CM agree very well. In order to illustrate the basic idea of the CM, the trajectories of the respective QM and LM are also shown. These bound an area (shaded) that contains the trajectory of the MOSM and CM. We can see that the trajectory of the less convective case 2 closely follows that of the QM, whereas the trajectory of the pronounced convective case 1 is shifted towards that of the LM.

Parametric oscillator analysis of the CM and the MOSM

The CM-oscillator is completely characterized by \mathbf{U}_{se} and both r_{cl} and r_{cq} , which together comprise ζ_{CM} or F_{CM} . \mathbf{U}_{se} represents the static part of the oscillator. Besides on \mathbf{U}_{g} , \mathbf{U}_{se} also depends on the total friction in the equilibrium state ($r_{\text{se}} = r_{\text{cl}} + r_{\text{cq}} |\mathbf{U}_{\text{se}}|$). Thus it also depends on the sum of the convective and the neutral contribution to friction, but not on their ratio (and therefore not on the stability measures F_{CM} and ζ_{CM} respectively). The dynamics of the oscillation, viz. damping and periodicity of $U_d(t)$, are of course determined by total friction as well. However, the way *in which* friction translates into damping and periodicity is characterized by the stability measures F_{CM} and ζ_{CM} , which basically represent the linearity of the friction-velocity relationship. Thus we can interpret them as a measure of the sim-

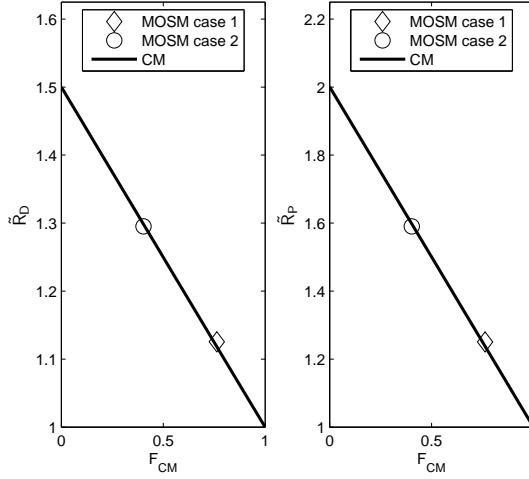


Figure E.12: Characteristic damping factor (left panel) \tilde{R}_D and characteristic restoring factor \tilde{R}_P (right panel) of the CM as a function of the convective friction factor F_{CM} . For comparison, the equivalent values of the MOSS for case 1 (diamonds) and case 2 (circles) are included.

ilarity of the CM to the LM, and thus as a measure of the harmonicity of the IO.

Similarly to what can be done for the LM and the QM (section E.4.3), we can conduct a parametric oscillator analysis for the CM in the whole stability range between the neutral and the free convection limit by varying F_{CM} . This enables us in turn to determine the relative characteristic damping factor \tilde{R}_D and characteristic restoration factor \tilde{R}_P numerically as defined above (Eq. (E.27) and (E.28)). Figure E.12 shows the results. As F_{CM} grows from 0 (neutral limit) to 1 (convective limit), \tilde{R}_D and \tilde{R}_P move as expected smoothly and monotonically from the characteristic values of the QM (neutral) to that of the LM (free convection limit). Furthermore the relationship even turns out to be linear within numerical precision (black lines). We presume that for the CM explicit values for \tilde{R}_D and \tilde{R}_P , as well as their linear dependency on F_{CM} could be derived in the same way as shown for the QM (Appendix E.7.3). We need only to replace the QS by the CS in Eq. (E.42) and the subsequent equations.

To demonstrate once again the consistency of the idea of the whole approach, we analyse the MOSM solutions for case 1 and case 2 in the same way as for the CM where we determined \tilde{R}_D and \tilde{R}_P as well as the parameters of the corresponding CM (Eq. (E.35)) and F_{CM} . As shown in Figure E.12, the respective values for case 1 (diamonds) and case 2 (small circle) are close to those of the CM (black line). We assume that the remaining small discrepancies between the MOSM and CM in Figure E.12 do not reflect real differences between the oscillators but are mainly caused by inaccuracies in the numerically sensitive estimates of \tilde{R}_D and \tilde{R}_P .

E.6 Conclusions

In section E.2 of this paper, we demonstrated that the dynamics of an (advection-free) Reynolds-averaged planetary wind field can be formulated as a 2nd-order system of differential equations, which for $f_c \neq 0$ represents the IO. On this basis, we investigated the influence of surface friction on the IO of a non-growing CBL. Of special interest here is the interaction between shear-induced turbulence and turbulent surface friction, which depends on stability. As the tool for our investigation, we used a CBL model, based on MOS for the SL friction and the mixed layer assumption. As a first step we considered the model's behaviour in the asymptotic neutral and free-convection limits, for which we showed that the model's velocity-surface-stress relationship coincides with a quadratic (QS) and tends to a linear stress law (LS) respectively.

With respect to the equilibrium velocity, \mathbf{U}_{se} , we found that it is always situated on a half-circle in the velocity space defined by \mathbf{U}_g as chord. The exact position of \mathbf{U}_{se} on that circle does not depend on stability itself but rather on the strength of friction in the equilibrium, which can be generated by both shear and convection. However, the dynamic properties of the IO depend not only on the strength of equilibrium friction but also on stability, as the relative contribution of shear driven friction determines the non-linearity of the stress-law around the equilibrium. This we found to have a significant impact on the IO. From the general wind oscillator equation, we concluded that friction not only leads to damping but also contributes to the restoring force of the oscillation, and that damping is not only steered by friction strength but also by its temporal variation and its dependence on velocity.

In the proximity of the free convection limit (represented by the LM), these features result in an analytically simple harmonic oscillation with exponential damping and a constant periodicity of $2\pi/f_c$. However, for the neutral limit (represented by the QM), this leads to rather complex oscillatory behaviour, which is highly dependent on the actual position in velocity space. By means of a parametric oscillator analysis we then further compared the LM and the QM. It turned out that in spite of identical equilibrium friction, the overall damping of the QM is generally 50% stronger than that of the LM. The contribution of friction to the restoring force (the undamped part of the oscillator) is even 100% stronger, but has only minor consequences for the periodicity.

Finally, we characterized the general stability dependence of the CBL by demonstrating that a linear combination of velocity-stress relation asymptotes, the LS and the QS, can generally approximate the MOSS very well. By using this finding in the combination model (CM), we established a relationship that links the set of the external parameters, h , z_0 , f_c , \mathbf{U}_g and $(w'\Theta'_v)_s$ with a set of three effective parameters, \mathbf{U}_{se} , r_{cl} and r_{cq} , which together with f_c , completely determine the CBL wind oscillation. The CM parameters directly comprise the convective friction factor F_{CM} as a clean measure of effective stability, which weighs shear-driven turbulent momentum transport in the equilibrium state against the convection-driven turbulent momentum transport. Moreover, as it expresses the similarity of the IO with that of the LM and the QM, we can also understand F_{CM} as a measure of the typology of any particular MOSM oscillator. In this way the CM systematizes all our findings.

E.7 Appendix

E.7.1 Estimation of C_{dl}

Assuming $z_0 \ll h_{SL}$ and with $\hat{R} = \{2.4 + \ln(h/z_0)\}^{-1}$ the neutral drag coefficient (Eq. E.8) of the MOSS can be rewritten as

$$C_{dq} = \hat{R} \kappa^2. \quad (\text{E.38})$$

The drag law at the neutral limit then reads

$$\overline{w'U'}_s = -\hat{R} \kappa^2 |U| U. \quad (\text{E.39})$$

To estimate C_{dl} we consider the dimensionless drag coefficient C_{dq}^{conv} as the convective analogue to the neutral drag coefficient C_{dq} . In the proximity of the free convection limit, the turbulent exchange of horizontal momentum is predominantly driven by convective turbulence and shear driven turbulence is negligible. Hence one may replace the horizontal velocity scale $|U|$ times κ in Eq. E.38 by a convective vertical velocity scale, e.g. the Deardorff velocity $w_* = [g h / \overline{\theta'_v} (w' \theta'_v)_s]^{1/3}$, and arrive at

$$\overline{w'U'}_s = -\hat{R} \kappa w_* U. \quad (\text{E.40})$$

This defines the dimensionless convective drag coefficient as $C_{dq}^{\text{conv}} = \hat{R} \kappa$ and finally C_{dl} as

$$C_{dl} = C_{dq}^{\text{conv}} w_*. \quad (\text{E.41})$$

This specification of C_{dl} is a rather formal construct. But together with C_{dq} , it turns out that the parameters of the CM are well-scaled by C_{dl} , as shown in Appendix E.7.2.

E.7.2 Dependency of C_{cl} and C_{cq} on w_*

In section E.5 we stated (a) that C_{cl} should scale well with w_* and (b) that C_{cq} should be independent of w_* . To verify this we determined C_{cl} and C_{cq} as a function of w_* for a series of cases. These were constructed by varying $(w' \theta'_v)_s$ between 0 and 0.5 Kms^{-1} , and the geostrophic forcing between 2 and 6 ms^{-1} , for two different CBL depths (600 and 2000 m) and for a given $z_0 = 0.1 \text{ m}$ and $f_c = 10^{-4} \text{ s}^{-1}$. To combine these cases in one plot we normalize C_{cq} and C_{cl} (as estimated in Appendix E.7.1), which represent shear-induced and convection driven surface stress for arbitrary realistic cases, with C_{dq} and C_{dl} , which represent the same processes but at the two hypothetical stability limits of the MOSM. Figure E.13 shows that the graphs of all cases group well and that C_{cq}/C_{dq} (white dots) and C_{cl}/C_{dl} (black dots) are rather constant over a wide range of w_* , which supports statements (a) and (b). For C_{cl}/C_{dl} the denominator is proportional to w_* (Eq. E.41) and thus the numerator should be as well. This is alternatively displayed by the ratio $C_{cl}/C_{dq}^{\text{conv}} \approx w_*$ (white diamonds) with C_{dq}^{conv} being independent of w_* (Appendix E.7.1). For C_{cq}/C_{dq} , both denominator (Eq. E.38) and numerator are basically independent of w_* . Remarkably, but to be expected, C_{cq}/C_{dq} comes very close to 1 for $w_* \rightarrow 0$. The fact that C_{cl}/C_{dl} as well C_{cq}/C_{dq} differ from 1 for most cases simply demonstrates that the CM approximates the MOSM locally, as it was designed for.

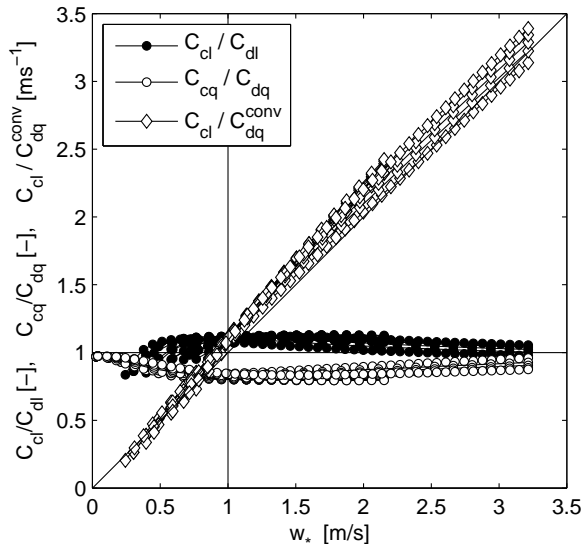


Figure E.13: Normalized parameters of the CM as a function of the Deardorff velocity w_* . Values based on C_{cl} are shown for $h/L_{se} < 3$.

E.7.3 The characteristic damping ratio \tilde{R}_D of the QM

The aim here is to demonstrate that the effective damping factor $D_{Qeff}(t)$ of the QM tends to be $3r_1$ compared to the $2r_1$ of the analogue LM. This is suggested by the numerical solutions for $R_D(t)$, which oscillate around a characteristic value $\tilde{R}_R = 3/2$ (section E.4.3). The numerical solution further suggests that this value is approached under the following conditions:

$$\begin{aligned} |\mathbf{U}_d(t)| &\ll |\mathbf{U}_{se}| && \text{(condition 1),} \\ \mathbf{U}_d(t) &\perp \mathbf{U}_{se} && \text{(condition 2).} \end{aligned}$$

We therefore wish to prove that $D_{Qeff} = 3 r_1$ under condition 1 and 2.

Under condition 1: Here, $|\mathbf{U}_d| \ll |\mathbf{U}_{se}|$. Therefore the angle β between \mathbf{U}_d and \mathbf{U}_{se} becomes small ($\beta(t) \rightarrow 0$) and we can approximate $\mathbf{U}(t)$ with its projection on \mathbf{U}_{se} (Figure E.14), which we call $\mathbf{U}_{pro}(t)$. This implies that we can express the quadratic stress law as follows:

$$\begin{aligned} \overline{w' \mathbf{U}'_s} &= -C_{dq} |\mathbf{U}_{pro}| \mathbf{U}, && \text{(E.42)} \\ \text{with } |\mathbf{U}_{pro}| &= u \cos(\alpha) + v \sin(\alpha), \end{aligned}$$

where α is the constant angle between u -component and \mathbf{U}_{se} (Figure E.14). Note that the modified stress law (Eq. (E.42)) is still 'quadratic' but omits the square root related to the use of the magnitude. Inserting this drag relationship in the momentum budget provides us with a replacement model (RM) for the QM for $|\mathbf{U}_d| \ll |\mathbf{U}_{se}|$. If we align the coordinate system with \mathbf{U}_{se} ($\alpha = 0$), the rotated replacement Model RRM reads (compare with the QM, Eq. (E.18))

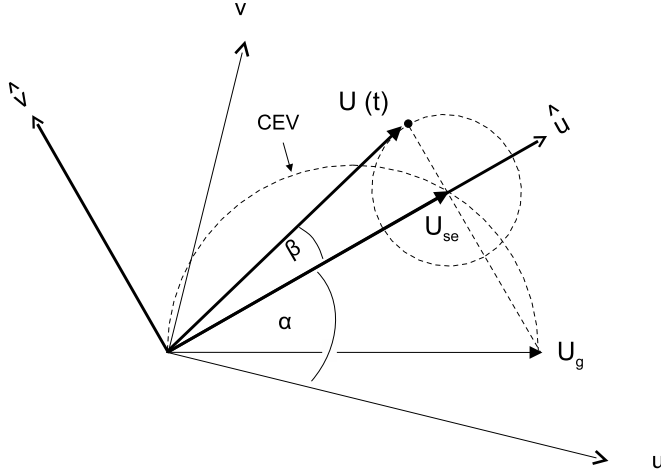


Figure E.14: Wind vector arrangement for the RM in an arbitrary coordinate system (u, v) and the rotated coordinate system (\hat{u}, \hat{v}) , aligned with \mathbf{U}_{se} . The velocity vector $\mathbf{U}(t)$ is displayed at a moment t , where $\hat{u}(t) = \hat{u}_{se}$ (condition 2 fulfilled). Furthermore, $\hat{\mathbf{U}}_{pro}$ is not displayed explicitly, as in this case $\hat{\mathbf{U}}_{pro} = \mathbf{U}_{se}$. The small circle around \mathbf{U}_{se} symbolises the rotational plane and does not represent the trajectory.

$$\frac{\partial \hat{u}}{\partial t} - f_c \hat{v} + f_c \hat{v}_g + r_q \hat{u}^2 = 0, \quad (\text{E.43})$$

$$\frac{\partial \hat{v}}{\partial t} + f_c \hat{u} - f_c \hat{u}_g + r_q \hat{u} \hat{v} = 0. \quad (\text{E.44})$$

The choice of the coordinate system implies that for equilibrium, $|\hat{\mathbf{U}}_{se}| = \hat{u}_{se}$ and $\hat{v}_{se} = 0$.

Remember that \mathbf{U}_{se} is situated somewhere on the CEV (Figure E.14). As a result, and by referring to Thales' theorem, the projection of \mathbf{U}_g on the \hat{u} -axis gives

$$\hat{u}_g = \hat{u}_{se}. \quad (\text{E.45})$$

Inserting this in the budget for u_{se} (Eq. (E.43)), with $\partial u_{se}/\partial t = 0$ and using $\hat{v}_{se} = 0$ and $r_1 = r_q \hat{u}_{se}$, we get

$$\hat{u}_{se}^2 r_q = \hat{u}_{se} r_1 = -f_c \hat{v}_g. \quad (\text{E.46})$$

Under conditions 1 & 2: For the rotated coordinate system, condition 2 implies that the \hat{u} -component of $\hat{\mathbf{U}}(t)$ equals \hat{u}_{se}

$$\hat{u}(t) = \hat{u}_{se}. \quad (\text{E.47})$$

Inserting expression (E.46) in the budget for the v -component gives

$$\frac{\partial \hat{v}}{\partial t} = -r_1 \hat{v}. \quad (\text{E.48})$$

With some manipulation and using expression (E.45), (E.46) and (E.48), we can finally formulate the oscillator equations for $\hat{\mathbf{U}}$ under condition 1 and 2 as

$$\begin{aligned} \frac{\partial^2 \hat{u}}{\partial t^2} + 3 r_1 \frac{\partial \hat{u}}{\partial t} + f_c^2 \hat{u} - f_c^2 \hat{u}_g &= 0, \\ \frac{\partial^2 \hat{v}}{\partial t^2} + (2 + \xi) r_1 \frac{\partial \hat{v}}{\partial t} & \end{aligned} \quad (\text{E.49})$$

$$+ (f_c^2 - r_q f_c \hat{v}_g) \hat{v} + r_q f_c \hat{v}^2 - \xi r_1 f_c \hat{u}_g - f_c^2 \hat{u}_g = 0,$$

$$\text{with } \xi = \frac{f_c}{f_c + r_q \hat{v}}.$$

This system of equations is homogeneous for both components. The second term on the left hand side is the damping term, as it is exclusively proportional to $\partial \hat{u} / \partial t$ or $\partial \hat{v} / \partial t$ respectively. For the u-component we directly find the damping factor $3r_1$. For the v-component we find the same value because under condition 1 $\hat{\mathbf{U}}_d(t) \rightarrow 0$, which implies $\hat{v} \rightarrow 0$ and therefore $\xi \rightarrow 1$.

Bibliography

- Akylas E, Tsakos Y, Tombrou M, Lalas DP. 2003. Considerations on minimum friction velocity. *Quart. J. Roy. Meteor. Soc.* **129**: 1929–1943.
- Arya S PS. 1977. Suggested revisions to certain boundary layer parameterization schemes used in atmospheric circulation models. *Mon. Wea. Rev.* **105**: 215–227.
- Baas P, Bosveld F, Lenderink G, van Meijgaard E, Holtslag AAM. 2010. How to design single-column model experiments for comparison with observed nocturnal low-level jets. *Quart. J. Roy. Meteor. Soc.* **136**: 671–648.
- Baker CJ. 2010. Discussion of ‘The macro-meteorological spectrum A preliminary study’ by R I Harris. *J. Wind Eng. Ind. Aerodyn.* **98**: 945–947.
- Ball FK. 1960. Control of inversion height by surface heating. *Quart. J. Roy. Meteor. Soc.* **86**: 483–494.
- Beljaars AC. 1994. The parametrization of surface fluxes in large-scale models under free convection. *Quart. J. Roy. Meteor. Soc.* **121**: 255–270.
- Beres JH. 2004. Gravity wave generation by a three-dimensional thermal forcing. *J. Atmos. Sci.* **61**: 1805–1815.
- Beyrich F, Klose B. 1988. Some aspects of modelling low-level jets. *Bound.-Layer Meteor.* **43**: 1–14.
- Blackadar AK. 1957. Boundary layer wind maxima and their significance for the growth of nocturnal inversions. *Bull. Amer. Meteor. Soc.* **38**: 283–290.
- Brown AR, Beljaars ACM, Hersbach H. 2006. Errors in parametrizations of convective boundary-layer turbulent momentum mixing. *Quart. J. Roy. Meteor. Soc.* **132**: 1859–1876.
- Brown AR, Grant AL. 1996. Large-eddy simulation and parametrisation of baroclinic boundary-layer. *Quart. J. Roy. Meteor. Soc.* **122**: 1779–1798.
- Brown AR, Grant AL. 1997. Non-local mixing of momentum in the convective boundary layer. *Bound.-Layer Meteor.* **84**: 1–22.
- Buajitti K, Blackadar AK. 1957. Theoretical studies of diurnal wind-structure variations in the planetary boundary layer. *Quart. J. Roy. Meteor. Soc.* **83**: 486–500.

- Byun DW, Arya SPS. 1986. A study of mixed layer momentum evolution. *Atmos. Env.* **20**: 715–728.
- Cadot, Couder Y, A D, S D, Tsinober A. 1997. Energy injection in closed turbulent flows: Stirring through boundary layers versus inertial stirring. *Phys. Rev. E* **56**.
- Cheinet S. 2003. A multiple mass-flux parameterization for the surface-generated convection. part i: Dry plumes. *J. Atmos. Sci.* **60**(18): 2313–2327.
- Conzemius RJ, Fedorovich E. 2006a. Dynamics of sheared convective boundary layer entrainment. part I: methodological background and large-eddy simulations. *J. Atmos. Sci.* **63**: 1151–1178.
- Conzemius RJ, Fedorovich E. 2006b. Dynamics of sheared convective boundary layer entrainment. part II: Evaluation of bulk model predictions of entrainment flux. *J. Atmos. Sci.* **63**: 1179–1199.
- Conzemius RJ, Fedorovich E. 2007. Bulk models of the sheared convective boundary layer: Evaluation through large eddy simulations. *J. Atmos. Sci.* **64**: 786–807.
- De Roode SR, Duynkerke PG, Jonker HJJ. 2004. Large-eddy simulation: how large is large enough? *J. Atmos. Sci.* **61**: 403–421.
- De Roode SR, Duynkerke PG, Siebesma AP. 2000. Analogies between mass-flux and reynolds-averaged equations. *J. Atmos. Sci.* **57**(10): 1585–1598.
- Deardorff JW. 1972. Numerical investigation of neutral and unstable planetary boundary layers. *J. Atmos. Sci.* **29**: 91–115.
- Deardorff JW. 1974a. Three-dimensional numerical study of the height and mean structure of a heated planetary boundary layer. *Bound.-Layer Meteor.* **7**.
- Deardorff JW. 1974b. Three-dimensional numerical study of turbulence in an entraining mixed layer. *Bound.-Layer Meteor.* **7**.
- Deardorff JW, Wilis GE. 1985. Further results from a laboratory model of the convective planetary boundary layer. *Bound.-Layer Meteor.* **32**: 205–236.
- Deardorff JW, Wilis GE, Killy DK. 1969. Laboratory investigation of non-steady penetrative convection. *J. Fluid Mech.* **35**: 7–31.
- Driedonks AGM. 1982. Models and observations of the growth of the atmospheric boundary layer. *Bound.-Layer Meteor.* **23**: 283–306.
- Dutton JA. 1976. *The ceaseless wind*. McGraw-Hill: New York, USA.
- Fedorovich E, Conzemius R, Esau I, Chow FK, Lewellen D, Moeng CH, Sullivan P, Pino D, Vilà-Guerau de Arellano J. 2004a. Entrainment into sheared convective boundary layers as predicted by different large eddy simulation codes. In: *Proceedings of the 16th conference on boundary layer and turbulence, American Meteorological Society*.

- Fedorovich E, Conzemius R, Mironov D. 2004b. Convective entrainment into a shear-free, linearly stratified atmosphere: Bulk models reevaluated through large eddy simulations. *J. Atmos. Sci.* **61**: 281–295.
- Fedorovich E, Nieuwstadt FMT, Kaiser R. 2001a. Numerical and laboratory study of horizontally evolving convective boundary layer. part I: Transition regimes and development of the mixed layer. *J. Atmos. Sci.* **58**: 70–86.
- Fedorovich E, Nieuwstadt FMT, Kaiser R. 2001b. Numerical and laboratory study of horizontally evolving convective boundary layer. part II: Effects of elevated wind shear and surface roughness. *J. Atmos. Sci.* **58**: 546–560.
- Garcia JR, Mellado JP. 2014. The two-layer structure of the entrainment zone in the convective boundary layer. *J. Atmos. Sci.* **71**: 1935–1955.
- Garratt JR, Wyngaard JC, Francey RJ. 1982. Winds in the atmospheric boundary layer - prediction and observation. *J. Atmos. Sci.* **39**: 1307–1316.
- Heus T, van Heerwaarden CC, Jonker HJJ, Siebesma AP, Axelsen S, van den Dries K, Geoffroy O, Moene AF, Pino D, de Roode SR, Vilà-Guerau de Arellano J. 2010. Formulation of the dutch atmospheric large-eddy simulation (dales) and overview of its applications. *Geosci. Model Dev.* **3**: 415–444.
- Holtzlag AAM. 1984. Estimates of diabatic wind speed profiles from near-surface weather observations. *Bound.-Layer Meteor.* **29**: 225–250.
- Hunt JCR, Durbin PA. 1999. Perturbed vortical layers and shear shelterings. *Fluid Dyn. Res.* **24**: 375–404.
- Jacobs CJM, De Bruin HAR. 1992. The sensitivity of regional transpiration to land-surface characteristics: significance of feedback. *J. Climate* **5**: 683–698.
- Jonker H, Jiménez M. 2014. Laboratory experiments on convective entrainment using a saline water tank. *Bound.-Layer Meteor.* **151**: 479–500.
- Jonker HJJ, van Reeuwijk M, Sullivan PP, Patton EG. 2013. On the scaling of shear-driven entrainment: a DNS study. *J. Fluid Mech.* **732**: 150–165.
- Khairoutdinov MF, Krueger SK, Moeng CH, Bogenschutz PA, Randall DA. 2009. Large-eddy simulation of maritime deep tropical convection. *Journal of Advances in Modeling Earth Systems* **1**(4). 15.
- Kim SW, Park SU, Moeng CH. 2003. Entrainment processes in the convective boundary layer with varying wind shear. *Bound.-Layer Meteor.* **108**: 221–245.
- Kim SW, Pino D, Vilà-Guerau de Arellano J. 2006. Parameterization of entrainment in a sheared convective boundary layer using a first-order jump model. *Bound.-Layer Meteor.* **120**: 455–475.
- Kolmogorov AN. 1941. The local structure of turbulence in incompressible viscous fluid for very large Reynolds numbers. In: *Turbulence and Stochastic Process: Kolmogorov's Ideas 50 Years On*, vol. 433. Proc. R. Soc. Lond., pp. 9–13.

- Kundu PK, Cohen IM. 2004. *Fluid mechanics*. Elsevier Academic Press: San Diego, USA.
- Lenschow DH. 1974. Model of the height variation of the turbulence kinetic energy budget in the unstable planetary. *J. Atmos. Sci.* **31**: 465–474.
- Lilly DK. 1968. Models of cloud-topped mixed layers under a strong inversion. *Quart. J. Roy. Meteor. Soc.* **94**: 292–309.
- Manins PC, Turner JS. 1978. The relation between the flux ratio and energy ratio in convectively mixed layers. *Quart. J. Roy. Meteor. Soc.* **104**: 39–44.
- Moeng CH, Sullivan Peter P. 1994. A comparison of shear-and buoyancy-driven planetary boundary layer flows. *J. Atmos. Sci.* **51**: 999–1022.
- Moeng CH, Sullivan PP. 2015. Large-eddy simulation. In: *Encyclopedia of Atmospheric Science, 2nd edition*, vol. 4, North GR, Pyle J, Zhang F (eds), Academic Press, pp. 232–240.
- Nguyen KX, Tong C. 2015. Investigation of subgrid-scale physics in the convective atmospheric surface layer using the budgets of the conditional mean subgrid-scale stress and temperature flux. *Journal of Fluid Mechanics* **772**: 295–329.
- Nieuwstadt FT, Westerweel J, Boersma BJ. 2016. *Turbulence: introduction to theory and applications of turbulent flows*. Springer.
- Ouwensloot HG, Vilà-Guerau de Arellano J. 2013. Analytical solution for the convectively-mixed atmospheric boundary layer. *Bound.-Layer Meteor.* **148**(3): 557–583.
- Paulson CA. 1970. The mathematical representation of wind speed and temperature profiles in the unstable atmospheric surface layer. *J. Applied Met.* **9**: 857–861.
- Peagle J, Rasch GE. 1973. Three-dimensional characteristics of diurnally varying boundary-layer. *Mon. Wea. Rev.* **101**: 746–750.
- Pham HT, Sarkar S, Bruckner KA. 2009. Dynamics of a stratified shear layer above a region of uniform stratification. *J. Fluid Mech.* **630**: 191–223.
- Pino D, Jonker HJJ, Vilà-Guerau de Arellano J, Dosio A. 2006a. Role of shear and the inversion strength during sunset turbulence over land: characteristic length scales. *Bound.-Layer Meteor.* **121**: 537–556.
- Pino D, Vilà-Guerau de Arellano J. 2008. Effects of shear in the convective boundary layer: analysis of the turbulent kinetic energy budget. *Acta Geophysica* **56**: 167–193.
- Pino D, Vilà-Guerau de Arellano J, Duynkerke PG. 2003. The contribution of shear to the evolution of a convective boundary layer. *J. Atmos. Sci.* **60**: 1913–1926.
- Pino D, Vilà-Guerau de Arellano J, Kim SW. 2006b. Representing sheared convective boundary layer by zeroth- and first-order-jump mixed-layer models: large-eddy simulation verification. *J. Applied Met.* **45**: 1224–1243.

- Randall DA. 1984. Buoyant production and consumption of turbulent kinetic energy in cloud-topped mixed layers. *J. Atmos. Sci.* **41**: 401–413.
- Rodier Q, Masson V, Couvreur F, Paci A. 2017. Evaluation of a buoyancy and shear based mixing length for a turbulence scheme. *Frontiers in Earth Science* **5**(65).
- Salesky S, Chamecki M, Bou-Zeid E. 2017. On the nature of the transition between roll and cellular organization in the convective boundary layer. *Bound.-Layer Meteor.* **163**: 41–68.
- Schalkwijk J, Jonker HJJ, Siebesma AP, Bosveld FC. 2015. A year-long large-eddy simulation of the weather over cabauw: An overview. *Monthly Weather Review* **143**(3): 828–844.
- Schröter JS, Moene AF, Holtslag AAM. 2013. Convective boundary layer wind dynamics and inertial oscillations: the influence of surface stress. *Quart. J. Roy. Meteor. Soc.* **139**: 1694–1711.
- Schumann U, Moeng CH. 1991. Plume budgets in clear and cloudy convective boundary layers. *J. Atmos. Sci.* **48**: 1758–1770.
- Shapiro A, Fedorovich E. 2010. Analytical description of a nocturnal low-level jet. *Quarterly Journal of the Royal Meteorological Society* **136**(650): 1255–1262.
- Siebesma AP, Cuijpers JWM. 1995. Evaluation of parametric assumptions for shallow cumulus convection. *J. Atmos. Sci.* **52**: 650–660.
- Siebesma AP, Soares PMM, Teixeira J. 2007. A combined eddy-diffusivity mass-flux approach for the convective boundary layer. *J. Atmos. Sci.* **64**: 1230–1248.
- Sing MP, McNider RT, Lin JT. 1993. An analytical study of diurnal wind-structure variations in the boundary layer and the low-level nocturnal jet. *Bound.-Layer Meteor.* **63**: 397–423.
- Song IS, Chun HY, Lane TP. 2003. Generation mechanisms of convectively forced internal gravity waves and their propagation to the stratosphere. *J. Atmos. Sci.* **60**: 1960–1980.
- Sorbjan Z. 2004. Large-eddy simulations of the baroclinic mixed layer. *Bound.-Layer Meteor.* **112**: 57–80.
- Stage SA, Businger JA. 1981. A model for entrainment into a cloud-topped marine boundary layer. part II: Discussion of model behavior and comparison with other models. *J. Atmos. Sci.* **38**: 2230–2241.
- Steenveld G, Mauritsen T, de Bruijn E, Vila-Guerau de Arellano J, G S, Holtslag A. 2008a. Evaluation of limited area models for the representation of the diurnal cycle and contrasting nights in cases99. *J. Applied Met.* **47**: 869–887.
- Steenveld GJ, Holtslag AAM, Nappo CJ, van de Wiel BJH, Mahrt L. 2008b. Exploring the possible role of small scale terrain drag on stable boundary layers over land. *J. Applied Met.* **47**: 2518 – 2530.

- Stevens B. 2002. Entrainment in stratocumulus-topped mixed layers. *Quarterly Journal of the Royal Meteorological Society* **128**(586): 2663–2690.
- Strang EA, Fernando HJS. 2001. Entrainment and mixing in stratified shear flows. *J. Fluid Mech.* **428**: 349–386.
- Stull RB. 1976a. The energetics of entrainment across a density interface. *J. Atmos. Sci.* **33**: 1260–1266.
- Stull RB. 1976b. Internal gravity waves generated by penetrative convection. *J. Atmos. Sci.* **33**: 1279–1286.
- Stull RB. 1988. *An introduction to boundary layer meteorology*. Kluwer Academic Publishers: Norwell, USA.
- Stull RB. 1994. A convective transport theory for surface fluxes. *J. Atmos. Sci.* **51**: 3–22.
- Sullivan PP, Moeng CH, Stevens B, Lenschow D, Mayor SD. 1998. Structure of the entrainment zone capping the convective atmospheric boundary layer. *J. Atmos. Sci.* **55**: 3042–3064.
- Sullivan PP, Patton EG. 2011. The effect of mesh resolution on convective boundary layer statistics and structures generated by large-eddy simulation. *J. Atmos. Sci.* **68**: 2395–2415.
- Tan ZM, Farahani MM. 1998. An analytical study of the diurnal variations of wind in a semi-geostrophic ekman boundary layer model. *Bound.-Layer Meteor.* **86**: 313–332.
- Taylor JR, Sarkar S. 2007. Internal gravity waves generated by a turbulent bottom ekman layer. *J. Fluid Mech.* **590**: 331–354.
- Taylor RJ. 1952. The dissipation of kinetic energy in the lowest layers of the atmosphere **78**: 179–185.
- Tennekes H. 1973. A model for the dynamics of the inversion above a convective boundary layer. *J. Atmos. Sci.* **30**: 558–567.
- Thorpe AJ, Guymer TH. 1977. The nocturnal jet. *Quart. J. Roy. Meteor. Soc.* **103**: 633–653.
- Tsinober A. 2001. *In informal introduction to turbulence*. Kluwer Academic Publishers: Dordrecht, The Netherlands.
- Van de Wiel BJH, Moene AF, Steeneveld GJ, Baas P, Bosveld FC, Holtslag AAM. 2010. A conceptual view on inertial oscillations and nocturnal low-level jets. *J. Atmos. Sci.* **67**: 2679–2689.
- Van Heerwaarden CC, Mellado JP. 2016. Growth and decay of a convective boundary layer over a surface with a constant temperature. *J. Atmos. Sci.* **73**: 2165–2177.

- Van Heerwaarden CC, Mellado JP, De Lozar A. 2014. Scaling laws for the heterogeneously heated free convective boundary layer. *J. Atmos. Sci.* **71**: 3975–4000.
- Van Heerwaarden CC, van Stratum BJH, Heus T, Gibbs JA, Fedorovich E, Mellado JP. 2017. Microhh 1.0: a computational fluid dynamics code for direct numerical simulation and large-eddy simulation of atmospheric boundary layer flows. *Geoscientific Model Development Discussions* **2017**: 1–33.
- Van Zanten MC, Duynkerke PG, Cuijpers JWM. 1999. Entrainment parameterization in convective boundary layers. *J. Atmos. Sci.* **56**: 813–828.
- Wilczak JM, Businger JA. 1983. Thermally indirect motions in the convective atmospheric boundary layer. *J. Atmos. Sci.* **40**: 343–358.
- Wyngaard JC. 2010. *Turbulence in the atmosphere*. Cambridge University Press: Cambridge, United Kingdom.
- Wyngaard JC, Brost RA. 1984. Top-down and bottom-up diffusion of a scalar in the convective boundary layer. *J. Atmos. Sci.* **41**: 102 – 112.
- Zilitinkevich S, Fedorovich EE, V SM. 1992. Numerical model of a non-steady atmospheric planetary boundary layer, based on similarity theory. *Bound.-Layer Meteor.* **59**: 387–411.
- Zilitinkevich SS. 1975. Comments on "A model for the dynamics of the inversion above a convective boundary layer". *J. Atmos. Sci.* **32**: 991 – 992.
- Zilitinkevich SS. 1991. *Turbulent penetrative convection*. Avebury Technical.
- Zilitinkevich SS, Esau IN. 2002. On integral measures of the neutral barotropic planetary boundary layer. *Bound.-Layer Meteor.* **104**: 371–379.

Research for the paper in appendix E (Schröter *et al.*, 2013) was financially supported in the framework of the project 'Integrated observations and modeling of Greenhouse Gasbudgets at the national level in the Netherlands', part of the program 'Climate changes Spatial Planning'.

Financial support from Wageningen University for printing this thesis is gratefully acknowledged.

The cover illustration shows a cross section through the vertical velocity field of a sheared LES-CBL in direction of the mean flow. Vigorous turbulence in the lower flow domain as well as gravity waves with tilted fronts in the upper non-turbulent flow domain are clearly recognizable.

Cover design by Joel S. Schröter

Printed by Digiforce || ProefschriftMaken



*Netherlands Research School for the
Socio-Economic and Natural Sciences of the Environment*

D I P L O M A

For specialised PhD training

The Netherlands Research School for the
Socio-Economic and Natural Sciences of the Environment
(SENSE) declares that

Joel Simon Schröter

born on 18 June 1975 in Villingen-Schwenningen, Germany

has successfully fulfilled all requirements of the
Educational Programme of SENSE.

Wageningen, 05 June 2018

the Chairman of the SENSE board

Prof. dr. Huub Rijnaarts

the SENSE Director of Education

Dr. Ad van Dommelen

The SENSE Research School has been accredited by the Royal Netherlands Academy of Arts and Sciences (KNAW)



K O N I N K L I J K E N E D E R L A N D S E
A K A D E M I E V A N W E T E N S C H A P P E N



The SENSE Research School declares that **Joel Simon Schröter** has successfully fulfilled all requirements of the Educational PhD Programme of SENSE with a work load of 49.1 EC, including the following activities:

SENSE PhD Courses

- o Physical Modelling (2007)
- o Environmental research in context (2010)
- o Research in context activity: 'Co-organizing Symposium on particular matter pollution in the Netherlands: Another one bites the dust? 10 May 2007, Wageningen, The Netherlands'

Other PhD and Advanced MSc Courses

- o JMBC course 'Turbulence', J. M. Burgerscentrum, TU Delft (2006)
- o CarboEurope-IP's Spring School 2006, University of Heidelberg, (2006)
- o Summer School Session "Atmospheric Boundary Layers: Concepts, Observations, and Numerical Simulations", IMAU, Utrecht University and Wageningen University (2008)
- o Boundary-Layer Processes, Wageningen University (2006)
- o Mesoscale Meteorological Modelling, Wageningen University (2006)

External training at a foreign research institute

- o Training in High performance Computing, Spanish High performance Computing Centre (BSC), Universitat Politècnica de Catalunya, Spain (2012)

Management and Didactic Skills Training

- o Assisting in the BSc. course 'Atmosphere-Vegetation-Soil Interactions' (2008-2009)

Selection of Oral Presentations

- o *Conceptual analysis of the non-stationarity of wind fields in the CBL.* American Meteorological Society (AMS) 18th Symposium on Boundary Layers and Turbulence, 09-13 June 2008, Stockholm, Sweden
- o *Advective influence on the CO₂-exchange of a forest site ... and the role of nocturnal subsidence!* BBOS-Boundary Layer and Turbulence workshop, 28 May 2009, Utrecht, The Netherlands
- o *Inertial oscillations of an entraining convective boundary layer flow.* Invited talk at MPI Hamburg, 16 April 2013, Hamburg Germany

Grants

- o HPC Europe 2 grant

SENSE Coordinator PhD Education

Dr. Peter Vermeulen